



**HAL**  
open science

# Atomistic Modelling of Environment Effects on Reactive Metal Interfaces

Stephan N. Steinmann

► **To cite this version:**

Stephan N. Steinmann. Atomistic Modelling of Environment Effects on Reactive Metal Interfaces. Theoretical and/or physical chemistry. Ecole Normale Supérieure de Lyon, 2019. tel-04721451

**HAL Id: tel-04721451**

**<https://hal.science/tel-04721451v1>**

Submitted on 4 Oct 2024

**HAL** is a multi-disciplinary open access archive for the deposit and dissemination of scientific research documents, whether they are published or not. The documents may come from teaching and research institutions in France or abroad, or from public or private research centers.

L'archive ouverte pluridisciplinaire **HAL**, est destinée au dépôt et à la diffusion de documents scientifiques de niveau recherche, publiés ou non, émanant des établissements d'enseignement et de recherche français ou étrangers, des laboratoires publics ou privés.

Habilitation à diriger des recherches

# Atomistic Modelling of Environment Effects on Reactive Metal Interfaces

Présentée le 17 décembre 2019

En vue d'obtenir l'Habilitation à diriger des Recherches  
de l'Ecole Normale Supérieure de Lyon  
par

Stephan N. Steinmann



Devant le jury composé de :

Prof. Carlo Adamo, rapporteur

Dr. Dominique Costa, rapporteur

Prof. Jean-François Paul, rapporteur

Dr. Monica Calatayud, membre du jury

Dr. Marie-Liesse Doublet, membre du jury

Prof. Dr. Elise Dumont, membre du jury

Prof. Wolfgang Schmickler, membre du jury

Lyon, ENS de Lyon, 2019



To Laëtitia

La fureur de la plupart des Français, c'est d'avoir de l'esprit, et la fureur de ceux qui  
veulent avoir de l'esprit c'est de faire des livres.  
— Montesquieu, Les lettres persannes



Cependant il n'y a rien de si mal imaginé : la Nature semble avoir sagement pourvu à ce que les sottises des hommes fussent passagères, et les livres les immortalisent. Un sot doit être content d'avoir ennuyé tout ceux qui ont vécu avec lui : il veut encore tourmenter les races futures ; il veut que sa sottise triomphe de l'oubli dont il aurait pu jouir comme du tombeau ; il veut que la postérité soit informée qu'il a vécu, et qu'elle sache à jamais qu'il a été un sot.

— Montesquieu, Les lettres persannes



## Acknowledgements

This “Habilitation à diriger des recherches” (HDR) is the results of the research I have done since my arrival in Lyon, in late 2013.

There are two persons who have determined the very existence of this HDR: first and foremost my beloved wife, Laëtitia, who has given me confidence, strength and has directed my efforts towards settling in Lyon. Philippe Sautet is the second most important person in this respect: he has provided me the opportunity to come to Lyon and to pursue an academic career by supporting and encouraging my strive to fit in the local research context.

Several other people have played important roles in my professional life of the past five years. In particular, Carine Michel has greatly facilitated my journey through the jungle of the french academic system and the introduction to the world of heterogeneous catalysis. My collaboration with Tangui Le Bahers has also been very enjoyable and, through his focusedness, very fruitful. Elise Dumont has been key for my integration into the network of French theoretical chemists and my lab-mate, Tao Jiang, enlightens the day through his sarcasm. I had many great scientific discussions with Paul Fleurat-Lessard, who, unfortunately for me, moved away to Dijon. Moreover, the current and previous members of the “Axe de chimie théorique” have contributed to a stimulating work environment where I have felt welcome for which I am grateful to all of them.

My warmest thanks go also to Chantal Andraud, director of the “Laboratoire de Chimie”, for accepting me in her research unit and to the members of the “pôle gestion” who are key for managing human resources and the participations at conferences. Last but not least, the IT support of Christian Melkonian is very valuable for a functional work environment

A lot of the work presented herein would not have been possible without the motivation, skills and energy of the students that I have been lucky to accompany in the last few years. The highest gratitude goes to Emanuele Vignola, Benjamin Schweitzer, Ruben Staub, Sarah Blanck and Paul Clabaut.

The funding agencies (mostly ANR and the ARA region) as well as industrial partners (mostly Total) are acknowledged for their generous contributions enabling basic research.

I am also honored and grateful to Carlo Adamo, Monica Calatayud, Dominique Costa, Marie-Liesse Doublet, Elise Dumont, Jean-François Paul and Wolfgang Schmickler for having accepted to be on my jury.





## Abstract

This habilitation thesis provides an overview on work accomplished during the last five years in the field of the atomistic modelling of reactive metal interfaces. Metal/gas and metal/liquid interfaces are key to many catalytic processes, as well as technologically relevant issues such as corrosion, lubrication and surface functionalization. All these processes have in common that the surface is subject to reactive conditions, which influence in turn the reactivity of the surface. In electrocatalysis, for example, the electrochemical potential can tune the adsorption energy of molecules and ions. Achieving reliable, atomistic models of the metal/liquid and metal/gas interface provides a multitude of opportunities for method developments, which make them very appealing. The general introduction discusses the importance of interfaces and the challenges the computational chemist faces. The semi-hydrogenation of acetylene, which is used to purify ethylene, sets the stage for the next two chapters. One develops a model Hamiltonian to describe the the surface rearrangements of alloy surfaces in the presence of a reactive gas and the other assesses the competition between the semi-hydrogenation and side-reactions which form complex oligomerization by-products. Then an energy decomposition analysis of the interaction of adsorbates with metallic surfaces has been developed to provide detailed insight in the governing interactions at metallic interfaces, which can also be exploited for developing force fields. Switching to the metal/liquid interface, we start by discussing how to rapidly explore complex reaction networks through group-additivity methods. Next, we introduce a method to compute solvation free energies at the solid/liquid interface and highlight the need to develop advanced force fields for the transition metal/water interface. Last but not least, we investigate the influence of the explicit modelling of the electrochemical potential on the reactivity of carbon dioxide in aprotic conditions. The scientific outlook is structured around ongoing projects, mostly related to modelling the metal/liquid interface. Nevertheless, the automatic establishment of model Hamiltonians and the development of beyond DFT methods, together with the sulfidation process leading to MoS<sub>2</sub> on a  $\gamma$ -alumina support express my continuing interest in the metal/gas interface.

**Keywords:** first principles simulations, heterogeneous (electro-)catalysis, metal/gas and metal/liquid interface





## Résumé

Cette thèse d'habilitation donne un aperçu des travaux accomplis au cours des cinq dernières années dans le domaine de la modélisation atomistique des interfaces métalliques. Les interfaces métal / gaz et métal / liquide sont essentielles pour de nombreux processus catalytiques, ainsi que pour des problèmes liés à la technologie, tels que la corrosion, la lubrification et la fonctionnalisation de surfaces. Tous ces processus ont en commun que la surface est soumise à des conditions réactives qui influent à leur tour sur la réactivité de la surface. Par exemple, dans l'électrocatalyse, le potentiel électrochimique peut inhiber ou améliorer l'adsorption de divers molécules et ions. Puisqu'une description atomistique fiable des interfaces métal / liquide et métal / gaz demande un développement de méthodes, ces interfaces sont particulièrement intéressantes. L'introduction générale traite de l'importance de ces interfaces et des défis auxquels le chimiste computationnel est confronté. La semi-hydrogénation de l'acétylène, utilisée pour purifier l'éthylène, est le sujet des deux chapitres suivants. L'un développe un hamiltonien modèle pour les réarrangements des surfaces d'alliages en contact avec un gaz réactif. L'autre chapitre décrit la concurrence entre la semi-hydrogénation et les réactions secondaires qui forment des sous-produits d'oligomérisation. L'analyse de décomposition énergétique de l'interaction d'adsorbats avec des surfaces métalliques, introduit dans le chapitre suivant, fournit des informations détaillées qui peuvent aussi être exploitées pour le développement de champs de force. Passant à l'interface métal / liquide, nous commencerons par discuter de la manière d'explorer rapidement des réseaux de réaction complexes au moyen de méthodes d'additivité de groupe. Ensuite, nous présenterons une méthode permettant de calculer les énergies sans solvatation à l'interface solide / liquide et soulignons la nécessité de développer des champs de force avancés pour l'interface métal de transition / eau. Enfin, nous étudions l'influence de la modélisation explicite du potentiel électrochimique sur la réactivité du dioxyde de carbone dans des conditions aprotiques. Les projets de recherche sont structurés autour de projets en cours, principalement liés à la modélisation de l'interface métal / liquide. Néanmoins, l'établissement automatique d'hamiltoniens modèles et le développement de méthodes au-delà de la DFT, ainsi que l'investigation du processus de sulfuration conduisant à un MoS<sub>2</sub> supporté sur de l'alumine- $\gamma$ , témoignent de mon intérêt pour l'interface métal / gaz.

**Mots-clés :** simulations ab initio, (electro-)catalyse hétérogène, interface métal/gaz et métal/liquide





# Contents

<b>Acknowledgements</b>	<b>v</b>
<b>Abstract</b>	<b>vii</b>
<b>Résumé</b>	<b>ix</b>
<b>Table of Contents</b>	<b>xi</b>
<b>1 Introduction</b>	<b>1</b>
1.1 Metallic Interfaces are Key for Science and Technology . . . . .	1
1.2 Structural Choices when Modelling Metallic Interfaces . . . . .	5
1.3 How to Validate Theoretical Models? . . . . .	7
1.4 Pillars for Convincingly and Reliably Model Metal/Liquid Interfaces . .	9
1.5 Choice of Included Works . . . . .	14
Bibliography . . . . .	14
<b>2 Acetylene Adsorption on Pd-Ag Alloys: Evidence for Limited Island Formation and Strong Reverse Segregation from Monte Carlo Simulations</b>	<b>23</b>
<b>3 Evaluating the Risk of C-C Bond Formation during Selective Hydrogenation of Acetylene on Palladium</b>	<b>33</b>
<b>4 Energy Decomposition Analysis for Metal Surface-Adsorbate Interactions by Block Localized Wave Functions</b>	<b>45</b>
<b>5 Group Additivity for Aqueous Phase Thermochemical Properties of Alcohols on Pt(111)</b>	<b>59</b>
<b>6 Solvation free energies for periodic surfaces: comparison of implicit and explicit solvation models</b>	<b>71</b>
<b>7 Force Field for Water over Pt(111): Development, Assessment, and Comparison</b>	<b>85</b>
<b>8 Impacts of electrode potentials and solvents on the electroreduction of CO<sub>2</sub>: a comparison of theoretical approaches</b>	<b>101</b>
<b>9 Electro-carboxylation of butadiene and ethene over Pt and Ni catalysts</b>	<b>119</b>



## Contents

---

<b>10 Projects</b>	<b>129</b>
10.1 Tools for Automatically Generate Lattice Based Cluster Expansions (2017–2020) . . . . .	129
10.2 Force Fields for Metal/Water Interactions (2018–2021) . . . . .	130
10.3 Towards an Atomistic Understanding of Wettability for Industrial Lubricants (2018–2021) . . . . .	131
10.4 Genesis of supported MoS <sub>2</sub> on $\gamma$ -alumina (2018–2021) . . . . .	132
10.5 Use of MoS <sub>2</sub> in Electrocatalysis for Hydrogen Evolution (2019–2023) . .	133
10.6 Evaluating Soot–Surface and Detergent–Surface Interactions for the Efficiency of Fuel Additives (2019–2020) . . . . .	134
10.7 Transition-metal Chalcogenides for Electrochemical CO <sub>2</sub> Reduction (2020?) . . . . .	134
10.8 Embedded Wave Function Approaches at the Metal Interface (2020?) .	135
Bibliography . . . . .	136
<b>11 General Conclusions</b>	<b>139</b>
<b>Curriculum Vitae</b>	<b>141</b>
<b>Publication List</b>	<b>149</b>



# 1 Introduction

## 1.1 Metallic Interfaces are Key for Science and Technology

Interfaces between metals and a liquid or gaseous phase are key in many areas of science and technology. In this section I will first highlight the importance of the metal/gaseous interfaces and the role of their atomistic structure and then turn to the metal/liquid interface.

For historic reasons of the theory group of the “Laboratoire de Chimie”, heterogeneous catalysis comes first. Metal catalysts are involved in many industrial processes, from petrochemistry (e.g., hydrogenations or epoxidation), to ammonia synthesis, but also for reforming fossil fuels to hydrogen.<sup>1</sup> The metal/gas interfaces have been studied in details over the last thirty years, both theoretically and experimentally with varying techniques, from molecular beam experiments on single-crystals<sup>2</sup> to operando spectroscopy of reactions occurring on nanoparticles.<sup>3</sup> In some more specialized applications, the metal is polarized by an electric field,<sup>4</sup> an applied electrochemical potential<sup>5</sup> or by strong metal support interactions.<sup>6</sup> The latter is inscribed in the larger context of support effects on nanoparticle catalysts, of which an example is given in Figure 1.1.

Still in a similar context, metallic films are also used in getters, where they adsorb and absorb reactive, residual gases in vacuum devices.<sup>7</sup> In these applications it becomes obvious that the metallic surface undergoes a severe transformation between production, typically as a pure metal, and its functional state. In a functional getter, hydrides, carbides and nitrides are formed for example. This change in composition affects the reactivity of the surface and ultimately leads to the death of the device. Similarly, metallic films can be used as membranes to separate gaseous hydrogen.<sup>8</sup> Hydrogen, a reactive gas, forms hydrides with many metals, which changes the physical properties (e.g., mechanical stability) of the initially metallic membranes.

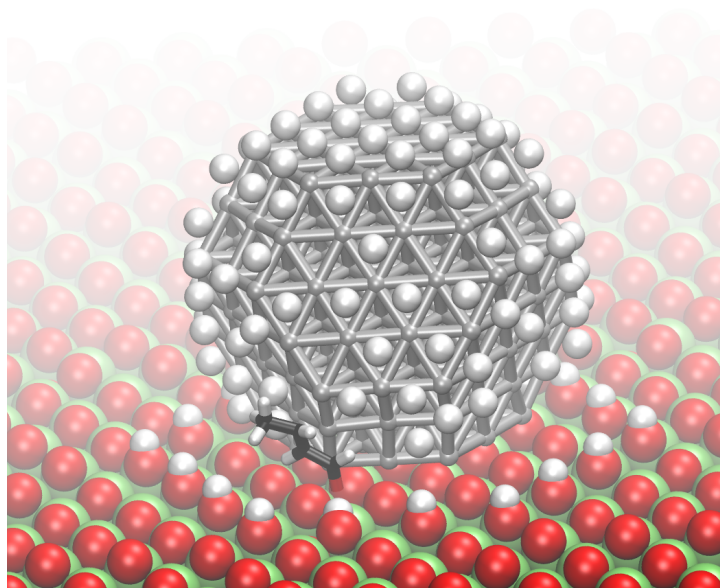


Figure 1.1 – Example of a Pd nanoparticle supported on CeO<sub>2</sub> under a hydrogen pressure. The adsorbate is crotonaldehyde. Colorcode: Pd: grey, Ce: green, O: red, H: white, C: black. Courtesy of David Loffreda.

The transformation of metals by reactive gases such as CO, H<sub>2</sub>S or F<sub>2</sub> is generally called “corrosion” and has a significant impact on chemical engineering. The impact of these corrosive gases is either reduced by metallurgical solutions, i.e., by choosing a resistant alloy, or by special coatings, for instance Teflon, which can be safer, cheaper or both. These corrosion phenomena are not only of concern in chemical industry working with reactive gases, but also affects large infrastructures such as oil-pipelines<sup>9</sup> and the public is made aware of regular re-painting of metallic buildings and infrastructures such as the Eifel tower<sup>10</sup> or the Golden Gate bridge<sup>11</sup>. Corrosion being an ill-controlled and slow phenomenon, its atomistic understanding is underdeveloped compared to other metal/gas interfaces, slowing down the development of improved but non-toxic corrosion inhibitors.<sup>12</sup>

Corrosion actually bridges the solid/gas and solid/liquid interfaces, as it may involve a liquid phase that acts as an accelerator for the electrochemical processes at its origin. Corrosion by sea water is maybe the best example in this context, where, in addition of special paints, the use of sacrificial anodes is wide-spread and still a topic of innovation.<sup>13</sup> But just like for solid/gas interfaces, corrosion at the solid/liquid interface is not often at the center of fundamental research. Overall, compared to the annual cost of ~2-3% of gross domestic product, the detailed understanding of corrosion is underdeveloped.<sup>14</sup>

Together with electrolysis for the production of reactive metals or halogens, metal

## 1.1. Metallic Interfaces are Key for Science and Technology

---

plating is one of the major industrial applications of electrochemistry.<sup>15</sup> Metal plating can be seen as the bright, reverse direction of corrosion, i.e., metal plating is a quite well controlled process. Therefore, it would lend itself to a fundamental understanding. Furthermore, compared with bulk electrolysis or electrometallurgy, the solid/liquid interface plays a more prominent role, simply because the critical step is the deposition of a (foreign) metal on a pre-existing surface, including plastic substrates.<sup>16</sup> In the later cases, the metal interface is being produced during the reaction, which is quite unusual considering the other topics discussed in this section.

Staying in the realm of electrochemistry, most batteries contain a liquid electrolyte and it is the reaction of the soluble species at the anode and cathode that is responsible for the voltage difference between charging and discharging and, thus, for the energy efficiency loss.<sup>17</sup> Furthermore, the reactions at the solid/liquid interface are responsible for the infamous batteries that burst into flames.<sup>18</sup> Due to these safety concerns, considerable research is now devoted to the understanding and mastering of these unwanted side reactions in complex environments.<sup>19</sup>

Lubrication, where a substance is added between two solids to reduce friction, mostly occurs at an other metal/liquid interface of immense technological importance. However, just like corrosion,<sup>12</sup> tribology is not investigated much among chemists and even less among computational chemists.<sup>20</sup> It is likely that the lack of atomistic modelling in these domains reflect the lack of atomically detailed knowledge (through characterization) *and* interest in the respective communities. Instead, macroscopic scale, “engineering”, models and empirical tests are considered sufficient and/or more trustworthy to rationalize the experimental observations.

The hybrid nature of self-assembled monolayers (SAMs) between the solid surface and the soft-matter adsorbates does not allow them to be classified in either solid/vacuum or solid/liquid interfaces.<sup>21</sup> Since SAMs feature intriguing physical properties,<sup>22;23</sup> they play a major role for functionalized materials and eventually in molecular electronics.<sup>24</sup>

To finish this overview as it started, let us turn back to catalysis: Heterogeneous catalysis at the metal/liquid interface is most relevant in two large categories: transformation of biomass derived molecules and electrocatalysis. In contrast to rather apolar petroleum sourced molecules, biomolecules are not very volatile and their transformation is, therefore, often carried out in aqueous solution, where they tend to be soluble.<sup>25</sup> Furthermore, water is a green solvent and allows to perform reactions at high, low or neutral pH, which tunes the reactivity, but also the surface state of catalysts. The presence of water has been shown to significantly affect the relative performances of different metal catalysts, so that the knowledge accumulated over decades of petrochemistry needs to be revised and novel catalytic systems need to be developed.<sup>26;27</sup> However, the exact role played by the solvent is not yet well understood and is likely to be multi-dimensional. First, the solvent is in competition with reactants and products

## Chapter 1. Introduction

---

for adsorption, second it influences the adsorption configuration of flexible molecules, third adsorbed water molecules can effectively act as co-catalysts and for instance “assist” proton transfers and fourth it can alter the catalyst support.<sup>28</sup>

Because in heterogeneous electrocatalysis the reactions are occurring at the electrode surface, the metal/liquid interface is key. Furthermore, the presence of the electrochemical potential structures the solvent and the electrolyte at the interface,<sup>29-31</sup> which can lead to peculiar reactivity.<sup>32</sup> Electrocatalysis is gaining impetus, mostly powered by the search for efficient energy storage of intermittent, renewable, electricity such as wind and solar power.<sup>33</sup> Indeed, electrocatalysis promises to convert electricity into chemical energy and vice versa with minimal energy loss. However, this supposes electrocatalysts with very low overpotentials. This conditions is essentially only met for the hydrogen evolution (HER) or the hydrogen oxidation (HOR) reaction over platinum. This is a severe limitation, as platinum is rare and very expensive. Furthermore, electrocatalysis always combines a reduction reaction at the cathode and an oxidation reaction at the anode. Hence, the opposite reaction to HER or HOR, typically the oxygen evolution (OER) or oxygen reduction (ORR) reaction, implies energy losses due to their overpotentials. Beyond these major electrocatalytic reactions, several other systems are studied intensively, with CO<sub>2</sub> reduction and NH<sub>3</sub> production being the most important ones. In contrast to water electrolysis and hydrogen fuel cells, these reactions are studied for their electro-synthetic potential, i.e., to convert green-house gas CO<sub>2</sub> into valuable chemicals<sup>34</sup> and to avoid the need for H<sub>2</sub> production for use in the Haber-Bosch process, which could also help to decentralize ammonia production.<sup>35</sup>

The next three sections mostly dive into the challenges encountered when investigating interfaces under reactive conditions via atomistic simulations. The discussion is heavily biased to issues in the context of heterogeneous (electro-)catalysis. Hence, despite the above appraisal of the almost universal importance of interfaces, the subsequent sections do not seek to encompass all relevant phenomena. For instance, pressure induced reactivity observed in some tribological applications will not be discussed any further. The aim is not to give a comprehensive overview on *how* to deal with the challenges, nor to give an exhaustive list, but rather to give personal overview on what seems to be holding the community back from making reliable, experimentally relevant predictions. Some of the topics also concern the interpretation of experimental observations, but in my experience most computational chemists have a flexible mind, so that they succeed in “bending” around most obstacles. This state of mind is at the same time a strength (only very few questions can be answered with certainty using computational chemistry) and weakness (overinterpretation) and can lead to rather heated debates.<sup>36;37</sup> Since the habits in the community are unlikely to change and there is a certain pressure from experimental colleagues to provide answers to any possible question, it seems judicious to steadily push the computational methods towards higher reliability by improving models on the one hand and more detailed validation on the other hand.

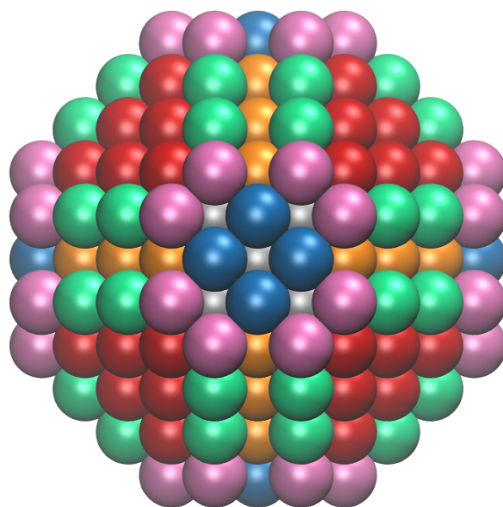


Figure 1.2 – Unreconstructed spherical fcc nanoparticle with 369 atoms ( $\sim 20$  Å diameter). Color code: Coordination number 12: silver; 11: orange; 9: red; 8: blue; 7: green; 6: pink.

## 1.2 Structural Choices when Modelling Metallic Interfaces

One of the most fundamental differences between modelling solution chemistry and systems involving solids is that molecules in solution have, in general, a well known geometry. There might be several conformers, but overall the structure is known: as long as you know how to draw it on paper, you can draw it in a computer. The same can only be said for (experimental) model systems when it comes to solids interfaces: Single-crystal surfaces have a well defined geometry that lends itself for straightforward computations. However, beyond model studies the importance of single crystals in actual chemical applications is very limited.<sup>38</sup> In practice, polycrystalline or amorphous surfaces are largely dominating and in catalysis one often deals with supported nanoparticles. Figure 1.1 shows an example of a Pd<sub>201</sub> nanoparticle on a ceria support under a pressure of H<sub>2</sub> for the hydrogenation of croton aldehyde. Depending on the morphology, a single nanoparticle features a multitude of sites. Consider, for instance, the near spherical, unreconstructed nanoparticle of Figure 1.2: at least 4 coordination numbers are present on the surface, which are expected to have different reactivities. Furthermore, for crystalline nanoparticles with diameters below 2 nm, the effects of edges and corners also tune the reactivity of the single-crystal like facets.<sup>39</sup> Nevertheless, for larger nanoparticles, the corresponding single-crystal surfaces can be considered representative models. To make matters worse, nanoparticles have been observed to be highly mobile during reaction conditions,<sup>40</sup> so that modelling a static geometry might not be relevant. Even for large, crystalline nanoparticles many surfaces can be nearly equally important, since their relative abundance depends on their relative surface free energies which are the parameters that determine the thermodynamic shape of (nano)crystals according to the Wulff reconstruction.<sup>41;42</sup>

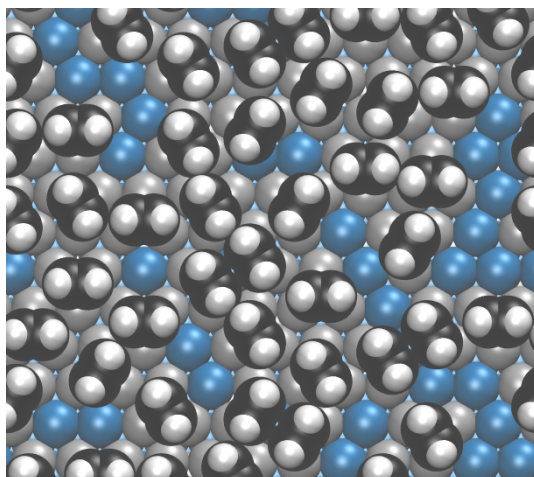


Figure 1.3 – A typical Pd<sub>0.24</sub>/Ag<sub>0.76</sub> alloy arrangement at 400 K under 1 bar of acetylene.<sup>47</sup> Pd is represented in gray and Ag in blue.

The surface free energies themselves depend on the reaction conditions, which means that the morphology might change between the nanoparticle synthesis and its steady-state under catalytic conditions.<sup>43</sup> Furthermore, nanoparticles are usually not used in suspension, but rather deposited on solid supports such as “carbon”, alumina, ceria etc. The role of the support can be manifold and, therefore, adds complexity to the choice of the relevant structural model. Instead of being inert, the most convenient assumption, the support can be catalytically active, which means that it should also be modelled. Alternatively, it can take part in “strong metal support interactions”,<sup>44</sup> where mobile species migrate from the support to the nanoparticles or vice versa, which is also known as (back-)spill over.<sup>6</sup> If the support interacts more weakly with the nanoparticle, it can modify some of its surface free energies and thus the overall shape. Last but not least, the interface between the support and the nanoparticle may possess specific catalytic properties, which necessitates an explicitly model of this three-phase boundary,<sup>45</sup> such as in Figure 1.1. This constitutes the most cumbersome, but also most complete structural model of catalysis on supported nanoparticles.<sup>46</sup>

Alloys provide yet another axis of complexity: depending on the particular alloy, it can be a solid solution (random distribution) or an ordered alloy. Similarly, segregation effects can lead to strong rearrangements under reactive conditions.<sup>48</sup> For these systems, one of the major complications compared to pure metals is the quickly growing number of individual sites that can have vastly differing catalytic effects. The resulting reverse segregated, disordered surface state is exemplified by the AgPd surface under an acetylene pressure of Figure 1.3. High entropy alloys are, in this category, the most challenging, with thousands of possible active sites. Therefore, only the simplest adsorbates can be efficiently modelled on such surfaces by exploiting cluster expansions and/or machine learning techniques.<sup>49</sup>

### 1.3. How to Validate Theoretical Models?

---

Given these complexities regarding the structural model, how should it be dealt with? - While there is probably not a unique answer to this question, there is at least a “rational” way address it: Following Occham’s razor, one starts with the simplest model, which tends to be the most stable single-crystal surface of a given metal under vacuum conditions. If this model does not reflect the experimental trends, improvements are gradually introduced. In which order depends on the experimental insight: are support effects observed? - Are the reaction conditions harsh, i.e., should one expect highly covered surfaces, so that the surface free energies in vacuum are not relevant anymore? - Are organic ligands remaining on the surface? Etc. The computationally worst case are particle size effects in combination with support effects. Not only are such systems structurally ill defined, i.e., only ensembles could provide a representative picture, and computationally costly (large unit cells), but additionally for each “structure”, there is a multitude of potentially active sites (see Figure 1.2), so that many computations would be necessary to describe the “activity” of a given structure. This is indeed the second reason for which starting with the “simplest” model is a rational starting point: the more complex the system is, the more possibilities need to be explored.

### 1.3 How to Validate Theoretical Models?

Since computational studies almost invariably invoke approximations, the chosen model requires validation. Even though there are different levels of “model validation”, in general only two possibilities exist to achieve it: (1) high-level computations are possible to benchmark computationally less expensive methods and thereby to assign an estimated confidence interval to the derived results. This has the advantage that strictly comparable quantities can be compared, such as relative energies, bond-length changes, adsorption sites etc. (2) In the absence of high-level theoretical results, experiments can serve to validate the chosen model. However, except in very favorable cases where experiments are performed under very well controlled, “ideal”, conditions many approximations are invoked when extracting comparable quantities from raw data on the theoretical and the experimental side.

Let us discuss this issue for the case of heterogeneous catalysis. *Experimentally*, measuring the production rate is rather straight forward. However, quantifying the number of active sites already poses a much more serious problem,<sup>50;51</sup> not to speak of the possibility of various active sites, the activity of which cannot be easily disentangled. Just consider a given reaction over a nanoparticle catalyst: Even in the best case, the particles have surfaces, edges and corners. They all could be active and even under perfect size and shape control, their respective catalytic activity can only be determined under the assumption that they do not change as a function of the overall morphology and size. *Computationally* the problem is even harder, since computing a realistic rate is far from trivial: First, the surface model needs to be relevant (e.g., single crystal surface for large nanoparticles, where the reaction occurs on the major exposed surface) and



the level of theory needs to provide accurate energies. Second, the assumed reaction pathway needs to correspond to the actual one and side reactions need to be negligible. Third, in order to get the kinetics right for the right reason, the surface needs to be in a realistic surface state, with realistic coverages of the various reactants, intermediates and products, while describing diffusion on the surface and the impact of the local neighbors on the reactivity. Such a description is commonly achieved by kinetic Monte Carlo simulations<sup>52</sup> but even there the diffusion is approximated and model Hamiltonians need to be used for simulating the individual reaction events to deal with the large number of states and events sampled. On top of that, engineering issues, related to the reactor geometry and mass transport (closed vessel with convection vs flow rate, for instance) would also come into play. Even though the different time and length scales are, in principle, coupled, they are only rarely simulated seamlessly.<sup>53;54</sup>

In short, especially in the context of catalysis, kinetic parameters are the most abundant quantities that could be used to validate theoretical models – but at the same time the hardest one to compute reliably. Quantitative agreement is, in general, not obtained without adjustment of parameters to fit to experiment. In these studies, the theoretical values are used as guidelines for numerical fits.<sup>55</sup> However, one has to admit that this reduces the predictive power of the obtained insight. Often, however, only trends are of interest (i.e., catalyst A is more active than catalyst B), which can be obtained with cruder models.<sup>56</sup> The disadvantage of crude models such as the energetic span for effective activation energies<sup>57</sup> or the thermodynamic overpotential in electrocatalysis<sup>58</sup> is that they can only be compatible with a given reaction mechanism, but are not specific enough to distinguish between competing reaction mechanisms or surface sites which can feature very similar “global” parameters. Such non-specific validations become problematic once the identified model is used to predict the activity of catalysts modified by, for instance, doping.

The validation of the chosen surface model should ideally be done by performing operando surface characterizations.<sup>3</sup> However, due to the challenges associated with such measurements, a comparison of the surface characteristics (composition, crystallinity, morphology etc) of the catalyst before running a catalytic test and after the experiment can yield precious information on the assumed stability of the surface. Except in rare instances where microscopy is used (atomic force or scanning tunneling microscopy (AFM/STM) for flat surfaces, transmission electron microscopy (TEM) for more three dimensional samples), the surface characterization (typically X-ray photoelectron spectroscopy (XPS), sometimes vibrational spectroscopy) provides an “average” view, lacking atomically precise information on the heterogeneities of surfaces. Hence, once again, the theoretical surface model can only be compatible with the experimental results. But such a compatibility is not sufficient to be confident that the structure is experimentally relevant, i.e., realistic.

## 1.4. Pillars for Convincingly and Reliably Model Metal/Liquid Interfaces

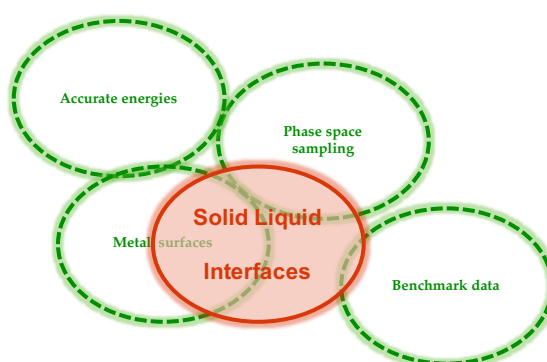


Figure 1.4 – Representation of the missing overlap between requirements and their state-of-the-art realization for metallic solid/liquid interfaces.

### 1.4 Pillars for Convincingly and Reliably Model Metal/Liquid Interfaces

Atomistic modelling of metal/liquid interfaces faces several intrinsic challenges: First, the structural model choices discussed in section 1.2 still need to be addressed. Second, the liquid part of the interface adds complexity (if treated explicitly) or approximations (if treated implicitly) that are difficult to control. Last but not least, the experimental characterization of the metal/liquid interface is also very challenging, leading to sparser experimental data that could be directly compared to computations. Figure 1.4 represents key requirements for any atomistic modelling approach that aims at a convincing, reliable and thus predictive description of these interfaces.

The first, seemingly trivial, requirement is that the electronic structure method needs to be able to describe metallic systems. This is, for instance, not the case for perturbative wave function methods such as Møller-Plesset theory,<sup>59</sup> which diverges for gap-less systems. Similarly, the most efficient, (near) linear scaling density matrix optimization algorithms<sup>60;61</sup> used for Kohn-Sham density functional theory (DFT),<sup>62</sup> rely on the existence of a gap between occupied and virtual orbitals (or, equivalently, valence and conduction band) and are, thus, not applicable to metals. One approach to overcome this technical limitation is to dispense with partially occupied orbitals altogether,<sup>63</sup> simulating a somewhat unphysical electronic structure with impacts that are difficult to predict. Alternatively, at the cost of a huge prefactor, near-linear scaling can be achieved while keeping the physics of the Fermi operator and thus of partially occupied orbitals.<sup>64;65</sup> However, the prefactor implies that the method only becomes competitive for large systems (> 1000 atoms) and thousands of available CPUs. Hence, it is neither suited for routine applications nor for systems where thousands or hundreds of thousands of energy evaluations are required.

This brings us to the second, equally trivial, requirement: phase-space sampling. For a metal/liquid interface as the one depicted in Figure 1.5, where pyridine is adsorbed

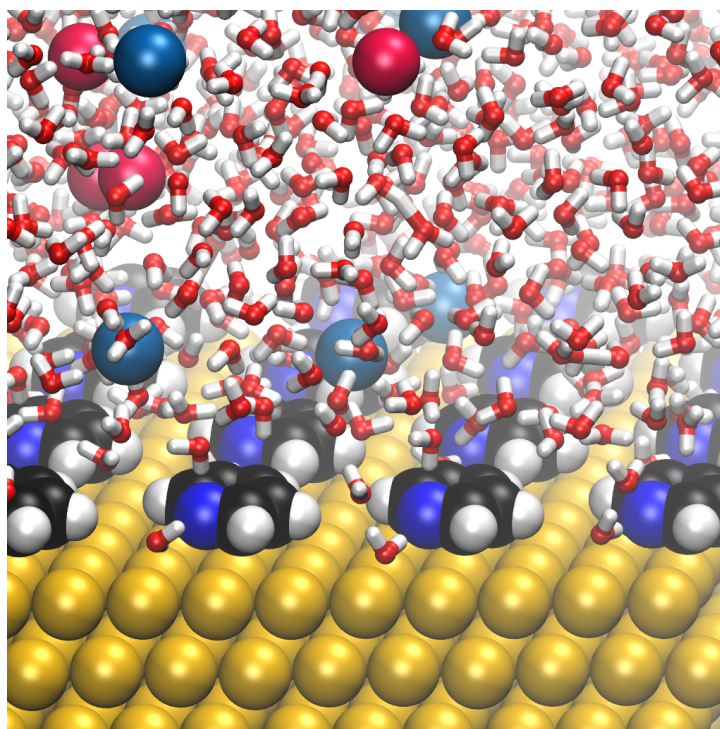


Figure 1.5 – Snapshot of a molecular mechanics simulation of pyridine adsorbed on Au(111) at 0.7 V vs SHE in aqueous 1 M NaCl. The anions and cations are represented in blue and red, respectively. The force field is UFF<sup>66</sup> except for water, where TIP3P is used.<sup>67</sup>

at a Au(111) surface in a 1 M aqueous electrolyte solution, an atomistic description is meaningless in the absence of a representative phase-space sampling. This implies that many, many (typically  $10^6$ ) configurations are to be computed to properly capture entropic effects. Hence, only computationally highly efficient methods are applicable. Insisting on this point of phase-space sampling does not mean that computationally efficient schemes such as implicit solvation models<sup>68;69</sup> or the in practice essentially equivalent<sup>70</sup> classical density functional theory for liquids<sup>71;72</sup> are not valuable tools. Indeed, these methods are very attractive, since they average out the “fast” solvent modes, reducing the effect of the solvent to that of an effective medium. This is particularly helpful at interfaces, where the diffusion coefficient is low<sup>73</sup> and therefore equilibration times of  $\sim 500$  ps are necessary.<sup>74;75</sup> In contrast with the explicit phase space sampling which is associated with a statistical uncertainty, the effective medium has also the advantage that it reproducibly provides with a single number. Since the electronic structure computations in the presence of an implicit solvent are essentially of the same cost as in vacuum, reaction pathways can be conveniently modelled.<sup>76–78</sup> However, these models come with several drawbacks: (1) intrinsically, the implicit solvent/electrolyte will never actively participate in the reaction e.g., acting as a proton transfer relay. Such “strong” or “explicit” solvation effects need to be included via the explicit inclusion of the crucial molecules.<sup>79;80</sup> (2) Some of the models, especially the ones based on polarizable continuum models, neglect the finite size of solvent

#### 1.4. Pillars for Convincingly and Reliably Model Metal/Liquid Interfaces

---

or electrolyte molecules, which means that the implicit medium can approach the quantum system too closely or even “infiltrate” into cavities or between weakly bound layers (e.g., in graphite), where physically there is no space for bulk solution.<sup>81</sup> (3) By construction, all of these models reside on more or less extensive parametrization. The abundance of solvation energies in bulk solution<sup>82</sup> makes this parametrization rather unproblematic for solvated molecules and ions. However, at the metal/liquid interface, such data is barely available, which brings us to the third requirement.

Benchmark data is crucial for atomistic modelling. Even though the fundamental equations which would lead to exact results are well established (one may think about the Schrödinger<sup>83</sup> or Dirac<sup>84</sup> equation and statistical thermodynamics as first comprehensively formulated by Gibbs<sup>85</sup>), they cannot be solved exactly for any system of practical interest. Therefore, approximations have to be introduced and the accuracy of these approximations are, in general, not known a priori, but have to be evaluated against experimental data. If a certain theoretical approximation is deemed “accurate”, it can then be used to derive theoretical benchmark data. One of the best known examples along this line is the use of coupled cluster methods,<sup>86</sup> in particular coupled cluster singles doubles with perturbative triples, CCSD(T), which gives chemically accurate total electronic energies when used in combination with sufficiently large basis sets and the true electronic structure does not possess a strong “multi-reference” character.<sup>87;88</sup> Hence, CCSD(T) data can be used to benchmark computationally cheaper electronic structure methods (e.g., density functional theory) for molecules which have not been measured experimentally. It is important to note that benchmark data is the more valuable the more “directly” it can be compared between theory and experiment, i.e., the less approximations are involved in the comparison. This means that the bigger and the more complex the system is, the more difficult it is to experimentally derive convenient benchmark data. Spectroscopy can measure electronic transitions and ionization energies of atoms, enabling direct comparisons to computations. For diatomics, the geometry in the gas-phase can still be determined accurately via rotational spectroscopy to benchmark the geometries produced by minimizing the energy with a given level of theory.<sup>89</sup> If we turn to the solid/vacuum interface, scanning tunneling microscopy (STM) can probe the local geometries, but only “from the top”, i.e., it does not provide truly three dimensional data, but rather two-dimensional maps.<sup>90</sup> Diffraction techniques allow to identify surface patterns if they are sufficiently long-ranged and to measure certain geometrical characteristics.<sup>91–93</sup> Single-crystal adsorption calorimetry can be used to determine adsorption energies<sup>94</sup> and various spectroscopic techniques to measure spectroscopic signatures.<sup>95–98</sup> However, most of these methods probe non-equilibrium situations, for instance under ultra-high vacuum, where the pumps are constantly running. Hence, connecting the measurement with a computation for equilibrium thermodynamics is not straight forward. Second, the computations will assume a crystalline (i.e., well-ordered) adsorbate film, an assumption that is only valid for certain systems. This hypothesis is reasonable

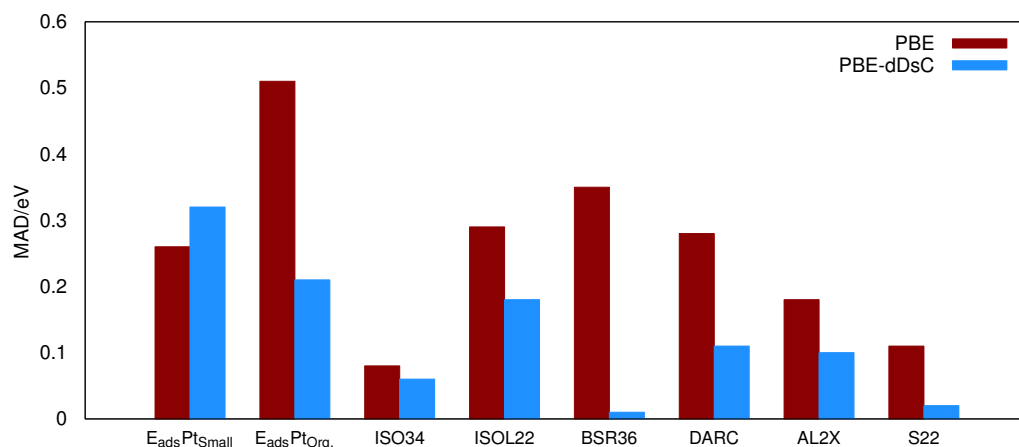


Figure 1.6 – Mean average deviations (MADs) for selected test sets, comparing the performance of PBE and its dispersion corrected variante PBE-dDsC. The  $E_{\text{adsPtSmall}}$  refers to H, O and CO adsorption on Pt(111), while  $E_{\text{adsPtOrg}}$  contains methane, ethane, ethylidyne, cyclohexene, benzene and naphtalene on Pt(111); the data is taken from 110. The other six sets are taken from GMTKN24<sup>111</sup> and the PBE-dDsC numbers come from ref. 112. In short, ISO36 assesses isomerization energies of small organic molecules; ISOL22 contains isomerization energies of large organic molecules. BSR36 contains bond separation energies of alkanes, i.e., alkanes are hydrogenated to methane. DARC measures the accuracy for Diels-Alder reaction energies, while AL2X reports dimerization energies of  $\text{AlX}_3$  species. Finally, S22 is devoted to weak intermolecular interactions such as dispersion and hydrogen bonding.

for systems for which diffraction reveals the major geometrical parameters. So, even at single-crystal solid/vacuum interface, geometries are rarely exactly known and single-crystal adsorption calorimetry data is available only for a limited number of systems.<sup>99</sup> Hence, relative energies between different surface arrangements are hardly accessible from experiments. The situation at the solid/liquid interface is even worse. These interfaces are not truly crystalline and hence structural information is, at best, limited to the adsorbates other than the solvent, e.g., pyridine in the case of Figure 1.5. Reliable energetics for adsorption or reaction energies are also extremely challenging to access and rely on various approximations. Hence, most information about the metal/liquid interface is indirect (e.g., capacitance, which is a combination of solvent and electrolyte effect). From such indirect data, relative energies of surface reconstructions as a function of the electrochemical potential can be retrieved<sup>100;101</sup> and, for non-wetting surfaces, the contact angle provides a measure for the surface/liquid interaction.<sup>78</sup> For the more specific case of adsorbates, electrochemical measurements and in-situ spectroscopy have led to a number of adsorption energies<sup>102–106</sup> and pKa values<sup>107–109</sup> at the metal/water interface that could, together with capacitances, be used benchmark atomistic modelling. However, the experimental conditions are rather complex to be simulated, so that a mismatch between theory and experiment is not easy to ascribe to one particular requirement that is not fulfilled.

The last general requirement is the robustness and accuracy of computed energies. For some applications, accurate relative energies can suffice, but heterogeneous catalysis might be among the most demanding applications with respect to the robustness of

#### 1.4. Pillars for Convincingly and Reliably Model Metal/Liquid Interfaces

---

electronic structure theory: Small molecules such as O<sub>2</sub>, CO<sub>2</sub>, N<sub>2</sub> and, of course, H<sub>2</sub> are key reactant or products in many processes. These molecules react with metal surfaces, replacing their covalent bonds by bonds with the metal surface. The electronic structure of molecules and the one of bulks or surfaces is quite different, which can even be seen in the context of the development of density functional approximations. PBE,<sup>113</sup> originally designed as a general purpose compromise functional, has been revised to yield revPBE,<sup>114</sup> more accurate for molecular data, or, alternatively, to RPBE<sup>115</sup> to have a better compromise between metallic surfaces and molecular adsorption. Yet another spin-off, PBEsol,<sup>116</sup> was later designed for better accuracy for solids. All of these functionals share the common philosophy of minimal parameterization with respect to experimental data, but, taken together, illustrate quite well the struggles when it comes to describing the electronic structure of molecules interacting with solids. The description of the liquid imposes yet other constraints on the reliability of density functionals. For instance, reproducing the structure, dynamics and density of liquid water with density functional approximations is far from trivial.<sup>117</sup> If this discussion started with density functional theory, this is not by accident: Only DFT is computationally efficient enough to envision first principles energy evaluations of atomistic metal/liquid interfaces. MP2, which has been shown to be promising for liquid water,<sup>118</sup> cannot be applied to metals due to its divergence for gapless systems and any other post-HF electronic structure is, so far, computationally prohibitively expensive for periodic computations of hundreds of atoms. This might not completely apply to quantum Monte Carlo methods,<sup>119;120</sup> although with a severe caveat: As discussed under requirement two (phase-space sampling) a single energy evaluation is of very limited use when simulating the metal/liquid interface and at least thousands of such computations are necessary. In the absence of rigorous theoretical benchmark data, what do we know or what can we infer with respect to the accuracy of DFT? Even though it has been recently claimed that an accuracy of 0.05 eV is almost routinely achievable in electrocatalysis,<sup>121</sup> the more direct benchmarking studies indicate a much lower accuracy. Based on the limited solid/gas interface benchmark data, we cannot expect an accuracy better than  $\sim 0.2$  eV.<sup>110;122</sup> This data is reported in Figure 1.6, where the mono- and diatomics are separated from the organic molecules and where the need for a dispersion correction at the metal/gas interface is clearly visible. Since error cancellation or accumulation occurs unpredictably, the accuracy of relative energies is, on average, expected to be in the order of  $\sim 0.2$  eV. For the gas-phase reactions, which govern the overall thermodynamics, the accuracy is also in the order of 0.2-0.3 eV for PBE or RPBE.<sup>123</sup> There is no reason to believe that the accuracy in solution would be higher – and the situation at the metal/liquid interface is likely to be worse, especially for electrolyte solutions: the delocalization error,<sup>124</sup> that follows GGAs like a shadow, is the more worrisome when charged ions are present. In short, the delocalization error refers to the observation that semi-local density functionals overstabilize fractional charges, which can also be seen as an unphysical smearing of charges within a given system. The archetypical systems for this failure are the dissocia-

tion limits of alkali metal halides, where GGAs lead to fractionally charged ions instead of neutral atoms.<sup>125</sup> Furthermore, the band-alignment at the metal/liquid interface is also problematic: Owing to the intrinsically delocalized nature of the electronic structure of metals, their workfunction is generally reasonably well reproduced by GGAs (within  $\sim 0.2$  eV).<sup>126</sup> The same does not apply to the band-gap of semi-conductors and insulators, where the gap is too small by 40% on average, which means errors of at least 0.5 eV for a candidate for water splitting.<sup>127</sup> Hence, the band alignment at the interface can have disastrous consequences.<sup>128</sup>

A promising strategy that balances phase-space sampling (more than 500 ps for equilibrated interfaces<sup>74;75</sup>) and computational cost is resampling or non-equilibrium molecular dynamics, where the difference between a low-level method (e.g., a force field) and a high-level methods (e.g., DFT) is estimated based on the sampling performed at the low-level theory.<sup>129–132</sup> Such methods have not yet been extensively applied to solid/liquid interfaces, but are part of the perspectives of this thesis (see section 10.2).

In summary, the metal/liquid interface constitutes a conundrum: At the one end, one would need to have access to accurate energies. At the other end, one cannot even properly judge if energies are accurate due to the lack of unambiguous benchmark data. Furthermore, the accurate energies are, intrinsically, incompatible with representative phase-space sampling which, itself is a requirement for a proper description of a liquid. Last but not least, the metallic nature of the solid phase adds further complications, regarding the applicable electronic structure methods and even the computational cost of a given method.

### 1.5 Choice of Included Works

The chapters following this fairly general introduction have been chosen among my publications, most of them published since I have joined the CNRS in 2016 and all of them during my affiliation to the “Laboratoire de Chimie” at the ENS Lyon. Furthermore, I have restricted my choice to publications where I am either (co-)corresponding or first author to minimize ambiguities regarding my role in the authorship. Last but not least, I have tried to make a selection that spans my current research interests. Their relevance for the on-going and upcoming projects (outlined in Chapter 10) and their connection with the chosen title have provided additional guidelines.

Each chapter is preceded by a very short text that summarizes the chapter and puts it into the context of this habilitation thesis.

This main body of the thesis is followed by a presentation of on-going and planned projects and a general conclusion.

---

## Bibliography

- [1] van Santen, R. *Modern heterogeneous catalysis: an introduction*; Wiley-VCH Verlag: Weinheim, 2017.
- [2] Libuda, J.; Freund, H. J. *Surf. Sci. Rep.* **2005**, *57*, 157.
- [3] Bañares, M. A. *Catal. Today* **2005**, *100*, 71.
- [4] Che, F.; Gray, J. T.; Ha, S.; Kruse, N.; Scott, S. L.; McEwen, J.-S. *ACS Catal.* **2018**, *8*, 5153.
- [5] Vayenas, C. G. *Catal. Lett.* **2013**, *143*, 1085.
- [6] Vernoux, P.; Lizarraga, L.; Tsampas, M. N.; Sapountzi, F. M.; De Lucas-Consuegra, A.; Valverde, J.-L.; Souentie, S.; Vayenas, C. G.; Tsiplakides, D.; Balomenou, S.; Baranova, E. A. *Chem. Rev.* **2013**, *113*, 8192.
- [7] Evans, A. G.; Hutchinson, J. W.; Wei, Y. *Acta Mater.* **1999**, *47*, 4093.
- [8] Adhikari, S.; Fernando, S. *Ind. Eng. Chem. Res.* **2006**, *45*, 875.
- [9] Tiu, B. D. B.; Advincula, R. C. *React. Funct. Polym.* **2015**, *95*, 25.
- [10] Une 20e campagne de peinture décapante. 2017; <https://www.tou Eiffel.paris/fr/actualites/chantiers/une-20e-campagne-de-peinture-decapante>.
- [11] Golden Gate Bridge. <http://goldengatebridge.org/research/facts.php#PaintHowOften>.
- [12] Gece, G. *Corros. Sci.* **2008**, *50*, 2981.
- [13] Matzdorf, C.; Grieve, A. US Patent, US 2019/0078179 A1.
- [14] Koch, G.; Varney, J.; Thompson, N.; Moghissi, O.; Gould, M.; Payer, J. Nace-International-Report. 2016; <http://impact.nace.org/documents/Nace-International-Report.pdf>.
- [15] Buschow, K. H. J. *Encyclopedia of materials : science and technology*. 2001.
- [16] Vaškelis, A.; Norkus, H. J.; Rozovskis, G.; Vinkevičius, H. J. *Transactions of the IMF* **1997**, *75*, 1.
- [17] Shen, Z.-Z.; Lang, S.-Y.; Shi, Y.; Ma, J.-M.; Wen, R.; Wan, L.-J. *J. Am. Chem. Soc.* **2019**, *141*, 6900.
- [18] Lisbona, D.; Snee, T. *Process Saf. Environ. Prot.* **2011**, *89*, 434.
- [19] Choi, N.-S.; Chen, Z.; Freunberger, S. A.; Ji, X.; Sun, Y.-K.; Amine, K.; Yushin, G.; Nazar, L. F.; Cho, J.; Bruce, P. G. *Angew. Chem. Int. Ed.* **2012**, *51*, 9994.



## Chapter 1. Introduction

---

- [20] Shenghua, L.; He, Y.; Yuansheng, J. *Int. J. Mol. Sci.* **2003**, *5*, 13.
- [21] Schreiber, F. *Prog. Surf. Sci.* **2000**, *65*, 151.
- [22] Love, J. C.; Estroff, L. A.; Kriebel, J. K.; Nuzzo, R. G.; Whitesides, G. M. *Chem. Rev.* **2005**, *105*, 1103.
- [23] Hakkinen, H. *Nat. Chem.* **2012**, *4*, 443.
- [24] Carroll, R. L.; Gorman, C. B. *Angew. Chem., Int. Ed.* **2002**, *41*, 4378.
- [25] Climent, M. J.; Corma, A.; Iborra, S. *Green Chem.* **2011**, *13*, 520.
- [26] Ravenelle, R. M.; Copeland, J. R.; Kim, W.-G.; Crittenden, J. C.; Sievers, C. *ACS Catal.* **2011**, *1*, 552.
- [27] Michel, C.; Zaffran, J.; Ruppert, A. M.; Matras-Michalska, J.; Jedrzejczyk, M.; Grams, J.; Sautet, P. *Chem. Comm.* **2014**, *50*, 12450.
- [28] Réocreux, R.; Girel, É.; Clabaut, P.; Tuel, A.; Besson, M.; Chaumonnot, A.; Cabiac, A.; Sautet, P.; Michel, C. *Nat. Commun.* **2019**, *10*, 3139.
- [29] Toney, M. F.; Howard, J. N.; Richer, J.; Borges, G. L.; Gordon, J. G.; Melroy, O. R.; Wiesler, D. G.; Yee, D.; Sorensen, L. B. *Nature* **1994**, *368*, 444.
- [30] Schiros, T.; Andersson, K. J.; Pettersson, L. G. M.; Nilsson, A.; Ogasawara, H. *J. Electron Spectrosc. Relat. Phenom.* **2010**, *177*, 85.
- [31] Velasco-Velez, J.-J.; Wu, C. H.; Pascal, T. A.; Wan, L. F.; Guo, J.; Prendergast, D.; Salmeron, M. *Science* **2014**, *346*, 831.
- [32] Neri, G.; Donaldson, P. M.; Cowan, A. J. *J. Am. Chem. Soc.* **2017**, *139*, 13791.
- [33] Seh, Z. W.; Kibsgaard, J.; Dickens, C. F.; Chorkendorff, I.; Nørskov, J. K.; Jaramillo, T. F. *Science* **2017**, *355*, eaad4998.
- [34] Mikkelsen, M.; Jørgensen, M.; Krebs, F. C. *Energy Environ. Sci.* **2010**, *3*, 43.
- [35] Foster, S. L.; Bakovic, S. I. P.; Duda, R. D.; Maheshwari, S.; Milton, R. D.; Minteer, S. D.; Janik, M. J.; Renner, J. N.; Greenlee, L. F. *Nature Catalysis* **2018**, *1*, 490.
- [36] Schaefer, H. F. *Science* **1986**, *231*, 1100.
- [37] Plata, R. E.; Singleton, D. A. *J. Am. Chem. Soc.* **2015**, *137*, 3811.
- [38] Bent, B. E. *Chem. Rev.* **1996**, *96*, 1361.
- [39] Li, L.; Larsen, A. H.; Romero, N. A.; Morozov, V. A.; Glinsvad, C.; Abild-Pedersen, F.; Greeley, J.; Jacobsen, K. W.; Nørskov, J. K. *J. Phys. Chem. Lett.* **2013**, *4*, 222.

- [40] Hansen, P. L.; Wagner, J. B.; Helveg, S.; Rostrup-Nielsen, J. R.; Clausen, B. S.; Topsøe, H. *Science* **2002**, 295, 2053.
- [41] Wulff G., *Zeitschrift für Kristallographie - Crystalline Materials* **1901**, 34, 449.
- [42] Ramamoorthy, M.; Vanderbilt, D.; King-Smith, R. D. *Phys. Rev. B* **1994**, 49, 16721.
- [43] Sachs, C.; Hildebrand, M.; Völkening, S.; Wintterlin, J.; Ertl, G. *Science* **2001**, 293, 1635.
- [44] Tauster, S. J.; Fung, S. C.; Baker, R. T. K.; Horsley, J. A. *Science* **1981**, 211, 1121.
- [45] Green, I. X.; Tang, W.; Neurock, M.; Yates, J. T. *Science* **2011**, 333, 736.
- [46] Schlögl, R. *Angew. Chem., Int. Ed.* **2015**, 54, 3465.
- [47] Vignola, E.; Steinmann, S. N.; Le Mapihan, K.; Vandegehuchte, B. D.; Curulla, D.; Sautet, P. J. *Phys. Chem. C* **2018**, 122, 15456.
- [48] Tao, F.; Grass, M. E.; Zhang, Y.; Butcher, D. R.; Renzas, J. R.; Liu, Z.; Chung, J. Y.; Mun, B. S.; Salmeron, M.; Somorjai, G. A. *Science* **2008**, 322, 932.
- [49] Batchelor, T. A. A.; Pedersen, J. K.; Winther, S. H.; Castelli, I. E.; Jacobsen, K. W.; Rossmeisl, J. *Joule* **2019**, 3, 834.
- [50] Boudart, M. *Chem. Rev.* **1995**, 95, 661.
- [51] Roeffaers, M. B. J.; Sels, B. F.; Uji-i, H.; Schryver, F. C. D.; Jacobs, P. A.; Vos, D. E. D.; Hofkens, J. *Nature* **2006**, 439, 572.
- [52] Saliccioli, M.; Stamatakis, M.; Caratzoulas, S.; Vlachos, D. G. *Chem. Eng. Sci.* **2011**, 66, 4319.
- [53] Matera, S.; Reuter, K. *Catal. Lett.* **2009**, 133, 156.
- [54] Wachs, A. *J. Eng. Math.* **2011**, 71, 131.
- [55] Gokhale, A. A.; Dumesic, J. A.; Mavrikakis, M. *J. Am. Chem. Soc.* **2008**, 130, 1402.
- [56] Medford, A. J.; Shi, C.; Hoffmann, M. J.; Lausche, A. C.; Fitzgibbon, S. R.; Bligaard, T.; Nørskov, J. K. *Catal. Lett.* **2015**, 145, 794.
- [57] Kozuch, S.; Shaik, S. *Acc. Chem. Res.* **2011**, 44, 101.
- [58] Nørskov, J. K.; Rossmeisl, J.; Logadottir, A.; Lindqvist, L.; Kitchin, J. R.; Bligaard, T.; Jonsson, H. *J. Phys. Chem. B* **2004**, 108, 17886.
- [59] Møller, C.; Plesset, M. S. *Phys. Rev.* **1934**, 46, 618.
- [60] VandeVondele, J.; Hutter, J. *J. Chem. Phys.* **2003**, 118, 4365.

## Chapter 1. Introduction

---

- [61] Mohr, S.; Ratcliff, L. E.; Boulanger, P.; Genovese, L.; Caliste, D.; Deutsch, T.; Goedecker, S. *J. Chem. Phys.* **2014**, *140*, 204110.
- [62] Kohn, W.; Sham, L. J. *Phys. Rev.* **1965**, *140*, A1133.
- [63] Kühne, T. D. *Wiley Inter. Rev. Comp. Mol. Sci.* **2014**, *4*, 391.
- [64] Lin, L.; Chen, M.; Yang, C.; He, L. *J. Phys.: Condens. Matter* **2013**, *25*, 295501.
- [65] Mohr, S.; Eixarch, M.; Amsler, M.; Mantsinen, M. J.; Genovese, L. *Nucl. Mater. Energy* **2018**, 64.
- [66] Rappe, A. K.; Casewit, C. J.; Colwell, K. S.; Goddard, W. A.; Skiff, W. M. *J. Am. Chem. Soc.* **1992**, *114*, 10024.
- [67] Jorgensen, W. L.; Chandrasekhar, J.; Madura, J. D.; Impey, R. W.; Klein, M. L. *J. Chem. Phys.* **1983**, *79*, 926.
- [68] Cramer, C. J.; Truhlar, D. G. *Chem. Rev.* **1999**, *99*, 2161.
- [69] Fattebert, J.-L.; Gygi, F. *Int. J. Quantum Chem.* **2003**, *93*, 139.
- [70] Ramirez, R.; Borgis, D. *J. Phys. Chem. B* **2005**, *109*, 6754.
- [71] Petrosyan, S. A.; Rigos, A. A.; Arias, T. A. *J. Phys. Chem. B* **2005**, *109*, 15436.
- [72] Jeanmairat, G.; Levesque, M.; Vuilleumier, R.; Borgis, D. *J. Phys. Chem. Lett.* **2013**, *4*, 619.
- [73] Réocreux, R.; Jiang, T.; Iannuzzi, M.; Michel, C.; Sautet, P. *ACS Appl. Nano Mater.* **2018**, *1*, 191.
- [74] Limmer, D. T.; Willard, A. P.; Madden, P.; Chandler, D. *Proc. Natl. Acad. Sci. U. S. A.* **2013**, *110*, 4200.
- [75] Steinmann, S. N.; Ferreira De Morais, R.; Götz, A. W.; Fleurat-Lessard, P.; Iannuzzi, M.; Sautet, P.; Michel, C. *J. Chem. Theory Comput.* **2018**, *14*, 3238.
- [76] Sundararaman, R.; Goddard, W. A. *J. Chem. Phys.* **2015**, *142*, 064107.
- [77] Mathew, K.; Hennig, R. G. *ArXiv e-prints* **2016**, 1601.03346.
- [78] Fisicaro, G.; Genovese, L.; Andreussi, O.; Mandal, S.; Nair, N. N.; Marzari, N.; Goedecker, S. *J. Chem. Theory Comput.* **2017**, *13*, 3829.
- [79] Desai, S. K.; Pallassana, V.; Neurock, M. *J. Phys. Chem. B* **2001**, *105*, 9171.
- [80] Schweitzer, B.; Steinmann, S. N.; Michel, C. *Phys. Chem. Chem. Phys.* **2019**, *21*, 5368.
- [81] Vatti, A. K.; Todorova, M.; Neugebauer, J. *Langmuir* **2016**, *32*, 1027.

- [82] Moine, E.; Privat, R.; Sirjean, B.; Jaubert, J.-N. *J. Phys. Chem. Ref. Data* **2017**, *46*, 033102.
- [83] Schrödinger, E. *Phys. Rev.* **1926**, *28*, 1049.
- [84] Dirac, P. A. M.; Fowler, R. H. *Proc. Royal Soc. London Ser. A* **1928**, *117*, 610.
- [85] Gibbs, J. W. *Elementary Principles in Statistical Mechanics: Developed with Especial Reference to the Rational Foundation of Thermodynamics*; Cambridge Library Collection - Mathematics; Cambridge University Press: Cambridge, 1902.
- [86] Tajti, A.; Szalay, P. G.; Császár, A. G.; Kállay, M.; Gauss, J.; Valeev, E. F.; Flowers, B. A.; Vázquez, J.; Stanton, J. F. *J. Chem. Phys.* **2004**, *121*, 11599.
- [87] Jiang, W.; DeYonker, N. J.; Determan, J. J.; Wilson, A. K. *J. Phys. Chem. A* **2012**, *116*, 870.
- [88] Shee, J.; Rudshiteyn, B.; Arthur, E. J.; Zhang, S.; Reichman, D. R.; Friesner, R. A. *J. Chem. Theory Comput.* **2019**, 2346.
- [89] Puzzarini, C.; Stanton, J. F.; Gauss, J. *Int. Rev. Phys. Chem.* **2010**, *29*, 273.
- [90] Binnig, G.; Rohrer, H.; Gerber, C.; Weibel, E. *Phys. Rev. Lett.* **1982**, *49*, 57.
- [91] Morgan, A. E.; Somorjai, G. A. *Surf. Sci.* **1968**, *12*, 405.
- [92] Feidenhans'l, R. *Surf. Sci. Rep.* **1989**, *10*, 105.
- [93] Woodruff, D. P.; Bradshaw, A. M. *Rep. Prog. Phys.* **1994**, *57*, 1029.
- [94] Borroni-Bird, C. E.; Al-Sarraf, N.; Andersoon, S.; King, D. A. *Chem. Phys. Lett.* **1991**, *183*, 516.
- [95] Moskovits, M. *Rev. Mod. Phys.* **1985**, *57*, 783.
- [96] Buffeteau, T.; Desbat, B.; Turlet, J. M. *Appl. Spectrosc.* **1991**, *45*, 380.
- [97] Richmond, G. L. *Chem. Rev.* **2002**, *102*, 2693.
- [98] Eisenthal, K. B. *Chem. Rev.* **2006**, *106*, 1462.
- [99] Schauer mann, S.; Silbaugh, T. L.; Campbell, C. T. *The Chemical Record* **2014**, *14*, 759.
- [100] Santos, E.; Schmickler, W. *Chem. Phys. Lett.* **2004**, *400*, 26.
- [101] Giesen, M.; Beltramo, G.; Dieluweit, S.; Müller, J.; Ibach, H.; Schmickler, W. *Surf. Sci.* **2005**, *595*, 127.
- [102] Lipkowski, J.; Stolberg, L.; Morin, S.; Irish, D.; Zelenay, P.; Gamboa, M.; Wieckowski, A. *J. Electroanal. Chem.* **1993**, *355*, 147.


## Chapter 1. Introduction

---

- [103] Foresti, M. L.; Innocenti, M.; Hamelin, A. *Langmuir* **1995**, *11*, 498.
- [104] Lust, E.; Jänes, A.; Lust, K.; Miidla, P. *J. Electroanal. Chem.* **1996**, *413*, 175.
- [105] Herrero, E.; Mostany, J.; Feliu, J. M.; Lipkowski, J. *J. Electroanal. Chem.* **2002**, *534*, 79.
- [106] Singh, N.; Sanyal, U.; Fulton, J. L.; Gutiérrez, O. Y.; Lercher, J. A.; Campbell, C. T. *ACS Catal.* **2019**, 6869.
- [107] Lachenwitzer, A.; Li, N.; Lipkowski, J. *J. Electroanal. Chem.* **2002**, *532*, 85.
- [108] Berná, A.; Delgado, J. M.; Orts, J. M.; Rodes, A.; Feliu, J. M. *Langmuir* **2006**, *22*, 7192.
- [109] Martínez-Hincapié, R.; Berná, A.; Rodes, A.; Climent, V.; Feliu, J. M. *J. Phys. Chem. C* **2016**, *120*, 16191.
- [110] Gautier, S.; Steinmann, S. N.; Michel, C.; Fleurat-Lessard, P.; Sautet, P. *Phys. Chem. Chem. Phys.* **2015**, *17*, 28921.
- [111] Goerigk, L.; Grimme, S. *J. Chem. Theory Comput.* **2010**, *6*, 107.
- [112] Steinmann, S. N.; Corminboeuf, C. *J. Chem. Theory Comput.* **2011**, *7*, 3567.
- [113] Perdew, J. P.; Burke, K.; Ernzerhof, M. *Phys. Rev. Lett.* **1996**, *77*, 3865.
- [114] Zhang, Y.; Yang, W. *Phys. Rev. Lett.* **1998**, *80*, 890.
- [115] Hammer, B.; Hansen, L. B.; Norskov, J. K. *Phys. Rev. B* **1999**, *59*, 7413.
- [116] Perdew, J. P.; Ruzsinszky, A.; Csonka, G. I.; Vydrov, O. A.; Scuseria, G. E.; Constantin, L. A.; Zhou, X.; Burke, K. *Phys. Rev. Lett.* **2008**, *100*, 136406.
- [117] Gillan, M. J.; Alfè, D.; Michaelides, A. *J. Chem. Phys.* **2016**, *144*, 130901.
- [118] Del Ben, M.; Schönherr, M.; Hutter, J.; VandeVondele, J. *J. Phys. Chem. Lett.* **2013**, *4*, 3753.
- [119] Alfè, D.; Bartók, A. P.; Csányi, G.; Gillan, M. J. *J. Chem. Phys.* **2014**, *141*, 014104.
- [120] Zen, A.; Luo, Y.; Mazzola, G.; Guidoni, L.; Sorella, S. *J. Chem. Phys.* **2015**, *142*, 144111.
- [121] Chen, Y.; Huang, Y.; Cheng, T.; Goddard, W. A. *J. Am. Chem. Soc.* **2019**, 11651.
- [122] Schmidt, P. S.; Thygesen, K. S. *J. Phys. Chem. C* **2018**, *122*, 4381.
- [123] Goerigk, L.; Hansen, A.; Bauer, C.; Ehrlich, S.; Najibi, A.; Grimme, S. *Phys. Chem. Chem. Phys.* **2017**, *19*, 32184.

- [124] Cohen, A. J.; Mori-Sanchez, P.; Yang, W. *Science* **2008**, *321*, 792.
- [125] Ruzsinszky, A.; Perdew, J. P.; Csonka, G. I.; Vydrov, O. A.; Scuseria, G. E. *J. Chem. Phys.* **2006**, *125*, 194112.
- [126] Patra, A.; Bates, J. E.; Sun, J.; Perdew, J. P. *Proc. Natl. Acad. Sci.* **2017**, *114*, E9188.
- [127] Le Bahers, T.; Rérat, M.; Sautet, P. *J. Phys. Chem. C* **2014**, *118*, 5997.
- [128] Bjorketun, M. E.; Zeng, Z.; Ahmed, R.; Tripkovic, V.; Thygesen, K. S.; Rossmeisl, J. *Chem. Phys. Lett.* **2013**, *555*, 145.
- [129] König, G.; Hudson, P. S.; Borech, S.; Woodcock, H. L. *J. Chem. Theory Comput.* **2014**, *10*, 1406.
- [130] Cave-Ayland, C.; Skylaris, C.-K.; Essex, J. W. *J. Chem. Theory Comput.* **2017**, *13*, 415.
- [131] Kearns, F. L.; Hudson, P. S.; Woodcock, H. L.; Borech, S. *J. Comput. Chem.* **2017**, *38*, 1376.
- [132] Hudson, P. S.; Woodcock, H. L.; Borech, S. *J. Chem. Theory Comput.* **2019**, *15*, 4632.





## **2 Acetylene Adsorption on Pd-Ag Alloys: Evidence for Limited Island Formation and Strong Reverse Segregation from Monte Carlo Simulations**

In this chapter we investigate the adsorbate induced segregation of Pd-Ag alloys. In vacuum, these alloys are solid solutions. Nevertheless, since Ag has a lower surface energy, a small Ag surface segregation is obtained in vacuum. Acetylene, which is a typical catalytic substrate, binds much more strongly on Pd than on Ag. Furthermore, acetylene binds preferentially to three surface atoms, suggesting that a surface ordering might be obtained in order to maximize the Pd<sub>3</sub> ensembles. However, in order to (in-)validate such a hypothesis, spatial correlations between adsorbates have to be taken into account. First principles computations are too slow to efficiently sample the phase space of the alloy surface at a given acetylene partial pressure. Therefore, we exploited extensive DFT computations to parametrize a cluster expansion model Hamiltonian. The accuracy of the model Hamiltonian has been carefully evaluated and the identified trends are robust with respect to the uncertainties in the model. This model Hamiltonian has then be used to determine the equilibrium structure of the Pd-Ag alloy as a function of the temperature and Ag molar fraction. While these simulations confirm a strong reverse segregation (Pd enrichment of the top most layer), surface ordering was not observed. This suggests that the Ag atoms can serve as inert spacers between Pd triangles that are covered by acetylene. From a modelling perspective, the main conclusion of the study is that establishing accurate model Hamiltonians for non-spherical adsorbates on alloy surfaces require a significant amount of training data, precluding the facile extension of such a model to complex mixtures.





# Acetylene Adsorption on Pd–Ag Alloys: Evidence for Limited Island Formation and Strong Reverse Segregation from Monte Carlo Simulations

Emanuele Vignola,<sup>†,‡</sup> Stephan N. Steinmann,<sup>\*,†,‡</sup> Katell Le Mapihan,<sup>§</sup> Bart D. Vandegehuchte,<sup>§</sup> Daniel Curulla,<sup>§</sup> and Philippe Sautet<sup>\*,†,||,⊥</sup>

<sup>†</sup>Univ Lyon, ENS de Lyon, CNRS, Université Lyon 1, Laboratoire de Chimie UMR 5182, F-69342 Lyon, France

<sup>‡</sup>Total Research and Technology, Gonfreville, BP 27, F-76700 Harfleur, France

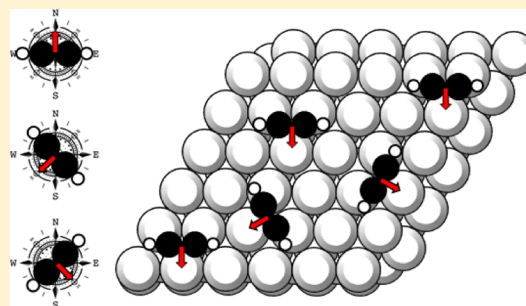
<sup>§</sup>Total Research and Technology Feluy, Zone Industrielle Feluy C, Seneffe 7181, Belgium

<sup>||</sup>Department of Chemical and Biomolecular Engineering, University of California, Los Angeles, Los Angeles, California 90095, United States

<sup>⊥</sup>Department of Chemistry and Biochemistry, University of California, Los Angeles, Los Angeles, California 90095, United States

## Supporting Information

**ABSTRACT:** Restructuring of alloy surfaces induced by strongly bound adsorbates is a well-established phenomenon occurring in catalysis and membrane science. In catalytic processes, this restructuring can have profound effects because it alters the ensemble distribution between the as-prepared state of the catalyst and the catalytic surface under operando conditions. This work assesses the restructuring of Pd–Ag alloys induced by adsorption of acetylene in the framework of the ensemble formalism. A detailed Ising-type model Hamiltonian of the (111) surface plane is fitted to extensive density functional theory computations. The equilibrium distributions under a realistic environment are then evaluated by a Monte Carlo approach as a function of temperature and alloy composition. Acetylene induces a strong reverse segregation within the relevant range of temperature. Therefore, the surface of Pd–Ag catalysts is almost entirely covered by Pd for bulk ratios <0.8 Ag–Pd, which is, in general, detrimental to the selectivity of Pd–Ag catalysts. Despite the very strong vertical segregation, acetylene only induces marginal in-plane ordering, that is, the surface triangular ensembles follow random distributions as a function of the surface layer Ag fraction quite closely. This can be explained by two factors: first, triangular sites are not sufficient to fully capture the diversity of acetylene binding energies on Pd–Ag alloy surfaces. Rather, an extended environment including the first coordination sphere is necessary and leads to an overlap in terms of binding energy between weakly binding Pd<sub>3</sub> ensembles and strongly binding Pd<sub>2</sub>Ag ensembles. The second critical aspect is related to lateral interactions, which preclude adsorption of acetylene molecules on nearest neighbor triangular sites. Therefore, in a Pd<sub>3</sub> island, roughly two thirds of Pd<sub>3</sub> sites would be lost. Our study suggests that the equilibrium structure of these alloy catalysts under operando conditions is far from the state targeted by the catalyst design, revealing a nearly unavoidable reason for loss of selectivity of the catalyst with time of operation.



## INTRODUCTION

Achieving novel properties by mixing of different substances is at the heart of chemistry. Solid solutions are particularly versatile for modifying condensed-phase properties, for example, impurities can enhance the hardness of metals. The effect of carbon or trace metals on steel properties<sup>1</sup> and the entropic hardening in highly disordered materials<sup>2,3</sup> are perhaps the best known examples. The thermodynamic description of alloys, as described in phase diagrams, allows to predict the evolution of a two-component solid system with

macroscopic constraints, and thus to forecast defects in materials, assess thermal stability and segregation.

Because catalysis and membrane science are particularly sensitive to surface phenomena, mastering alloy restructuring effects at surfaces are key. In this respect, building reliable models of the system's energetics is essential as shown before.<sup>4</sup> Let us consider, for instance, the study of Pt–Pd nanoalloys by De Clercq and Mottet.<sup>5</sup> Here, a tight-binding, semiempirical

Received: April 30, 2018

Published: June 7, 2018

## Chapter 2. Acetylene Adsorption on Pd-Ag Alloys: Evidence for Limited Island Formation and Strong Reverse Segregation from Monte Carlo Simulations

potential was fitted to density functional theory (DFT) data and provided as an input to a Monte Carlo algorithm. Along with the prediction of the segregation profile, decorations of onion-shell structures were explored as a function of particle size and of temperature. Apart from detailed insight on the alloy structure, this study was vital to understand changes in catalyst performance which is driven by surface effects.<sup>6</sup> A full comprehension of these phenomena can only be achieved by accounting for adsorbate–catalyst interactions in the model Hamiltonian. It is nowadays clear that environmental factors may significantly alter the compositional profile of the alloy's topmost layers, especially if they are in contact with a gaseous reservoir, a typical situation in catalysis.<sup>7</sup> For instance, when atoms and molecules adsorb preferentially on one component, the segregation profile can be reversed compared to vacuum conditions, where surface energies of the pure metal dominate. For example, some of us showed before that the adsorption of unsaturated aldehydes on the PtFe(111) surface induces the segregation of Fe toward the surface.<sup>8</sup> This is also the case of CO adsorption on the (100) plane of Pd–Au alloys, where competition between metal–adsorbate adsorption energy and adsorbate–adsorbate lateral interactions generates stripes of Pd at room temperature.<sup>9</sup> An analogous example has been provided in the computational study of Chen et al.,<sup>10</sup> which highlights the effect of oxygen binding on Au–Ag on pattern formation. In the latter two mentioned studies, the energy was modeled by Ising-type Hamiltonians fitted to DFT calculations. Indeed, Ising-type Hamiltonians are extremely efficient to deal with large unit cells of alloys that do not undergo severe geometric rearrangements and are dominated by rather short-ranged interatomic interactions. Another remarkable case in this sense is the restructuring of Pd–Ag alloys for the selective hydrogenation of acetylene to ethylene. Extensive research has shown<sup>11–13</sup> that the presence of adsorbates on the catalytic surface reverts the composition at the gas–metal interface compared to that at vacuum. It is found that the Pd enrichment under a reactive atmosphere is detrimental for the selectivity of the catalyst.<sup>6,14</sup> This phenomenon was also investigated along the two directions parallel to the surface. The topmost layer of the alloy (111) plane has been described in terms of triangular ensembles,<sup>15</sup> that is, arrangements of three metal atoms. In high vacuum conditions, STM measurements found that the ensembles (Pd<sub>3</sub>, Pd<sub>2</sub>Ag, PdAg<sub>2</sub>, and Ag<sub>3</sub>) are randomly distributed for a wide span of conditions.<sup>16</sup> This finding was attributed to the small difference between Pd–Pd, Pd–Ag, and Ag–Ag pair interactions. Our recent study<sup>17</sup> revealed that adsorption of acetylene modifies the ensemble distributions. In particular, island formation was predicted for layers close to chemical purity, that is, with an Ag fraction either close to 0 or 1, whereas mixed ensembles prevail for equimolar ratios. These results were explained by the layer energy/entropy balance: the entropically driven random distributions are counterbalanced by the adsorption energy of acetylene which is much stronger on pure Pd than that on mixed Ag–Pd ensembles. However, in that study, the complexity of the system required rather strong approximations, among which a mean-field-like treatment of lateral interactions and a local interpretation of the acetylene-ensemble bonding. Additionally, vertical segregation was completely neglected, and interactions between molecules were assumed to be independent of the surface ensemble on which the acetylene molecule is adsorbed.

In order to overcome these limitations of the previous study and give an atomistic view on the surface state under realistic conditions, this paper describes the surface restructuring of Pd–Ag using a model Hamiltonian based on DFT calculations and integrated in a Monte Carlo code. Ensemble distributions are then computed as a function of temperature and alloy composition.

**Computational Details.** All configurations were fully optimized at the density functional level of theory in the PAW formalism.<sup>18,19</sup> The computations were performed with VASP 5.3.3.<sup>20,21</sup> The functional of Perdew, Burke, and Ernzerhof<sup>22</sup> was used, with the dispersion correction of Steinmann and Corminboeuf.<sup>23</sup> The (111) surface was modeled by a  $p(3 \times 3)$  unit cell with 4 metallic layers, 2 of which were held fixed to simulate bulk properties. A vacuum layer of 15 Å was used and the lattice parameter determined according to Vegard's law, based on the optimized values at the PBE-dDsC level of theory for bulk Pd and Ag, which correspond to nearest neighbor distances of 2.78 and 2.92 Å, respectively. The plane-wave basis set was chosen to have a cutoff energy of 400 eV. Brillouin zone integration was performed by a  $3 \times 3 \times 1$  Monkhorst–Pack<sup>24</sup>  $k$ -point grid and a Methfessel and Paxton<sup>25</sup> smearing of 0.2 eV. The wave function and geometric gradient were converged to  $10^{-6}$  eV and  $5 \times 10^{-2}$  eV/Å, respectively.

Numerical simulations were performed with an in-house Fortran 90 Monte Carlo code provided in the [Supporting Information](#). The code is based on repetitions of a 4-layer,  $p(2 \times 2)$  cell through real space. The number of repetitions is left as an input parameter. The user can choose the simulation temperature and the acetylene reservoir pressure, along with the Ag molar fraction of the four layers and the number of iterations. The system is then initialized to a random configuration. The configuration sampling is based on the Metropolis algorithm.<sup>26</sup> The chemical potential of the gaseous reservoir in the ideal gas approximation is calculated from statistical mechanics,<sup>27</sup> where the partition sum includes translational and rotational contributions (vibrational and electronic degrees of freedom are neglected). The output files provide ensemble distributions, their coverage, and the accepted geometries.

**Ab Initio Computations, Construction of the Model Hamiltonian and Its Validation.** In order to access large unit cells and being able to equilibrate the ensemble distribution, we chose to model the system with an Ising-type Hamiltonian represented on a cluster basis.<sup>28</sup> Such a model requires a lattice of points distributed through the three dimensions of space. Each point in the lattice may be occupied by a Pd or Ag atom. A specific chemical realization of the lattice is called a configuration of the system. For our purposes, the most important function of the system's configuration is the configurational energy. In the present work, the configurational energy is expanded in terms of two-body cluster contributions relative to atoms and adsorption sites. Ising-type Hamiltonians of alloys are analogous to the spin Hamiltonians employed to model magnetic phenomena, but with one severe difference. As it is known, spins not only interact with each other but also with an external field to which they can align to. Prediction of alloy phase diagrams does not require any contact with external fields. Nevertheless, a mathematical equivalence between external fields and gaseous reservoirs has been demonstrated.<sup>29</sup> This equivalence is of essence in the present context, although it must undergo some rewriting because of the heterogeneity of acetylene adsorption.

In fact, the acetylenic “field” will be described by an additional two-dimensional gas-lattice layer superimposed to the lattice of metallic atoms. The local orientation of the acetylenic field relative to an adsorption site will be depicted with an arrow, as shown in Figure 1.

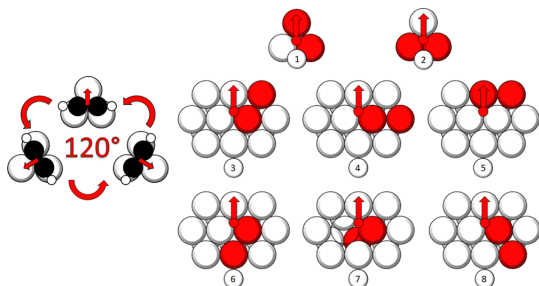


**Figure 1.** Effect of acetylene adsorption on pair interactions at the surface hollow site. Red atoms stand for atoms included in the cluster, white atoms for sites excluded. The red arrow is perpendicular to the C–C bond of acetylene, thus pointing toward the “weakly” interacting atom in the metal site (see text for more explanations).

An aspect common to alloy systems is that the energy of a particular metallic species depends on its position with respect to the catalyst surface.<sup>30</sup> As a result, at equilibrium, one of the species (Pd or Ag) is expected to segregate at the surface. Distinct energy coefficients were therefore assigned to Pd and Ag atoms for each of the positions in the four layers. This is depicted in Figure 2, where interactions between nearest

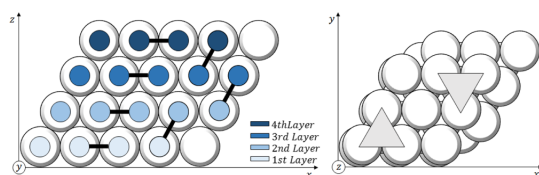


**Figure 2.** Catalyst model and selected interactions. Triangles in the top view (right part of the picture) denote acetylene adsorption sites.

neighbors are also displayed. Because of linear dependencies between single and two-body clusters, we only included pair interactions in the model. Third-order and higher coefficients were neglected based on the previous knowledge of the system.<sup>16</sup> Note that both intra- and interlayer contributions were considered in agreement with the symmetry loss along the normal axis ( $z$  axis of Figure 2). The number of metallic atom interaction terms to be included into the model amounts, therefore, to 24. These coefficients have been fitted on a set of 226 configurations of the bare surfaces.

To assess the effect of acetylene on the (111) surface plane of Pd–Ag alloys, the geometry of adsorption on palladium must be considered in the first place. It is known<sup>31</sup> that acetylene adsorbs on palladium (111) at triangular hollow sites (see Figures 1 and 2). At low pressure and temperature, a molecule of acetylene lies in the middle of such sites and the geometry of this di- $\sigma$  mode suggests that the molecule is strongly bound to two of the site’s atoms and weakly to the third one. The molecule seldom jumps to another site via a diffusional transition state where it interacts with two of the

site’s metallic atoms—the so-called “bridge” mode. An additional local minimum is the  $\pi$  mode, where acetylene sits only on one metallic atom. Because triangles of three metallic atoms are enough to capture acetylene adsorption, surface–acetylene interactions are effectively described in terms of triangular ensembles. These triangular ensembles are reported in Figure 1, which also shows an important characteristic of the di- $\sigma$  mode: the site accommodates the molecule in three different orientations, generated by rotations of  $120^\circ$ . In the case of pure metal ensembles, that is, Pd<sub>3</sub> and Ag<sub>3</sub>, the three rotations are degenerated in energy because of symmetry considerations. However, for the mixed ensembles, Pd<sub>2</sub>Ag and PdAg<sub>2</sub>, the site symmetry is lower, requiring the distinction between “weakly” and “strongly” interacting atoms. In other words, acetylene exhibits different orientations, as represented by an arrow normal to the C–C axis on Figure 1, pointing to the weakly interacting metal atom. The two kinds of atom (weakly and strongly interacting) may be either palladium or silver. This makes seven energy coefficients describing the isolated acetylene adsorption with the triangular site in the model Hamiltonian. However, when considering various configurations of the Pd–Ag alloy, we found that the triangular model is oversimplified. Indeed, in order to have a reasonably accurate fit for the low coverage adsorption of acetylene, an extended environment has to be considered: on the surface, the complete set of nearest neighbors of the “strong” pair has to be included. Furthermore, the second layer atoms close to the adsorption site [1 or 2 for face-centered cubic and hexagonal close-packed (hcp), respectively] also influence the adsorption energy. Interestingly, the central subsurface atom (i.e., the one below the hcp site) does not play any role. To parametrize this extended environment, 24 more coefficients are required. The 31 two-body interaction terms for the single adsorption mode of acetylene have been fitted to 150 configurations.

The 55 coefficients considered up to this point describe the adsorption process of an ideal lattice-gas adsorbed layer. As we have shown previously,<sup>17</sup> acetylene molecules adsorbed on the Pd–Ag catalyst exert rather strong interactions between each other at short intermolecular distances. These lateral interactions must, therefore, be included in the model as well. Lateral interactions of nearest neighbor pairs (red to blue points in Figure 3) are found to be unphysical and are, therefore, excluded in the model Hamiltonian. Second (red to green) and third (red to yellow) nearest neighbor interactions were identified for various relative orientations (see Figure 3). Orientations not covered by the model Hamiltonian correspond to arrangements that do not exist on the relaxed DFT potential energy surface.

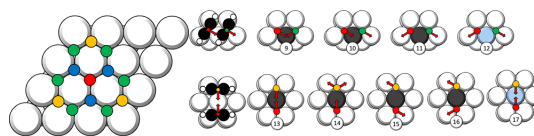


**Figure 3.** Lateral interactions parametrized in the model Hamiltonian. Red: central adsorption site; dark blue: first nearest neighbor; green: second nearest neighbor; and yellow: third nearest neighbor. The red arrow indicates the orientation of acetylene with respect to the triangular site (see also Figure 1). Gray and light blue represent Pd and Ag atoms, respectively. White atoms stand for sites not included in the cluster.

## Chapter 2. Acetylene Adsorption on Pd-Ag Alloys: Evidence for Limited Island Formation and Strong Reverse Segregation from Monte Carlo Simulations

As displayed in Figure 3, lateral interactions are parametrized by a further set of 9 three-body terms. These parameters were fitted to 52 configurations with varying surface coverage and silver/palladium content. Hence, in total, the model Hamiltonian contains 64 terms, fitted to a set of 428 DFT computations.

The fitting was done in three separate steps, one for the pure catalyst, one for the low coverage adsorption of acetylene, and finally, one for the lateral interactions. The numerical values were obtained by a least-squares fit, exploiting the Moore–Penrose pseudoinversion<sup>32</sup> of the following equation

$$E_{\text{DFT}} = \mathbf{A} \cdot \mathbf{e} \quad (1)$$

Here,  $\mathbf{A}$  is a  $c \times p$  matrix whose elements are the occurrences of cluster in a given configuration,  $E_{\text{DFT}}$  the  $1 \times c$  column vector of the  $c$  configuration total energies, and  $\mathbf{e}$  is the  $1 \times p$  column vector of  $p$  the cluster coefficients, also called parameters. We have checked that Cook's distances are below  $4/c$  as suggested by Bollen and Jackman,<sup>33</sup> so that all parameters are statistically well defined. Additionally, we have computed the uncertainties in the model parameters. As shown in Tables S1 to S3, except for the lateral interactions, all parameters have low uncertainties. Furthermore, the values are chemically rather reasonable. Regarding the pure surface, the major surprise is that the segregation is not visible in the Ag–Ag versus Pd–Pd coefficients as a function of the position in the layer. Nevertheless, the numerical simulations (vide infra) clearly show the expected segregation of Ag to the surface in the absence of acetylene adsorption, that is, at high temperatures. We have found that the model Hamiltonian slightly overestimates the tendency of mixing Pd with Ag on the surface, so that mixed ensembles are more probable than that in a perfectly random alloy (see the Supporting Information). However, extensive tests have shown that this tendency is so small that it has no visible influence on the obtained results. Coefficients associated with adsorption on Pd all favor the process, whereas interaction of acetylene with Ag is of little importance. The weak/strong relation between acetylene and metallic atoms is captured for Pd, with an energy difference between the two coefficients of 0.09 eV. In an analogous way, the coefficient of a weakly interacting Ag atom is 0.07 eV higher in energy than the strongly bonded one.

While least-squares interpolations are potentially subjected to overfitting,<sup>34</sup> that is, not only do they model relevant information but also noise as well, our parity plots (Figure 4) clearly show that the complexity of our systems is larger than the (effective) number of parameters used to describe them. By effective parameters, we mean the rank of the occurrence matrix, that is, the number of linearly independent variables. Limitations in the model, that is, the truncation of the cluster expansion and the absence of coefficients describing stress or strain due to lattice constant mismatch, are responsible for the inaccuracies observed in Figure 4.

The model's predictive power was tested toward atomic swaps of the pure catalyst (Figure 4, top). The energetics of swapping atom positions are already reasonably well captured at the singly body level (blue points), where the energy of Pd and Ag only depends on the layer they are found in, which would be characteristic of a random alloy. The determination coefficient can, however, be further improved (from 0.76 to 0.82) by including two-body terms. These corrective terms are found to be rather small ( $<0.1$  eV). Therefore, extending the alloy description to computationally significantly more costly

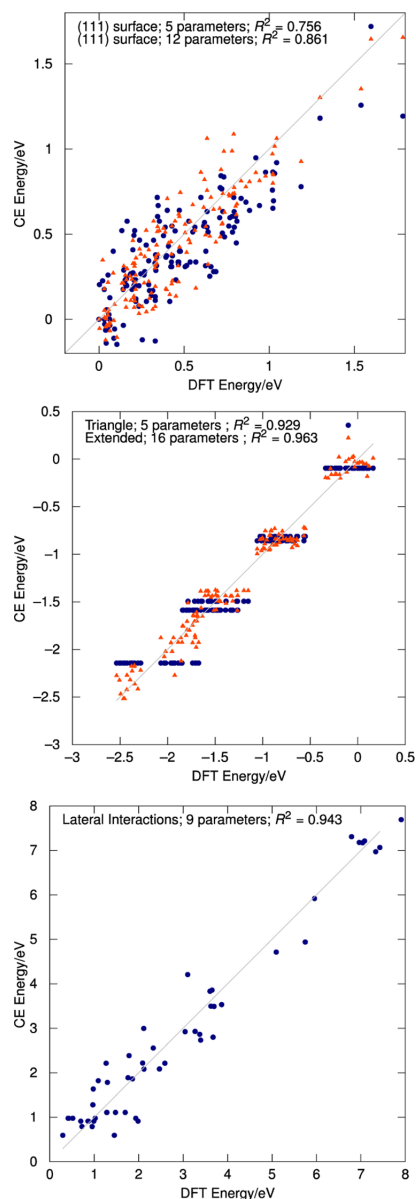


Figure 4. Parity plots of atomic swaps in bare surface models (top) and adsorption energies of a single acetylene molecule on various PdAg alloy surfaces (middle). Total lateral interactions for systems with 3 to 8 acetylene molecules on a  $p(4 \times 4)$  surface are given in the bottom graph. The number of independent variables is given in the legend.

three-body terms does not seem necessary, and we adopt the model with two-body terms only, which gives a standard error of 0.14 eV for our simulations.

Regarding the adsorption energies of a single acetylene molecule on a  $p(3 \times 3)$  cell (Figure 4, middle), the simplified triangular sites capture the overall tendency well (determination coefficient of 0.93). However, the straight “lines”



formed by the blue dots demonstrate that the triangles fail to provide a realistic picture of the variations of adsorption energies as a function of the surface composition. Therefore, we have included an extended environment in the cluster expansion at the single molecule adsorption level. The additional six sites allow to increase the determination coefficient to 0.96 and to lower the standard error from 0.19 to 0.14 eV. This demonstrates that the adsorption of acetylene on PdAg alloy surfaces is more complex to describe than that previously thought, that is, that more than only three atoms are required to capture the full spectrum of adsorption energies on the alloy surface.

Finally, the bottom graph of Figure 4 shows the parity plot for the lateral interactions. The absolute values of the lateral interactions are very high (up to 8 eV) because it corresponds 3–8 acetylene molecules interacting with each other on a  $p(4 \times 4)$  unit cell. Note that all of these systems have been fully optimized to the nearest local minimum, starting either from manually constructed systems or from structures reconstructed based on simulations on a  $p(4 \times 4)$  cell using our Monte Carlo code. A large spread is observed within these configurations, with an  $R^2$  of 0.94 and a standard error of 0.54 eV. Indeed, the parameters for the lateral interactions are associated with the largest uncertainty (see Table S3). To analyze the lateral interactions, we have first considered the obtained parameters: lateral interactions are generally strongly repulsive ( $\sim 0.8$  eV for third and  $\sim 1.2$  eV for second nearest neighbors), with the modulation between different terms being in line with expectations based on steric repulsion and unfavorable sharing of metallic sites. There is one exception, though: the Ag variant of third nearest neighbor interaction turns out to be slightly attractive ( $-0.3$  eV). Test simulations with the specific term set to a slightly positive value (within the 95% uncertainty range of this parameter, see the Supporting Information) are in full agreement with the conclusions drawn based on the mean parameters from the least-squares fit. Second, Figure 5

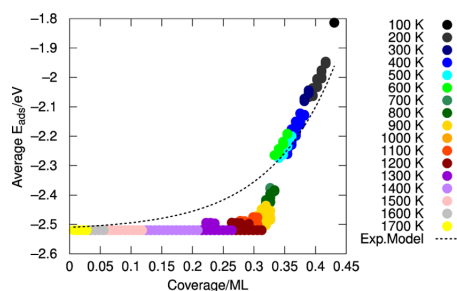


**Figure 5.** Average adsorption energy per acetylene molecule on Pd(111) as a function of the coverage, as obtained from simulations at 1 bar and varying the temperature. The dotted line indicates the exponential model proposed in ref 16.

compares the results from our simulations for pure Pd(111) with the mean field model proposed in our previous work. As can be seen, the simulations up to about 500 K probe coverages larger than 0.3 ML and lower than 0.45 ML, a region in which the model prediction and the simulated data are in quite good agreement. Even at 100 K, higher coverages are prohibited by steric repulsion. The absence of long-ranged repulsive terms mostly affects the agreement between the model Hamiltonian and the continuum model between 0.2 and

0.3 ML, a region which is relevant only at temperatures well above 500 K. Therefore, our model is quite accurate in the realistic region of coverages. Because the lateral interactions are not determined very precisely but could be potentially very important (vide infra), we have performed additional sets of simulations that probe the influence of the precise value of these terms on the results (see the Supporting Information). These simulations show that the observed results are overall robust with respect to such variations.

## RESULTS AND DISCUSSION

Numerical experiments were designed bearing two goals in mind, namely, (1) to predict the equilibrium distribution of Ag through the model, with special focus on the topmost layer and (2) to assess the effect of the temperature on this distribution. To this end, the global molar fraction of Ag and the temperature were used as control parameters, maintaining the simulated pressure of acetylene at the constant value of 1 bar. The fraction of Ag was scanned with steps of 0.1 or finer in regions with quickly changing properties. The temperature was scanned between 100 and 1700 K, whereas the catalytically relevant temperature is between 300 and 400 K. Note that the simulations of temperatures above 500 K are of little practical relevance but shed light on the physics of the system (order–disorder transition). The simulated systems consisted of 576 metallic atoms distributed through the four-layer model, with 288 hollow sites available for adsorption. The configurational energy starts to fluctuate around its final value after about 10 000 steps (see Figure S1). All simulations were carried out to reach a total of 100 000 steps, with the last 90 000 steps, sampled every 100 steps, being used for analysis.

Figure 6 shows segregation profiles of the model, that is, the fractional amount of Ag in the topmost layer as a function of

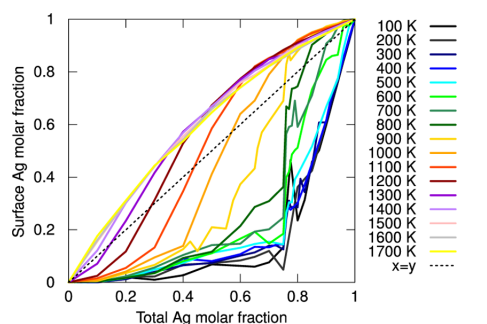


**Figure 6.** Segregation of the surface model as a function of the temperature.

the total Ag fraction. The straight dotted line, corresponding to an ideal model in which Ag and Pd are randomly placed into the surface, is included as a guide to the eye. As long as the temperature is low enough, 100–600 K, the profile of the Ag layer fraction lies well below the random distribution line, that is, the surface is Pd rich. At catalysis temperature, the surface Pd fraction can be up to  $\sim$ four times higher than that in the bulk. At 900 K, the profile intersects the ideal distribution at 0.75 and its curvature changes; this trend continues at higher temperatures. At temperatures below 900 K, the simulations corresponding to total Ag molar fractions between 0.75 and 0.8 exhibit significant fluctuations, indicating that two arrange-

## Chapter 2. Acetylene Adsorption on Pd-Ag Alloys: Evidence for Limited Island Formation and Strong Reverse Segregation from Monte Carlo Simulations

ments are in competition (*vide infra*). Because the acetylene coverage drops with increasing temperature, starting from 1300 K, the surface is Ag rich for all molar fractions, in agreement with expectations based on the lower surface energy of Ag compared to Pd.

In summary, the segregation profiles show two regimes: at low (high) temperature and high (low) acetylene coverage, a Pd and Ag enrichment is obtained, respectively. Indeed, at low temperatures, acetylene adsorption is stable enough to attract a large fraction of Pd atoms from the subsurface to the topmost layer. As the temperature increases, thermal effects interfere with adsorption and Ag atoms tend to populate the surface as a result of their more favorable segregation energy and the increased importance of configurational entropy in the alloy. It is interesting to note that above 800 K, the segregation profiles start to cross the random distribution. In other words, while at low Ag fraction, Pd still segregates to the surface, the high temperature induces an increasingly large range of Ag fractions corresponding to a Ag-rich surface. However, because the transition temperature for this mixed behavior is very high (above 800 K), it is not important for technologically relevant applications, such as membrane science or catalysis. In conclusion, acetylene severely modulates the surface composition, leading to a reverse segregation compared to vacuum conditions.

As mentioned in the **Introduction**, acetylene binds to more than one surface atom. One is then naturally led to assess the effect of this multidentate adsorption on the ordering of the topmost layer, that is, island formation. In order to separate the vertical segregation from the “horizontal” in-plane ordering, **Figure 7** top shows the populations of ensembles at different temperatures as a function of the Ag fraction in the topmost layer and compares it to random distributions. The bottom panel provides the acetylene coverage of these ensembles. Note that the saturation coverage obtained on Pd(111) agrees well with the measured value (1/3 ML), hence validating the accuracy of the model.<sup>35,36</sup> In **Figure 7** top panel, overall, the points stay rather close to the random distributions: acetylene is not capable of strongly reorganizing the layer laterally even at low temperatures. This contrasts with our previous assessment based on a continuum model that showed marked deviations from random distributions upon acetylene adsorption.<sup>17</sup> Because the simulation at 100 K yields distributions very similar to that at 300 K, the effect of entropy does not seem to be a determining factor for the in-plane (dis-)ordering. However, in contrast to the results of the continuum model, Pd<sub>2</sub>Ag ensembles are also covered by acetylene at 300 K (see **Figure 7** bottom). This is due to two effects. First, **Figure 4** (middle) shows that the horizontal line of blue dots around  $-1.5$  eV, which corresponds to adsorption on Pd<sub>2</sub>Ag, can go down to adsorption energies as low as  $-1.8$  eV depending on the environment, whereas the adsorption energy on a Pd<sub>3</sub> ensemble can be as high as  $-1.6$  eV if embedded in silver. In other words, the environment leads to a large distribution of binding energies that are overlapping between Pd<sub>3</sub> and Pd<sub>2</sub>Ag ensembles, counteracting the intrinsic island formation preference. Furthermore, even on Pd<sub>3</sub>, only a bit more than one-third of the triangular ensembles is occupied at 300 K (see **Figure 7**, bottom), which reduces the drive for island formation even more: in the continuum model, the mixed ensembles acted as inactive spacers, which allowed to maximize the coverage on Pd<sub>3</sub> ensembles. However, in the real space model presented herein, islands of Pd<sub>3</sub> are only covered by up to 0.4

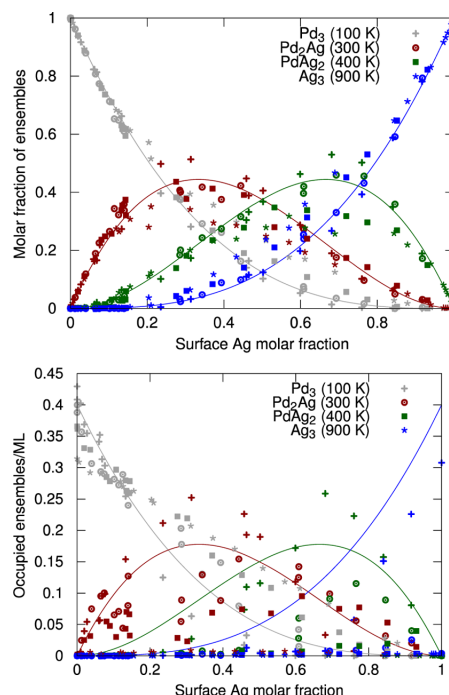


**Figure 7.** Surface ensemble populations (top, Pd<sub>3</sub> gray, Pd<sub>2</sub>Ag red, PdAg<sub>2</sub> green, and Ag<sub>3</sub> blue) and their acetylene coverage (bottom) at 100 K (crosses), 300 K (circles), 400 K (squares), 900 K (stars), and random distribution (full lines) as a function of the surface layer Ag molar fraction.

ML and the mixed sites can still be occupied. Together, this correlation between occupied and unoccupied sites strongly reduces the island formation tendency. The intrinsic island formation tendency can be estimated by a back on the envelope calculation: the transformation of 2 Pd<sub>3</sub> and 1 Ag<sub>3</sub> ensembles into 3 Pd<sub>2</sub>Ag ensembles has only a relatively small effect ( $\{3 \times -1.5\} - \{2 \times -2.1\}$  eV =  $-0.3$  eV). The small energetic difference rationalizes that the intrinsic ordering tendency of the system is not dominating if entropy and realistic lateral interactions are taken into account.

In **Figure 7**, we also present data for 400 and 900 K. These temperatures illustrate that the Pd<sub>3</sub> ensembles become more important with an increase in temperature: adsorption on PdAg<sub>2</sub> drops to zero at 400 K (green squares) and at 900 K also Pd<sub>2</sub>Ag (red crosses) is empty. Hence, we see a relative increase in the population of Pd<sub>3</sub> sites at surface Ag molar fractions larger than 0.5 with respect to lower temperatures, deviating from random distribution.

The sensitivity of our results to the lateral interactions is shown in the **Supporting Information**. Although the overall conclusions are not affected by the strength of the lateral interactions, more repulsive lateral interactions reduce the coverage of the mixed ensembles significantly.

The rapid change occurring at 0.7–0.8 Ag molar fraction is characteristic of the system and holds for all temperatures below 1000 K. Above 1000 K, Ag surface segregation is dominating, suppressing phase transitions. Given that we are modeling a four-layer system, the rapid change is suspiciously

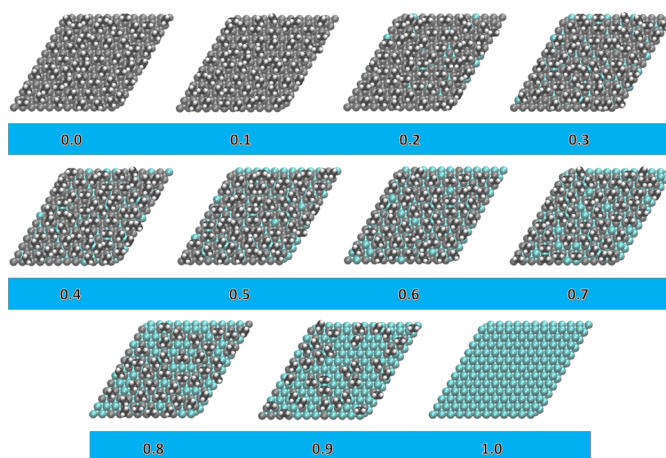


Figure 8. Snapshots of last accepted configuration at 300 K as a function of total Ag molar fraction.

close to the composition where a full Pd layer cannot be formed anymore. However, according to Figure 7, the near random distributions are maintained over most Ag fractions. Nevertheless, the surface Ag content “jumps” from  $<0.2$  to  $>0.3$  for moderate temperatures, indicating a phase transition. It might be no coincidence that it is in this region where the random distributions of Pd<sub>3</sub> and Pd<sub>2</sub>Ag cross (0.25). In other words, the system changes from being dominated by (covered) Pd<sub>3</sub> ensembles to a very disordered system where the coverage of Pd<sub>3</sub> and Pd<sub>2</sub>Ag ensembles is of similar magnitude.

Figure 8 depicts snapshots of the last accepted configuration at 300 K as a function of the total Ag content. The first observation is that the acetylene overlayer is quite disordered. Second, despite the general impression gained from Figure 7 that many Pd<sub>3</sub> ensembles remain empty, Figure 8 clarifies that for surfaces with a significant Ag content ( $>0.7$ ) almost all of the Pd atoms are involved in binding acetylene, which contrasts with the Ag atoms which are frequently observed to act as inactive spacers between the Pd-rich ensembles, in agreement with intuition. This also contributes to the overall low driving force toward island formation: in a Pd island (similar to that on pure Pd), Pd atoms are sometimes “wasted” to lower the steric repulsion, that is, the lateral interactions. At high temperatures, a partial ordering in the surface layer is obtained: the PdAg<sub>2</sub> sites being unoccupied, only the Pd<sub>3</sub> ensembles contribute to the enthalpic stabilization of the system and they tend to organize into small islands or strips (not shown). Therefore, we have the untypical situation where higher temperatures lead to more ordered surfaces than lower temperatures, which follow the random distributions more closely.

## CONCLUSIONS

In this work, we have established a detailed model Hamiltonian for the Pd–Ag alloy configurations and for the acetylene adsorption on this alloy. We show that the adsorption energy of acetylene depends not only on the nature of the triangular site on which it is bound but also on the extended environment, that is, the nine nearest metallic atoms. Using the simple triangular sites does not provide an accurate description of the adsorption energy as a function of surface

composition. The 24 interaction energy parameters have been fitted to roughly 400 DFT energies and provide overall an RMSD in the range of 0.2 eV. Lateral interactions are generally strongly repulsive and play a central role to determine the surface structure.

By performing Monte Carlo simulations based on this model Hamiltonian, we demonstrate that at realistic pressures, acetylene adsorption strongly modifies the composition of the Pd–Ag topmost layers in a wide range of operational conditions (300–500 K). Reverse segregation pushes Pd atoms to populate the catalyst surface almost completely. This strong vertical reorganization of the alloy upon acetylene adsorption contrasts with the very moderate changes in the lateral organization (at a given surface concentration). Around an Ag fraction of 0.8 Ag, a phase transition is observed for temperatures below 1000 K. Above this transition point, the alloy surface is no longer dominated by Pd<sub>3</sub> ensembles. Because the Pd–Ag surface sticks closely to random distributions, at low enough temperatures ( $<400$  K) and high total Ag fractions ( $>0.8$ ), a majority of acetylene molecules can be adsorbed on Pd<sub>2</sub>Ag ensembles.

This thermodynamic vertical reorganization of the alloy surface under a pressure of acetylene is likely to be involved in the experimentally observed aging process of AgPd selective hydrogenation catalysts. In other words, because acetylene induces reverse segregation, the ideal selective hydrogenation catalyst with well-dispersed Pd ensembles, surrounded by Ag, is thermodynamically unstable. However, if the ideal catalyst can be prepared and the temperature is maintained low in order to reduce the diffusion process leading to surface reordering, the catalyst lifespan is likely to be increased. Similarly, structural agents, be it third metal, supports or ligands, that would slow down diffusion and/or counteract the effect of acetylene would increase the stability of the active catalyst.

## ASSOCIATED CONTENT

### Supporting Information

The Supporting Information is available free of charge on the ACS Publications website at DOI: 10.1021/acs.jpcc.8b04108.



## Chapter 2. Acetylene Adsorption on Pd-Ag Alloys: Evidence for Limited Island Formation and Strong Reverse Segregation from Monte Carlo Simulations

Cluster expansion parameters, convergence behavior of typical Monte Carlo simulations; rank correlation for relative energies of Pd/Ag (111) alloy surfaces; relative energies from DFT and cluster expansion; and sensitivity of selected features on the lateral interaction parameters (PDF)  
Geometry for each structure (POSCAR file for VASP) (ZIP)  
Programs for numerical simulations (ZIP)

### AUTHOR INFORMATION

#### Corresponding Authors

\*E-mail: [Stephan.steinmann@ens-lyon.fr](mailto:Stephan.steinmann@ens-lyon.fr) (S.N.S.).

\*E-mail: [sautet@ucla.edu](mailto:sautet@ucla.edu). Phone: 1-310-825-8485 (P.S.).

#### ORCID

Stephan N. Steinmann: 0000-0002-2777-356X

Philippe Sautet: 0000-0002-8444-3348

#### Notes


The authors declare no competing financial interest.

### ACKNOWLEDGMENTS

Ab initio calculations were performed using the local HPC resources of PSMN at ENS-Lyon. This work was granted access to the HPC resources of CINES and IDRIS under the allocation 2014-080609 made by GENCI. Selective Hydrogenation of Acetylene in an Ethylene-Rich Flow: Insights from Molecular Modeling is a research project funded by TOTAL Refining & Chemicals and the ANRT.

### REFERENCES

- (1) Callister, W. D.; Rethwisch, D. G. *Materials Science and Engineering: An Introduction*, 7th ed.; Wiley Publishers: New York, 2006.
- (2) Tsai, M.-H.; Yeh, J.-W. High-Entropy Alloys: A Critical Review. *Mater. Res. Lett.* **2014**, *2*, 107–123.
- (3) Zou, Y.; Ma, H.; Spolenak, R. Ultrastrong Ductile and Stable High-Entropy Alloys at Small Scales. *Nat. Commun.* **2015**, *6*, 7748.
- (4) Dowben, P. A.; Miller, A. *Surface Segregation Phenomena*; CRC Press: Boca Raton, FL, 1990.
- (5) De Clercq, A.; Giorgio, S.; Mottet, C. Pd surface and Pt subsurface segregation in Pt1–cPd nanoalloys. *J. Phys. Condens. Matter* **2016**, *28*, 064006.
- (6) Clarke, J. K. A. Selectivity in Catalysis by Alloys. *Chem. Rev.* **1975**, *75*, 291–305.
- (7) Tao, F.; Salmeron, M. In Situ Studies of Chemistry and Structure of Materials in Reactive Environments. *Science* **2011**, *331*, 171–174.
- (8) Hirschl, R.; Delbecq, F.; Sautet, P.; Hafner, J. Adsorption of Unsaturated Aldehydes on the (111) Surface of a Pt-Fe Alloy Catalyst from First Principles. *J. Catal.* **2003**, *217*, 354–366.
- (9) Zhu, B.; Creuze, J.; Mottet, C.; Legrand, B.; Guesmi, H. CO Adsorption-Induced Surface Segregation and Formation of Pd Chains on AuPd(100) Alloy: Density Functional Theory Based Ising Model and Monte Carlo Simulations. *J. Phys. Chem. C* **2016**, *120*, 350–359.
- (10) Chen, W.; Schmidt, D.; Schneider, W. F.; Wolverton, C. Ordering and Oxygen Adsorption in Au-Pt/Pt(111) Surface Alloys. *J. Phys. Chem. C* **2011**, *115*, 17915–17924.
- (11) Løvrik, O. M.; Opalka, S. M. Reversed Surface Segregation in Palladium-Silver Alloys due to Hydrogen Adsorption. *Surf. Sci.* **2008**, *602*, 2840–2844.
- (12) Svenum, I.-H.; Herron, J. A.; Mavrikakis, M.; Venvik, H. J. Adsorbate-induced segregation in a PdAg membrane model system: Pd3Ag(111). *Catal. Today* **2012**, *193*, 111–119.
- (13) Padama, A. A. B.; Kasai, H.; Budhi, Y. W. Hydrogen Absorption and Hydrogen-Induced Reverse Segregation in Palladium-Silver Surface. *Int. J. Hydrogen Energy* **2013**, *38*, 14715–14724.
- (14) Vignola, E.; Steinmann, S. N.; Al Farra, A.; Vandegehuchte, B. D.; Curulla, D.; Sautet, P. Evaluating the Risk of C-C Bond Formation during Selective Hydrogenation of Acetylene on Palladium. *ACS Catal.* **2018**, *8*, 1662–1671.
- (15) Ponc, V.; Bond, G. C. *Catalysis by Metals and Alloys*; Elsevier: Amsterdam, 1995.
- (16) Engstfeld, A. K.; Hoster, H. E.; Behm, R. J. Formation, atomic distribution and mixing energy in two-dimensional PdxAg1–x surface alloys on Pd(111). *Phys. Chem. Chem. Phys.* **2012**, *14*, 10754.
- (17) Vignola, E.; Steinmann, S. N.; Vandegehuchte, B. D.; Curulla, D.; Sautet, P. C2H2-Induced Surface Restructuring of Pd-Ag Catalysts: Insights from Theoretical Modeling. *J. Phys. Chem. C* **2016**, *120*, 26320–26327.
- (18) Blöchl, P. E. Projector Augmented-Wave Method. *Phys. Rev. B: Condens. Matter Mater. Phys.* **1994**, *50*, 17953–17979.
- (19) Kresse, G.; Joubert, D. From Ultrasoft Pseudopotentials to the Projector Augmented-Wave Method. *Phys. Rev. B: Condens. Matter Mater. Phys.* **1999**, *59*, 1758–1775.
- (20) Kresse, G.; Hafner, J. Ab initio molecular dynamics for liquid metals. *Phys. Rev. B: Condens. Matter Mater. Phys.* **1993**, *47*, 558–561.
- (21) Kresse, G.; Furthmüller, J. Efficient iterative schemes for ab initio total-energy calculations using a plane-wave basis set. *Phys. Rev. B: Condens. Matter Mater. Phys.* **1996**, *54*, 11169–11186.
- (22) Perdew, J. P.; Burke, K.; Ernzerhof, M. Generalized Gradient Approximation Made Simple. *Phys. Rev. Lett.* **1996**, *77*, 3865–3868.
- (23) Steinmann, S. N.; Corminboeuf, C. Comprehensive Benchmarking of a Density-Dependent Dispersion Correction. *J. Chem. Theory Comput.* **2011**, *7*, 3567–3577.
- (24) Monkhorst, H. J.; Pack, J. D. Special Points for Brillouin-Zone Integrations. *Phys. Rev. B: Condens. Matter Mater. Phys.* **1976**, *13*, 5188–5192.
- (25) Methfessel, M.; Paxton, A. T. High-Precision Sampling for Brillouin-Zone Integration in Metals. *Phys. Rev. B: Condens. Matter Mater. Phys.* **1989**, *40*, 3616–3621.
- (26) Frenkel, D.; Smit, B. *Understanding Molecular Simulations*; Academic Press: San Diego, 1996.
- (27) Hill, T. L. *An Introduction to Statistical Thermodynamics*; Dover Publications: New York, 1960.
- (28) Sanchez, J. M.; Ducastelle, F.; Gratias, D. Generalized Cluster Description of Multicomponent Systems. *Phys. Stat. Mech. Appl.* **1984**, *128*, 334–350.
- (29) Lee, T. D.; Yang, C. N. Statistical Theory of Equations of State and Phase Transitions. II. Lattice Gas and Ising Model. *Phys. Rev.* **1952**, *87*, 410–419.
- (30) Ruban, A. V.; Abrikosov, I. A. Configurational Thermodynamics of Alloys from First Principles: Effective Cluster Interactions. *Rep. Prog. Phys.* **2008**, *71*, 046501.
- (31) Dunphy, J. C.; Rose, M.; Behler, S.; Ogletree, D. F.; Salmeron, M.; Sautet, P. Acetylene Structure and Dynamics on Pd(111). *Phys. Rev. B: Condens. Matter Mater. Phys.* **1998**, *57*, R12705–R12708.
- (32) Barata, J. C. A.; Hussein, M. S. The Moore-Penrose Pseudoinverse: A Tutorial Review of the Theory. *Braz. J. Phys.* **2012**, *42*, 146–165.
- (33) Bollen, K. A.; Jackman, R. W. Regression Diagnostics: An Expository Treatment of Outliers and Influential Cases. *Modern Methods of Data Analysis*; Sage: Newbury Park, 1990; pp 257–291.
- (34) Bishop, C. M. *Pattern Recognition and Machine Learning*; Springer-Verlag: New York, 2006.
- (35) Janssens, T. V. W.; Völkening, S.; Zambelli, T.; Wintterlin, J. Direct Observation of Surface Reactions of Acetylene on Pd(111) with Scanning Tunneling Microscopy. *J. Phys. Chem. B* **1998**, *102*, 6521–6528.
- (36) Gates, J. A.; Kesmodel, L. L. Thermal Evolution of Acetylene and Ethylene on Pd(111). *Surf. Sci.* **1983**, *124*, 68–86.



### **3 Evaluating the Risk of C-C Bond Formation during Selective Hydrogenation of Acetylene on Palladium**

During the industrially relevant semi-hydrogenation of acetylene over Pd-Ag alloy catalysts, the formation of what is called “green oil” is leading to catalyst deactivation since green-oil is not desorbed from the catalyst and thus prevents fresh reactants to reach the surface. Chemically, green oil is a partially hydrogenated oligomerization product of acetylene. Experimentally, alloying Pd with Ag has been found beneficial, although it is not precisely known how the green-oil formation is slowed down. In this work, we have extensively investigated the various intermediates susceptible to C-C bond formation, which is the initial step of the oligomerization process. Furthermore, we have assessed the site requirements (i.e., how many Pd atoms need to be clustered together to facilitate the C-C bond formation) of the kinetically favored processes. We have revealed that the intermediates that oligomerize are unavoidable during the semi-hydrogenation of acetylene. Furthermore, already small ensembles of Pd are sufficient to facilitate this unwanted side reaction. Hence, in combination with the insights of chapter 2, very high Ag molar fractions are required to significantly reduce the green oil formation. However, even at high Ag content the reverse segregation (exposing more and more Pd atoms) becomes dominant for aged catalysts, which favors the oligomerization side reaction. This study illustrates the need to thoroughly investigate the entire relevant reaction network in order to pin-point the weak spots of the process. Such extensive, systematic, investigations are, however, only possible on model catalysts.



## Evaluating the Risk of C–C Bond Formation during Selective Hydrogenation of Acetylene on Palladium

Emanuele Vignola,<sup>†,‡</sup> Stephan N. Steinmann,<sup>\*,†,§</sup> Ahmad Al Farra,<sup>‡</sup> Bart D. Vandegehuchte,<sup>§</sup> Daniel Curulla,<sup>§</sup> and Philippe Sautet<sup>\*,†,||,⊥</sup>

<sup>†</sup>Univ Lyon, ENS de Lyon, CNRS, Université Lyon 1, Laboratoire de Chimie UMR 5182, F-69342, Lyon, France

<sup>‡</sup>Total Research and Technology Gonfreville, BP 27, F-76700 Harfleur, France

<sup>§</sup>Total Research and Technology Feluy, Zone Industrielle Feluy C, Seneffe, Hainaut 7181, Belgium

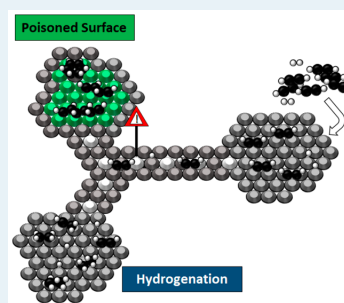
<sup>||</sup>Department of Chemical and Biomolecular Engineering, University of California, Los Angeles, Los Angeles, California 90095, United States

<sup>⊥</sup>Department of Chemistry and Biochemistry, University of California, Los Angeles, Los Angeles, California 90095, United States

### Supporting Information

**ABSTRACT:** Palladium-based catalysts are known to promote the selective hydrogenation of acetylene to ethylene. Unfortunately, coupling reactions between the numerous surface intermediates generated in this process occur alongside. These side reactions are undesired, generating the so-called “green oil”, i.e., C<sub>4</sub>+ hydrocarbons that poison the active sites of the catalyst. The current work assesses the energetic and kinetic aspects of C<sub>4</sub> side products formation from the standpoint of computational chemistry. Our results demonstrate that the C–C coupling of common surface species, in particular acetylene, vinylidene, and vinyl, is competitive with selective hydrogenation. These C–C couplings are particularly easy for intermediates where the C–Pd bond can largely remain intact during the coupling. Furthermore, the thus formed oligomers tend to be hydrogenated more easily, consuming hydrogen normally spent on acetylene hydrogenation. The analysis of site requirement suggests that isolated Pd<sub>2</sub> ensembles are sufficient for selective hydrogenation and would suppress oligomerization. However, upon aging, the PdAg alloy is likely to undergo reverse segregation, and in this case, our computations suggest that the selectivity of the catalyst is lost, with enhanced C–C couplings interfering even more strongly. Hence, small Pd ensembles are crucial to avoid oligomerization side reactions of acetylene.

**KEYWORDS:** palladium-based catalysts, “green oil”, C–C coupling, DFT, acetylene hydrogenation



### INTRODUCTION

Carbon–carbon coupling reactions are among the most useful transformations in organic chemistry.<sup>1</sup> They allow chemists to build complex carbon frameworks from their reagents, thereby achieving products of greater complexity, spreading benefits from daily laboratory practice to the pharmaceutical, the biochemical, and the polymer industry. Palladium is at the core of this chemistry for fine chemicals, since it is the elected metallic catalyst promoting carbon–carbon coupling.<sup>2</sup> Although the majority of catalysts are homogeneous palladium complexes to be used in solution phase reactions, supported heterogeneous palladium catalysts start to attract interest as a promising alternative. Today, Pd-based heterogeneous catalysts are particularly important in the industrial production of polyethylene. Ethylene streams from oil refineries contain about 1% acetylene. Leaving acetylene in the ethylene feedstock for polyethylene would lead to deteriorated material properties and decreased catalyst life spans. Therefore, the ethylene stream is subjected to a partial hydrogenation process,<sup>3</sup> where acetylene is selectively hydrogenated to ethylene, while avoiding overhydrogenation toward ethane. This selective hydrogenation

is carried out over Pd alloy catalysts, with Pd surface atoms constituting the active sites.

Unfortunately, during this process Pd can also catalyze oligomerization of hydrogenation intermediates. Indeed, Pd acts as a C–C coupling catalyst, producing complex mixtures of oligomeric compounds.<sup>4</sup> This mixture contains three main fractions: a light end fraction which remains in the gas phase, a liquid portion that is entrained by the gas in the form of fine droplets (denoted as “green oil”), and a heavy fraction, the “sticky green oil”. These oligomeric species have several deleterious effects: first, they reduce the atom efficiency of the process, since the carbon contained in green oil cannot be valorized. Second, the sticky green oil blocks active sites and therefore slowly deactivates the catalyst. Therefore, the catalyst needs to be regenerated periodically by oxidation followed by reactivation through reduction. High-temperature reduction has been found to be especially crucial for Pd alloy catalysts, most

Received: November 3, 2017

Revised: January 9, 2018

Published: January 11, 2018

## Chapter 3. Evaluating the Risk of C-C Bond Formation during Selective Hydrogenation of Acetylene on Palladium

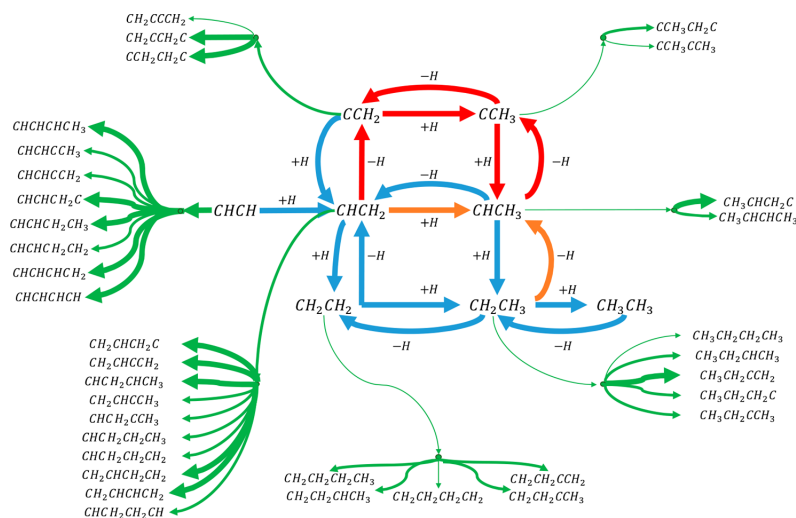


**Figure 1.** Reaction scheme considered. The green arrows indicate unwanted oligomerization, the blue ones indicate the “direct” hydrogenation of acetylene, and the red ones refer to the isomerization process to asymmetric C<sub>2</sub> species. Arrows in thin, medium, and bold lines represent activation energies <1.5 eV, between 1.5 and 2.0 eV, and >2 eV, respectively. For the various hydrogenation elementary reactions of C<sub>4</sub> species considered, the reader is referred to Figure 5.

likely since the high temperature favors solid solution, rather than segregation of the two metals.<sup>5,6</sup> However, green oil is present not only on the catalyst but also on the support.<sup>7</sup> This leads to an increased mobility of the catalyst and, therefore, to an accelerated sintering during the regeneration process. Hence, suppressing green-oil formation would improve catalyst life span and increase atom efficiency at the same time. While alloying Pd with Ag, Cu, or Au either keeps the amount of green oil produced constant or reduces it somewhat, it clearly does not completely suppress it.<sup>8–10</sup> Furthermore, even on pure Ag some green-oil formation is observed;<sup>11</sup> and some supports, such as  $\gamma$ -alumina catalyze part of the C–C couplings, leading to the heavier fractions.<sup>12</sup> Nevertheless, the secondary metal not only forms C–C bonds more slowly, but it also binds the intermediates less strongly and thus favors desorption of the intermediates into the gas-phase, leading to less heavy green oil.<sup>13</sup>

The characterization of these coupling derivatives is not a trivial task. Few groups have tried to analyze the carbonaceous deposits, and their results are not always in agreement.<sup>14</sup> While it is commonly agreed that the gaseous fraction is prevalently composed of C<sub>4</sub> and C<sub>6</sub> hydrocarbons,<sup>4</sup> discrepancies are more obvious regarding the composition of green oil. Yayun et al.<sup>15</sup> reported that the liquid heavy polymers have an average composition of C<sub>n</sub>H<sub>(1.8–1.9)n</sub> with a number of carbon atoms between 14 and 17, and an olefin/paraffin ratio between 0.1 and 0.4. Most remarkably, no aromatics were detected although palladium is renowned to boost acetylene trimerization.<sup>16</sup> Gandman et al.<sup>17</sup> have presented a different green-oil composition, with a content of aromatic compounds as high as 74.5% in weight, 23.0% of olefins, and a small fraction of diolefins. The origin of the oligomers is also controversial. Most authors agree that the oligomers are exclusively derived from acetylene. Nevertheless, according to the results obtained by Yayun et al.,<sup>15</sup> ethylene in the feed participates in the process as well. The influence of the hydrogen partial pressure is rather complex: oligomerization only occurs in the presence of

adsorbed hydrogen. Therefore, the reaction is often referred to as acetylene hydro-oligomerization. At high H<sub>2</sub> partial pressures, the formation of green oil decreases, however at the cost of a lack of selectivity toward ethylene.<sup>18,19</sup> According to isotopic labeling and spectroscopic techniques, the most likely molecular precursors for green oil are acetylene, CCH<sub>2</sub> (vinylidene), and CHCH<sub>2</sub> (vinyl).<sup>14,20</sup>

In addition to C–C coupling, C–C decomposition products are expected as well. In particular, carbon atoms penetrate the surface layer and preferentially occupy the octahedral vacancies of the lattice to form an interstitial alloy.<sup>21,22</sup> This Pd/C phase crucially alters the adsorption energetics of the reagents,<sup>23</sup> thereby lowering acetylene conversion but improving the selectivity toward ethylene as it weakens ethylene adsorption and hinders the kinetics of subsurface hydrogen diffusion in model catalysts.<sup>3</sup> However, the hydrides and carbide phases are largely suppressed by the industrially relevant addition of CO, which has been shown to be a beneficial additive.<sup>24,25</sup> Since these C<sub>1</sub> species have been extensively investigated by Mei et al.<sup>26</sup> and are, according to isotopic labeling studies,<sup>20</sup> not expected to play a major role in C–C coupling reactions, we do not reinvestigate them in this paper.

The complete reaction network encompasses Horiuti-Polanyi additions of hydrogen atoms to acetylene,<sup>27</sup> as well as oligomerization by C–C bond formation and decomposition of intermediates into carbon and hydrogen. Consecutive hydrogenation and dehydrogenation lead to ethylidyne (CCH<sub>3</sub>) as an asymmetric side-intermediate, either via vinyl (CHCH<sub>2</sub>) or ethylidene (CHCH<sub>3</sub>) (see Figure 1). Ethylidyne has been identified experimentally as early as 1986 and its hydrogenation is significantly slower than the direct hydrogenation of ethylene.<sup>28</sup> The interconversion of ethylidyne, ethylene, and acetylene was computationally investigated in 2002.<sup>29</sup> A later refinement was proposed by Moskaleva et al.<sup>30</sup> and IR measurements finally complemented the understanding of the role of this intriguing species.<sup>31</sup> Ethylidene formation seems to be kinetically preferred when subsurface hydrogen is

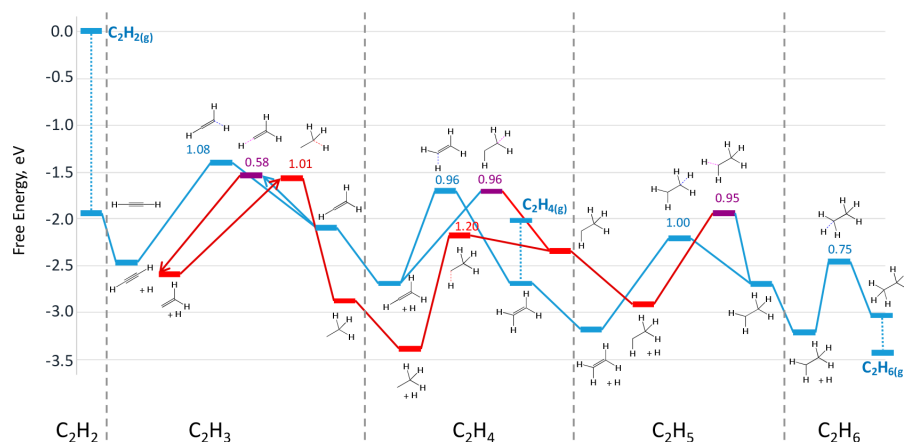


**Figure 2.** C<sub>2</sub> hydrogenation network free energy (eV) on Pd(111) at standard conditions. The path in blue is the “direct” hydrogenation path to ethylene and ethane. The path in red involves a rearrangement of hydrogen atoms, leading to the asymmetric ethylidyne intermediate. In purple are the transition states that connect the two pathways. All depicted intermediates are chemisorbed on the surface. Numbers indicate the activation energies of the elementary steps.

allowed to take part in vinyl hydrogenation,<sup>24</sup> but it otherwise acts as a pure spectator of the reaction. Herein, we consider only C<sub>2</sub> and C<sub>4</sub> species, in order to focus on the competition between oligomerization and selective hydrogenation of acetylene. The elementary steps considered herein are shown in Figure 1, where the hydrogenation reactions converting C<sub>4</sub> species into each other are excluded for the sake of clarity (see Figure 5 for the C<sub>4</sub> species).

Even though the C–C coupling is a very important reaction for side-product formation, only very few theoretical studies have tackled this complex reaction network. Based on the accepted view that butadiene is involved in the formation of the heavy hydrocarbons, Lopez and Vargas-Fuentes proposed<sup>32</sup> an acetylene–acetylene cis coupling step to C<sub>4</sub>H<sub>4</sub> requiring an ensemble of at least 4 active metal atoms. Yang et al.<sup>33</sup> compared three paths to 1,3-butadiene on plain and stepped surfaces in the presence of subsurface carbon and alloyed silver atoms. They proposed that, on a clean Pd(111) surface, acetylene–acetylene coupling followed by hydrogenation is the preferred route to butadiene, while the Pd(211) stepped surface favors vinyl–vinyl coupling. The presence of subsurface carbon or small amounts of alloy metals reduces the adsorption energies for all intermediates and slightly raises activation energies (~0.1 eV). The effect of molecular spacers on the selectivity versus oligomers formation was also explored for the case of carbon monoxide. Computations showed<sup>24,25</sup> that this adsorbate reduces the size of active ensembles available for coupling steps; however, only one oligomerization step (namely, the acetylene–vinyl coupling) was included into the network, and the ethylidyne route was not considered. To the best of our knowledge, even the experimentally proposed pathway involving CCH<sub>2</sub><sup>14</sup> has not yet been investigated computationally. Hence, although there have been valuable first steps, a comprehensive assessment of the various possibilities for C–C bond formation between surface intermediates has been lacking so far. Figure 1 illustrates the large spectrum of theoretically possible carbon–carbon couplings.

This paper addresses the aspects of acetylene hydrogenation and oligomerization on palladium from first-principle computations. Since CO acts mainly as a molecular spacer and

suppresses the hydride and carbide phases, we consider a bare Pd surface as a relevant, albeit simplified model. Particular attention has been given to the roles of vinylidene, ethylene, and the ethylidyne-related fragments for green-oil formation. The presented detailed mechanistic study emphasizes the role of early hydrogenation intermediates, both responsible for the selectivity toward ethylene, rather than ethane, and of the undesired oligomerization reactions. To put the results into a broader perspective, implications for catalysis on the industrially important Pd–Ag alloy catalysts are discussed. At the extreme of well mixed solid solutions, we discuss the site and ensemble-requirements for the selectivity-controlling steps. At the other extreme of reverse segregated catalysts, the most salient kinetic and thermodynamic features are compared to those acquired on a Pd–Ag model.

## ■ COMPUTATIONAL DETAILS

Total energies were computed at the density functional level of theory in the PAW formalism,<sup>34,35</sup> with the Vienna ab initio simulation package.<sup>36,37</sup> The functional of Perdew, Burke, and Ernzerhoff<sup>38</sup> was employed, corrected for intermolecular forces following the scheme of Steinmann and Corminboeuf,<sup>39</sup> which was shown to perform very well for adsorption energies of organic molecules on a closely related system, Pt(111), when compared to experiment.<sup>40</sup> A plane wave basis set was used, with a cutoff energy of 400 eV. Surface models were cut out of the f.c.c. bulk structure along the 111 crystal direction. A p(3 × 3) unit cell with 4 metallic layers was used for the surface model, keeping the bottom-most two layers fixed, in order to simulate bulk properties. Fifteen angstrom of vacuum were inserted between periodic images along the axis normal to the surface, which proved to be sufficient to avoid spurious interactions between repeated images of the cell. Sampling of the Brillouin zone was performed with a Monkhorst–Pack<sup>41</sup> generated 3 × 3 × 1 k-points grid. The Methfessel–Paxton<sup>42</sup> smearing scheme was employed in all computations, with a broadening value of 0.2 eV. No normal-mode analysis was performed except for transition states (TS). The transition states have been located as follows: the coadsorbed state



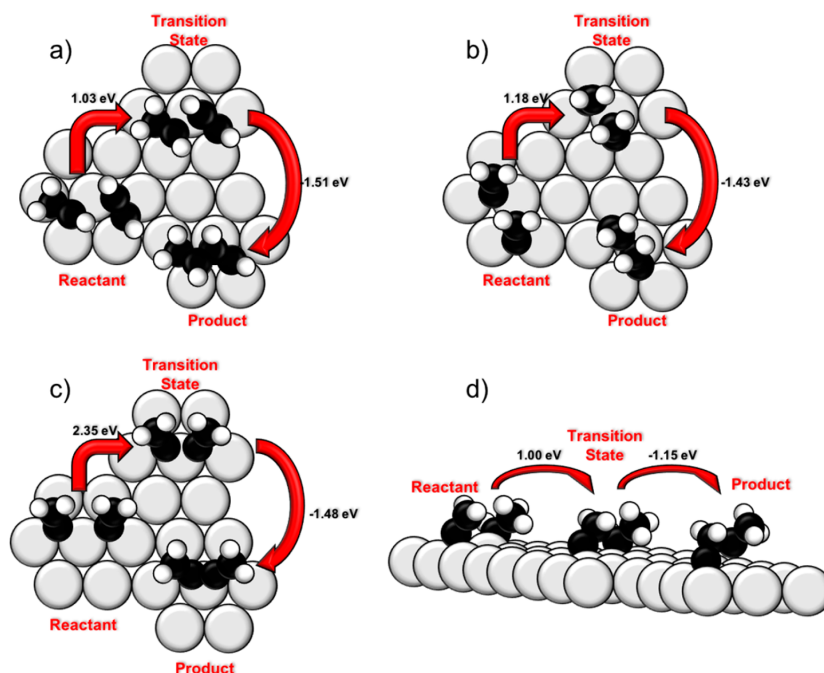


Figure 3. Selected, typical C–C coupling steps between C<sub>2</sub> surface species. (a) CHCH + CHCH<sub>2</sub> to give CHCHCHCH<sub>2</sub>; (b) and CCH<sub>2</sub> + CCH<sub>2</sub> to give CCH<sub>2</sub>CH<sub>2</sub>C; (c) CCH<sub>2</sub> + CCH<sub>2</sub> to give CH<sub>2</sub>CCCH<sub>2</sub>; (d) CHCH<sub>3</sub> + CCH<sub>2</sub> to give CH<sub>3</sub>CHCH<sub>2</sub>C.

corresponding to the two reacting fragments has been constructed based on the adsorption mode of the individual fragments, moved to neighboring positions. Then, a nudged-elastic band (NEB)<sup>43</sup> computation with 8 images between the initial and final state was performed, seeded by interpolations between the two states obtained by the Opt'n Path code,<sup>44</sup> which uses a combination of internal and Cartesian coordinates. After about 50 cycles of NEB, the improved guess for the transition state was fully optimized to a first order saddle point by the dimer method<sup>45</sup> and the normal modes checked to contain only one imaginary frequency corresponding to the bond formation process.

Chemical potentials of gaseous species were calculated from statistical mechanics,<sup>46</sup> ignoring the vibrational contributions to partition functions, at 300 K and 1 bar.

## RESULTS AND DISCUSSIONS

**Hydrogenation of C<sub>2</sub> species.** We first present the thermodynamics and kinetics for the hydrogenation/dehydrogenation steps of C<sub>2</sub> intermediates derived from acetylene.

Industrially, the reaction is carried out on Ag–Pd-based catalysts in the range of 300 to 380 K in a large excess of ethylene. For this model study on Pd(111), we have chosen standard conditions to reduce the complexity, i.e., 300 K and 1 bar for all gases. Figure 2 shows the free energy profile for the C<sub>2</sub> hydrogenation reaction network subset of Figure 1. The adsorption free energy of acetylene on Pd(111) is determined to –1.95 eV. Addition of a surface hydrogen (referenced as 1/2 H<sub>2</sub>), leads to vinyl (CHCH<sub>2</sub>) corresponding to a barrier of 1.08 eV. At this point, the system may evolve along two different pathways (red and blue in Figure 2). On the one hand, an additional atom of hydrogen results in ethylene requiring an

activation energy of 0.96 eV. Either ethylene desorbs quickly (the process is nonactivated but endergonic by 0.7 eV), or hydrogenates further to ethyl with an activation energy of 1.00 eV. Note that the difference in adsorption energy between acetylene and ethylene, which has been used as a primer for the selectivity of the hydrogenation,<sup>47</sup> is only affected by 0.1 eV when accounting for dispersion interactions, since the adsorption of acetylene and ethylene are more exothermic by 0.3 and 0.4 eV, respectively. On the other hand, vinyl may dissociate relatively fast (barrier of 0.58 eV) to atomic hydrogen and vinylidene, CCH<sub>2</sub>. Vinylidene may be hydrogenated to ethylidyne, CCH<sub>3</sub>, with an activation energy of 1.01 eV (the reverse barrier is 1.26 eV). Ethylidyne plus hydrogen is a particularly interesting intermediate, being both the global free energy minimum and the kinetically most inert point. The activation energy of CCH<sub>3</sub> to CHCH<sub>3</sub> is 1.20 eV, while the reverse barrier is only 0.17 eV). In any event, if CHCH<sub>3</sub> is produced, its hydrogenation to CH<sub>2</sub>CH<sub>3</sub> can proceed with an activation energy of 0.95 eV. Ethyl can be finally hydrogenated to ethane with a barrier of only 0.75 eV, and the weakly bound ethane product quickly desorbs. An additional interconnection between the “direct” (in blue) and the “asymmetric” (in red) pathways comes from the asymmetric hydrogenation of vinyl. Here, vinyl goes directly into CHCH<sub>3</sub> by an activation energy of 0.95 eV.

From these free energy pathways, the experimentally observed CCH<sub>3</sub> can either be formed from CCH<sub>2</sub> (barrier of 1.01 eV) or by the dehydrogenation of CHCH<sub>3</sub> ( $\Delta E^\ddagger=0.17$  eV), which converts an ethane precursor into an inert spectator. The hydrogenation of CHCH<sub>2</sub> is found to be the most critical step for ethylene selectivity, since the barriers toward ethylene and toward the unwanted CHCH<sub>3</sub> are found to be equivalent

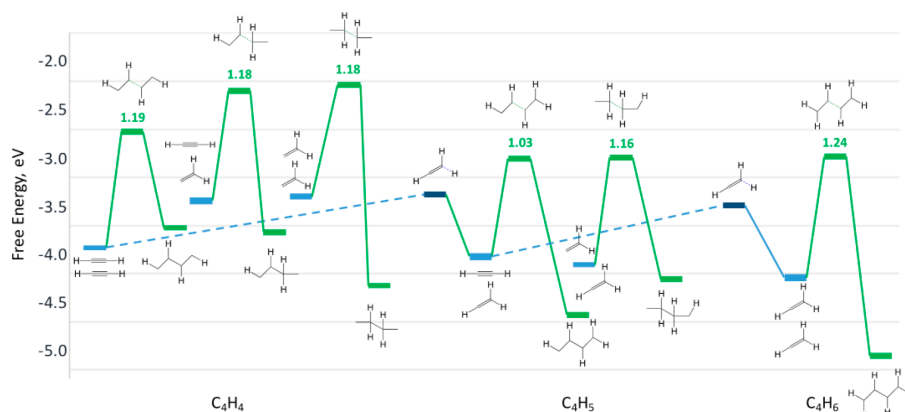


**Figure 4.** Key oligomerization steps forming  $C_4$  intermediates by coupling of  $C_2$  fragments. All energies are referenced to acetylene and hydrogen in the gas-phase under standard conditions. For the paths between  $C_2$  intermediates of the same stoichiometry, see Figure 2.

(0.96 eV). Once ethylene is formed, its desorption is easier than its further hydrogenation implying that little ethane should be formed this way. Based on the stability of intermediates and the energy barriers, we expect that the surface would be predominantly covered by hydrogen,  $C_2H_2$ , and  $CCH_3$ . This predicted state of the surface constitutes a first approximation to a more realistic state to be determined by atomically detailed kinetic simulations.

**$C_4$  derivatives formation.** Figure 2 only includes reactions leading to the hydrogenation and isomerization of  $C_2$  species. We include now the elementary steps involved in oligomerization. All  $C_2$  coupling reactions were considered, since an *a priori* identification of thermodynamic and kinetic restrictions is difficult. Most of the  $C_2$  intermediates are asymmetric and therefore have two nonequivalent carbons that can form a new C–C bond. A convenient way to classify these chemical functionalities is to count the number of hydrogens bound to the carbon atom. If S stands for the catalytic surface, C for the carbon atom involved in the coupling and R for the second carbon fragment of the  $C_2$  intermediate, the chemical functions available for C–C coupling are the carbyne group,  $R-C\equiv S$ , the methylidyne group,  $R-CH\equiv S$ , and the methylene group,  $R-CH_2-S$ . Following this logic, acetylene has only one functional group,  $S=CH-CH\equiv S$ , while vinyl has two, i.e.,  $R-CH\equiv S$  and  $S-CH_2-R$ . Applying these rules leads to a total of 58 distinct  $C_4$  intermediates. On top of that, E/Z isomers may exist and the activation energy might depend on the type of surface site (top, hollow etc.). We explored all the possible intermediates and, for the stable ones, located the E or Z transition state, considering three possibilities for the newly formed C–C bond: top, bridge and hollow. With this approach, we were able to identify 50 reaction steps as reported in Table S2 in the SI.

Figure 3 illustrates four distinct C–C couplings. Figure 3a shows the *trans* acetylene–vinyl coupling on a surface top site, which has an activation energy of only 1.03 eV. It can be seen how closely the reactant positions and especially the transition states resemble the final product structure. The acetylene carbon–carbon axis stays nearly parallel to the Pd–Pd bond and the methylidyne group in vinyl remains completely unperturbed on top of one Pd atom. Only the methylene group is displaced during the transformation. This mode of C–

C coupling is typical for fast reactions during which the  $\pi$  systems remain parallel to the surface.

Coupling carbon atoms showing little or no interaction with the catalytic surface is a process with a moderate barrier. In contrast, those steps requiring strongly bound carbons to be desorbed from the surface are disfavored (see Table S2). This is demonstrated with the coupling of two  $CCH_2$  species, one of the experimentally proposed precursors of green oil. The coupling leading to  $CH_2CCCH_2$  implies a partial cleavage of both triple bonds between the  $CCH_2$  sp carbon atoms and the catalyst. As shown in Figure 3c, the molecules are coupled on top of a surface Pd atom, resulting in a high activation energy of 2.35 eV. This sharply contrasts with the alternative coupling to  $CCH_2CH_2C$ : for the coupling of two vinylidene molecules via their methylene functional groups, an activation barrier of only 1.18 eV is obtained. The spatial arrangement exhibited by this transformation is shown in Figure 3b, confirming that no significant alteration of the adsorbate/surface interaction is necessary for this step.

The reaction of  $CHCH_3$  and  $CCH_2$  to give  $CH_3CHCH_2C$  has the lowest activation energy, 1.00 eV. Figure 3d shows the transition state, in which  $CHCH_3$  is slightly lifted from the surface and couples to the spectating  $-CH_2-$  group. Since  $CHCH_3$  is rather unstable (it dehydrogenates with a barrier <0.2 eV), its partial desorption is rather easy, agreeing with the fact that weakly bound functional groups are activated more easily.

Regarding thermodynamics on the Pd surface, formation of  $C_4$  molecules such as *cis*- and *trans*-butene, butadiene, and butane are among the most exothermic reactions (see Table S2). The balance between formation of alkyl chains and desorption of strongly bound functional groups drives the formation of less common oligomeric precursors. In this perspective, the most exergonic reaction comes from the coupling of ethyl and vinylidene to give  $CH_3CH_2CH_2C$ : the gain in free energy is  $-1.05$  eV. Close to this value is the free energy gain for 1,3-butadiene formation,  $-0.86$  eV. Reactions involving ethylene are mostly endergonic, spanning an interval between  $-0.04$  and 1.05 eV. Together with the relatively large activation energies for ethylene couplings ( $>1.3$  eV), the absence of a thermodynamic driving force does not support the experiment based suggestion of Yayun et al.<sup>15</sup> that ethylene



## Chapter 3. Evaluating the Risk of C-C Bond Formation during Selective Hydrogenation of Acetylene on Palladium

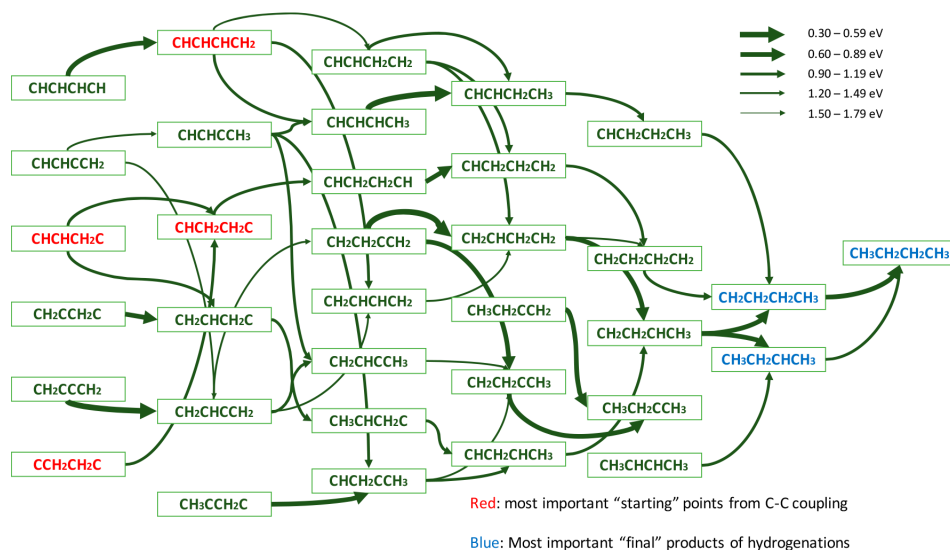


Figure 5. C<sub>4</sub> hydrogenation network. Arrow thicknesses relate to the activation energies.

participates in oligomerization. Again, our results rather support that green oil only involves hydrogen and acetylene derivatives. Similarly, just as for hydrogenations, ethylidyne requires significant activation energies for C–C couplings (>1.6 eV), confirming its role as a spectator in the reaction network.

The focus is now turned on oligomerization steps that are competitive with acetylene hydrogenation. Figure 4 summarizes the least activated processes starting from acetylene and vinyl, as certain surface species, and ethylidyne (CCH<sub>2</sub>) exhibiting a comparable barrier for coupling and hydrogenation. The coupling of acetylene with another acetylene molecule, which has often been invoked in the literature, last but not least due to the characterization of the corresponding intermediate,<sup>48</sup> is 0.1 eV more activated than its hydrogenation. This difference drops to 0.05 eV for the coupling of acetylene with vinyl (CHCH<sub>2</sub>), a step that is also quite exothermic. Similarly, the hydrogenation of vinyl toward ethylene is only favored by 0.07 eV over this C–C coupling reaction. Prior to the formation of the “safe” ethylene surface intermediate, oligomerization of C<sub>2</sub> species is probable if they approach each other too closely. As discussed below, the required spacing might be provided either by a high hydrogen coverage or by highly dispersed Pd ensembles in PdAg alloys. When ethylene is overhydrogenated, CHCH<sub>3</sub> and CH<sub>2</sub>CH<sub>3</sub> constitute an additional pair of intermediates that poses a high risk for oligomerization (see Table S2).

**Hydrogenation of C<sub>4</sub> derivatives.** Couplings of C<sub>2</sub> species are of crucial importance in identifying the most competitive events generating the components of green oil. However, C<sub>4</sub> species can also be hydrogenated. Hydrogenation pathways were all assumed to be of the Horiuti-Polanyi type at low coverage (only one H atom on the p(3 × 3) Pd(111) surface). 52 direct hydrogenation steps were identified. These pathways complement the hydrogenation of butadiene (CH<sub>2</sub>CHCHCH<sub>2</sub>), previously published by our group.<sup>49</sup>

Figure 5 and Table S-3 (see SI) indicate that the hydrogenations of C<sub>4</sub> species tend to be less activated (and thus faster) than C<sub>2</sub> hydrogenations. The average activation energy to hydrogenate a C<sub>4</sub> fragment is 0.97 eV, which is

competitive with the hydrogenation of acetylene (1.08 eV) and vinyl (0.96 eV). Beyond this average value, we found cases of extremely fast hydrogenations: 22 intermediates are hydrogenated faster than vinyl and six have an activation barrier lying under 0.70 eV. The fastest C<sub>4</sub> hydrogenation is, with  $\Delta E^\ddagger = 0.31$  eV, the hydrogenation of CHCHCHCH<sub>3</sub> to CHCHCH<sub>2</sub>CH<sub>3</sub>. The C<sub>4</sub> coupling products starting from vinylidene (CCH<sub>2</sub>) most likely go through CHCH<sub>2</sub>CH<sub>2</sub>C, followed by the hydrogenation of the terminal carbon, leading to CHCH<sub>2</sub>CH<sub>2</sub>CH, which is then converted to CHCH<sub>2</sub>CH<sub>2</sub>CH<sub>2</sub>. The other important route starts with the most commonly formed oligomer, CHCHCHCH<sub>2</sub>. This species can hydrogenate as quickly at one or the other terminal position. If the methylene carbon atom is hydrogenated, the resulting CHCHCHCH<sub>3</sub> intermediate quickly hydrogenates to CHCHCH<sub>2</sub>CH<sub>3</sub>. Alternatively, if hydrogenation occurs at the methylidyne end group,<sup>49</sup> butadiene is obtained. Experimentally, butadiene is commonly observed during acetylene hydrogenation, especially at intermediate stages of catalyst deactivation.<sup>50</sup> According to a previous study of our group,<sup>49</sup> butadiene hydrogenates rather quickly (activation energies of 0.7–0.9 eV) to 1- and 2-butene, both of which are also observed experimentally.

The result that C<sub>4</sub> hydrogenations are competitive with C<sub>2</sub> hydrogenations is in good agreement with experimental evidence.<sup>14,50</sup> This situation is not only problematic in terms of hydrogen atom efficiency, but also since acetylene and CHCH<sub>2</sub> are involved in the oligomerization reaction. Hence, if the C<sub>2</sub> species are not hydrogenated fast enough to ethylene, they are more likely to oligomerize. The oligomers in turn increase the hydrogen demand for C<sub>4</sub> hydrogenations. Hence, a significant hydrogen partial pressure might be necessary to maintain a sufficient surface hydrogen coverage. The hydrogen coverage might also help to slow down the C–C coupling by isolating C<sub>2</sub> species from each other through adsorbed hydrogen atoms. This scenario is in agreement with experimental findings that green-oil formation goes through a maximum upon increasing the hydrogen partial pressure.<sup>8,19</sup>

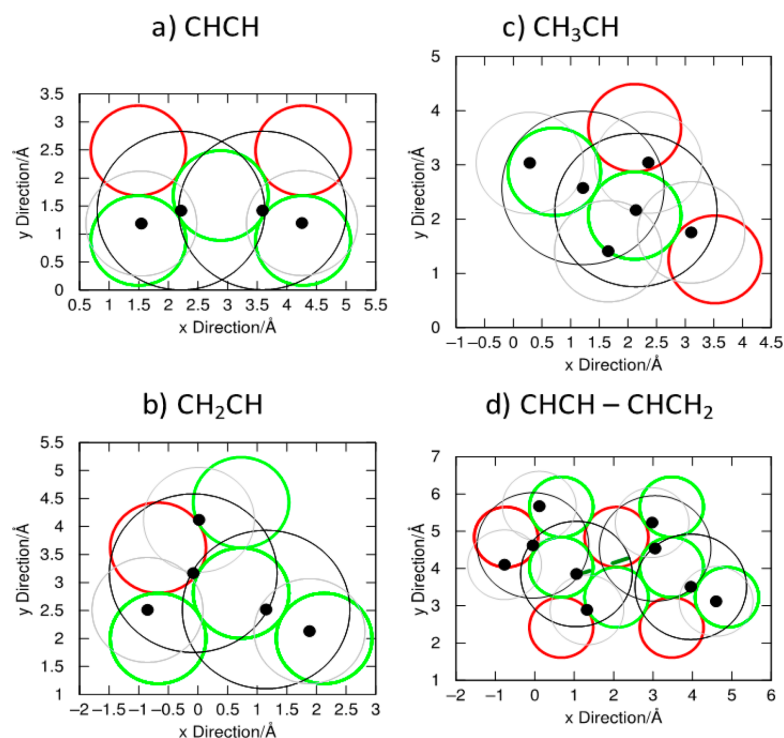


**Figure 6.** Site requirements for key intermediates on a Pd(111) surface. Occupied top sites (in red) and 3-fold hollow sites (in green) are highlighted. The atomic nuclei of the adsorbate are given as black dots, and the size of the atoms is indicated as black and gray circles for carbon and hydrogen, respectively. The bond being formed in (d) is indicated by a dashed green line.

Unfortunately, however, too high hydrogen partial pressures diminish the selectivity of acetylene hydrogenation, leading to large amounts of ethane.

In the following two subsections, we will consider two extreme cases, relevant for AgPd catalysts. On the one hand, we assess well mixed solid solutions, where the ensembles for Pd atoms can be rather small and we therefore might have a chance to largely suppress green-oil formation due to the geometric effect. On the other hand, surface reorganization under reactive conditions might lead to large patches of Pd surrounded by Ag. In such a situation, only the electronic effect of Ag alloying comes into play. As will be shown, this electronic effect might slightly increase green-oil formation.

#### ■ ENSEMBLE REQUIREMENTS FOR KEY REACTION STEPS

A key question for the design of optimal catalysts for hydrogenation of acetylene in order to improve selectivity and avoid unwanted oligomers such as green oil is to determine the ensemble of atoms required for each elementary step in the mechanistic network. One way to depict this active site requirement is to determine the surface atoms that are formally occupied by a given intermediate or transition state. As we have established in a previous study<sup>51</sup> the projection of atomic radii on a graphical lattice including top and 3 fold hollow sites is an accurate method to assign sites to a given adsorbate. Here, we apply this approach to four key species in the mechanism: (a) acetylene, which needs to be adsorbed strongly for hydro-

genation (b)  $\text{CHCH}_2$ , which is a certain intermediate in the selective hydrogenation toward ethylene (c)  $\text{CHCH}_3$ , which might proceed to nonselective ethane formation and cause surface poisoning through  $\text{CCH}_3$  accumulation, and (d) the transition state for the C–C bond formation between acetylene and  $\text{CHCH}_2$ . The latter process has a competitive barrier (1.03 eV) compared to that for the hydrogenation to ethylene (0.96 eV) and represents the path leading to unwanted oligomers. The corresponding site requirements are given in Figure 6.

In agreement with our previous study on the Pd–Ag alloy,<sup>52</sup> Figure 6a indicates that there are two top sites (red circles) which are crucial for the binding energy of acetylene. Furthermore, the C–C bond is close to the hollow site (green circle), defined by a third top site. The latter is, however, not directly occupied by the molecule. This implies that an ensemble of 2 Pd atoms will strongly bind acetylene, with a third surface atom modulating the strength of the interaction (Ag for weaker binding, Pd for strong binding). Two additional hollow sites are blocked by the hydrogen atoms.

Moving to the key intermediate for hydrogenation,  $\text{CHCH}_2$ , only one top site is occupied by the adsorbate (see Figure 6b). However, similarly to acetylene, a hollow site is found below the C–C bond. Hence, the neighboring atoms of this hollow site are predicted to have a strong impact on the stability of this intermediate. Since, however, the site requirements of  $\text{CHCH}_2$  are rather less (1 instead of 2 top sites) than more stringent compared to acetylene, the first hydrogenation reaction should be able to proceed on the very same ensemble as for acetylene

## Chapter 3. Evaluating the Risk of C-C Bond Formation during Selective Hydrogenation of Acetylene on Palladium

adsorption, implying that surface diffusion is not required for hydrogenation.

Looking at the third intermediate ( $\text{CHCH}_3$ ), leading to total hydrogenation, Figure 6c suggests that it is also stabilized by essentially the same ensemble of sites as the previous intermediates. Hence, it seems difficult to improve the selectivity toward ethylene, versus ethane, just by controlling the ensemble of Pd atoms: one should rely instead on electronic effects weakening the adsorption of ethylene and favoring its desorption versus further hydrogenation. As one might have expected, the oligomerization process (Figure 6d) requires a larger ensemble of Pd atoms: Four top sites (and six hollow sites) are occupied by the transition state. Hence, if one of the top sites is exchanged for a less reactive metal (e.g., Ag), a significant increase in the activation energy can be expected. This explains the decrease of oligomer production when a PdAg alloy is used, instead of Pd, although other alloys of Pd with metals that bind carbon more weakly (as PdAu) should lead to the same effect.<sup>17</sup>

To conclude, the site requirements for the main  $\text{C}_2$  species are all quite similar. Hence, only specific electronic effects could affect the relative barriers and intermediate energies and hence the selectivity toward ethylene. The C–C coupling, on the other hand, required a markedly larger ensemble and oligomer formation is likely to be strongly slowed down by catalysts composed of exclusively Pd<sub>2</sub> (or maybe Pd<sub>3</sub>) ensembles embedded in a less reactive metal. Our analysis has hence identified the configuration of the sites affecting the stability of intermediates and transition states, which could open to more detailed selective catalyst design using transition metal alloys.

### ■ REVERSE SEGREGATION AND ITS INFLUENCE ON THE SELECTIVITY

When two different metals are mixed together, those atoms showing the least surface formation energy tends to accumulate at the top of the surface, a phenomenon known as *surface segregation*. Pd–Ag alloys pose no exception to this.<sup>55</sup> In vacuum condition, Ag atoms are seen to accumulate at the surface. However, the presence of adsorbates on the surface may significantly enrich the surface in Pd, as it was predicted for atomic adsorbates,<sup>54,55</sup> and for acetylene.<sup>56</sup> In particular, by exploiting large-scale Monte Carlo simulations, we have predicted that, the equilibrium segregation profile is reversed for a wide range of compositions (0.0–0.7) and temperature (300–800 K) in an atmosphere of 1 bar of acetylene, i.e., Pd accumulates at the surface. A comparison between the most striking catalytic features acquired on Pd and the same features as computed on a Pd–Ag model is, therefore, appropriate. We have chosen a 4-layer slab of Pd<sub>25</sub>Ag<sub>75</sub> (111), with all Pd atoms placed on the topmost layer, as the most representative model of the thermodynamically most likely surface state after long exposure to the reactive atmosphere.

Table 1 displays activation energy and reaction parameters for selected key reaction steps: the hydrogenation of vinyl to ethylene and to ethylidene, of ethylidene to ethyl, and of  $\text{C}_4\text{H}_4$  on its terminal carbon atom. Subsurface Ag exerts a tensile strain on the Pd surface layer (unit-cell expansion) and modifies the electronic structure of the surface atoms. This causes a general increase in the catalyst's activity toward hydrogenation, with a lowering of activation energy barriers by  $\sim 0.1$  eV. However, with an activation energy of  $\sim 0.5$  eV, the unwanted acetylene–vinyl coupling for oligomerization experiences an even more important acceleration. If kinetics does not privilege

Table 1. Most Salient Kinetic Features as Computed on a Reverse-Segregated Pd<sub>25</sub>Ag<sub>75</sub> Alloy Model

Reaction Step	R, Å	Freq, cm <sup>-1</sup>	$\Delta E_{\text{act}}$ , eV
$\text{CHCH}_2 + \text{H} \rightarrow \text{CH}_2\text{CH}_2$	1.82	715.24	0.88
$\text{CHCH}_3 + \text{H} \rightarrow \text{CH}_2\text{CH}_3$	1.71	820.38	0.89
$\text{CHCH}_2 + \text{H} \rightarrow \text{CHCH}_3$	1.65	928.46	0.83
$(\text{CHCH})_2 + \text{H} \rightarrow \text{CHCHCHCH}_2$	1.47	855.51	0.79
$\text{CHCH} + \text{CHCH}_2 \rightarrow \text{CHCHCHCH}_2$	2.15	383.84	0.46

selective hydrogenation versus oligomerization on this catalyst, one might still argue that selectivity is due to a profitable difference between acetylene and ethylene adsorption energy. However, we find that the change between pure Pd and reverse-segregated Pd<sub>25</sub>Ag<sub>75</sub> is small, and that the difference in adsorption energy is even slightly decreased (by 0.05 eV) on the alloy model surface.

Both, the ensemble requirements and the unselective reactivity of the reverse-segregated alloy, reinforce the idea that well-mixed catalysts are crucial for selectivity in acetylene hydrogenation. Once the segregation reversal reaches its equilibrium stage, the catalyst is to be considered as aged and formation of oligomers will be favored kinetically and thermodynamically. An estimate of the time scale of the surface restructuring would be of great benefit, but clearly exceeds the scope of the present work. We are not aware of any data in the literature on the evolution of the green-oil formation and surface structure of AgPd catalysts on an industrially relevant time scale (at least months). Therefore, we cannot compare our theoretical predictions on reverse segregation under relevant reaction conditions with any experimental data at this point. Furthermore, realistic kinetic simulations on a surface of an alloy that can undergo both (reverse) segregation and island formation for such a vast reaction network (roughly 40 intermediates) is beyond the capabilities of today's simulation techniques. The major challenge for these simulations is to establish the cluster expansion for all the intermediates as a function of the surface state, i.e., the ensemble on which the intermediate is adsorbed and the lateral interactions due to the presence of other intermediates on the surface.

### ■ CONCLUSIONS

This paper has explored the vast network of chemical reaction steps leading to coupling byproducts during selective hydrogenation of acetylene on a Pd(111) surface. Activation and reaction energies for the coupling between all plausible  $\text{C}_2$  fragments, their interconversion and the key hydrogenation steps of  $\text{C}_4$  intermediates have been computed.

Hydrogenation of  $\text{C}_2$  intermediates is in general faster than C–C coupling. Nevertheless, some dimer formation steps are found to compete with hydrogenation, especially those not requiring cleavage of highly stable carbon–surface bonds, such as the coupling of early intermediates, including acetylene (CHCH) and vinyl (CHCH<sub>2</sub>), and of vinylidene (CCH<sub>2</sub>) provided the strongly bound carbon atom is not involved in the reaction. Ethylene is found to be kinetically inert toward dimer formation. This suggests that its role in the formation of green oil is of little or no importance. These findings are in good agreement with earlier experimental evidence, that acetylene, vinyl and vinylidene are the fragments which are most likely to participate in the formation of green oil.

Hydrogenation of C<sub>4</sub> intermediates is kinetically favored on average compared to the hydrogenation of C<sub>2</sub> species, most likely due to an easier deformation of the intermediate, which on a per carbon basis is less strongly bound than, for instance, acetylene. Hence, C<sub>4</sub> intermediates are likely to consume a significant fraction of the surface hydrogen species. This could promote further coupling of early intermediates, which in turn would exhaust the surface from adsorbed hydrogen, decreasing the atom efficiency of the process. This emphasizes the detrimental role of “green oil” beyond catalyst deactivation. In analogy with the easier C–H bond formation in C<sub>4</sub> compared to C<sub>2</sub> species, the C–C coupling between C<sub>4</sub> intermediates or, statistically more likely, chain elongation by adding a C<sub>2</sub> unit to C<sub>4</sub> intermediates, can also be expected to be faster than the C<sub>2</sub>–C<sub>2</sub> couplings. Together, these observations rationalize the accumulation of long, almost completely saturated hydrocarbons as the main constituents of green oil.

Coupling steps were also investigated for their ensemble requirements, i.e., the size and geometry of a surface site required for reaction. Computations showed that an ensemble of 4 sites of Pd is required to permit acetylene oligomerization. Pd-based alloyed catalyst should then really be well-mixed in order to prevent green-oil formation. Furthermore, we have demonstrated that once the reversed segregation has taken place, the selectivity of the catalyst is lost and green-oil formation is predicted to be fast. This insight sheds a new light on the design of novel catalysts for acetylene selective hydrogenation, emphasizing the need for stable, small, isolated dimers and trimers of the active metal surrounded by an inactive metal in order to avoid competitive oligomerization pathways.

## ■ ASSOCIATED CONTENT

### Supporting Information

The Supporting Information is available free of charge on the ACS Publications website at DOI: 10.1021/acscatal.7b03752.

Reaction and activation energies (PDF)

All geometries (ZIP)

## ■ AUTHOR INFORMATION

### Corresponding Authors

\*E-mail: [stephan.steinmann@ens-lyon.fr](mailto:stephan.steinmann@ens-lyon.fr); tel.: 0033-4-72-72-81-55.

\*E-mail: [sautet@ucla.edu](mailto:sautet@ucla.edu); tel.: 1-310-825-8485.

### ORCID

Stephan N. Steinmann: 0000-0002-2777-356X

Philippe Sautet: 0000-0002-8444-3348

### Notes

The authors declare no competing financial interest.

## ■ ACKNOWLEDGMENTS

*Ab initio* computations were performed using the local HPC resources of PSMN at ENS-Lyon. *Selective Hydrogenation of Acetylene in an Ethylene-Rich Flow: Insights from Molecular Modelling* is a research project funded by TOTAL Refining & Chemicals and the ANRT. This work was granted access to the HPC resources of CINES and IDRIS under the allocation 2014-080609 made by GENCI.

## ■ REFERENCES

- (1) Nicolaou, K. C.; Bulger, P. G.; Sarlah, D. *Angew. Chem., Int. Ed.* **2005**, *44*, 4442–4489.
- (2) Yin, L.; Liebscher, J. *Chem. Rev.* **2007**, *107*, 133–137.
- (3) Borodziński, A.; Bond, G. C. *Catal. Rev.: Sci. Eng.* **2006**, *48*, 91–144.
- (4) Bos, A. N. R.; Westerterp, K. R. *Chem. Eng. Process.* **1993**, *32*, 1–7.
- (5) Jin, Y. *J. Catal.* **2001**, *203*, 292–306.
- (6) Friedrich, M.; Villaseca, S. A.; Szentmiklósi, L.; Teschner, D.; Armbrüster, M. *Materials* **2013**, *6*, 2958–2977.
- (7) Liu, R. J.; Crozier, P. a.; Smith, C. M.; Hucul, D. a.; Blackson, J.; Salaita, G. *Appl. Catal., A* **2005**, *282*, 111–121.
- (8) Leviness, S.; Weiss, A. H.; Schay, Z.; Guzzi, L. *J. Mol. Catal.* **1984**, *25*, 131–140.
- (9) Ahn, I. Y.; Lee, J. H.; Kim, S. K.; Moon, S. H. *Appl. Catal., A* **2009**, *360*, 38–42.
- (10) Pachulski, A.; Schödel, R.; Claus, P. *Appl. Catal., A* **2011**, *400*, 14–24.
- (11) Sárkány, A.; Révay, Z. *Appl. Catal., A* **2003**, *243*, 347–355.
- (12) Asplund, S. *J. Catal.* **1996**, *158*, 267–278.
- (13) Kim, W.-J.; Moon, S. H. *Catal. Today* **2012**, *185*, 2–16.
- (14) Molnár, A.; Sárkány, A.; Varga, M. *J. Mol. Catal. A: Chem.* **2001**, *173*, 185–221.
- (15) Yayun, L.; Jing, Z.; Xueru, M. *Proc. Jt. Meet. Chem. Eng., Chem. Ind. Eng. Soc. China. AIChE. Beijing* **1982**, *2*, 688–702.
- (16) Gentle, M.; Muetterties, E. L. *J. Phys. Chem.* **1983**, *87*, 2469–2472.
- (17) Gandman, Z. E.; Aerov, M. E.; Men'shchikov, V. A.; Getmantsev, V. S. *Int. Chem. Eng.* **1975**, *15*, 183–185.
- (18) Kim, W. J.; Shin, E. W.; Kang, J. H.; Moon, S. H. *Appl. Catal. A Gen.* **2003**, *251*, 305–313.
- (19) Zhang, J.; Sui, Z.; Zhu, Y. A.; Chen, D.; Zhou, X.; Yuan, W. *Chem. Eng. Technol.* **2016**, *39*, 865–873.
- (20) Larsson, M.; Jansson, J.; Asplund, S. *J. Catal.* **1996**, *162*, 365–367.
- (21) Sautet, P.; Cinquini, F. *ChemCatChem* **2010**, *2*, 636–639.
- (22) Armbrüster, M.; Behrens, M.; Cinquini, F.; Föttinger, K.; Grin, Y.; Haghofner, A.; Klötzer, B.; Knop-Gericke, A.; Lorenz, H.; Ota, A.; Penner, S.; Prinz, J.; Rameshan, C.; Révay, Z.; Rosenthal, D.; Ruppel, G.; Sautet, P.; Schlögl, R.; Shao, L.; Szentmiklósi, L.; Teschner, D.; Torres, D.; Wagner, R.; Widmer, R.; Wownick, G. *ChemCatChem* **2012**, *4*, 1048–1063.
- (23) Torres, D.; Cinquini, F.; Sautet, P. *J. Phys. Chem. C* **2013**, *117*, 11059–11065.
- (24) García-Mota, M.; Bridier, B.; Pérez-Ramírez, J.; López, N. *J. Catal.* **2010**, *273*, 92–102.
- (25) Bridier, B.; Lopez, N.; Perez-Ramirez, J. *Dalt. Trans* **2010**, *39*, 8412–8419.
- (26) Mei, D.; Sheth, P.; Neurock, M.; Smith, C. *J. Catal.* **2006**, *242*, 1–15.
- (27) Sheth, P. A.; Neurock, M.; Smith, C. M. *J. Phys. Chem. B* **2003**, *107*, 2009–2017.
- (28) Beebe, T. P.; Yates, J. T. *J. Am. Chem. Soc.* **1986**, *108*, 663–671.
- (29) Pallassana, V.; Neurock, M.; Lusvardi, V. S.; Lerou, J. J.; Kragten, D. D.; van Santen, R. A. *J. Phys. Chem. B* **2002**, *106*, 1656–1669.
- (30) Moskaleva, L. V.; Chen, Z. X.; Aleksandrov, H. a.; Mohammed, A. B.; Sun, Q.; Rösch, N. *J. Phys. Chem. C* **2009**, *113*, 2512–2520.
- (31) Stacchiola, D.; Tysoc, W. T. *J. Phys. Chem. C* **2009**, *113*, 8000–8001.
- (32) López, N.; Vargas-Fuentes, C. *Chem. Commun.* **2012**, *48*, 1379–1391.
- (33) Yang, B.; Burch, R.; Hardacre, C.; Hu, P.; Hughes, P. *J. Phys. Chem. C* **2014**, *118*, 1560–1567.
- (34) Blochl, P. E. *Phys. Rev. B: Condens. Matter Mater. Phys.* **1994**, *50*, 17953–17979.
- (35) Kresse, G.; Joubert, D. *Phys. Rev. B: Condens. Matter Mater. Phys.* **1999**, *59*, 1758–1775.

## Chapter 3. Evaluating the Risk of C-C Bond Formation during Selective Hydrogenation of Acetylene on Palladium

- (36) Kresse, G.; Hafner, J. *Phys. Rev. B: Condens. Matter Mater. Phys.* **1993**, *47*, 558–561.
- (37) Kresse, G.; Furthmüller, J. *Phys. Rev. B: Condens. Matter Mater. Phys.* **1996**, *54*, 11169–11186.
- (38) Perdew, J. P.; Burke, K.; Ernzerhof, M. *Phys. Rev. Lett.* **1996**, *77*, 3865–3868.
- (39) Steinmann, S. N.; Corminboeuf, C. *J. Chem. Theory Comput.* **2011**, *7*, 3567–3577.
- (40) Gautier, S.; Steinmann, S.; Michel, C.; Fleurat-Lessard, P.; Sautet, P. *Phys. Chem. Chem. Phys.* **2015**, *17*, 28921–28930.
- (41) Pack, J. D.; Monkhorst, H. J. *Phys. Rev. B* **1976**, *13*, 5188–5192.
- (42) Methfessel, M.; Paxton, A. T. *Phys. Rev. B: Condens. Matter Mater. Phys.* **1989**, *40*, 3616–3621.
- (43) Henkelman, G.; Jónsson, H. *J. Chem. Phys.* **2000**, *113*, 9978–9985.
- (44) Fleurat-Lessard, P.; Dayal, P. Opt'n Path, <http://perso.ens-lyon.fr/paul.fleurat-lessard/ReactionPath.html> (accessed 2015).
- (45) Henkelman, G.; Jónsson, H. *J. Chem. Phys.* **1999**, *111*, 7010–7022.
- (46) Hill, T. L. *An Introduction to Statistical Thermodynamics*; Dover Publications, 1960.
- (47) Studt, F.; Abild-Pedersen, F.; Bligaard, T.; Sørensen, R. Z.; Christensen, C. H.; Nørskov, J. K. *Angew. Chem., Int. Ed.* **2008**, *47*, 9299–9302.
- (48) Ormerod, R. M.; Lambert, R. M.; Hoffmann, H.; Zaera, F.; Yao, J. M.; Saldin, D. K.; Wang, L. P.; Bennett, D. W.; Tysoe, W. T. *Surf. Sci.* **1993**, *295*, 277–286.
- (49) Valcárcel, A.; Clotet, A.; Ricart, J. M.; Delbecq, F.; Sautet, P. *J. Phys. Chem. B* **2005**, *109*, 14175–14182.
- (50) Ahn, I. Y.; Lee, J. H.; Kum, S. S.; Moon, S. H. *Catal. Today* **2007**, *123*, 151–157.
- (51) Vignola, E.; Steinmann, S. N.; Vandegehuchte, B. D.; Curulla, D.; Stamatakis, M.; Sautet, P. *J. Chem. Phys.* **2017**, *147*, 054106.
- (52) Vignola, E.; Steinmann, S. N.; Vandegehuchte, B. D.; Curulla, D.; Sautet, P. *J. Phys. Chem. C* **2016**, *120*, 26320–26327.
- (53) Padama, A. A. B.; Kasai, H.; Budhi, Y. W. *Int. J. Hydrogen Energy* **2013**, *38*, 14715–14724.
- (54) Lovvik, O. M.; Opalka, S. M. *Surf. Sci.* **2008**, *602*, 2840–2844.
- (55) Svenum, I. H.; Herron, J. A.; Mavrikakis, M.; Venvik, H. J. *Catal. Today* **2012**, *193*, 111–119.
- (56) Vignola, E.; Steinmann, S. N.; Vandegehuchte, B. D.; Le Mapihan, K.; Curulla, D.; Sautet, P. Under revision in *J. Phys. Chem. C*.



## **4 Energy Decomposition Analysis for Metal Surface–Adsorbate Interactions by Block Localized Wave Functions**

The extension of the energy decomposition analysis (EDA) to metal surfaces is related to the combination of my secondary topic during my PhD thesis, where I worked on the use of the block-localized wave function (BLW) in various contexts, and my present interests which are centered around adsorbates on metal surfaces. Even though energy decomposition analysis has a long history in molecular chemistry, only few of the available schemes have been adopted by the heterogeneous catalysis community. This is even more surprising given that the very same community is very interested in rationalizing the origin of the difference between various surfaces. One of the explanations might be that the EDAs are often devised by chemists, while the theoretical framework for the interpretation of heterogeneous catalysis is dominated by physicists. Indeed, the most used tool in the catalysis community is the d-band model, where the average energy level of the d-electrons explains the differences in adsorption energies. The premise of this chapter is that a scheme which has been successful in molecular chemistry might also help understanding surface chemistry. However, the block-localized wave function could not be directly applied to metals, for the simple reason that the algorithm for the wave function optimization is based on doubly occupied orbitals. Alas, for metals such a self-consistent scheme has a very poor convergence behavior and finite temperature extensions need to be applied. Therefore, we have generalized BLW to fractionally occupied orbitals. It turned out that the rigorous formulation is computationally untractable. Fortunately, a mean-field approximation allows us to retrieve a computationally simple scheme with low estimated errors. This tool opens the door for a detailed understanding of the adsorbate/surface interaction, which will also be helpful in force field development as outlined in section 10.2.





# Energy Decomposition Analysis for Metal Surface–Adsorbate Interactions by Block Localized Wave Functions

Ruben Staub,<sup>†</sup> Marcella Iannuzzi,<sup>‡</sup> Rustam Z. Khaliullin,<sup>¶</sup> and Stephan N. Steinmann<sup>\*,†</sup>

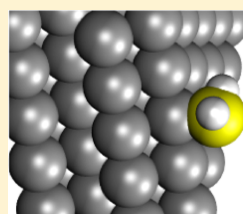
<sup>†</sup>Univ Lyon, Ecole Normale Supérieure de Lyon, CNRS Université Lyon 1, Laboratoire de Chimie UMR 5182, 46 allée d'Italie, Lyon, F-69364, France

<sup>‡</sup>Institut für Chemie, University of Zurich, Winterthurerstrasse 190, Zurich, CH-8057, Switzerland

<sup>¶</sup>Department of Chemistry, McGill University, 801 Sherbrooke Street West, Montreal, Québec H3A 0B8, Canada

## Supporting Information

**ABSTRACT:** The energy decomposition analysis based on block localized wave functions (BLW-EDA) allows one to gain physical insight into the nature of chemical bonding, decomposing the interaction energy in (1) a “frozen” term, accounting for the attraction due to electrostatic and dispersion interactions, modulated by Pauli repulsion, (2) the variationally assessed polarization energy, and (3) the charge transfer. This method has so far been applied to gas- and condensed-phase molecular systems. However, its standard version is not compatible with fractionally occupied orbitals (i.e., electronic smearing) and, as a consequence, cannot be applied to metallic surfaces. In this work, we propose a simple and practical extension of BLW-EDA to fractionally occupied orbitals, termed Ensemble BLW-EDA. As illustrative examples, we have applied the developed method to analyze the nature of the interaction of various adsorbates on Pt(111), ranging from physisorbed water to strongly chemisorbed ethylene. Our results show that polarization and charge transfer both contribute significantly at the adsorption minimum for all studied systems. The energy decomposition analysis provides details with respect to competing adsorption sites (e.g., CO on atop vs hollow sites) and elucidates the respective importance of polarization and charge transfer for the increased adsorption energy of H<sub>2</sub>S compared to H<sub>2</sub>O. Our development will enable a deeper understanding of the impact of charge transfer on catalytic processes in general.



BLW-EDA for  
Quantification of:  
✓ Polarization  
✓ Charge Transfer  
✓ On Metal Surface

## 1. INTRODUCTION

Analyzing the chemical bond to understand the driving force and diversity of bonding is almost as old as quantum mechanics.<sup>1,2</sup> Bader’s quantum theory of the atom in a molecule<sup>3</sup> and the natural bond orbitals by Weinhold et al.<sup>4</sup> are among the most popular approaches, but since the decomposition of the chemical bond energy into different contributions is not unique,<sup>5</sup> a multitude of other energy decomposition analysis (EDA) schemes have been developed.<sup>6</sup> All these different schemes come with their advantages and weaknesses, so that application of several tools can either bring contradicting results or provide confidence that at least the trend is captured accurately.<sup>7</sup> Most of these tools are developed having molecules in mind, and their application to the bonding between surfaces and adsorbates is comparatively rare.<sup>8–11</sup> As one of the few examples, Tonner and co-workers have demonstrated that EDAs on semiconducting surfaces can provide a deep understanding of coverage effects<sup>12</sup> and elucidate peculiar bonding mechanisms.<sup>13</sup> Our goal is to extend the EDA based on the block localized wave function (BLW)<sup>14,15</sup> to metallic surfaces. The BLW is designed to localize the electrons in Hilbert space in the Mulliken sense, i.e., in terms of atom-centered basis functions. A typical choice is to restrict the expansion to basis functions of atoms of a

given molecule and thus exclude contributions from all other basis functions in the system, thus defining one block per molecule. The BLW, also known in this context as absolutely localized molecular orbitals (ALMO), is variationally optimized, and the different blocks polarize each other. The main advantage of the BLW-EDA compared to other EDAs is that the polarization of fragments in their mutual presence is computed fully variationally. This allows one to rigorously separate the polarization energy from charge transfer. The charge transfer in BLW-EDA includes bonding orbital interactions between the fragments, which distinguishes it from the charge transfer obtained by constrained density functional theory (CDFT),<sup>16,17</sup> where the charge transfer is defined in real space, rather than Hilbert space.<sup>18</sup>

The formulation of the theoretical framework exploited for optimizing the BLW goes back to the works of Stoll et al.,<sup>19</sup> who aimed at reducing the computational cost of the self-consistent field (SCF) procedure by using ALMOs. The variational optimization of blocks that are localized in Hilbert space has found other applications over the years, exploiting other properties of the BLW unrelated to computational

Received: September 20, 2018

Published: November 21, 2018



# Chapter 4. Energy Decomposition Analysis for Metal Surface–Adsorbate Interactions by Block Localized Wave Functions

speed-ups. For instance, BLW has been proposed to be used to remove the basis set superposition error (BSSE),<sup>20,21</sup> and BLW-EDA has been applied to molecular complexes at the DFT<sup>22–24</sup> or correlated wave function level of theory,<sup>25,26</sup> quantifying hyperconjugation,<sup>27,28</sup> strain energies,<sup>29</sup> and even covalent bonds.<sup>30,31</sup> Furthermore, ALMOs can provide transferable molecular orbitals (where they are also called ELMOs for extremely localized molecular orbitals)<sup>32–35</sup> or fragment densities to be used in X-ray structure elucidations.<sup>36</sup> Through its variational character, BLW also provides the unique opportunity to directly assess the impact of electron delocalization on the properties of molecules by comparing computed NMR chemical shifts<sup>37,38</sup> and J-couplings<sup>39</sup> for (de)localized states, which can be seen as the comparison between a single Lewis structure and the true, electron delocalized state. Similarly, the electronic structure of the electron localized state can be analyzed by scalar fields such as the electron localization function (ELF) or the localized orbital locator (LOL) in order to shed more light on the consequences of electron delocalization on the electronic structure.<sup>40,41</sup> Due to the variational definition of the polarization energy, other applications involve investigation of the impact of polarization on the hydration shell of ionic solutes<sup>42</sup> and comparison between the BLW polarization energy and polarizable force fields, which has also been exploited to parameterize first-principles based force fields.<sup>43,44</sup>

Heterogeneous catalytic reactions involving metal surfaces or particles are involved in many major industrial processes, such as selective hydrogenations in refineries, ammonia synthesis, steam reforming, etc. Furthermore, metal catalysts are key in heterogeneous electrocatalysis, which is the technology used in electrolysis, fuel cells, and CO<sub>2</sub> reduction but also the synthesis of fine chemicals.<sup>45</sup> Therefore, analysis of the interaction of adsorbates with metallic surfaces can provide valuable insights for the design of novel, more efficient catalysts. Furthermore, when considering metal alloys, the difference between electronic and ensemble effects is a widely discussed topic.<sup>46</sup> BLW would allow one to construct an electron localized (neutral) state of a given secondary element, clearly resolving the electronic (charge transfer between the two metals) and ensemble effect.

The formulation of BLW is based on the assumption of doubly occupied orbitals, although extensions to spin-unrestricted systems exist,<sup>47,48</sup> where the system is assumed to have a gap between the highest occupied molecular orbital (HOMO) and the lowest unoccupied molecular orbital (LUMO). Metallic electronic structures are, instead, characterized by a continuum of energy levels over the Fermi energy, leading to partially occupied states.

In this work, we propose an extension of the BLW approach based on a mean field approximation, to which we refer to as Ensemble BLW-EDA. In the following, we first present the conventional SCF procedure for metallic systems, followed by the main notions of BLW. Then, we combine the two, extending BLW to metallic systems. Finally, we provide computational details and applications to the prototypical adsorption of molecules (H<sub>2</sub>O, H<sub>2</sub>S, C<sub>2</sub>H<sub>4</sub>, and CO) on Pt(111).

## 2. METHODOLOGY

**2.1. Ensemble DFT.** The ground state of a metallic system, i.e., where the density of states around the Fermi level is continuous, cannot be described by a single quantum state.

Rather, an ensemble of states is required, both for a physically sound description and for a smooth convergence of the wave function optimization in a self-consistent field (SCF) process. The different quantum states within the ensemble are weighted according to their probability in order to determine observables. Let  $\hat{A}$  be an operator, and  $\Omega$  is the set of all possible quantum states of a given system. Then, the expectation value  $\langle A \rangle_{\Omega}$  of the ensemble is

$$\langle A \rangle_{\Omega} = \sum_{\chi \in \Omega} \langle \Psi_{\chi} | \hat{A} | \Psi_{\chi} \rangle p_{\chi} \quad (1)$$

where  $\Psi_{\chi}$  is the wave function associated with the quantum state  $\chi$ .  $\Psi_{\chi}$  spans the ground- and single excited-state determinants of the system.  $p_{\chi}$  is the probability that the real system is in the quantum state  $\chi$ , based on the energy of  $\chi$ .

In the present context, we are interested in the reformulation of the 1-electron density operator  $\hat{\rho}$ . In the Hartree–Fock approximation and in the case of orthonormal molecular orbitals  $\psi_i$ ,  $\hat{\rho}$  can be written as

$$\hat{\rho} = \sum_{\text{occ } \psi_i \in \Psi} |\psi_i\rangle \langle \psi_i| \quad (2)$$

Dealing explicitly with ensembles is computationally inefficient and would require dedicated implementations. Since singly excited determinants do not overlap with the ground-state determinant, the same set of molecular orbitals can be used to construct all the relevant quantum states of the system. Therefore, the ensemble 1-electron density ( $\langle \hat{\rho} \rangle_{\Omega}$ ) can be written in a convenient manner by considering the population of the orbitals (also known as occupation numbers,  $n_i$ ) instead of the probability of quantum states:

$$\langle \hat{\rho} \rangle_{\Omega} = \sum_{\chi \in \Omega} p_{\chi} \hat{\rho}_{\chi} = \sum_{\chi \in \Omega} p_{\chi} \sum_{\psi_i \in \Psi_{\chi}} |\psi_i\rangle \langle \psi_i| \quad (3)$$

$$\langle \hat{\rho} \rangle_{\Omega} = \sum_i |\psi_i\rangle \langle \psi_i| n_i = \sum_i |\sqrt{n_i} \psi_i\rangle \langle \sqrt{n_i} \psi_i| = \sum_i |\psi_i'\rangle \langle \psi_i'| \quad (4)$$

where  $i$  is the sum over all molecular orbitals, i.e., solutions of the Fock equation. In eq 4, we have introduced the rescaled orbitals:

$$|\psi_i'\rangle = \sqrt{n_i} |\psi_i\rangle \quad (5)$$

which are particularly convenient computationally. The occupation number  $n_i$  is related to the probability for the orbital  $\psi_i$  to be occupied. For finite temperatures, they are determined on the basis of the energy  $\epsilon_i$  of  $\psi_i$ , invoking Fermi–Dirac statistics:

$$n_i = \frac{1}{\exp\left(\frac{\epsilon_i - \mu}{kT}\right) + 1} \quad (6)$$

where  $\mu$  is the Fermi level,  $k$  is Boltzmann's constant, and  $T$  is the (electronic) temperature. With these rescaled orbitals  $|\psi_i'\rangle$ , the mixed-state 1-electron density  $R_{\Omega}$  can be easily computed.

$$R_{\Omega} = \mathbf{CNC}^{\dagger} \quad (7)$$

where  $\mathbf{C}$  is the molecular coefficient matrix and  $\mathbf{N}$  is a diagonal matrix of Fermi weights  $n_i$  according to eq 6. Yang et al. have generalized this reformulation to any method that can be reformulated on the basis of the noninteracting Greens function, allowing one to apply the orbital scaling to virtual

orbitals and thus to compute correlation energies with MP2 or RPA for systems with fractional electrons.<sup>49</sup> With a mild approximation, these scaled orbitals can also be used for coupled cluster computations for systems with fractional electrons.<sup>50</sup>

**2.2. BLW Formalism.** The basic idea of the BLW formalism is to express the wave function of the system in terms of blocks of localized orbitals. In the present context, the orbitals are always localized on a subset of atoms, so that the BLW partitions the atom-centered basis functions in mutually exclusive blocks and imposes thereby a localization of the wave function in Hilbert space.

Formally, a block  $B_m$  is defined as a set of  $N_m$  basis functions  $\{\phi_1^m \dots \phi_{N_m}^m\}$ , such that each basis function is associated with exactly one block, i.e.,  $\sum_m N_m = N$ , where  $N$  is the total number of basis functions of the system. In this work, the set of basis functions  $\{\phi_1^m \dots \phi_{N_m}^m\}$  associated with the block  $B_m$  is the union of all  $N_j$  basis set functions  $\{\phi_1^j \dots \phi_{N_j}^j\}$  used to describe the  $j_m$  atoms of  $B_m$ , so that  $\sum_m j_m$  equals the total number of atoms in the system. Similarly, the electrons of the system are assigned to a given block. In our case, all blocks are neutral.

An ALMO is defined as a linear combination of basis functions associated with the same block. Therefore, an orbital  $\psi_i^m$  pertaining to block  $B_m$  is written:

$$|\psi_i^m\rangle = \sum_{\nu} C_{\nu,i}^m |\phi_{\nu}^m\rangle \quad (8)$$

where  $C$  is the orbital coefficient matrix for the entire system, while  $C^m$  is the matrix of block  $B_m$ . We have used greek letters to label atomic orbital basis functions and  $i^m$  indexes ALMOs of a given block  $B_m$ .

The global orbital coefficient matrix  $C$ , which spans all molecular orbitals and thus, has dimensions of  $N \times N$ , has a block-diagonal structure:

$$C = \begin{pmatrix} C^1 & 0 & \dots & 0 \\ 0 & C^m & \dots & 0 \\ \vdots & \vdots & \ddots & \vdots \\ 0 & 0 & \dots & C^{\Sigma_m} \end{pmatrix} \quad (9)$$

where  $C^m$  is the orbital coefficient matrix restricted to the block  $B_m$ . The orbital coefficients  $C_{\nu,i}^m$  are variationally optimized according to the local diagonalization based SCF algorithm developed by Stoll et al.<sup>19</sup> and implemented in CP2K as the first stage of the two-step "ALMO-SCF" scheme.<sup>51</sup>

In general, both locality and orthogonality constraints cannot be satisfied simultaneously.<sup>52</sup> Therefore, ALMOs are inherently nonorthogonal between blocks, although they can be kept orthonormal within a block without loss of generality. In this study, we will work under this assumption. Hence, the ALMO overlap matrix ( $\sigma$ ) has identity-like diagonal blocks but nonzero entries for overlaps between blocks.

In practice, the so-called reciprocal (or biorthogonal) occupied orbitals  $|\tilde{\psi}_i^m\rangle$  are defined such that  $\langle \tilde{\psi}_i^m | \psi_j^m \rangle = \delta_{i,j}$ :

$$|\tilde{\psi}_i^m\rangle = \sum_{l,j} |\psi_j^m\rangle \sigma_{i,j}^{-1}, \quad \tilde{\mathbf{T}} = \mathbf{T}\sigma^{-1} \quad (10)$$

where  $l$  goes over all blocks and  $j^l$  indexes the occupied orbitals of block  $B_j$ ;  $\tilde{\mathbf{T}}$  is the coefficient matrix of reciprocal occupied

orbitals, and  $\mathbf{T}$  is the occupied part of eq 9. To be explicit,  $|\tilde{\psi}_i^m\rangle$  is expanded in terms of all basis functions of the system and not only of block  $B_m$ .

Reciprocal orbitals enable one to rewrite the Fock equations. As Stoll et al.<sup>19</sup> have demonstrated, the self-consistent solution of projected eigenvalue equations for each block is equivalent to finding variationally optimal ALMOs.

$$\hat{F}^m |\psi_i^m\rangle = \epsilon_i^m |\psi_i^m\rangle, \quad \hat{F}^m = (\hat{I} - \hat{\rho} + \hat{\rho}^{m\dagger}) \hat{F} (\hat{I} - \hat{\rho} + \hat{\rho}^m) \quad (11)$$

$$\hat{\rho}^m = \sum_{i \in B_m} |\tilde{\psi}_i^m\rangle \langle \psi_i^m| = \sum_{l, \xi, \nu} R_{\xi\nu}^m |\phi_{\xi}^l\rangle \langle \phi_{\nu}^m| \quad (12)$$

where  $\hat{I}$  is the identity matrix,  $\hat{F}$  is the conventional Fock operator,  $\hat{F}^m$  is the Fock operator projected on block  $B_m$ ,  $\hat{\rho}$  is the density operator of the entire system,  $\hat{\rho}^m$  is the non-Hermitian operator that represents the density of the block defined by using only ALMOs of block  $B_m$ , and  $R^m$  is the associated block density matrix.  $\nu$  is a basis function of block  $B_m$  (see eq 8), while  $\xi$  indexes the atom centered basis function of blocks  $B_l$ .

At each SCF iteration, these projected Fock equations are solved independently for each block but coupled to each other between successive iterations due to the projection operators. In other words, each block  $B_m$  is optimized in the environment generated by all other blocks.

Since in mixed-state theory it is common to deal with orthonormal orbitals, we briefly discuss the connection between the use of reciprocal orbitals and a Lowdin orthonormalization:

$$|^L\psi_i\rangle = \sum_{\text{occ } j} |\psi_j\rangle \sigma_{ij}^{-1/2}, \quad {}^L\mathbf{T} = \mathbf{T}\sigma^{-1/2} \quad (13)$$

where  $i$  and  $j$  are general indexes of occupied orbitals,  $\sigma^{-1/2}$  is the square root inverse of the overlap matrix, and  ${}^L\mathbf{T}$  is the Lowdin orbital coefficient matrix. The 1-electron density is equivalently expressed through the Lowdin orthonormalized molecular orbitals and the use of reciprocal orbitals, the latter avoiding the expensive computation of  $\sigma^{-1/2}$ :

$$\begin{aligned} \hat{\rho} &= \sum_{\text{occ } i} |^L\psi_i\rangle \langle ^L\psi_i| = \sum_{\text{occ } i} |\tilde{\psi}_i^m\rangle \langle \psi_i^m| = \sum_{\text{occ } i} \sum_{\nu, \xi} \tilde{T}_{\nu i} |\phi_{\nu}^i\rangle \langle \phi_{\xi}^i| T_{\xi i} \\ &= \sum_{\nu, \xi} \sum_{\text{occ } i} T_{\xi i} \tilde{T}_{\nu i} |\phi_{\nu}^i\rangle \langle \phi_{\xi}^i| = \sum_{\nu, \xi} R_{\nu \xi} |\phi_{\nu}^i\rangle \langle \phi_{\xi}^i| \end{aligned} \quad (14)$$

$$\mathbf{R} = {}^L\mathbf{T} {}^L\mathbf{T}^\dagger = \mathbf{T} \tilde{\mathbf{T}}^\dagger = \mathbf{T} (\mathbf{T}\sigma^{-1})^\dagger = \mathbf{T}\sigma^{-1} \mathbf{T}^\dagger \quad (15)$$

where  $\mathbf{R}$  is the conventional 1-electron density matrix.  $\mathbf{R}$  can then be fed to standard routines to determine the electron density in real space, compute gradients, and so forth.

**2.3. Ensemble BLW.** 2.3.1. *Exact Ensemble Formulation.* In order to adapt the BLW formalism to an ensemble formulation, we need to adapt the density matrices  $\mathbf{R}$  or, equivalently, the construction of the reciprocal orbitals (eq 10). In other words, we apply the general formula (eq 3) for the computation of an ensemble density matrix  $\mathbf{R}_\Omega$  to nonorthogonal molecular orbitals:

## Chapter 4. Energy Decomposition Analysis for Metal Surface–Adsorbate Interactions by Block Localized Wave Functions

$$\begin{aligned} \mathbf{R}_\Omega &= \sum_{\chi \in \Omega} p_\chi \mathbf{T}_\chi = \sum_{\chi \in \Omega} p_\chi \mathbf{T}_\chi \sigma_\chi^{-1} \mathbf{R}_\chi^\dagger \\ &= \sum_{\chi \in \Omega} p_\chi \mathbf{T}_\chi (\mathbf{T}_\chi^\dagger \mathbf{S} \mathbf{T}_\chi)^{-1} \mathbf{T}_\chi^\dagger \end{aligned} \quad (16)$$

where  $p_\chi$  is the probability that the real system is in the quantum state  $\chi$ ,  $\mathbf{R}_\chi$  is the density matrix of this quantum state,  $\mathbf{T}_\chi$  is the occupied orbital coefficient matrix associated with the wave function  $\Psi_\chi$ ,  $\sigma_\chi^{-1}$  is the overlap matrix of the quantum state  $\chi$ , and  $\mathbf{S}$  is the basis set function overlap matrix which is common for all quantum states, since it is a property of the geometry and basis set.

Let us consider a general orbital coefficient matrix  $\mathbf{C}$  containing all the localized orbitals used to construct every  $\mathbf{T}_\chi$ , the occupied orbital matrix of quantum state  $\chi$ . Therefore, one can construct any  $\mathbf{T}_\chi$  from  $\mathbf{C}$ :

$$\mathbf{T}_\chi = \mathbf{C} \Delta_\chi = \mathbf{C} \begin{pmatrix} \delta_{1\chi} & 0 & \cdots & 0 \\ 0 & \delta_{2\chi} & \cdots & 0 \\ \vdots & \vdots & \ddots & \vdots \\ 0 & 0 & \cdots & \delta_{n+k\chi} \end{pmatrix}, \quad \delta_{i\chi} = \begin{cases} 1 & \text{if } \psi_i \in \Psi_\chi, \\ 0 & \text{otherwise} \end{cases} \quad (17)$$

where  $\Delta_\chi$  can be seen as a rescaling matrix with a dimension of  $N \times N$ .

Combining eq 17 with eq 16, we obtain the following reformulation:

$$\begin{aligned} \mathbf{R} &= \sum_{\chi \in \Omega} p_\chi \mathbf{R}_\chi = \sum_{\chi \in \Omega} p_\chi \mathbf{T}_\chi \sigma_\chi^{-1} \mathbf{T}_\chi^\dagger = \sum_{\chi \in \Omega} p_\chi \mathbf{C} \Delta_\chi \sigma_\chi^{-1} \Delta_\chi^\dagger \mathbf{C}^\dagger \\ &= \mathbf{C} \left( \sum_{\chi \in \Omega} p_\chi \Delta_\chi \sigma_\chi^{-1} \Delta_\chi^\dagger \right) \mathbf{C}^\dagger = \mathbf{C}^\Omega \sigma^{-1} \mathbf{C}^\dagger \end{aligned} \quad (18)$$

where  $\sigma^{-1} = \sum_{\chi \in \Omega} p_\chi \Delta_\chi \sigma_\chi^{-1} \Delta_\chi^\dagger$ .

Equation 18 requires  $\sigma_\chi^{-1}$  to be computed for each state involved separately; i.e., it is not an efficient reformulation of eq 16. This contrasts with the canonical case, where eq 4 provides an efficient reformulation of eq 3, since the different quantum states involved are orthonormal among each other.

If we have  $k$  orbitals in addition to the  $n$  formally doubly occupied orbitals, then the maximum number  $|\Omega|$  of quantum states to evaluate eq 17 is

$$|\Omega| = \binom{n+k}{n} = \frac{(n+k)!}{n!k!} \quad (19)$$

In the worst case,  $k = n$ ,  $|\Omega| \approx \frac{2^{2n}}{\sqrt{\pi n}}$ ; i.e., the number of states to be considered is exponential in  $n$ . Hence, such a method is not applicable to sizable systems (e.g., a little more than  $7 \times 10^{201}$  states for the Pt(111) surface investigated in the later sections).

Why can there not be a simple reformulation of ensemble BLW, just like in the canonical case? Considering eq 14, we can understand that ALMOs are treated as if they would be orthonormalized when computing the density matrix. Therefore, scaling them by their occupation number is not an option, since this lack of normalization will simply be offset by the corresponding  $\sigma^{-1}$ . A second point of interference when aiming at a simplified ensemble description comes from the interdependence of blocks. Let us consider a two block system. According to eq 10, the reciprocal orbitals of block 1 depend on the occupied orbitals of all blocks. Hence, in general (i.e., when the orbitals between blocks overlap), varying the

occupations in block 2 results in a varying environment for block 1 (and vice versa). In other words, the different quantum states in block 1 are subjected to different environments, depending on the quantum states of block 2. To put this in mathematical terms, let us consider two quantum states  $\chi$  and  $\chi'$ , with associated wave function  $\Psi_\chi$  and  $\Psi_{\chi'}$  and three different orbitals  $\psi_1$ ,  $\psi_2$ , and  $\psi_3$  (considered doubly occupied) such that  $\{\psi_1, \psi_2\} \subseteq \Psi_\chi$  and  $\{\psi_1, \psi_3\} \subseteq \Psi_{\chi'}$ , but  $\psi_3 \notin \Psi_\chi$  and  $\psi_2 \notin \Psi_{\chi'}$ . If we would like to use the same set of ALMOs for describing  $\Psi_\chi$  and  $\Psi_{\chi'}$ , then we would like  $\tilde{\psi}_1$  to be equal to  $\tilde{\psi}_1'$  (respectively, the reciprocal orbital of  $\psi_1$  computed in the quantum state  $\chi$  and  $\chi'$ ), so that eq 18 can be simplified in full analogy with the situation when using orthonormalized orbitals. However, the reciprocal orbital  $\tilde{\psi}_1$  in the quantum state  $\chi$  does not change by replacing the orbital  $\psi_2$  by  $\psi_3$ , if and only if  $\psi_1$  does not overlap with neither  $\psi_2$  nor  $\psi_3$ , and there exists no  $\psi_i \notin \{\psi_1, \psi_2, \psi_3\}$  in any quantum state  $\chi_i \in \Omega$  such that both  $\psi_1$  and  $\psi_2$  (or  $\psi_3$ ) overlap with  $\psi_i$ :

$$\tilde{\psi}_1 = \tilde{\psi}_1' \Leftrightarrow \begin{cases} \langle \psi_1 | \psi_2 \rangle = 0 \\ \wedge (\forall \chi \in \Omega, \exists \psi_i \in \Psi_\chi \setminus \{\psi_1, \psi_2\}, \\ \psi_i \in \Psi_\chi \rightarrow (\langle \psi_1 | \psi_i \rangle \neq 0 \wedge \langle \psi_2 | \psi_i \rangle \neq 0)) \\ \wedge (\text{idem for } \psi_3 \text{ instead of } \psi_2) \end{cases} \quad (20)$$

Therefore, the occupation-state dependency of the orthonormalized orbitals is always present, except when the added or removed orbitals do not overlap with the rest of the system. Due to this occupation-state dependency of the orthonormalized orbitals, they cannot be used to construct an ensemble density matrix by rescaling them, in contrast to the canonical case.

As a conclusion, since the orbitals are nonorthogonal, when an orbital occupation is modified, the whole system has to readapt. Note that this conclusion applies to the use of any nonorthogonal orbitals and not only to ALMOs.

**2.3.2. Mean-Field Approximation to Ensemble BLW.** The condition to formulate a computationally tractable approximation to ensemble BLW is that the contribution of each orbital to the ensemble density can be computed only once per SCF iteration and can then be weighted by the probability that the real system is in a quantum state containing this orbital (or equivalently, the probability that this orbital is occupied in the real system). In other words, we need to devise a scheme in which we have a common overlap matrix  $\sigma$  for all quantum states involved; i.e., we generate an average interaction field (over all quantum states) that is applied to every quantum state. Furthermore, we require that the scheme is equivalent to standard ensemble theory for a single block. This implies that eq 6 is applied to each block separately (with the block specific chemical potential  $\mu^m$ ), so that the total number of electrons in each block remains an integer. With these two requirements, we arrive at a mean-field approximation to the overlap matrix ( ${}^\alpha\sigma$ ).

The interaction (i.e., overlap) between  $|\psi_i\rangle$  and  $|\psi_j\rangle$  from any block is rescaled by  $\sqrt{n_i} \sqrt{n_j}$ , while the self-overlap remains unmodified. This rescaling provides an approximate overlap matrix  ${}^\alpha\sigma$ :

$${}^\alpha\sigma_{ij} = \begin{cases} \langle \psi_i | \psi_i \rangle = 1 \\ \langle \psi_i | \psi_j \rangle \sqrt{n_i} \sqrt{n_j} \end{cases} \quad (21)$$

Hence, the density matrix  ${}^\alpha\mathbf{R}_\Omega$  can be written:

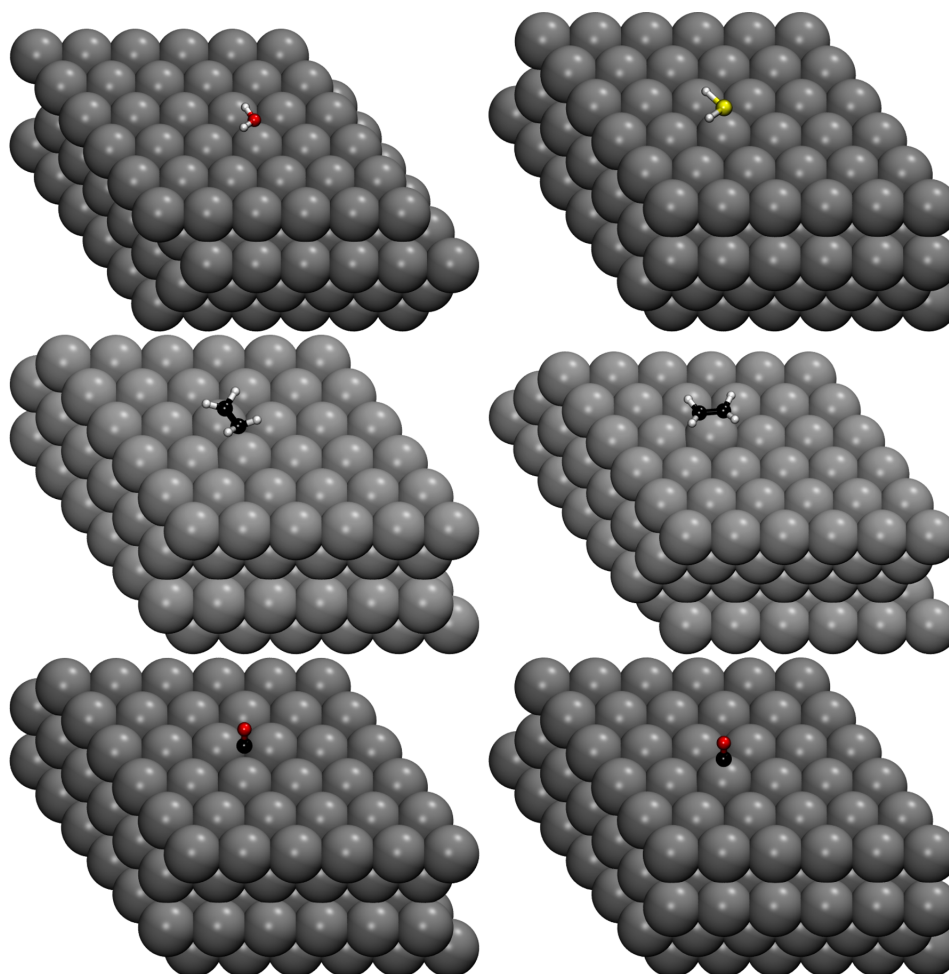


**Figure 1.** Top: H<sub>2</sub>O (left) and H<sub>2</sub>S (right) top adsorption on Pt(111). Middle: Ethylene adsorption in a di- $\sigma$  (left) and  $\pi$  (right) adsorption mode. Bottom: CO on fcc (left) and top (right) adsorption sites. All images refer to the equilibrium distance with respect to the surface.

$${}^{\alpha}\mathbf{R}_{\Omega} = \mathbf{T}'^{\alpha}\sigma^{-1}\mathbf{T}'^{\dagger} \quad (22)$$

where  $\mathbf{T}'$  is the rescaled orbital coefficient matrix, in close analogy to eq 5, for the canonical case.

We use  $|\psi_{i,m}\rangle$  to denote the presence of fractionally occupied ALMOs, i.e., the ones that necessitate the use of  ${}^{\alpha}\sigma$ .  $|\psi_{i,m}\rangle$  has rescaled interactions (overlap), except with themselves. Therefore, we call them “selfish orbitals”. Unlike the canonical rescaled orbitals, selfish orbitals cannot be considered “shrunk”; they just interact less with their environment:

$$\forall j \neq i \quad \langle \psi_{i,m} | \psi_{j,l} \rangle = \sqrt{n_i} \sqrt{n_j} \langle \psi_{i,m} | \psi_{j,l} \rangle; \text{ but } \langle \psi_{i,m} | \psi_{i,m} \rangle = \langle \psi_{i,m} | \psi_{i,m} \rangle \quad (23)$$

where  $j$  goes over ALMOs of all blocks.

In practice, at each SCF iteration, the orbital coefficients  $\mathbf{T}$  are scaled according to the (updated) occupation number, yielding  $\mathbf{T}'$ . With these scaled coefficients, the overlap matrix  $\sigma$  is computed. Then, the diagonal of  $\sigma$  is set to unity to obtain  ${}^{\alpha}\sigma$ . The density matrix is computed using eq 22. In brief,

except for the use of  $\mathbf{T}'$  and  ${}^{\alpha}\sigma$ , the SCF procedure by Stoll et al.<sup>19</sup> is not modified.

Please note that, for noninteracting systems (blocks that are far apart), the mean-field approximation reverts back to the canonical answer. Similarly, if the orbital occupations are either 0 or 2 (0 K limit of a system with a nonvanishing gap), our approximation provides the regular BLW result.

In our implementation in CP2K, we exploit the eigenvalue based optimization,<sup>15,19</sup> which has been implemented in CP2K<sup>51,53</sup> and allows a variational optimization of the ensemble BLW. The computational cost of the extension to partially occupied orbitals is negligible thanks to the use of selfish orbitals, and the additional storage used is limited to an array containing the orbital energies.

As discussed in the [Supporting Information](#), the error introduced by the mean-field approximation turns out to lead to losses of electrons in the Ensemble BLW. For example, for H<sub>2</sub>O, up to 0.005 electrons are lost when the molecule is closest to the metal surface. The energetic consequence on the polarization energy of this electron loss can be estimated to be



# Chapter 4. Energy Decomposition Analysis for Metal Surface–Adsorbate Interactions by Block Localized Wave Functions

up to 0.5 kcal mol<sup>-1</sup> assuming a metallic system with a typical work function of around 5 eV. As a result, the charge-transfer energy, which does not suffer from this electron loss, is slightly overestimated compared to the polarization energy. Given that water, which is the least strongly adsorbed molecule studied herein, has an adsorption energy of -9.7 kcal mol<sup>-1</sup>, such an error is deemed acceptable. In all cases, no loss or a small loss of electrons is encountered, never a gain in electrons. This can be rationalized in analogy to Hartree–Fock, where the average electron repulsion overestimates the actual electron repulsion. Hence, our mean-field approximation is an upper bound to exact ensemble BLW. Since ensemble DFT formulation is variational with respect to the electronic free energy (i.e., when accounting for the entropy related to the fractionally occupied orbitals), our Ensemble BLW-EDA defines the charge transfer through a variational principle for the interaction of adsorbates with metallic surfaces.

### 3. COMPUTATIONAL DETAILS

The adsorbed structures were optimized with VASP 5.4.1<sup>54,55</sup> using periodic boundary conditions applying the reoptimized Perdew, Burke and Ernzerhofer (PBE) functional to make it compatible with the nonlocal van der Waals (vdW) functional, in short optPBE-vdW<sup>56</sup> functional, which has been found to be, together with PBE-dDsC,<sup>57</sup> another dispersion corrected density functional, most accurate for adsorption energies on Pt(111),<sup>58</sup> and is available in CP2K, the code that is used for all Ensemble BLW-EDA computations. An energy cutoff of 400 eV is chosen for the expansion of the plane-wave basis set. The electron–ion interactions are described by the PAW formalism.<sup>59,60</sup> The p(6 × 6) unit cell is built from bulk platinum (2.821 Å nearest neighbor distance) with four metallic layers. Additional tests regarding the need for K-point sampling reveal that the  $\Gamma$ -point optimized geometries are very close to the ones obtained with a 3 × 3 × 1 K-point mesh. The adsorption energy at the  $\Gamma$ -point is overestimated by 1–5 kcal mol<sup>-1</sup>, corresponding to up to 10% at the equilibrium distance (see Table S2). This accuracy is deemed acceptable for the current purpose, where the relative importance of different interaction energy components and their evolution as a function of the surface–adsorbate distance is analyzed. The out-of-plane vector of the unit cell was chosen to be ~23 Å to achieve a negligible interaction between periodic images.

In CP2K, the molecular orbitals were represented by a double- $\zeta$  Gaussian basis set with one set of polarization functions, called DZVP-MOLOPT-SR-GTH for both BLW-EDA and BSSE corrected SCF DFT simulations.<sup>61</sup> A cutoff of 400 Ry was used to describe the electron density. The exchange–correlation (XC) energy was approximated with the optPBE-vdW<sup>56</sup> functional. The Brillouin zone was described at the  $\Gamma$ -point. Goedecker, Teter and Hutter (GTH) pseudopotentials<sup>62</sup> based on the PBE functional were used to describe the interactions between the valence electrons and the ionic cores, and the electronic smearing was approximated by a Fermi–Dirac distribution at 300 K, applied to all computations.

Figure S1 provides a comparison between the total interaction energy ( $\Delta E_{\text{int}}$ , vide infra, eq 24) as computed by standard KS-DFT with VASP and CP2K. In both codes, we compare a 10 and a 18 valence electron pseudopotential. The 18 valence electron potential of CP2K gives interaction energies very close to the one provided by VASP, independently if the latter uses 10 or 18 valence electrons.

**3.1. Energy Decomposition Analysis.** The newly extended EDA scheme is now applied to charge transfer analysis of adsorption at a metallic surface. We select three prototypical couples of systems (see Figure 1), aiming at describing different types of bonding. The first couple is H<sub>2</sub>O and H<sub>2</sub>S, for which no strong bond formation is expected, although H<sub>2</sub>S is interacting more strongly with Pt(111) than water. The second couple compares the di- $\sigma$  and  $\pi$  adsorption modes of ethylene, while the third couple investigates the difference between CO adsorbed on fcc and top sites.

For all these systems, we have computed the interaction energy as a function of the distance between the surface and the adsorbate. All coordinates are fully optimized, except the z-coordinate of the heavy atoms closest to the surface and the two bottom layers that are kept fixed in their bulk position. We define the total interaction energy  $\Delta E_{\text{tot}}$  as

$$\Delta E_{\text{tot}} = E_{\text{system}} - E_{\text{frag1,opt}} - E_{\text{frag2,opt}} - \Delta E_{\text{BSSE}} \quad (24)$$

where  $E_{\text{system}}$  is the standard KS-SCF energy of the full system and  $E_{\text{frag,opt}}$  is the corresponding energy of the freely optimized fragments. Since the BLW is only defined in a localized basis set, we have to correct for the basis set superposition error (BSSE), which we do according to the counterpoise procedure of Boys and Bernardi,<sup>63</sup> giving rise to the energy correction  $\Delta E_{\text{BSSE}}$ . Note, however, that BSSE only affects the charge-transfer term, as all other terms are evaluated using exclusively the fragment basis set.

For the energy decomposition analysis, each system is divided into two blocks: a metallic block containing the metal surface and an adsorbate block containing the adsorbed molecule. As common in BLW-EDA,<sup>22,23,64</sup> we decompose the total interaction energy  $\Delta E_{\text{tot}}$  into the following terms: preparation or deformation ( $\Delta E_{\text{deform}}$ ), the frozen energy term ( $\Delta E_{\text{frozen}}$ ) that describes the interaction of the two isolated fragment densities brought together and covering electrostatic interaction and Pauli repulsion<sup>22</sup> as well as dispersion interactions,<sup>64</sup> polarization ( $\Delta E_{\text{pol}}$ ) energy, obtained by variationally optimizing the BLW, and finally, the charge transfer ( $\Delta E_{\text{CT}}$ ) interaction that includes covalent bond formation.

$$\Delta E_{\text{tot}} = \Delta E_{\text{deform}} + \Delta E_{\text{frozen}} + \Delta E_{\text{pol}} + \Delta E_{\text{CT}} \quad (25)$$

These terms can be expressed as

$$\Delta E_{\text{deform}} = E_{\text{frag1,sys}} - E_{\text{frag1,opt}} + E_{\text{frag2,sys}} - E_{\text{frag2,opt}} \quad (26a)$$

$$\Delta E_{\text{frozen}} = E_{\text{guess}} - E_{\text{frag1,sys}} - E_{\text{frag2,sys}} \quad (26b)$$

$$\Delta E_{\text{pol}} = E_{\text{BLW}} - E_{\text{guess}} \quad (26c)$$

$$\Delta E_{\text{CT}} = E_{\text{system}} - E_{\text{BLW}} - \Delta E_{\text{BSSE}} \quad (26d)$$

where  $E_{\text{frag,sys}}$  corresponds to the energy of a fragment in its final geometry adopted in the presence of the other fragment.  $E_{\text{guess}}$  is the systems energy obtained by a superposition of the fragment density matrices, which corresponds to the “frozen” density interaction energy approximation.  $E_{\text{BLW}}$  is the energy obtained by Ensemble BLW.

### 4. RESULTS AND DISCUSSION

As a first application of Ensemble BLW-EDA to metal surfaces, we compare the adsorption of H<sub>2</sub>O and H<sub>2</sub>S on Pt(111). As shown in Figure 1 for both molecules, the most favorable

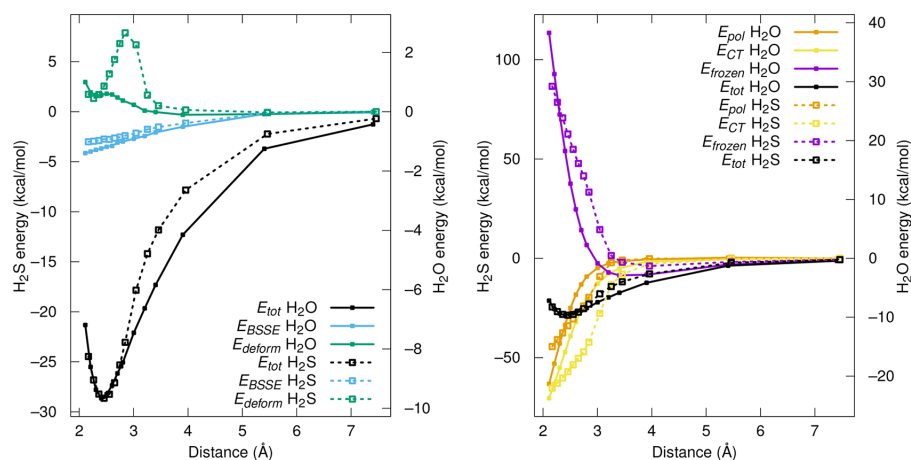


**Figure 2.** Energy decomposition analysis for H<sub>2</sub>O (solid lines, right y-axis) and H<sub>2</sub>S (dashed lines, left y-axis). The total interaction energy is compared to the BSSE and the deformation energy on the left, while the right quantifies the frozen monomers, polarization, and charge transfer interaction energy. Note that the y-scales are aligned in such a way that the equilibrium interaction energy and the zero interaction energy are aligned for both systems; see [Supporting Information](#) for separated figures.

adsorption configuration is atop, with the molecular plane approximately parallel to the surface. The total interaction energy as a function of the Pt–O or Pt–S distance shows that, despite the nominally larger noncovalent radius of sulfur with respect to oxygen (1.8 and 1.5 Å according to Bondi<sup>65</sup>), the minimum is found around 2.4 Å in both cases. This can be rationalized by the overall stronger interaction of Pt–H<sub>2</sub>S (29 kcal mol<sup>-1</sup>) compared to Pt–H<sub>2</sub>O (9 kcal mol<sup>-1</sup>), which allows S to approach the surface more closely than O with respect to its size. The BSSE contribution to the interaction energy is similar for H<sub>2</sub>O and H<sub>2</sub>S (roughly 10% of the total interaction energy). Therefore, the comparison between the two systems could be performed with a 10% accuracy without the BSSE correction, for instance for molecular dynamics simulations of H<sub>2</sub>S dissolved in water. The deformation energy of the two systems show different patterns. While the energetic cost to deform water/Pt(111) to its optimal geometry is very small (at most 0.5 kcal mol<sup>-1</sup>), H<sub>2</sub>S/Pt(111) undergoes a deformation up to 7 kcal mol<sup>-1</sup> at a distance that is only slightly longer than the equilibrium distance, while it drops at shorter distances to about 1 kcal mol<sup>-1</sup>. Analyzing the origin of the deformation energy, we identify the deformation of the metal surface as the major contributor. As shown in [Figure S2](#), the Pt atom, on which the adsorbate is adsorbed, is “pulled out” of the surface at intermediate distances. After a certain elongation, it goes back to the original position, almost as if the spring had been overstretched and thus broken. Moving to the interaction energy components of the fragments after paying the preparation (deformation) energy (right-hand graph of [Figure 2](#)), we first observe that the “frozen” term, i.e., the energy cost (or gain) of putting the fragments together without electronic density changes, follows the expected increase in atomic size when replacing oxygen by sulfur: The energy of assembly becomes positive for distances below 2.8 and 3.2 Å for H<sub>2</sub>O and H<sub>2</sub>S, respectively. At larger distances, the interaction energy is already negative without any further electronic relaxation. This is due to the subtle balance between Pauli repulsion and attraction by dispersion interactions. Note that electrostatic interactions are also included at this stage, but

since the isolated metal surfaces do not have significant electrostatic moments (dipole, quadrupole, etc.), it barely contributes in the present systems. Allowing the electron density to relax in the presence of the other fragment, but prohibiting any charge transfer or direct orbital interaction, affords the stabilizing polarization energy  $\Delta E_{\text{pol}}$ . H<sub>2</sub>S has a 2.7 times larger polarizability than H<sub>2</sub>O (26.7 and 9.8 au<sup>3</sup>, respectively,<sup>66</sup>). Indeed, there is roughly a factor of 3 between  $\Delta E_{\text{pol}}$  for H<sub>2</sub>S compared to H<sub>2</sub>O at all relevant distances (>2.3 Å), in close agreement with the corresponding factor for the total interaction energy. The charge transfer between the metal surface and the adsorbate is, however, much more important for H<sub>2</sub>S than for H<sub>2</sub>O. This contrasting energy decomposition can be rationalized recalling that sulfides are softer bases than oxides and that platinum is a soft acid. Furthermore, interactions with sulfur can benefit from stabilization through hypervalence by increasing the ionic character of bonds.<sup>67</sup>

As a conclusion, the stabilizing interaction of a single water molecule with Pt(111) is due to equal amounts of polarization and charge transfer. In other words, even in this case of rather weak physisorption, the use of a polarizable force field is unlikely to be enough to capture the physics of the interaction energy accurately. However, a good approximation can be obtained since the two components are well correlated; i.e., counting the polarization energy twice, BLW could capture a reasonable approximation of the total interaction energy. This insight might help the development of more accurate Pt/H<sub>2</sub>O force fields.<sup>68,69</sup> The situation for H<sub>2</sub>S is more challenging to approximate: charge transfer dominates the interaction energy, which also induces significant deformations of the surface. Hence, already for H<sub>2</sub>S adsorption, explicit terms to mimic orbital/charge-transfer interactions are required. The situation can be simplified by excluding surface deformation. Given the scarcity of accurate force fields for the deformation of metal surfaces, this is the preferred setup anyway. [Figure S3](#) shows that on an ideal surface the deformation energy is negligible and the charge-transfer and polarization energies are now as smooth as for water. Furthermore, on an ideal surface, a very similar relative importance of the various contributions is

## Chapter 4. Energy Decomposition Analysis for Metal Surface–Adsorbate Interactions by Block Localized Wave Functions

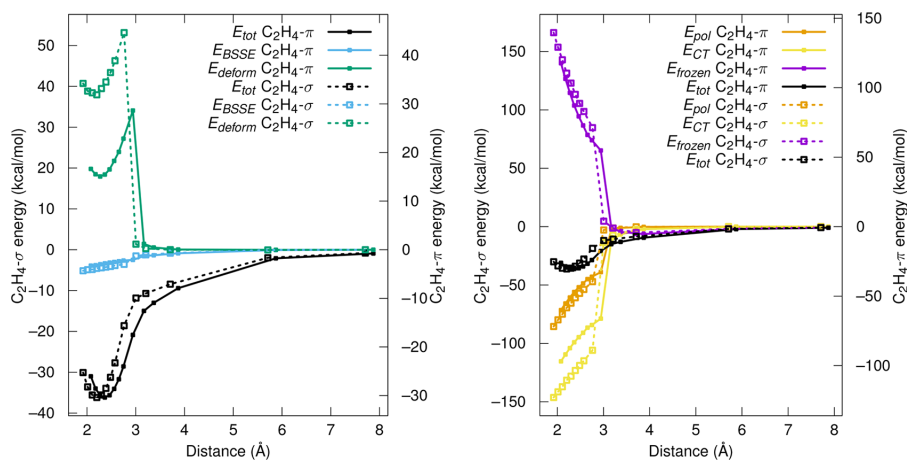


**Figure 3.** Energy decomposition analysis for di- $\sigma$  (dashed lines, left y-axis) and  $\pi$  (solid lines, right y-axis)  $C_2H_4$ . The total interaction energy is compared to the BSSE and the deformation energy on the left, while the right quantifies the frozen monomers, polarization, and charge-transfer interaction energy.

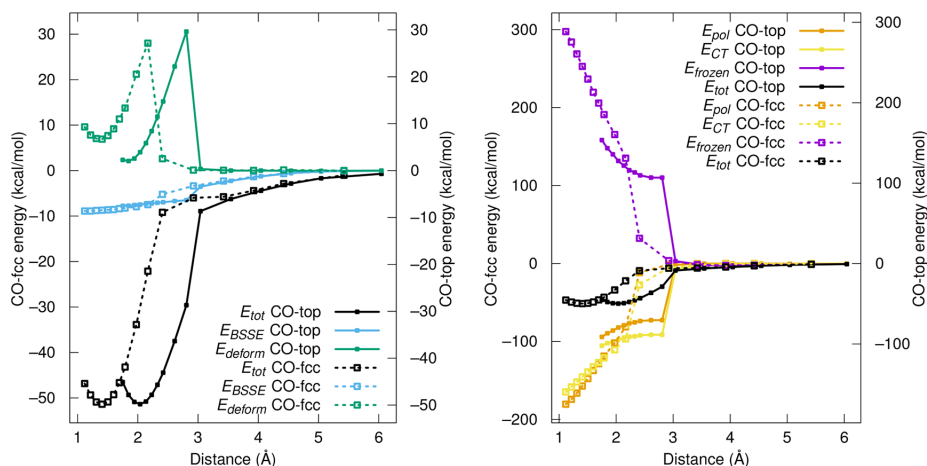


**Figure 4.** Energy decomposition analysis for top (solid lines, right y-axis) and fcc (dashed lines, left y-axis) CO on Pt(111). The total interaction energy is compared to the BSSE and the deformation energy on the left, while the right quantifies the frozen monomers, polarization, and charge transfer interaction energy.

obtained for  $H_2O$  and  $H_2S$ . Since  $\Delta E_{tot}$  is not very different when using an ideal Pt(111) surface,  $H_2S$  adsorption can be described without taking into account the surface deformation with only a small loss in accuracy. Given that  $\Delta E_{CT}$  is most strongly affected, this analysis also identifies the charge transfer as the origin of the deformation.

On a more technical level, we have also investigated the influence of the electronic smearing temperature on the results. In Figure S4, we show that increasing the electronic temperature from 300 to 1000 K does not visibly affect the results. Even at 2000 K, only changes of 3–4 kcal mol<sup>-1</sup> are observed, leaving the relative importance of different terms unchanged. As detailed in the Supporting Information, the small changes observed can be rationalized keeping in mind that higher electronic temperatures lead to the occupation of orbitals lying above the Fermi level.

The deformation energy observed for  $H_2S$  is small compared to the one obtained for ethylene adsorption (see Figure 3). This does not come as a surprise, given that the adsorbed geometry (Figure 1) suggests a rehybridization of the  $sp^2$  carbon atoms. This significant geometric rearrangement is best associated with a “state crossing”:  $sp^2$  at long distances but  $\sim sp^3$  at short distances. This state-crossing is noncontinuous, as best seen in the deformation energy, although other interaction energy components show a similar discontinuity. As mentioned above, the deformation is mainly due to the deformation of the metal surface, where the Pt atom is partially lifted out of the surface (see Figure S2). The BSSE is again in the order of 10% of the total interaction energy around the minimum, and the total interaction energy is, with 30 and 37 kcal mol<sup>-1</sup> for  $\pi$  and di- $\sigma$ , respectively, similar. Furthermore, the larger geometric deformation (H–C–C–H dihedral angles of 132° and 156°) for the di- $\sigma$  mode compared to the  $\pi$  mode

is nicely captured by the deformation energy. Similar to H<sub>2</sub>S, the maximum deformation energy is obtained when the molecule is close enough to the surface to actually “feel” it but not close enough to form strong covalent bonds. The deformation and the total interaction energy reflect quite well that the  $\pi$  mode approaches the surface less closely than the di- $\sigma$  mode (Pt–C distance of 2.20 Å in  $\pi$  and 2.13 Å in di- $\sigma$ ). The right-hand side of the graph provides a rationalization: the Pauli repulsion (contained in  $E_{\text{frozen}}$ ) is longer-ranged for the  $\pi$  bond, at the top of a Pt atom, than between the bridge site and carbon atoms that are not strictly on top of Pt atoms. The same observation also applies to the polarization and charge-transfer energy. However, the relative importance of repulsion, polarization, and charge transfer is surprisingly similar for both modes, demonstrating that the nature of the bonding interaction is the same. Nevertheless, the di- $\sigma$  mode maximizes this bonding type which is characterized by ~40% polarization energy and ~60% charge transfer, very similar to the interaction of H<sub>2</sub>S with the same surface.

The last example we are discussing here is the classic case of CO adsorption on Pt(111). One of the challenging questions is whether CO is adsorbed on top or on bridge/hollow sites and how this evolves as a function of the surface charge.<sup>70</sup> The following analysis investigates exclusively the bonding patterns at the respective adsorption sites, without drawing any conclusions, neither on the reliability of the chosen density functional nor on the actual site preference of CO on Pt(111).

In Figure 4, the data for CO adsorption on top and fcc sites is compared. At our level of theory, the fcc adsorption site is slightly preferred (–52 vs –49 kcal mol<sup>–1</sup>). However, these graphs show very clearly the contrasting behavior of CO on these two sites: The top site experiences a significantly stronger Pauli repulsion, resulting in a longer equilibrium distance (2 Å compared to 1.5 Å). The deformation energy, on the other hand, is slightly lower at the equilibrium distance on the top site than on the fcc site, although the barrier for the state-crossing is roughly equal (~30 kcal mol<sup>–1</sup>), shifted by 0.75 Å to longer distances for the top mode. Regarding the decomposition of the interaction energy, we can first note that the Pauli repulsion at long distances is lower for the fcc mode compared to the top adsorption mode but, at shorter distances, rises more quickly for the fcc site. Second, in contrast to the case of C<sub>2</sub>H<sub>4</sub>, the ratio of polarization and charge-transfer energy is quite different for the two adsorption modes. Somewhat surprisingly, the fcc mode shows a similar pattern as H<sub>2</sub>O adsorption, with  $\Delta E_{\text{pol}}$  and  $\Delta E_{\text{CT}}$  being roughly equal over the entire range of distances. In other words, polarization contributes more to the total binding than for the adsorption of C<sub>2</sub>H<sub>4</sub>. While charge transfer is relatively more important for the top adsorption mode, it is still far from reaching the importance it takes for ethylene adsorption. We suggest that this “lower than expected” importance of charge transfer for the adsorption of CO on Pt(111) is due to the intricate donation and back-donation involved in CO adsorption, which can be seen as a particularly strong polarization effect. In other words, it is the polarization which is particularly strong for CO adsorption, not the charge transfer that is small: this dative bond is the strongest bond investigated herein, and orbital interactions are without any doubt key for its accurate description. However, our analysis demonstrates that the top site is more sensitive to charge transfer than adsorption on the hollow site. This is in good agreement with previous reports,<sup>70</sup> but it is the first time that

such a difference is clearly traced back to charge transfer and disentangled from polarization effects.

## 5. CONCLUSIONS

In this work, we have presented the extension of the BLW formalism to systems that require fractionally occupied orbitals such as metals at finite temperature. Since the computational cost of the rigorous combinatorial formulation is unpractical, our extension relies on a mean-field approximation to ensemble BLW in the context of mixed-state theory. This approximation is based on a new concept: selfish orbitals. Selfish orbitals are normalized, but their interactions with other orbitals are scaled down according to their occupation number. This mean-field approximation is exact in the case of infinitesimal smearing (i.e., BLW with a gap) and/or 1-block systems (i.e., ensemble KS-DFT). Furthermore, in numerical examples studied, the estimated error in the polarization energy is roughly 0.5 kcal mol<sup>–1</sup>.

The method has been implemented in CP2K, and numerical applications have shown that H<sub>2</sub>S is much more strongly bound to Pt(111) due to charge transfer, while the contribution of polarization is on a similar level as for H<sub>2</sub>O. The chemisorption of ethylene on Pt(111) is, however, dominated by the charge transfer, and the two modes (di- $\sigma$  and  $\pi$ ) show the same type of bonding, with proportions of different interaction energy components close to the ones of H<sub>2</sub>S. CO adsorption, on the other hand, is shown to depend significantly on the adsorption site: although the bond is five times stronger than for H<sub>2</sub>O, the hollow-site adsorption is characterized by a roughly equal contribution of polarization and charge transfer, just like water adsorption. On the top site, charge transfer is somewhat more important, but even in this case, its importance is relatively smaller than for H<sub>2</sub>S or C<sub>2</sub>H<sub>4</sub>. We ascribe this particularity to the donation/back-donation of CO, which can be seen as a particularly strong polarization contribution.

As demonstrated herein, BLW-EDA provides a convenient (i.e., easy to use) tool, providing polarization and charge-transfer energies at the metal interface, which is expected to provide valuable insight for catalysis and the understanding of the metal/gas and metal/liquid interface.

## ■ ASSOCIATED CONTENT

### Supporting Information

The Supporting Information is available free of charge on the ACS Publications website at DOI: 10.1021/acs.jctc.8b00957.

Density recovery; comparison of results with two different Pt pseudopotentials and results from VASP; further analysis of the deformation energy; influence of the electronic temperature; expanded Figures 2, 3, and 4; numerical results (PDF)

Archive with optimized geometries and their opt-PBE-vdW energies as obtained by VASP (ZIP)

## ■ AUTHOR INFORMATION

### Corresponding Author

\*E-mail: [stephan.steinmann@ens-lyon.fr](mailto:stephan.steinmann@ens-lyon.fr)

### ORCID

Marcella Iannuzzi: 0000-0001-9717-2527

Rustam Z. Khaliullin: 0000-0002-9073-6753

Stephan N. Steinmann: 0000-0002-2777-356X



# Chapter 4. Energy Decomposition Analysis for Metal Surface–Adsorbate Interactions by Block Localized Wave Functions

## Funding

Computational resources were generously provided by the mesocenter PSMN. This work was also granted access to the HPC resources of CINES and IDRIS under the allocation 2014-080609 made by GENCI. The PHC Germaine de Staël program “Reactivity at the solid/liquid interface: Better simulation for a better comprehension”, number 30617PA, is acknowledged for supporting the collaboration between S.N.S. and M.I.

## Notes

The authors declare no competing financial interest.

## ACKNOWLEDGMENTS

The authors thank J. Hutter for insightful discussions.

## REFERENCES

- (1) Heitler, W.; London, F. Wechselwirkung neutraler Atome und homo-polare Bindung nach der Quantenmechanik. *Eur. Phys. J. A* **1927**, *44*, 455–472.
- (2) Ruedenberg, K. The Physical Nature of the Chemical Bond. *Rev. Mod. Phys.* **1962**, *34*, 326–376.
- (3) Bader, R. F. W. *Atoms in Molecules: A Quantum Theory*; Oxford University Press: New York, 1990.
- (4) Reed, A. E.; Curtiss, L. A.; Weinhold, F. Intermolecular interactions from a natural bond orbital, donor-acceptor viewpoint. *Chem. Rev.* **1988**, *88*, 899–926.
- (5) Gonthier, J. F.; Steinmann, S. N.; Wodrich, M. D.; Corminboeuf, C. Quantification of “fuzzy” chemical concepts: a computational perspective. *Chem. Soc. Rev.* **2012**, *41*, 4671–4687.
- (6) Tsepis, A. C. DFT challenge of intermetallic interactions: From metallophilicity and metallaromaticity to sextuple bonding. *Coord. Chem. Rev.* **2017**, *345*, 229–262.
- (7) Pastorczak, E.; Corminboeuf, C. Perspective: Found in translation: Quantum chemical tools for grasping non-covalent interactions. *J. Chem. Phys.* **2017**, *146*, 120901.
- (8) Philipsen, P. H. T.; Baerends, E. J. Role of the Fermi Surface in Adsorbate-Metal Interactions: An Energy Decomposition Analysis. *J. Phys. Chem. B* **2006**, *110*, 12470–12479.
- (9) Cruz Hernandez, N.; Zicovich-Wilson, C. M.; Fdez. Sanz, J. The constrained space orbital variation analysis for periodic *ab initio* calculations. *J. Chem. Phys.* **2006**, *124*, 194105.
- (10) Raupach, M.; Tonner, R. A periodic energy decomposition analysis method for the investigation of chemical bonding in extended systems. *J. Chem. Phys.* **2015**, *142*, 194105.
- (11) Xin, H.; Linic, S. Analyzing relationships between surface perturbations and local chemical reactivity of metal sites: Alkali promotion of O<sub>2</sub> dissociation on Ag(111). *J. Chem. Phys.* **2016**, *144*, 234704.
- (12) Pecher, J.; Mette, G.; Durr, M.; Tonner, R. Site-Specific Reactivity of Ethylene at Distorted Dangling-Bond Configurations on Si(001). *ChemPhysChem* **2017**, *18*, 357–365.
- (13) Pecher, J.; Schober, C.; Tonner, R. Chemisorption of a Strained but Flexible Molecule: Cyclooctyne on Si(001). *Chem. - Eur. J.* **2017**, *23*, 5459–5466.
- (14) Mo, Y.; Song, L.; Wu, W.; Zhang, Q. Charge transfer in the electron donor-acceptor complex BH<sub>3</sub>NH<sub>3</sub>. *J. Am. Chem. Soc.* **2004**, *126*, 3974–3982.
- (15) Khaliullin, R. Z.; Head-Gordon, M.; Bell, A. T. An efficient self-consistent field method for large systems of weakly interacting components. *J. Chem. Phys.* **2006**, *124*, 204105.
- (16) Kaduk, B.; Kowalczyk, T.; Van Voorhis, T. Constrained Density Functional Theory. *Chem. Rev.* **2012**, *112*, 321–370.
- (17) Plaisance, C. P.; van Santen, R. A.; Reuter, K. Constrained-Orbital Density Functional Theory. Computational Method and Applications to Surface Chemical Processes. *J. Chem. Theory Comput.* **2017**, *13*, 3561–3574.
- (18) Mao, Y.; Ge, Q.; Horn, P. R.; Head-Gordon, M. On the Computational Characterization of Charge-Transfer Effects in Noncovalently Bound Molecular Complexes. *J. Chem. Theory Comput.* **2018**, *14*, 2401–2417.
- (19) Stoll, H.; Wagenblast, G.; Preuss, H. On the use of local basis sets for localized molecular orbitals. *Theor. Chim. Acta* **1980**, *57*, 169–178.
- (20) Gianinetti, E.; Raimondi, M.; Tornaghi, E. Modification of the Roothaan equations to exclude BSSE from molecular interaction calculations. *Int. J. Quantum Chem.* **1996**, *60*, 157–166.
- (21) Nagata, T.; Takahashi, O.; Saito, K.; Iwata, S. Basis set superposition error free self-consistent field method for molecular interaction in multi-component systems: Projection operator formalism. *J. Chem. Phys.* **2001**, *115*, 3553–3560.
- (22) Mo, Y.; Gao, J.; Peyerimhoff, S. D. Energy decomposition analysis of intermolecular interactions using a block-localized wave function approach. *J. Chem. Phys.* **2000**, *112*, 5530–5538.
- (23) Khaliullin, R. Z.; Cobar, E. A.; Lochan, R. C.; Bell, A. T.; Head-Gordon, M. Unravelling the Origin of Intermolecular Interactions Using Absolutely Localized Molecular Orbitals. *J. Phys. Chem. A* **2007**, *111*, 8753–8765.
- (24) Khaliullin, R. Z.; Bell, A. T.; Head-Gordon, M. Analysis of charge transfer effects in molecular complexes based on absolutely localized molecular orbitals. *J. Chem. Phys.* **2008**, *128*, 184112.
- (25) Azar, R. J.; Head-Gordon, M. An energy decomposition analysis for intermolecular interactions from an absolutely localized molecular orbital reference at the coupled-cluster singles and doubles level. *J. Chem. Phys.* **2012**, *136*, 024103.
- (26) Thirman, J.; Head-Gordon, M. An energy decomposition analysis for second-order Møller-Plesset perturbation theory based on absolutely localized molecular orbitals. *J. Chem. Phys.* **2015**, *143*, 084124.
- (27) Smits, G. F.; Krol, M. C.; van der Hart, W. J.; Altona, C. Theoretical investigations of the nature of intramolecular interactions. *Mol. Phys.* **1986**, *59*, 209–225.
- (28) Mo, Y.; Wu, W.; Song, L.; Lin, M.; Zhang, Q.; Gao, J. The Magnitude of Hyperconjugation in Ethane: A Perspective from Ab Initio Valence Bond Theory. *Angew. Chem., Int. Ed.* **2004**, *43*, 1986–1990.
- (29) Wodrich, M. D.; Gonthier, J. F.; Steinmann, S. N.; Corminboeuf, C. How Strained are Carbomeric-Cycloalkanes? *J. Phys. Chem. A* **2010**, *114*, 6705–6712.
- (30) Levine, D. S.; Horn, P. R.; Mao, Y.; Head-Gordon, M. Variational Energy Decomposition Analysis of Chemical Bonding. I. Spin-Pure Analysis of Single Bonds. *J. Chem. Theory Comput.* **2016**, *12*, 4812–4820.
- (31) Levine, D. S.; Head-Gordon, M. Energy decomposition analysis of single bonds within Kohn–Sham density functional theory. *Proc. Natl. Acad. Sci. U. S. A.* **2017**, *114*, 12649–12656.
- (32) Couty, M.; Bayse, C. A.; Hall, M. B. Extremely localized molecular orbitals (ELMO): a non-orthogonal Hartree-Fock method. *Theor. Chem. Acc.* **1997**, *97*, 96–109.
- (33) Fornili, A.; Sironi, M.; Raimondi, M. Determination of extremely localized molecular orbitals and their application to quantum mechanics/molecular mechanics methods and to the study of intramolecular hydrogen bonding. *J. Mol. Struct.: THEOCHEM* **2003**, *632*, 157–172.
- (34) Genoni, A.; Ghitti, M.; Pieraccini, S.; Sironi, M. A novel extremely localized molecular orbitals based technique for the one-electron density matrix computation. *Chem. Phys. Lett.* **2005**, *415*, 256–260.
- (35) Fornili, A.; Moreau, Y.; Sironi, M.; Assfeld, X. On the suitability of strictly localized orbitals for hybrid QM/MM calculations. *J. Comput. Chem.* **2006**, *27*, 515–523.
- (36) Genoni, A. X-ray Constrained Extremely Localized Molecular Orbitals: Theory and Critical Assessment of the New Technique. *J. Chem. Theory Comput.* **2013**, *9*, 3004–3019.
- (37) Steinmann, S. N.; Jana, D. F.; Wu, J. I.-C.; Schleyer, P. v. R.; Mo, Y.; Corminboeuf, C. Direct Assessment of Electron Delocaliza-

- tion Using NMR Chemical Shifts. *Angew. Chem., Int. Ed.* **2009**, *48*, 9828–9833.
- (38) Elgabarty, H.; Khaliullin, R. Z.; Kuhne, T. D. Covalency of hydrogen bonds in liquid water can be probed by proton nuclear magnetic resonance experiments. *Nat. Commun.* **2015**, *6*, 8318.
- (39) Steinmann, S. N.; Vogel, P.; Mo, Y.; Corminboeuf, C. The norbornene mystery revealed. *Chem. Commun.* **2011**, *47*, 227–229.
- (40) Steinmann, S. N.; Mo, Y.; Corminboeuf, C. How do electron localization functions describe  $\pi$ -electron delocalization? *Phys. Chem. Chem. Phys.* **2011**, *13*, 20584–20592.
- (41) Bomble, L.; Steinmann, S. N.; Perez-Peralta, N.; Merino, G.; Corminboeuf, C. Bonding analysis of planar hypercoordinate atoms via the generalized BLW-LOL. *J. Comput. Chem.* **2013**, *34*, 2242–2248.
- (42) Mo, Y.; Gao, J. Polarization and Charge-Transfer Effects in Aqueous Solution via Ab Initio QM/MM Simulations. *J. Phys. Chem. B* **2006**, *110*, 2976–2980.
- (43) Giese, T. J.; Chen, H.; Huang, M.; York, D. M. Parametrization of an Orbital-Based Linear-Scaling Quantum Force Field for Noncovalent Interactions. *J. Chem. Theory Comput.* **2014**, *10*, 1086–1098.
- (44) Demerdash, O.; Mao, Y.; Liu, T.; Head-Gordon, M.; Head-Gordon, T. Assessing many-body contributions to intermolecular interactions of the AMOEBA force field using energy decomposition analysis of electronic structure calculations. *J. Chem. Phys.* **2017**, *147*, 161721.
- (45) Bambagioni, V.; Bevilacqua, M.; Bianchini, C.; Filippi, J.; Lavacchi, A.; Marchionni, A.; Vizza, F.; Shen, P. K. Cover Picture: Self-Sustainable Production of Hydrogen, Chemicals, and Energy from Renewable Alcohols by Electrocatalysis (ChemSusChem 7/2010). *ChemSusChem* **2010**, *3*, 765–765.
- (46) Liu, P.; Norskov, J. K. Ligand and ensemble effects in adsorption on alloy surfaces. *Phys. Chem. Chem. Phys.* **2001**, *3*, 3814–3818.
- (47) Gianinetti, E.; Vandoni, I.; Famulari, A.; Raimondi, M. Extension of the SCF-MI method to the case of K fragments one of which is an open-shell system. *Adv. Quantum Chem.* **1998**, *31*, 251–266.
- (48) Horn, P. R.; Sundstrom, E. J.; Baker, T. A.; Head-Gordon, M. Unrestricted absolutely localized molecular orbitals for energy decomposition analysis: Theory and applications to intermolecular interactions involving radicals. *J. Chem. Phys.* **2013**, *138*, 134119.
- (49) Yang, W.; Mori-Sanchez, P.; Cohen, A. J. Extension of many-body theory and approximate density functionals to fractional charges and fractional spins. *J. Chem. Phys.* **2013**, *139*, 104114.
- (50) Steinmann, S. N.; Yang, W. Wave function methods for fractional electrons. *J. Chem. Phys.* **2013**, *139*, 074107.
- (51) Khaliullin, R. Z.; VandeVondele, J.; Hutter, J. Efficient Linear-Scaling Density Functional Theory for Molecular Systems. *J. Chem. Theory Comput.* **2013**, *9*, 4421–4427.
- (52) Mayer, I.; Surjan, P. R. Localization and delocalization. II. Role of overlap in interbond interactions. *J. Chem. Phys.* **1984**, *80*, 5649–5658.
- (53) CP2K Open Source Molecular Dynamics, available at <https://www.cp2k.org/>.
- (54) Kresse, G.; Hafner, J. Ab initio molecular dynamics for liquid metals. *Phys. Rev. B: Condens. Matter Mater. Phys.* **1993**, *47*, 558.
- (55) Kresse, G.; Furthmuller, J. Efficient iterative schemes for ab initio total-energy calculations using a plane-wave basis set. *Phys. Rev. B: Condens. Matter Mater. Phys.* **1996**, *54*, 11169.
- (56) Klimes, J.; Bowler, D. R.; Michaelides, A. Chemical accuracy for the van der Waals density functional. *J. Phys.: Condens. Matter* **2010**, *22*, 022201.
- (57) Steinmann, S. N.; Corminboeuf, C. Comprehensive Benchmarking of a Density-Dependent Dispersion Correction. *J. Chem. Theory Comput.* **2011**, *7*, 3567–3577.
- (58) Gautier, S.; Steinmann, S. N.; Michel, C.; Fleurat-Lessard, P.; Sautet, P. Molecular adsorption at Pt(111). How accurate are DFT functionals? *Phys. Chem. Chem. Phys.* **2015**, *17*, 28921–28930.
- (59) Blochl, P. E. Projector augmented-wave method. *Phys. Rev. B: Condens. Matter Mater. Phys.* **1994**, *50*, 17953.
- (60) Kresse, G.; Joubert, D. From ultrasoft pseudopotentials to the projector augmented-wave method. *Phys. Rev. B: Condens. Matter Mater. Phys.* **1999**, *59*, 1758.
- (61) VandeVondele, J.; Hutter, J. Gaussian basis sets for accurate calculations on molecular systems in gas and condensed phases. *J. Chem. Phys.* **2007**, *127*, 114105.
- (62) Goedecker, S.; Teter, M.; Hutter, J. Separable dual-space Gaussian pseudopotentials. *Phys. Rev. B: Condens. Matter Mater. Phys.* **1996**, *54*, 1703–1710.
- (63) Boys, S. F.; Bernardi, F. The calculation of small molecular interactions by the differences of separate total energies. Some procedures with reduced errors. *Mol. Phys.* **1970**, *19*, 553–566.
- (64) Steinmann, S. N.; Corminboeuf, C.; Wu, W.; Mo, Y. Dispersion-Corrected Energy Decomposition Analysis for Intermolecular Interactions Based on the BLW and dDXDM Methods. *J. Phys. Chem. A* **2011**, *115*, 5467–5477.
- (65) Bondi, A. van der Waals Volumes and Radii. *J. Phys. Chem.* **1964**, *68*, 441–451.
- (66) Miller, T. M. *CRC Handbook of Chemistry and Physics*; Taylor & Francis Group: Boca Raton, FL, 2010.
- (67) Reed, A. E.; Schleyer, P. v. R. Chemical bonding in hypervalent molecules. The dominance of ionic bonding and negative hyperconjugation over d-orbital participation. *J. Am. Chem. Soc.* **1990**, *112*, 1434–1445.
- (68) Steinmann, S. N.; Fleurat-Lessard, P.; Gotz, A. W.; Michel, C.; Ferreira de Morais, R.; Sautet, P. Molecular mechanics models for the image charge, a comment on “Including image charge effects in the molecular dynamics simulations of molecules on metal surfaces. *J. Comput. Chem.* **2017**, *38*, 2127–2129.
- (69) Steinmann, S. N.; Ferreira De Morais, R.; Gotz, A. W.; Fleurat-Lessard, P.; Iannuzzi, M.; Sautet, P.; Michel, C. Force Field for Water over Pt(111): Development, Assessment, and Comparison. *J. Chem. Theory Comput.* **2018**, *14*, 3238–3251.
- (70) Kalhara Gunasooriya, G. T. K.; Saeys, M. CO Adsorption Site Preference on Platinum: Charge Is the Essence. *ACS Catal.* **2018**, *8*, 3770–3774.



## 5 Group Additivity for Aqueous Phase Thermochemical Properties of Alcohols on Pt(111)

Compared to the semi-hydrogenation of acetylene studied in chapter 3, the aqueous phase reforming of polyols generates much more, and more diverse, reaction intermediates. Assuming a complete decomposition, i.e., into  $\text{CO}_2$  and  $\text{H}_2$ , the complexity of the reaction network steeply rises with the length of the polyol. This comes from the fact that the C-C, C-H and O-H bonds need to be broken and C-O bonds need to be formed, without any clearly defined sequence of the different steps. The resulting number for possible intermediates is 67 for ethanol, while it is more than  $10^4$  for sorbitol ( $\text{C}_6\text{O}_6\text{H}_{14}$ ). Hence, DFT is not suitable to investigate the whole range of intermediates. In the ANR funded project MUSIC, we have adopted a multi-scale approach, where we pre-screen reaction networks at an approximate, but very rapid level of theory to identify the most important reaction intermediates. The lowest level of this hierarchy is presented in the present chapter. It is based on group additivity, i.e., each adsorbate is divided into functional groups that are connected (or not) with the metal surface. Based on this connectivity, the heat of formation of adsorbates can be estimated in a fraction of a second instead of hours of a DFT computation. The accuracy (root mean square deviation of about 4 kcal/mol) of this very cheap method is deemed sufficient to rapidly go through the thousands of intermediates and do DFT computations only on the most important ones. In combination with Bell-Evans-Polanyi relations to estimate the barrier heights between the intermediates that we developed in a subsequent work, the bricks to perform microkinetic simulations to identify the dominant pathways are now available. As a secondary point of view, we have also investigated the importance of the presence of a solvent (water) on the thermodynamics of the various reactions at the metal/liquid interface. In view of the hundreds of DFT computations performed, we included the solvation effect through an implicit solvent model. The solvation energy at the solid/liquid interface provided by the implicit solvent is, however, found to be rather small and mainly restricted to reactions where O-H bonds are broken or re-oriented.



# Group Additivity for Aqueous Phase Thermochemical Properties of Alcohols on Pt(111)

Geun Ho Gu,<sup>†</sup> Benjamin Schweitzer,<sup>‡</sup> Carine Michel,<sup>‡,§</sup> Stephan N. Steinmann,<sup>\*,‡,§</sup> Philippe Sautet,<sup>\*,‡,§,⊥</sup> and Dionisios G. Vlachos<sup>\*,†</sup>

<sup>†</sup>Department of Chemical and Biomolecular Engineering, Catalysis Center for Energy Innovation, University of Delaware, Newark, Delaware 19716, United States

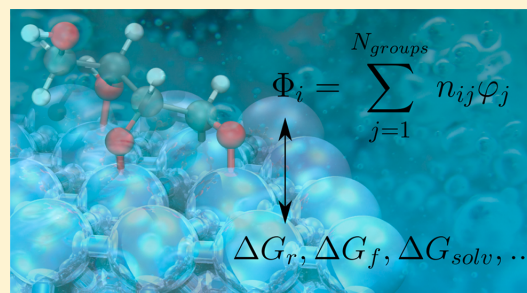
<sup>‡</sup>Univ Lyon, ENS de Lyon, CNRS, Université Lyon 1, Laboratoire de Chimie UMR 5182, F-69342, Lyon, France

<sup>§</sup>Department of Chemical and Biomolecular Engineering, University of California, Los Angeles, Los Angeles, California 90095, United States

<sup>⊥</sup>Department of Chemistry and Biochemistry, University of California, Los Angeles, Los Angeles, California 90095, United States

## Supporting Information

**ABSTRACT:** Despite progress in theoretical tools, the influence of solvation in heterogeneous catalysis remains poorly understood and predicted due to the large computational burden. In this work, we show that the inclusion of the solvation by water using a continuum model thermodynamically inhibits the O–H bond scissions involved in the ethanol aqueous phase reforming reaction over Pt(111), while it tends to favor the C–H, C–C, and C–O scissions. Then, we present a novel group additivity scheme for the free energy of adsorbates at the Pt/water interface that is able to capture this solvent effect. The mean absolute error (MeanAE) for the Gibbs free energy of formation is 3.3 kcal/mol over the investigated set of 200 species at the interface and the MeanAE for the 151 reaction free energies of ethanol aqueous phase reforming is 2.8 kcal/mol. Regarding the effect of solvation, our scheme is able to predict it with a MeanAE of about 1 kcal/mol. Together, the scheme promises to be accurate enough for narrowing down the most important reaction pathways in complex reaction networks as encountered in biomass conversion.



## INTRODUCTION

Biomass processing occurs often in water. Aqueous phase reforming is one of the processes and converts polyols and sugars in water to H<sub>2</sub> and CO<sub>2</sub> at relatively low temperatures under pressure, as popularized by Dumesic and co-workers.<sup>1</sup> An alternative large scale use of biomass conversion is bio-oil production via pyrolysis, which contains 15–30% water<sup>2</sup> and which needs to be further upgraded via hydrodeoxygenation. Here solvation effects are important due to the deactivation of well-studied NiMo sulfides in aqueous environment.<sup>3</sup> Another alternative is the selective transformation of sugar derivatives to largely used monomers such as acrylic or adipic acid.<sup>4,5</sup> All of these processes involve hydrogenations, C–C and C–OH bond breakings in the presence of water, which impose different conditions than for the current petro-chemistry. As demonstrated by several experimental studies, the presence of water is not innocent, even beyond catalyst stability, driving the need for new catalytic systems.<sup>6–9</sup>

The difference between chemistry in the gas- and solution-phase can be dissected into several distinct effects: (1) solubility influences the concentration of reactants, intermediates and products and hence impacts the kinetics even if the rate constants

would not change compared to the gas-phase; (2) the solvent can participate directly in the reaction, either as a reactant or as cocatalyst (e.g., in relay mechanisms of proton transfers); (3) the averaged interaction between the solvent and the solute changes the energetics compared to the gas-phase, stabilizing large dipole moments and charge-separations (heterolytic bond dissociations); (4) entropic contributions arise as the available phase-space can be significantly different in solution compared to the gas-phase, both in terms of translations/rotations and accessible configurations; and (5) the occurrence of homogeneous reactions in solvent phase such as dehydration and aldol condensation.<sup>10</sup>

Despite the wide use of solvent in biomass conversion, only a limited number of theoretical studies have explicitly addressed solvation effects.<sup>11–19</sup> This shortcoming is due to the methodology: there are no computationally affordable, broadly validated and general methods to include solvent effects in heterogeneous catalysis. The most rigorous way to describe reactivity in

Received: July 25, 2017

Revised: September 4, 2017

Published: September 7, 2017



# Chapter 5. Group Additivity for Aqueous Phase Thermochemical Properties of Alcohols on Pt(111)

condensed phases is to perform thermodynamic integration at the *ab initio* molecular dynamics (AIMD) level.<sup>20,21</sup> However, these computations are prohibitively expensive, as equilibration of the solid–liquid interface and convergence of the free energy would require more than 100 ps of simulations,<sup>22</sup> but today's computing power only allows to obtain about 10 ps for metallic surfaces with a reasonable effort.<sup>23</sup> Therefore, different approximations have been proposed: inclusion of only a couple of solvent molecules (called microsolvation),<sup>24,25</sup> adsorption of ice-like water layers on metallic surfaces,<sup>26,27</sup> the use of a combination of optimization and AIMD,<sup>11,18,19</sup> the classical treatment of solvent interactions<sup>16,28</sup> or the application of implicit solvent models.<sup>29–31</sup> In terms of interpretable differences between gas-phase and solution-phase reactivity, the advantage of implicit solvents is that solvation energies are directly accessible, which is not the case for AIMD simulations. On the other hand, the main limitation of implicit solvents is that no direct participation of the solvent can be described, in contrast to microsolvation approaches. As a compromise between efficiency and general accuracy, the combination of an implicit solvent with microsolvation has been explored.<sup>25,32–35</sup>

The main conclusions of the various theoretical studies are that adsorbate bindings are weaker in solution than in gas-phase given that the surface needs to be desolvated and only roughly half of the adsorbate is exposed to the solvent.<sup>13</sup> Second, reaction barriers are minimally affected, except for proton transfers for which water can act as a relay or at least activates O–H bonds<sup>25</sup> and when hydroxyl groups are well-exposed to the solvent in the course of the elementary step.<sup>12,28</sup> As a minor variant, elementary steps that drastically change the surface dipole moment are also influenced by the solvent.<sup>12,14</sup> This phenomenon can, in the case of acidic protons, lead to heterolytic bond breakings at the water/metal interface.<sup>24</sup> Furthermore, solvent effects are critical when surfaces are partially charged, either in electrochemistry<sup>36</sup> or when assessing the influence of a base which promotes the reaction through coadsorption.<sup>37</sup> Despite these progress, investigation of the effect of solvent on the entire reaction networks using density functional theory (DFT) remains challenging due to the tremendous computational burden, especially for large alcohols and polyols.<sup>38</sup>

Previously, group contribution methods were pioneered by Benson to predict thermodynamic properties of molecules at a greatly reduced computational cost.<sup>39</sup> Those methods use molecular fragments to correlate thermodynamic properties. The simplest form is to estimate the property of a given component as the sum of its molecular fragments or groups and is simply called group additivity.<sup>39</sup> It is based on the observation that state properties of molecules can be expressed as simple sums over values assigned to the functional groups. As an example, elongating a linear alkane by one additional methylene (CH<sub>2</sub>) group decreases the heat of formation of the alkane by ~5 kcal/mol. This simple picture can be refined by applying various corrections for neighboring groups. Nevertheless, the property evaluations are extremely simple compared to quantum mechanical computations. This method was initially developed for closed-shell gas molecules,<sup>39–41</sup> and it has since been extended to open-shell radicals,<sup>42</sup> transition states,<sup>43,44</sup> and carbenium ions.<sup>45</sup> Additionally, group additivity has been applied to pure liquids and dilute solutes,<sup>46</sup> and it has been shown to accurately predict various state properties such as the volume, density, viscosity, boiling point, melting point, critical temperature, and pressure.<sup>47–50</sup>

The group additivity scheme accounts for intramolecular interactions, whereas solution nonideality requires inclusion of intermolecular interactions, whose strength depends on the composition of the mixture. To address this issue, group contribution methods that include group interactions were developed. For instance, universal quasichemical functional-group activity coefficients (UNIFAC),<sup>51,52</sup> computes the average interaction between groups using Flory–Huggins statistical-mechanics model. This method employs the surface area and volume of each group, in addition to the interactions between groups as descriptors, which are then correlated to activity coefficients. More recently, the group contribution method has been extended to equations of state, with the statistical associating fluid theory (SAFT) and conductor-like screening model-segment activity coefficient (COSMO-SAC) models demonstrating promising performance.<sup>53,54</sup> These methods apply to bulk fluid mixtures but do not consider catalyst surfaces. The Delaware group has been developing group contribution methods<sup>55</sup> to predict adsorbate properties for hydrocarbons, oxygenates, furanics and aromatics,<sup>56–58</sup> which, combined with linear scaling relationships, can predict thermochemistry on metal surfaces.<sup>59,60</sup> However, such a group additivity method for the prediction of thermodynamic properties of adsorbates *in the presence of a solvent* has yet to be developed.

In this paper, we demonstrate that the introduction of an implicit solvent changes the reaction equilibrium constants of specific reaction types (e.g., C–H and O–H dissociations). Then, we build a group additivity method for Gibbs free energy of formation of linear alcohol adsorbates in vacuum and solvent using the polarizable continuum method (PCM) for implicit solvation. Cross-validation reveals that the mean absolute error (MeanAE) is 1.0 and 3.3 kcal/mol for the solvation free energy and the Gibbs free energy of formation, respectively. We further assess our model by comparing DFT computed reaction energies to those predicted via group additivity.

## METHODS

**Density Functional Theory and Polarizable Continuum Model.** The DFT computations are carried out with the Vienna Ab initio Simulation Package VASP 5.3.5.<sup>61</sup> The electronic structure is described within the generalized gradient approximation using the PBE<sup>62</sup> exchange correlation functional. The dispersion correction is included using the dDSC approach.<sup>63,64</sup> The projector augmented wave method (PAW) is used to describe the ion–electron interactions.<sup>65,66</sup> The plane wave basis set is cut off at 400 eV. The electronic energy is converged to 10<sup>–6</sup> eV and the forces to 0.02 eV Å<sup>–1</sup>. The solvation is described using an implicit solvation model as implemented in the package VASPsol.<sup>29,67</sup> Dipole correction in the *z* direction is applied for adsorbates to avoid periodic summation of induced dipole and solvent model effects.<sup>16</sup>

The platinum surface is simulated as a p(4 × 4) slab consisting of four layers. The two bottom layers are kept fixed at the optimal bulk position in which the Pt–Pt distance is 2.80 Å. The vacuum distance is large enough to avoid spurious interactions (the norm of the vector perpendicular to the surface is 22.86 Å). The integration of the Brillouin zone is performed using a Monkhorst–Pack mesh of with 3 × 3 × 1 *k*-points for surfaces. The gas phase calculations are done at the gamma point in a cubic box of 20 Å in length.

**Thermodynamic Property Calculations of Molecules.** The Gibbs free energy of formation of a species *i* in gas-phase,  $\Delta G_{f,i(g)}^\circ$  is

$$\Delta G_{f,i(\text{gp})} = \Delta H_{f,i(\text{gp})} - TS_{i(\text{gp})} \quad (1)$$

where  $\Delta H_{f,i(\text{gp})}$  is the enthalpy of formation of the molecule  $i$  in gas-phase,  $T$  is the temperature, and  $S_{i(\text{gp})}$  is the entropy of the species  $i$  in gas-phase computed using statistical mechanics, atoms' coordinates, and vibrational frequencies (see ref 57 for details). We consider two type of species  $i$ : a gaseous molecule and an adsorbate.  $\Delta H_{f,i(\text{gp})}$  is estimated as

$$\Delta H_{f,i(\text{gp})} = \begin{cases} E_{i(\text{vac})} + H_{\text{rt},i(\text{gp})} + H_{\text{v},i(\text{gp})} + \Delta H_{\text{ref},i}: i \\ \text{is gaseous molecule} \\ E_{i(\text{vac})}^* - E_{\text{vac}}^* + H_{\text{v},i(\text{gp})} + \Delta H_{\text{ref},i}: i \\ \text{is adsorbate} \end{cases} \quad (2)$$

where  $E_{i(\text{vac})}$  is the DFT electronic energy of the gaseous species  $i$  in vacuum,  $E_{i(\text{vac})}^*$  is the DFT electronic energy of the adsorbate  $i$  and the slab,  $E_{\text{vac}}^*$  is the DFT electronic energy of the empty slab,  $H_{\text{rt},i(\text{gp})}$  and  $H_{\text{v},i(\text{gp})}$  are the rotational (r), translational (t), and vibrational (v) contribution to the heat of formation for the species  $i$  computed in the gas-phase, respectively (see ref 57 for calculation details). For a strongly bounded adsorbate, the rotational and translational degrees of freedom of atomic motion become vibrational upon binding, thus  $H_{\text{rt},i(\text{gp})}$  does not exist for adsorbates. To change from DFT reference system (infinitely separated atoms and electrons) to conventional heat of formations, we introduce the adjustment  $\Delta H_{\text{ref},i}$  (see refs 57 and 60 for computational details and the Supporting Information for the structures and properties of reference molecules). For the computation of the Gibbs free energy of formation of a solute  $i$  in water or an adsorbate  $i$  at water/metal interface ( $\Delta G_{f,i(\text{aq})}^0$ ), we assume that solvation does not depend on temperature (see the Supporting Information for further discussion) and that the entropy of a species is the same in gas-phase and water. In particular the later approximation is rather severe for adsorption from the liquid phase on the catalyst: Although for ideal solutions the entropy of a solute is the same as the one in the corresponding gas-phase when appropriately taking into account the available volume,<sup>68,69</sup> the entropy in aqueous solution for real solutes differs by roughly a factor of 2.<sup>10,70</sup> Since an adsorbate competes with the solvent for adsorption sites, the entropy of the adsorbate is, in general, even more challenging to assess than the entropy in solution. Although the structure of the solid–liquid interface remains a matter of debate, it is well established that the solvent properties at the interface are different compared to the bulk liquid.<sup>71–74</sup> Determining the change in entropy upon adsorption requires large-scale molecular dynamics simulations, which are difficult to converge, both in terms of size and time scale.<sup>73,75–77</sup> While AIMD would be ideal for such studies, the corresponding computational effort is tremendous.<sup>74,78–80</sup> On the other hand, force field methods, which make such investigations affordable,<sup>81,82</sup> suffer from low availability for general interfaces and very limited accuracy, best exemplified for the seemingly trivial water–metal interface, for which many potentials exist,<sup>21,78,83,84</sup> but only for the case of Cu/H<sub>2</sub>O does there exist a well validated force field.<sup>76</sup> Because of all these considerations, the simplistic approximation taken herein makes our approach transparent, and once established, the corresponding entropy corrections can be trivially applied to our model. Hence,  $\Delta G_{f,i(\text{aq})}$  is

$$\Delta G_{f,i(\text{aq})} = \Delta H_{f,i(\text{aq})} - TS_{i(\text{aq})} \quad (3)$$

$$S_{i(\text{aq})} \cong S_{i(\text{gp})} \quad (3)$$

where  $\Delta H_{f,i(\text{aq})}$  and  $S_{i(\text{aq})}$  are the enthalpy of formation and the entropy of species  $i$  in aqueous solvent, respectively. The effect of the implicit solvation is included in  $\Delta H_{f,i(\text{aq})}$  as the change in electronic energy:

$$\Delta H_{f,i(\text{aq})} = \Delta H_{f,i(\text{gp})} + E_{\text{sol},i} + E_{\text{cav},i} \quad (4)$$

$$E_{\text{sol},i} = \begin{cases} E_{i(\text{aq})} - E_{i(\text{vac})}: i \text{ is gaseous molecule or solute} \\ E_{i(\text{aq})}^* (-E_{i(\text{vac})}^*) - (E_{\text{aq}}^* - E_{\text{vac}}^*): i \\ \text{is adsorbate} \end{cases} \quad (5)$$

Here  $E_{\text{sol},i}$  is the solvation electronic energy of a species  $i$ ,  $E_{i(\text{aq})}$  is the DFT electronic energy of the solute  $i$  in implicit water,  $E_{i(\text{aq})}^*$  is the electronic energy of the solvated adsorbate  $i$  and the slab,  $E_{\text{aq}}^*$  is the electronic energy of solvated empty slab (all without cavitation energy). The cavitation energy approximates the energetic cost to insert a solute in a solvent, such as solvent reorganization and (Pauli) repulsion. Its energy is usually assumed to be proportional to the solvent accessible surface area. We introduce an empirical cavitation energy correction term,  $E_{\text{cav},i}$ . The computation of cavitation energy using PCM is difficult for the adsorbates and the slab due to numerical instability. Instead, we compute cavitation energy for a small subset of our data, and regress the cavitation energy contribution for each element. The computation of  $E_{\text{cav},i}$  is discussed below in detail. The Gibbs free energy of solvation of a species  $i$ ,  $\Delta G_{\text{sol},i}$  is the Gibbs free energy to transfer a species  $i$  from the gas-phase to the liquid bulk, which, using the equations above, is

$$\Delta G_{\text{sol},i} = \Delta G_{f,i(\text{aq})} - \Delta G_{f,i(\text{vac})} = E_{\text{sol},i} + E_{\text{cav},i} \quad (6)$$

The accuracy of the PCM is further assessed in Figure S1 in Supporting Information, where the DFT-computed values of  $\Delta G_{\text{sol},i}$  are in a good agreement with the experimental  $\Delta G_{\text{sol},i}$  at 298 K, with a mean absolute deviation of 1.1 kcal/mol. Unfortunately, such data are not available for species at the interface. Hence, the accuracy of the herein applied PCM cannot be assessed. Furthermore, computationally feasible alternatives to implicit solvents to produce a consistent set of undoubtedly reliable solvation free energies at the interface are, to the best of our knowledge, not yet available. More reliable solvation free energies could be obtained with an accurate force field<sup>16</sup> or with long-time-scale ab initio molecular dynamics simulations; in the first case, the force field is currently missing, and the second option is not yet computationally affordable.

In addition to the heat of formation and entropy, we also compute the heat capacity at any temperature  $T$  for the species  $i$ ,  $C_{p,T,i(\text{gp})}$  ( $C_{p,T,i(\text{aq})} \cong C_{p,T,i(\text{gp})}$ ; see ref 57 for calculation detail) for the group additivity regression in order to transfer properties to different temperatures. We surveyed  $C_{p,T,i(\text{gp})}$  between 100 and 1500 at 100 K intervals. Figure 1 summarizes the relationship between gaseous molecules, molecule in the bulk liquid, adsorbates, and solvated adsorbates in a thermodynamic cycle.

**Group Additivity.** The group additivity method assumes that a thermodynamic property,  $\Phi$ , is a linear combination of the thermodynamic properties of groups found within a molecule



# Chapter 5. Group Additivity for Aqueous Phase Thermochemical Properties of Alcohols on Pt(111)

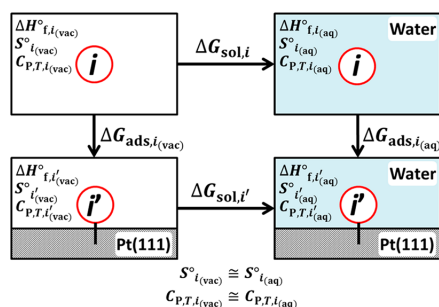


**Figure 1.** Various considered states for the system, summarized in a thermodynamic cycle. *i* is an arbitrary species, and *i'* is the species *i* adsorbed on the surface. Boxes represent a molecule in the gaseous state, in the bulk liquid, adsorbed on Pt(111), and adsorbed and solvated on Pt(111) going from left to right and from top to bottom. The three thermodynamic properties in each box represent the parameters predicted by our method. We assume that the solvation effect is temperature independent, and thus the entropy and heat capacity are the same in vacuum and in water.

$$\Phi_i = \sum_{j=1}^{N_{\text{groups}}} n_{ij} \varphi_j \quad (7)$$

where  $n_{ij}$  is the number of times group *j* appears in a species *i* and  $\varphi_j$  is group *j*'s contribution to the thermodynamic property.  $\varphi_j$  values can be derived via linear regression of experimental data or quantum chemical calculations (*vide infra*).

Conventionally, the linear regression is performed for three thermodynamic properties: standard heat of formation, standard entropy, and heat capacity at temperature *T*.<sup>39,42</sup> To account for the solvation effect, we perform the regression to one additional property, the standard heat of formation of solvated species. In order to perform regression to properties of both gaseous molecules and adsorbate molecules together, we found that subtracting rotational and translational contribution from the heat of formation of gaseous molecules improves the fitting.<sup>56,57,59</sup> Hence, the dependent variables for the regression are

$$\Delta H_{f,i(\text{gp}),\text{GA}} = \begin{cases} \Delta H_{f,i(\text{gp})} - H_{\text{rt},i(\text{gp})}; & i \text{ is gaseous molecule} \\ \Delta H_{f,i(\text{gp})}; & i \text{ is adsorbate} \end{cases}$$

$$\Delta H_{f,i(\text{aq}),\text{GA}} = \begin{cases} \Delta H_{f,i(\text{aq})} - H_{\text{rt},i(\text{vac})}; & i \text{ is gaseous molecule or} \\ \text{solute} \\ \Delta H_{f,i(\text{aq})}; & i \text{ is adsorbate} \end{cases}$$

$$C_{P,T,i(\text{gp}),\text{GA}} = \begin{cases} C_{P,T,i(\text{gp})} - C_{P,T,\text{rt},i(\text{gp})}; & i \text{ is gaseous molecule} \\ C_{P,T,i(\text{gp})}; & i \text{ is adsorbate} \end{cases} \quad (8)$$

where the subscript “GA” represents the part of the quantity which is expressed in terms of a group additivity scheme.  $C_{P,T,\text{rt},i(\text{gp})}$  is rotational and translational contribution to the heat capacity. For the entropy, we do not correct for rotational and translational contribution but correct for the symmetric number ( $\sigma$ ) contribution following Benson’s group additivity formulation:<sup>39</sup>

$$S_{i(\text{gp}),\text{GA}} = \begin{cases} S_{i(\text{gp})} + \ln(\sigma); & i \text{ is gaseous molecule} \\ S_{i(\text{gp})}; & i \text{ is adsorbate} \end{cases} \quad (9)$$

We assume that there is no symmetry contribution for adsorbates. The rotational and translational corrections are only applied to the heat of formation and heat capacity as the rotational and translational contributions do not depend on the groups, but are a constant shift (e.g.,  $H_{\text{rt},i(\text{gp})} = C_{P,T,\text{rt},i(\text{gp})} = 4RT$  for nonlinear molecules, or  $7/2RT$  for linear molecules). However, the rotational and translational corrections for entropy depend on the atoms’ weight and coordinates, and hence group additivity approach can describe these terms. For the computation of gaseous molecule properties, these subtracted terms needed to be added back when using the group additivity.

The group additivity parameters,  $\varphi_{(N \times 1)}$ , are computed by exploiting the Moore–Penrose pseudoinverse, indicated by  $^+$ , in the linear regression:

$$\varphi = (\mathbf{n}^T \mathbf{n})^+ \mathbf{n}^T \Phi \quad (10)$$

Here *N* is the number of groups,  $\mathbf{n}_{(M \times N)}$  is the group contribution matrix, *M* is the number of data points, and  $\Phi_{(M \times 1)}$  is the vector of thermodynamic parameters. The predictive accuracy of the model is assessed using *k*-fold cross validation.<sup>85,86</sup> In this method, the data set is randomly partitioned into *k* subsamples of equal size. The model is trained using *k*-1 subsamples, and the remaining subsample is used as the validation set to compute the model error. This process is repeated *k* times with each subsample used as a validation set once. Since the data partitioning involves randomization, Monte Carlo sampling is employed to compute the average error of each molecule. We used 10 as the value of *k* and 1000 repetitions of random partitioning which results in 95% confidence interval of predicted values less than 0.1 kcal/mol for  $\Delta H_{f,i(\text{gp}),\text{GA}}$  and  $\Delta H_{f,i(\text{gp}),\text{GA}}$  and 0.1 cal/(mol K) for  $S_{i(\text{gp}),\text{GA}}$  and  $C_{P,T,i(\text{gp}),\text{GA}}$ .

**Training Set.** Our training set consists of 200 data points that are divided into three subcategories: (i) 27 gas molecules, (ii) 53 adsorbates found in the ethanol aqueous phase reforming reaction network, and (iii) 110 adsorbates and 10 gas molecules from the butanetetraol reaction network.<sup>87</sup> The adsorbates in the ethanol reaction network include the dissociation products of ethanol as well as species from the water–gas-shift reaction and are used to examine the solvation effect on the reaction energies. The adsorbates from the reaction network of butanetetraol supplement the polyol backbone of our group-additivity scheme. This reaction network, generated using the R.I.N.G. software package,<sup>88,89</sup> contains a total of 5374 species, of which 120 species have been chosen randomly under the constraint that each nonunique group is found in at least seven points of the complete training set. The gas molecules are computed to test the effect of the PCM on the vibrational frequencies (see Figure S2 in the Supporting Information). The computed thermodynamic properties and structures of the training set species are also provided in the Supporting Information.

**Cavitation Energy Corrections.** The cavitation energy correction introduced above,  $E_{\text{cav},i}$  corrects the solvation energy computed using DFT calculations without the cavitation energy. To determine the corrections, we compute cavitation energies,  $E_{\text{cav},i}$  of 20 solutes and nine solvated adsorbates using the equation below:

$$E_{\text{cav},i} = E_{\text{sol},i,+c} - E_{\text{sol},i,-c} \quad (11)$$

Here  $E_{\text{sol},i,+c}$  and  $E_{\text{sol},i,-c}$  are  $E_{\text{sol},i}$  using eq 5 with the cavitation energy accounted and unaccounted, respectively. Here,  $E_{\text{sol},i,+c}$  is computed using energy cut off of 600 eV to improve the accuracy of this numerically delicate quantity. In a similar spirit to group additivity, we perform a regression of cavitation contribution for each element (C, H, O) to 29 data

$$E_{\text{cav},i} = \sum_j^{\text{C,H,O}} n_{ij} e_{\text{cav},j} \quad (12)$$

where  $n_{ij}$  is the number of occurrence of element  $j$  in species  $i$ , and  $e_{\text{cav},j}$  is the cavitation energy of element  $j$  computed using the linear regression method introduced above. The MeanAE and MaxAE (training error, not cross-validation error) are 0.18 and 0.47 kcal/mol, respectively. The training set data and regression coefficients are provided in [Supporting Information](#).

## RESULTS AND DISCUSSION

Having presented the methodological approach, we now turn to the results of our study. First, we discuss the influence of the implicit solvent on geometries and reaction free energies. Then, we present the performance of our group additivity scheme for gas- and solution-phase species and reactions.

### Influence of the Solvation on the DFT Geometries.

Upon solvation by water using a continuum model, isolated molecules showed limited structural changes with a root-mean-square deviation (RMSD) of 0.02 Å and a maximum RMSD of 0.09 Å. The RMSD have been evaluated using the Kabsch algorithm.<sup>90–92</sup> This algorithm optimally superposes the two molecules to minimize translational and rotational error and computes the RMSD. For the surface species, we disregarded the change in surface atom's position. These small positional changes are induced by the dipolar interactions with the continuum solvent mostly affecting the relative orientation of the C–O bonds. The structures of the adsorbed species are slightly more sensitive to the solvation with a mean RMSD of 0.03 Å and a maximum RMSD of 0.16 Å. This maximum corresponds to a change in the orientation of the OH bonds of COH–C–CH<sub>2</sub>–CHOH that rotates from pointing toward the surface to pointing toward the solvent. To better analyze this effect, we considered this reorientation for surface intermediates in the ethanol steam reforming reaction network. While the conformer with the OH bond pointing *down* is the most stable in vacuum, pointing the OH bond *up* becomes more stable in water. This effect, illustrated in the simple case of the CHOH fragment in [Figure 2](#), is assigned to a better solvation of the OH by up 3 to 5 kcal/mol compared to OH *down*.

**Influence of the Solvation on Reactions.** We assess the influence of PCM on ethanol aqueous reforming, including water-gas shift reactions, by considering the corresponding

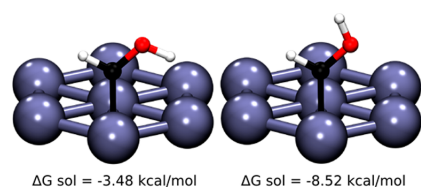


**Figure 2.** DFT structures of the HCOH fragment adsorbed on a Pt(111) slab: (left) the H down configuration; (right) the H up configuration. Associated solvation energies are also given.

standard Gibbs free energy of reactions in gas-phase (gp) and solution (aq):

$$\Delta G_{\text{r},(\text{gp})} = \sum_i \nu_i \Delta G_{\text{r},i(\text{gp})}$$

$$\Delta G_{\text{r},(\text{aq})} = \sum_i \nu_i \Delta G_{\text{r},i(\text{aq})} \quad (13)$$

where the reaction involves species  $i$  with the stoichiometric coefficient  $\nu_i$  with  $\nu_i > 0$  if  $i$  is a product. To assess the change in the standard Gibbs free energy of reaction upon solvation, we further define  $\Lambda_{\text{sol}}$  as the change of a reaction energy upon solvation:

$$\Lambda_{\text{sol}} = \Delta G_{\text{r},(\text{aq})} - \Delta G_{\text{r},(\text{gp})} \quad (14)$$

When  $\Lambda_{\text{sol}}$  is negative, the reaction is favored by solvation, the Gibbs energy of reaction at the solid–liquid interface being more exergonic than in the gas-phase. This change can also be seen as the sum of the solvation energies of each species  $i$  involved in the chemical reaction with a stoichiometric coefficient  $\nu_i$ :

$$\Lambda_{\text{sol}} = \sum_i^{N_{\text{species}}} \nu_i \Delta G_{\text{sol},i} \quad (15)$$

$\Lambda_{\text{sol}}$  is reported as a box plot on [Figure 3a](#) for each type of reaction under consideration: adsorption, C–H, O–H, C–C and C–O bond scissions.

In general, the adsorption of close-shell molecules is only slightly disfavored by the solvation with a mean of 0.2 kcal/mol for  $\Lambda_{\text{sol}}$ . The most affected species is acetaldehyde with  $\Lambda_{\text{sol}} = 2.4$  kcal/mol: its adsorption at the Pt(111) surface is disfavored by the stronger solvation in the solution ( $\Delta G_{\text{sol}} = -5.6$  kcal/mol) than at the surface ( $\Delta G_{\text{sol}} = -3.3$  kcal/mol).

Since the solvation energy does not change significantly upon adsorption, the analysis of the solvation energy of different species is done jointly for the molecules in bulk water and the ones adsorbed at the interface. The species have been split into three groups to represent the solvation Gibbs energy  $\Delta G_{\text{sol}}$  with box plots in [Figure 3b](#): (1) *Hydroxyl* contains at least one hydroxyl group, including water; (2) *aprotic oxygenate* includes all the species that contain an oxygen atom but not a hydroxyl group, for instance acetaldehyde; (3) *hydrocarbon* selects species that do not contain any oxygen atom. As expected, *hydrocarbon* members are weakly solvated by water (on average,  $\Delta G_{\text{sol}} = -1.7$  kcal/mol, standard deviation of  $\sigma = 1.0$  kcal/mol). *Aprotic oxygenates* are more solvated (on average,  $\Delta G_{\text{sol}} = -2.9$  kcal/mol,  $\sigma = 0.9$  kcal/mol) with a small standard deviation ( $\sigma$ ). The *hydroxyl* species show a stronger Gibbs solvation energy (on average,  $\Delta G_{\text{sol}} = -5.6$  kcal/mol,  $\sigma = 1.9$  kcal/mol) and, more importantly, a large standard deviation, with a maximum and minimum of  $-2.5$  and  $-9.8$  kcal/mol, respectively. For the surface species, the strong variations can be directly related to the two possible orientations of the O–H bond, *up* or *down*. In most cases, the OH *down* is the most stable configuration and is poorly solvated (for instance,  $\Delta G_{\text{sol}} = -3.5$  kcal/mol in CHOH). In some cases, the O–H *up* is the most stable configuration and is strongly solvated such as in CCHOH ( $\Delta G_{\text{sol}} = -9.3$  kcal/mol, the *up* configuration being more stable by 0.3 kcal/mol).

While most bond dissociations are made more exergonic by the solvation ( $\Lambda_{\text{sol}} < 0$ ), the O–H scission is generally disfavored ( $\Lambda_{\text{sol}} > 0$ ). This  $\Lambda_{\text{sol}}$  dependency on the reaction type is in agreement with that computed using the report by Behtash et al.<sup>12–14</sup> With the loss of the most solvated functional group, the

# Chapter 5. Group Additivity for Aqueous Phase Thermochemical Properties of Alcohols on Pt(111)

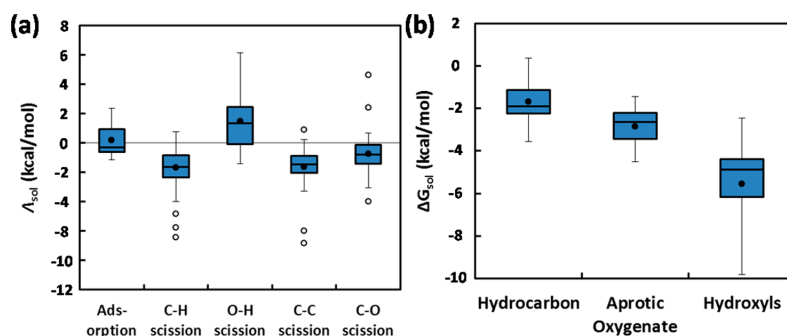


**Figure 3.** Box plot for the change of (a) the Gibbs energy of a reaction upon solvation  $\Lambda_{\text{sol}}$  (see text for definition) and (b) the solvation Gibbs energy  $\Delta G_{\text{sol}}$  of each species using DFT in the ethanol reforming reaction network (without water–gas shift reactions and species). Black dots and white dots represent mean and outliers, respectively. The box represents the second and third quartiles while the whisker represents the first and fourth quartiles. Outliers are at least 1.5 times the box range (between the second and third quartile) from the edge of the box.

O–H scission leads to a net loss in solvation, explaining why such a reaction is less likely in water than at the metal/gas-phase interface. This thermodynamic observation contrasts with our previous kinetic study using microsolvation, where the O–H breaking was found to be slightly accelerated by the presence of a water molecule.<sup>93</sup> On the other hand, it agrees with the study of Lopez and co-workers, who have employed implicit solvation in combination with some explicit water molecules.<sup>94</sup> In the absence of a detailed study at an explicit water/Pt(111) interface, it is not possible to assert that one or the other study captures the essential effect. The outliers identified in Figure 3a correspond to reactions where the solvation effect between reactants and products is the most unbalanced. For instance, the three outliers of the C–O scission all correspond to reactions that generate the OH fragment. Two reactions are strongly disfavored at the water-metal interface, due to a strong solvation of the reactants (CCOH,  $\Delta G_{\text{sol}} = -9.8$  kcal/mol and COH,  $\Delta G_{\text{sol}} = -7.9$  kcal/mol) that exhibit an OH bond that is pointing toward the solvent. Conversely, the CH<sub>3</sub>COH fragmentation is favored at the water/Pt interface, since this species is only weakly solvated when adsorbed on Pt(111) ( $\Delta G_{\text{sol}} = -2.5$  kcal/mol), with a OH bond that points downward.

In summary, most of the steps along the ethanol reforming process are favored by the presence of the water solvent except O–H scission (disfavored) and adsorption (neutral). The solvation Gibbs energy of an adsorbate can be related to the presence of a hydroxyl group and more precisely to its orientation: when an OH bond points toward the bulk water, the corresponding adsorbate is particularly well solvated. This aspect allows rationalizing and predicting the effect of water on most elementary steps.

**Group Additivity Schemes.** In this section, we present a group additivity scheme to predict  $\Delta G_{\text{f}(gp)}$  and  $\Delta G_{\text{f}(aq)}$ . These two quantities are computed using the equations described in the Methods. The group additivity scheme for these quantities follows the strategy of Benson’s original group additivity. Groups are given as  $A(B)_b(C)_c\dots$ , where A is a group center, B and C are group peripherals, and  $b$  and  $c$  are the numbers of connectivity to the B and C group peripherals. A, B, and C are typically an atom and sometimes a group of atoms. A, B, and C are further categorized by their hybridization. For example, C<sub>=</sub> indicates a carbon with a double bonded neighbor. Also, if the bond order between group center and group peripherals is higher than single bond, the bond order is described (e.g., A(=B) for A

double bonded to B). Every atom must be accounted once as a group center with the exception of hydrogen.

Previously, we have extended this formulation to the adsorbate on surface.<sup>56,57,95</sup> In these schemes, the valence electrons covalently interacting with the surface electrons are denoted as (Pt)<sub>x</sub> group peripheral. For example, the group C(H)(Pt)<sub>2</sub>(O) contains a carbon central atom single-bonded to peripheral groups, a hydrogen and an oxygen, and has 2 valence electrons interacting with the surface denoted as (Pt)<sub>2</sub>. This scheme does not distinguish whether the central carbon sits on an atop, bridge, or hollow site; thus, the scheme only requires adsorbates’ connectivity to compute their energy. We also adopt ring-strain correction as implemented in a previous study.<sup>56</sup> These corrections account for the strain of the ring formed by surface atoms and adsorbate atoms. For example, a ring is formed when two connected carbons are bonded to two surface atoms, forming Pt–C–C–Pt ring where two Pt atoms are connected. Additionally, we introduce 16 pair corrections that describe the valence electrons of pairs of central atoms, e.g., C(Pt)<sub>3</sub>C(Pt)<sub>3</sub>, C(Pt)<sub>3</sub>C(Pt)<sub>2</sub>, C(Pt)<sub>3</sub>C(Pt), C(Pt)<sub>2</sub>C(Pt)<sub>2</sub>, and so on. These corrections account for the partial  $\pi$ -mode interaction between the two surface-bound organic atoms. Previous studies<sup>58,96</sup> have shown that when two connected atoms are bonded to the surface, the bond between two connected atoms remains partially conjugated whereas we previously assumed that the bond between two atoms are single bonds. These inadequately defined bond order causes an error as the group additivity relies on transferable electron spatial density profile of the homologous groups between molecules. Thus, groups accounting for conjugation are essential to the group additivity scheme.<sup>58</sup> These corrections improve the model significantly (reduce the MeanAE in  $\Delta G_{\text{f}(gp)}$  from 4.6 to 3.3 kcal/mol using 10-fold cross-validation). Additionally, we add a group specific to an outlier, CCOH. CCOH has a unique structure that leads to high deviation for  $\Delta G_{\text{sol}}$ . This correction improves the MaxAE of  $\Delta G_{\text{sol}}$  from 6.4 to 5.3 kcal/mol.

Following the formulation described above, the model results in total of 82 groups/corrections. The effective rank of this model is 75; i.e., it is rank-deficient. Five of seven linearly dependent descriptors are C(Pt)<sub>3</sub>C(Pt)<sub>3</sub>, OC, OC(Pt)<sub>1</sub>, OC(Pt)<sub>2</sub>, and OC(Pt)<sub>3</sub>, which are part of the new corrections introduced in this work. Since these corrections are already implicitly accounted by the scheme, we remove these corrections. The last two rank deficiency comes from the C<sub>=</sub>(CO)(C<sub>=</sub>)(H) group’s depend-

ence to CO(C<sub>=</sub>)(H), and O(CO)(H) group's dependence to CO(O)(Pt) (determined using reduced row echelon form). These groups are found in gas/solute molecules, which are not the focus of this study, and the related methods have been previously developed extensively, thus we combine these groups together as a single multigroup. The list of group centers and peripherals as well as corrections and unique groups are summarized in Table 1, and their values are listed in the Supporting Information.

**Table 1.** List of group centers and peripherals that constitute groups (See manuscript for group description), corrections and unique groups

group centers	group peripherals	corrections/outlier correction
C	C	corrections:
CO <sup>a</sup>	CO <sup>a</sup>	C(Pt) <sub>x</sub> , C(Pt) <sub>x</sub>
O	O	C(Pt) <sub>x</sub> , O(Pt) <sub>x</sub>
C <sub>=</sub>	C <sub>=</sub>	(5 linearly dependent corrections removed)
C <sub>≡</sub>	C <sub>≡</sub>	surface ring strain <sup>56</sup>
	H	outlier correction:
	Pt	CCOH (chemisorbed)

<sup>a</sup>CO indicates a C=O carbonyl group.

**Model Validation.** The predictive accuracy of the group additivity model is assessed using *k*-fold cross validation as described in the computational details.<sup>85,86</sup> Parts a and b of Figure 4 show the average of predicted values using the group

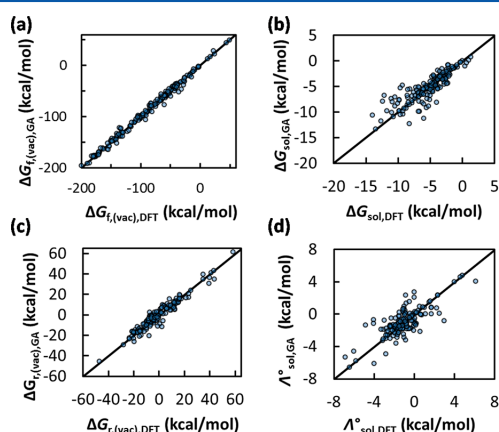


**Figure 4.** Parity plot between 10-fold cross-validation computed prediction and DFT data for (a) Gibbs free energy of formation,  $\Delta G_{f,(\text{gp})}$ , (b) Gibbs free energy of solvation,  $\Delta G_{\text{sol}}$ , (c) Gibbs free energy of reaction,  $\Delta G_{r,(\text{vac})}$ , and (d) the change of reaction energies upon solvation,  $\Lambda_{\text{sol}}$ , as defined in eqs 14 and 15. A total of 151 reactions of the ethanol reaction network are considered (see Supporting Information for the details).

additivity models vs the DFT computed  $\Delta G_{f,(\text{gp})}$  and  $\Delta G_{\text{sol}}$ . Cross validation reveals a reasonable MeanAE in  $\Delta G_{f,(\text{gp})}$  of 3.3 kcal/mol, and the MaxAE of 16.5 kcal/mol as shown in Table 2. The large errors are attributed to unaccounted binding modes (e.g., adsorption conformation of polyols). Our previous group additivity model has shown that including binding modes' information to the group descriptors results in large improve-

**Table 2.** Mean and Maximum (Max) Absolute Errors (AEs) and Root Mean Square Error (RMSE) for 10-Fold Cross-Validation of Thermodynamic Properties in kcal/mol

properties	MeanAE	MaxAE	RMSE
$\Delta G_{f,(\text{gp})}$	3.3	16.5	4.8
$\Delta G_{r,(\text{aq})}$	3.3	17.5	4.8
$\Delta G_{\text{sol}}$	1.0	5.4	1.6
$\Delta G_{r,(\text{gp})}$	2.9	13.8	4.0
$\Delta G_{r,(\text{aq})}$	2.8	15.1	3.9
$\Lambda_{\text{sol}}$	0.9	3.8	1.2

ment of the cross-validation error.<sup>58</sup> However, including these unaccounted binding modes requires a significantly larger data set. Since the main utility of the group additivity is to rapidly screen large reaction networks before computing the most promising intermediates at the DFT level, a huge computational effort is not justified. The MeanAE and MaxAE for  $\Delta G_{\text{sol}}$  are as small as 1.0 and 5.4 kcal/mol, respectively. Importantly, the MeanAE is within chemical accuracy; therefore, the solvation free energy scheme from group additivity provides a good first approximation to estimate the thermochemistry.

We also assess the model's predictive ability for the (151) reaction free energies in the ethanol steam reforming reaction network.<sup>87</sup> Specifically, we compare the Gibbs free energy of reaction in gas-phase,  $\Delta G_{r,(\text{gp})}$ , and the change in Gibbs free energy of reaction upon solvation,  $\Lambda_{\text{sol}}$ .

Parts c and d of Figure 4 show the parity plot of the group additivity computed values vs the DFT-derived  $\Delta G_{r,(\text{gp})}$  and  $\Lambda_{\text{sol}}$ . The MeanAE and MaxAE for  $\Delta G_{r,(\text{gp})}$  are 2.9 and 13.8 kcal/mol, which are smaller than those for  $\Delta G_{f,(\text{gp})}$ . Considering that the number of groups constituting a molecule is typically larger than the number of groups changing in a reaction, the variance is likely smaller for the reaction energy, explaining the smaller error. The MeanAE and MaxAE for  $\Lambda_{\text{sol}}$  are reasonable at 0.9 and 3.8 kcal/mol, respectively. However, as can be seen in Figure 4d, the parity plot is not perfect, i.e., the predicted change of solvation energies along a reaction is not very well correlated to the DFT data. One of the main issues is the evidenced reorientation of OH-groups discussed above: in the GA, the orientation of the OH group is not accounted for, implying that these subtle effects cannot be investigated by the present group additivity scheme. However, since the Gibbs reaction energy prediction is rather accurate, the main goal of the GA is still achieved: rapid prediction of various reaction energies at a solvated metal surface.

For a further assessment of the quality of the solvation free energy group additivity, we compare the trends we obtained in Figure 3 with the DFT calculations with the trends we obtain using our group additivity scheme (Figure S3 in Supporting Information). Overall, the solvation free energy group additivity captures the trend very well. The mean and median between the DFT and the group additivity are close, signifying that our model captures the general dependency on the reaction type and functional groups. However, the boxes and whiskers are tighter for the model than the DFT (i.e., variance is not captured by the model). Especially, the model computed  $\Lambda_{\text{sol}}$  for O–H scission and  $\Delta G_{\text{sol}}$  for Hydroxyls have significantly lower variance than the DFT-computed values. Future work will be based on information from explicit water simulations and include heterolytic bond breakings involving protons, which may be important in biomass conversion. These improvements would, ultimately, allow to investigate the pH dependence of reaction schemes at the group additivity level.



# Chapter 5. Group Additivity for Aqueous Phase Thermochemical Properties of Alcohols on Pt(111)

## CONCLUSIONS

The impact of an implicit solvent on adsorption of alcohols on the Pt(111) surface has first been investigated by DFT computations. We evidenced only minor changes in the geometries upon solvation, with the reorientation of an O–H bond pointing toward the surface in vacuum and being more stable pointing into the solvent being the rare exception. Examination of the ethanol reforming reaction network reveals, however, that equilibrium constants of surface reactions change significantly in solvent depending on the reaction type. In aqueous environment, C–H scission is slightly favored as the oxygen group of the oxygenate is raised toward bulk water, whereas O–H scission is thermodynamically disfavored as the oxygen binds to the surface which decreases the oxygen–water interaction. In order to cut down the computational expense of such studies, we have developed a simple group additivity scheme for the Gibbs free energy of linear alcohols at the Pt(111) water interface by computing the thermodynamic properties of 200 adsorbates and gaseous species using DFT and an implicit solvent. The 10-fold cross-validation yields a MeanAE for the Gibbs free energy of formation and the Gibbs free energy of solvation of 3.3 and 1.0 kcal/mol, respectively, and smaller error for reaction energies (MeanAE = 2.8 kcal/mol). Despite severe approximations regarding the entropy of adsorption, this development allows addressing large and complex reaction networks, e.g., the hydro-deoxygenations of polyols such as glycerol, erythritol, or even sorbitol, in order to narrow down the most likely reaction routes, which then can be studied by DFT computations. Furthermore, the corresponding solvent effects can be improved in order to refine the subtle enthalpy–entropy balance at the solid–liquid interface.

## ASSOCIATED CONTENT

### Supporting Information

The Supporting Information is available free of charge on the ACS Publications website at DOI: 10.1021/acs.jpcc.7b07340.

Supplementary figures for assumptions made, PCM method validation, and the ethanol reforming reaction network information (PDF)

DFT energies and vibrational frequencies for reference and training set, as well as their groups, and group values (XLSX)

DFT structures (xyz format) for the data set (ZIP)

## AUTHOR INFORMATION

### Corresponding Authors

\*(D.G.V.) E-mail: vlachos@udel.edu. Telephone: 1-302-831-2830.

\*(S.N.S.) E-mail: stephan.steinmann@ens-lyon.fr. Telephone: 0033-472-72-8155.

\*(P.S.) E-mail: sautet@ucla.edu.

### ORCID

Carine Michel: 0000-0002-4501-7194

Stephan N. Steinmann: 0000-0002-2777-356X

Philippe Sautet: 0000-0002-8444-3348

### Notes

The authors declare no competing financial interest.

We have built a python package to find group additivity descriptors and compute thermodynamic properties, available at <https://github.com/vlachosgroup>.

## ACKNOWLEDGMENTS

G.H.G. is grateful to Dr. Glen R. Jenness for the paper writing improvement. We acknowledge Angela Norton for performing COSMO-SAC calculations (Figure S2 in Supporting Information). G.H.G. developed the group additivity model, B.S. performed DFT calculations, D.G.V., P.S., C.M., and S.N.S. conceptualized the research and advised the research direction. This research was supported by the NSF under Grant No. CHE-1415828. This work benefited from the support of the project MuSIC ANR-14-CE06-0030 of the French National Research Agency (ANR). This work was granted access to the HPC resources of CINES and IDRIS under the allocation A0010810119 and x2015080609 made by GENCI. Computational resources from the Pôle Scientifique de Modélisation Numérique (PSMN) at ENS Lyon are greatly acknowledged as well.

## REFERENCES

- (1) Huber, G. W.; Shabaker, J. W.; Dumesic, J. A. Raney Ni–Sn Catalyst for H<sub>2</sub> Production from Biomass-Derived Hydrocarbons. *Science* **2003**, *300*, 2075–2077.
- (2) Dickerson, T.; Soria, J. Catalytic Fast Pyrolysis: A Review. *Energies* **2013**, *6*, 514–538.
- (3) Laurent, E.; Delmon, B. Influence of Water in the Deactivation of a Sulfided NiMoγ-Al<sub>2</sub>O<sub>3</sub> Catalyst During Hydrodeoxygenation. *J. Catal.* **1994**, *146*, 281–291.
- (4) Beerthuis, R.; Rothenberg, G.; Shiju, N. R. Catalytic Routes Towards Acrylic Acid, Adipic Acid and ε-Caprolactam Starting from Biorenewables. *Green Chem.* **2015**, *17*, 1341–1361.
- (5) Yan, N.; Zhao, C.; Luo, C.; Dyson, P. J.; Liu, H.; Kou, Y. One-Step Conversion of Cellobiose to C6-Alcohols Using a Ruthenium Nanocluster Catalyst. *J. Am. Chem. Soc.* **2006**, *128*, 8714–8715.
- (6) Xiao, C.-x.; Cai, Z.-p.; Wang, T.; Kou, Y.; Yan, N. Aqueous-Phase Fischer–Tropsch Synthesis with a Ruthenium Nanocluster Catalyst. *Angew. Chem., Int. Ed.* **2008**, *47*, 746–749.
- (7) Cortright, R. D.; Davda, R. R.; Dumesic, J. A. Hydrogen from Catalytic Reforming of Biomass-Derived Hydrocarbons in Liquid Water. *Nature* **2002**, *418*, 964–967.
- (8) Lee, J.; Xu, Y.; Huber, G. W. High-Throughput Screening of Monometallic Catalysts for Aqueous-Phase Hydrogenation of Biomass-Derived Oxygenates. *Appl. Catal., B* **2013**, *140–141*, 98–107.
- (9) Wang, Y.; Yao, J.; Li, H.; Su, D.; Antonietti, M. Highly Selective Hydrogenation of Phenol and Derivatives over a Pd@Carbon Nitride Catalyst in Aqueous Media. *J. Am. Chem. Soc.* **2011**, *133*, 2362–2365.
- (10) Wertz, D. H. Relationship between the Gas-Phase Entropies of Molecules and Their Entropies of Solvation in Water and 1-Octanol. *J. Am. Chem. Soc.* **1980**, *102*, 5316–5322.
- (11) Yoon, Y.; Rousseau, R.; Weber, R. S.; Mei, D.; Lercher, J. A. First-Principles Study of Phenol Hydrogenation on Pt and Ni Catalysts in Aqueous Phase. *J. Am. Chem. Soc.* **2014**, *136*, 10287–10298.
- (12) Behtash, S.; Lu, J.; Mamun, O.; Williams, C. T.; Monnier, J. R.; Heyden, A. Solvation Effects in the Hydrodeoxygenation of Propanoic Acid over a Model Pd(211) Catalyst. *J. Phys. Chem. C* **2016**, *120*, 2724–2736.
- (13) Behtash, S.; Lu, J.; Walker, E.; Mamun, O.; Heyden, A. Solvent Effects in the Liquid Phase Hydrodeoxygenation of Methyl Propionate over a Pd(111) Catalyst Model. *J. Catal.* **2016**, *333*, 171–183.
- (14) Behtash, S.; Lu, J.; Faheem, M.; Heyden, A. Solvent Effects on the Hydrodeoxygenation of Propanoic Acid over Pd(111) Model Surfaces. *Green Chem.* **2014**, *16*, 605–616.
- (15) Desai, S. K.; Neurock, M. First-Principles Study of the Role of Solvent in the Dissociation of Water over a Pt–Ru Alloy. *Phys. Rev. B: Condens. Matter Mater. Phys.* **2003**, *68*, 075420.
- (16) Steinmann, S. N.; Sautet, P.; Michel, C. Solvation Free Energies for Periodic Surfaces: Comparison of Implicit and Explicit Solvation Models. *Phys. Chem. Chem. Phys.* **2016**, *18*, 31850–31861.

- (17) Taylor, C. D.; Neurock, M. Theoretical Insights into the Structure and Reactivity of the Aqueous/Metal Interface. *Curr. Opin. Solid State Mater. Sci.* **2005**, *9*, 49–65.
- (18) Akpa, B. S.; D'Agostino, C.; Gladden, L. F.; Hindle, K.; Manyar, H.; McGregor, J.; Li, R.; Neurock, M.; Sinha, N.; Stitt, E. H.; Weber, D.; Zeitler, J. A.; Rooney, D. W. Solvent Effects in the Hydrogenation of 2-Butanone. *J. Catal.* **2012**, *289*, 30–41.
- (19) Liu, J.; Cao, X.-M.; Hu, P. Density Functional Theory Study on the Activation of Molecular Oxygen on a Stepped Gold Surface in an Aqueous Environment: a New Approach for Simulating Reactions in Solution. *Phys. Chem. Chem. Phys.* **2014**, *16*, 4176–4185.
- (20) Carter, E. A.; Ciccotti, G.; Hynes, J. T.; Kapral, R. Constrained Reaction Coordinate Dynamics for the Simulation of Rare Events. *Chem. Phys. Lett.* **1989**, *156*, 472–477.
- (21) Sprik, M.; Ciccotti, G. Free Energy from Constrained Molecular Dynamics. *J. Chem. Phys.* **1998**, *109*, 7737–7744.
- (22) Jindal, G.; Warshel, A. Exploring the Dependence of QM/MM Calculations of Enzyme Catalysis on the Size of the QM Region. *J. Phys. Chem. B* **2016**, *120*, 9913–9921.
- (23) Bellarosa, L.; García-Muelas, R.; Revilla-López, G.; López, N. Diversity at the Water–Metal Interface: Metal, Water Thickness, and Confinement Effects. *ACS Cent. Sci.* **2016**, *2*, 109–116.
- (24) Desai, S. K.; Pallassana, V.; Neurock, M. A Periodic Density Functional Theory Analysis of the Effect of Water Molecules on Deprotonation of Acetic Acid over Pd(111). *J. Phys. Chem. B* **2001**, *105*, 9171–9182.
- (25) Michel, C.; Zaffran, J.; Ruppert, A. M.; Matras-Michalska, J.; Jedrzejczyk, M.; Grams, J.; Sautet, P. Role of Water in Metal Catalyst Performance for Ketone Hydrogenation: a Joint Experimental and Theoretical Study on Levulinic Acid Conversion into Gamma-Valerolactone. *Chem. Commun.* **2014**, *50*, 12450–12453.
- (26) Cao, D.; Lu, G. Q.; Wieckowski, A.; Wasileski, S. A.; Neurock, M. Mechanisms of Methanol Decomposition on Platinum: A Combined Experimental and *ab Initio* Approach. *J. Phys. Chem. B* **2005**, *109*, 11622–11633.
- (27) Zope, B. N.; Hibbitts, D. D.; Neurock, M.; Davis, R. J. Reactivity of the Gold/Water Interface During Selective Oxidation Catalysis. *Science* **2010**, *330*, 74–78.
- (28) Faheem, M.; Heyden, A. Hybrid Quantum Mechanics/Molecular Mechanics Solvation Scheme for Computing Free Energies of Reactions at Metal–Water Interfaces. *J. Chem. Theory Comput.* **2014**, *10*, 3354–3368.
- (29) Mathew, K.; Sundaraman, R.; Letchworth-Weaver, K.; Arias, T. A.; Hennig, R. G. Implicit Solvation Model for Density-Functional Study of Nanocrystal Surfaces and Reaction Pathways. *J. Chem. Phys.* **2014**, *140*, 084106.
- (30) Faheem, M.; Suthirakun, S.; Heyden, A. New Implicit Solvation Scheme for Solid Surfaces. *J. Phys. Chem. C* **2012**, *116*, 22458–22462.
- (31) Garcia-Ratés, M.; López, N. Multigrid-Based Methodology for Implicit Solvation Models in Periodic DFT. *J. Chem. Theory Comput.* **2016**, *12*, 1331–1341.
- (32) Pliego, J. R.; Riveros, J. M. The Cluster–Continuum Model for the Calculation of the Solvation Free Energy of Ionic Species. *J. Phys. Chem. A* **2001**, *105*, 7241–7247.
- (33) Asthagiri, D.; Pratt, L. R.; Ashbaugh, H. S. Absolute Hydration Free Energies of Ions, Ion–Water Clusters, and Quasichemical Theory. *J. Chem. Phys.* **2003**, *119*, 2702–2708.
- (34) Bryantsev, V. S.; Diallo, M. S.; Goddard, W. A., III Calculation of Solvation Free Energies of Charged Solutes Using Mixed Cluster/Continuum Models. *J. Phys. Chem. B* **2008**, *112*, 9709–9719.
- (35) Wang, H.-F.; Liu, Z.-P. Formic Acid Oxidation at Pt/H<sub>2</sub>O Interface from Periodic DFT Calculations Integrated with a Continuum Solvation Model. *J. Phys. Chem. C* **2009**, *113*, 17502–17508.
- (36) Steinmann, S. N.; Michel, C.; Schwiedernoch, R.; Sautet, P. Impacts of Electrode Potentials and Solvents on the Electroreduction of CO<sub>2</sub>: a Comparison of Theoretical Approaches. *Phys. Chem. Chem. Phys.* **2015**, *17*, 13949–13963.
- (37) Wang, P.; Steinmann, S. N.; Fu, G.; Michel, C.; Sautet, P. Key Role of Anionic Doping for H<sub>2</sub> Production from Formic Acid on Pd(111). *ACS Catal.* **2017**, *7*, 1955–1959.
- (38) Sutton, J. E.; Vlachos, D. G. Building Large Microkinetic Models with First-Principles' Accuracy at Reduced Computational Cost. *Chem. Eng. Sci.* **2015**, *121*, 190–199.
- (39) Benson, S. W.; Buss, J. H. Additivity Rules for the Estimation of Molecular Properties. Thermodynamic Properties. *J. Chem. Phys.* **1958**, *29*, 546–572.
- (40) Eigenmann, H. K.; Golden, D. M.; Benson, S. W. Revised Group Additivity Parameters for the Enthalpies of Formation of Oxygen-Containing Organic Compounds. *J. Phys. Chem.* **1973**, *77*, 1687–1691.
- (41) Stein, S. E.; Golden, D. M.; Benson, S. W. Predictive Scheme for Thermochemical Properties of Polycyclic Aromatic Hydrocarbons. *J. Phys. Chem.* **1977**, *81*, 314–317.
- (42) Benson, S. W. Thermochemistry and Kinetics of Sulfur-Containing Molecules and Radicals. *Chem. Rev.* **1978**, *78*, 23–35.
- (43) Willems, P. A.; Froment, G. F. Kinetic Modeling of the Thermal Cracking of Hydrocarbons. 1. Calculation of Frequency Factors. *Ind. Eng. Chem. Res.* **1988**, *27*, 1959–1966.
- (44) Willems, P. A.; Froment, G. F. Kinetic Modeling of the Thermal Cracking of Hydrocarbons. 2. Calculation of Activation Energies. *Ind. Eng. Chem. Res.* **1988**, *27*, 1966–1971.
- (45) Martinis, J. M.; Froment, G. F. Alkylation on Solid Acids. Part 2. Single-Event Kinetic Modeling. *Ind. Eng. Chem. Res.* **2006**, *45*, 954–967.
- (46) Luria, M.; Benson, S. W. Heat Capacities of Liquid Hydrocarbons. Estimation of Heat Capacities at Constant Pressure as a Temperature Function, Using Additivity Rules. *J. Chem. Eng. Data* **1977**, *22*, 90–100.
- (47) Constantinou, L.; Gani, R.; O'Connell, J. P. Estimation of the Acentric Factor and the Liquid Molar Volume at 298 K Using a New Group Contribution Method. *Fluid Phase Equilib.* **1995**, *103*, 11–22.
- (48) Constantinou, L.; Gani, R. New Group Contribution Method for Estimating Properties of Pure Compounds. *AIChE J.* **1994**, *40*, 1697–1710.
- (49) Wu, D. T. Proceedings of the Fourth International Conference: Prediction of Viscosities of Liquid Mixtures by a Group Contribution Method. *Fluid Phase Equilib.* **1986**, *30*, 149–156.
- (50) Ihmels, E. C.; Gmehling, J. Extension and Revision of the Group Contribution Method GCVOL for the Prediction of Pure Compound Liquid Densities. *Ind. Eng. Chem. Res.* **2003**, *42*, 408–412.
- (51) Abrams, D. S.; Prausnitz, J. M. Statistical Thermodynamics of Liquid Mixtures: A New Expression for the Excess Gibbs Energy of Partly or Completely Miscible Systems. *AIChE J.* **1975**, *21*, 116–128.
- (52) Fredenslund, A.; Jones, R. L.; Prausnitz, J. M. Group-Contribution Estimation of Activity Coefficients in Nonideal Liquid Mixtures. *AIChE J.* **1975**, *21*, 1086–1099.
- (53) Chapman, W. G.; Gubbins, K. E.; Jackson, G.; Radosz, M. New Reference Equation of State for Associating Liquids. *Ind. Eng. Chem. Res.* **1990**, *29*, 1709–1721.
- (54) Lymperiadis, A.; Adjiman, C. S.; Galindo, A.; Jackson, G. A Group Contribution Method for Associating Chain Molecules Based on the Statistical Associating Fluid Theory (SAFT- $\gamma$ ). *J. Chem. Phys.* **2007**, *127*, 234903.
- (55) Kua, J.; Faglioni, F.; Goddard, W. A. Thermochemistry for Hydrocarbon Intermediates Chemisorbed on Metal Surfaces: CH<sub>n-m</sub>(CH<sub>3</sub>)<sub>m</sub> with n = 1, 2, 3 and m ≤ n on Pt, Ir, Os, Pd, Rh, and Ru. *J. Am. Chem. Soc.* **2000**, *122*, 2309–2321.
- (56) Saliccioli, M.; Edie, S. M.; Vlachos, D. G. Adsorption of Acid, Ester, and Ether Functional Groups on Pt: Fast Prediction of Thermochemical Properties of Adsorbed Oxygenates via DFT-Based Group Additivity Methods. *J. Phys. Chem. C* **2012**, *116*, 1873–1886.
- (57) Vorotnikov, V.; Wang, S.; Vlachos, D. G. Group Additivity for Estimating Thermochemical Properties of Furanic Compounds on Pd(111). *Ind. Eng. Chem. Res.* **2014**, *53*, 11929–11938.
- (58) Gu, G. H.; Vlachos, D. G. Group Additivity for Thermochemical Property Estimation of Lignin Monomers on Pt(111). *J. Phys. Chem. C* **2016**, *120*, 19234–19241.
- (59) Saliccioli, M.; Chen, Y.; Vlachos, D. G. Density Functional Theory-Derived Group Additivity and Linear Scaling Methods for

## Chapter 5. Group Additivity for Aqueous Phase Thermochemical Properties of Alcohols on Pt(111)

Prediction of Oxygenate Stability on Metal Catalysts: Adsorption of Open-Ring Alcohol and Polyol Dehydrogenation Intermediates on Pt-Based Metals. *J. Phys. Chem. C* **2010**, *114*, 20155–20166.

(60) Vorotnikov, V.; Vlachos, D. G. Group Additivity and Modified Linear Scaling Relations for Estimating Surface Thermochemistry on Transition Metal Surfaces: Application to Furanics. *J. Phys. Chem. C* **2015**, *119*, 10417–10426.

(61) Kresse, G.; Hafner, J. *Ab initio* Molecular Dynamics for Liquid Metals. *Phys. Rev. B: Condens. Matter Mater. Phys.* **1993**, *47*, 558–561.

(62) Perdew, J. P.; Burke, K.; Ernzerhof, M. Generalized Gradient Approximation Made Simple. *Phys. Rev. Lett.* **1996**, *77*, 3865–3868.

(63) Steinmann, S. N.; Corminboeuf, C. Comprehensive Benchmarking of a Density-Dependent Dispersion Correction. *J. Chem. Theory Comput.* **2011**, *7*, 3567–3577.

(64) Steinmann, S. N.; Corminboeuf, C. A Generalized-Gradient Approximation Exchange Hole Model for Dispersion Coefficients. *J. Chem. Phys.* **2011**, *134*, 044117.

(65) Blöchl, P. E. Projector Augmented-Wave Method. *Phys. Rev. B: Condens. Matter Mater. Phys.* **1994**, *50*, 17953–17979.

(66) Kresse, G.; Joubert, D. From Ultrasoft Pseudopotentials to the Projector Augmented-Wave Method. *Phys. Rev. B: Condens. Matter Mater. Phys.* **1999**, *59*, 1758–1775.

(67) Fishman, M.; Zhuang, H. L.; Mathew, K.; Dirschka, W.; Hennig, R. G. Accuracy of Exchange-Correlation Functionals and Effect of Solvation on the Surface Energy of Copper. *Phys. Rev. B: Condens. Matter Mater. Phys.* **2013**, *87*, 245402.

(68) Ben-Naim, A. *Solvation Thermodynamics*; Springer US: New York, 1987.

(69) Ben-Naim, A. *Statistical Thermodynamics for Chemists and Biochemists*; Springer US: New York, 1992.

(70) Cooper, J.; Ziegler, T. A Density Functional Study of SN2 Substitution at Square-Planar Platinum(II) Complexes. *Inorg. Chem.* **2002**, *41*, 6614–6622.

(71) Golze, D.; Iannuzzi, M.; Nguyen, M.-T.; Passerone, D.; Hutter, J. Simulation of Adsorption Processes at Metallic Interfaces: An Image Charge Augmented QM/MM Approach. *J. Chem. Theory Comput.* **2013**, *9*, 5086–5097.

(72) Schiros, T.; Andersson, K. J.; Pettersson, L. G. M.; Nilsson, A.; Ogasawara, H. Chemical Bonding of Water to Metal Surfaces Studied with Core-Level Spectroscopies. *J. Electron Spectrosc. Relat. Phenom.* **2010**, *177*, 85–98.

(73) Limmer, D. T.; Willard, A. P.; Madden, P.; Chandler, D. Hydration of Metal Surfaces Can be Dynamically Heterogeneous and Hydrophobic. *Proc. Natl. Acad. Sci. U. S. A.* **2013**, *110*, 4200–4205.

(74) Sakong, S.; Forster-Tonigold, K.; Groß, A. The Structure of Water at a Pt(111) Electrode and the Potential of Zero Charge Studied from First Principles. *J. Chem. Phys.* **2016**, *144*, 194701.

(75) Carlsson, J.; Åqvist, J. Absolute and Relative Entropies from Computer Simulation with Applications to Ligand Binding. *J. Phys. Chem. B* **2005**, *109*, 6448–6456.

(76) Natarajan, S. K.; Behler, J. Neural Network Molecular Dynamics Simulations of Solid-Liquid Interfaces: Water at Low-Index Copper Surfaces. *Phys. Chem. Chem. Phys.* **2016**, *18*, 28704–28725.

(77) Kelly, E.; Seth, M.; Ziegler, T. Calculation of Free Energy Profiles for Elementary Bimolecular Reactions by *ab Initio* Molecular Dynamics: Sampling Methods and Thermostat Considerations. *J. Phys. Chem. A* **2004**, *108*, 2167–2180.

(78) Price, D. L.; Halley, J. W. Molecular Dynamics, Density Functional Theory of the Metal–Electrolyte Interface. *J. Chem. Phys.* **1995**, *102*, 6603–6612.

(79) Lee, M.-S.; Peter McGrail, B.; Rousseau, R.; Glezakou, V.-A. Structure, Dynamics and Stability of Water/scCO<sub>2</sub>/Mineral Interfaces from *ab initio* Molecular Dynamics Simulations. *Sci. Rep.* **2015**, *5*, 14857.

(80) Cheng, T.; Xiao, H.; Goddard, W. A. Full Atomistic Reaction Mechanism with Kinetics for CO Reduction on Cu(100) from *ab initio* Molecular Dynamics Free-Energy Calculations at 298 K. *Proc. Natl. Acad. Sci. U. S. A.* **2017**, *114*, 1795–1800.

(81) Cantu, D. C.; Wang, Y.-G.; Yoon, Y.; Glezakou, V.-A.; Rousseau, R.; Weber, R. S. Heterogeneous Catalysis in Complex, Condensed Reaction Media. *Catal. Today* **2017**, *289*, 231–236.

(82) Schravendijk, P.; van der Vegt, N.; Delle Site, L.; Kremer, K. Dual-Scale Modeling of Benzene Adsorption onto Ni(111) and Au(111) Surfaces in Explicit Water. *ChemPhysChem* **2005**, *6*, 1866–1871.

(83) Li, X.; Ågren, H. Molecular Dynamics Simulations Using a Capacitance–Polarizability Force Field. *J. Phys. Chem. C* **2015**, *119*, 19430–19437.

(84) Spohr, E. Computer simulation of the water/platinum interface. *J. Phys. Chem.* **1989**, *93*, 6171–6180.

(85) Bengio, Y.; Grandvalet, Y. No Unbiased Estimator of the Variance of K-Fold Cross-Validation. *J. Mach. Learn. Res.* **2004**, *5*, 1089–1105.

(86) Kohavi, R. A Study of Cross-Validation and Bootstrap for Accuracy Estimation and Model Selection. In *Proceedings of the 14th international joint conference on Artificial intelligence*; Morgan Kaufmann Publishers Inc.: Montreal, Quebec, Canada, 1995; Vol. 2, pp 1137–1143.

(87) Sutton, J. E.; Panagiotopoulou, P.; Verykios, X. E.; Vlachos, D. G. Combined DFT, Microkinetic, and Experimental Study of Ethanol Steam Reforming on Pt. *J. Phys. Chem. C* **2013**, *117*, 4691–4706.

(88) Rangarajan, S.; Bhan, A.; Daoutidis, P. Language-oriented rule-based reaction network generation and analysis: Applications of RING. *Comput. Chem. Eng.* **2012**, *46*, 141–152.

(89) Rangarajan, S.; Bhan, A.; Daoutidis, P. Language-oriented rule-based reaction network generation and analysis: Description of RING. *Comput. Chem. Eng.* **2012**, *45*, 114–123.

(90) Kabsch, W. A Solution for the Best Rotation to Relate Two Sets of Vectors. *Acta Crystallogr., Sect. A: Cryst. Phys., Diffr., Theor. Gen. Crystallogr.* **1976**, *32*, 922–923.

(91) Walker, M. W.; Shao, L.; Volz, R. A. Estimating 3-D Location Parameters Using Dual Number Quaternions. *CVGIP: Image Understanding* **1991**, *54*, 358–367.


(92) Kromann, J. C.; Steinmann, C.; Iarsbratholm, a.; Lauritzen, K. P. *RMSD: Small Release Update*; 2016 10.5281/zenodo.46697.

(93) Zaffran, J.; Michel, C.; Delbecq, F.; Sautet, P. Towards More Accurate Prediction of Activation Energies for Polyalcohol Dehydrogenation on Transition Metal Catalysts in Water. *Catal. Sci. Technol.* **2016**, *6*, 6615–6624.

(94) García-Ratés, M.; García-Muelas, R.; López, N. Solvation Effects on Methanol Decomposition on Pd(111), Pt(111), and Ru(0001). *J. Phys. Chem. C* **2017**, *121*, 13803–13809.

(95) Saliccioli, M.; Stamatakis, M.; Caratzoulas, S.; Vlachos, D. G. A Review of Multiscale Modeling of Metal-Catalyzed Reactions: Mechanism Development for Complexity and Emergent Behavior. *Chem. Eng. Sci.* **2011**, *66*, 4319–4355.

(96) Bader, R. F. W.; Bayles, D. Properties of Atoms in Molecules: Group Additivity. *J. Phys. Chem. A* **2000**, *104*, 5579–5589.



## **6 Solvation free energies for periodic surfaces: comparison of implicit and explicit solvation models**

The solvation at the metal/liquid interface is experimentally extremely hard to measure. Therefore, essentially no experimental benchmark data exists that would permit to assess the accuracy of the implicit solvent models on wetting surfaces. Given that the implicit solvent models rely on electrostatic considerations i.e., polarization of the solute and the modification of the electrostatic interactions due to dielectric screening, it is questionable that they accurately depict the solvation at metal/water interfaces, where water benefits from (weak) chemisorption, such as on the platinum group metal surfaces. Hence, we suspect that the solvation effects predicted by the implicit solvent are not strong enough. However, since neither experimental nor theoretical benchmark values are available, no definite answer can be provided. The present chapter presents a scheme that efficiently combines quantum mechanical computations for the adsorbate and metal surface with a molecular mechanics description of the solvent. This scheme is used to determine solvation energies at the metal/liquid interface. The strength of the approach is that it can be systematically improved from a level which is practically equivalent to the implicit solvent (weak water/metal interaction as in the current chapter) to a true benchmark level, where the interaction of the solvent is treated at the quantum mechanical level through resampling techniques.







Cite this: *Phys. Chem. Chem. Phys.*,  
2016, **18**, 31850

## Solvation free energies for periodic surfaces: comparison of implicit and explicit solvation models<sup>†‡</sup>

Stephan N. Steinmann,<sup>\*a</sup> Philippe Sautet<sup>ab</sup> and Carine Michel<sup>a</sup>

The evaluation of solvation energies is a great challenge. We focus here on an organic molecule chemisorbed at a metal–liquid interface, as a prototypical system, essential in tribology, electrochemistry and heterogeneous catalysis. We compare an established implicit solvation scheme with a strategy based on molecular mechanics (MM) free energy perturbation (FEP) seeded by QM computations. First, we benchmark the approaches against experimental hydration energies of standard (organic) molecules and find acceptable errors in the order of 0.06 eV (1.3 kcal mol<sup>-1</sup>). Then, the impact of various parameters on the solvation energy of an adsorbate have been assessed on a typical system of interest, levulinic acid adsorbed at a Ru(0001)/water interface. We identify the need for dipole corrections or symmetric slabs when including solvation effects on metallic surfaces. The MM-FEP scheme is revealed to be as reliable as the implicit solvent for water. In the case of levulinic acid, both PCM and MM-FEP agree that the bulk solvation effect is not sufficient to change the adsorption mode from bidentate to mono-dentate, despite the fact that the COOH group is desolvated in the bidentate case. MM-FEP has the great advantage of being more easily generalized to other solvents and to be further improved which will be particularly useful to study solvent and (counter-)ion effects on interfacial reactions.

Received 13th June 2016,  
Accepted 27th October 2016

DOI: 10.1039/c6cp04094b

www.rsc.org/pccp

### 1 Introduction

The adsorption/desorption processes of organic molecules and ions at solid–liquid interfaces are key in heterogeneous catalysis, electrochemistry and tribology. The most extreme example is probably the electrochemical double layer where the electrolyte plays a major role in the competition between the adsorption of reactants and desorption of products. Another illustration is, as it has been shown particularly for biomass-related heterogeneous catalysis, that liquid water can modify significantly the catalytic activity of metallic supported catalysts compared to the more traditional gas-phase conditions.<sup>1–3</sup> However, first

principles modeling of reactions under such conditions is still a great challenge, especially when the adsorbate is chemisorbed, forming covalent bonds with the catalyst.

For around a decade, several attempts have been made to include the influence of water on (electro-)catalytic processes based on micro-solvation at the first principles based density functional theory (DFT) level. In a pioneering study of the de-protonation of acetic acid at water/Pd(111) interface, Neurock and co-workers included several water molecules in their surface model.<sup>4</sup> This approach was successfully used to assess the impact of water molecules on catalytic steps by several groups. The explicit solvent included varies from one or few selected water molecules<sup>5,6</sup> to ice-like water<sup>7–10</sup> or the optimization of several snapshots extracted from short *ab initio* molecular dynamics simulations.<sup>1,11</sup>

These schemes focus on surface reaction energies, *i.e.*, they allow a reasonably balanced description of the reaction energy of reactions of the type A\* → B\* where the asterisk indicates surface adsorbed species. However, the adsorption of reactants from solution and desorption of products back into solution is not easily accessible in schemes based on microsolvation.

Another strategy has been recently proposed by Heyden and co-workers.<sup>12</sup> In their implicit solvation model for surfaces (iSMS), reaction energies are computed with DFT applying periodic boundary conditions and solvation effects are estimated

<sup>a</sup> Univ Lyon, Ecole Normale Supérieure de Lyon, CNRS Université Lyon 1, Laboratoire de Chimie UMR 5182, 46 allée d'Italie, F-69364, Lyon, France.  
E-mail: stephan.steinmann@ens-lyon.fr

<sup>b</sup> Department of Chemical and Biomolecular Engineering, University of California, Los Angeles, Los Angeles, CA 90095, USA

<sup>†</sup> Computational resources generously provided by the mesocenter PSMN. This work was granted access to the HPC resources of CINES and IDRIS under the allocation 2014-080609 made by GENCI.

<sup>‡</sup> Electronic supplementary information (ESI) available: It contains the full list of molecules and their solvation free energies as computed herein. Data comparing FEP computations based on DFT with and without the dipole correction and the influence of the geometry on the adsorption energy is presented as well. The effect of changing the energy of adsorption of H<sub>2</sub>O on Ru(0001) on solvation energies is discussed. See DOI: 10.1039/c6cp04094b

## Chapter 6. Solvation free energies for periodic surfaces: comparison of implicit and explicit solvation models

View Article Online

Paper

PCCP

separately on large metallic clusters using a polarizable continuum model (PCM) for the solvent description.<sup>12</sup> PCM, which accounts for the electrostatic interaction between the solute and the solvent, is well-established in molecular chemistry<sup>13</sup> but less common for metal/liquid interfaces<sup>14,15</sup> since it has only recently become available to the public for periodic boundary conditions.<sup>16</sup> PCM can not describe any direct solvent effects and might be inaccurate for specific hydrogen bonds,<sup>17</sup> which makes the combination of micro-solvation with PCM particularly attractive.<sup>2,18–21</sup> In aprotic solvents, the non-electrostatic solvent effects can become dominating, which is particularly challenging for PCM.<sup>22</sup> In subsequent work, Heyden turned the iSMS approach into an explicit solvent scheme, dubbed eSMS.<sup>23</sup> Borrowing the idea of Yang and co-workers to optimize geometries on an approximate QM/MM free energy surface,<sup>24</sup> the cluster is no longer immersed in a PCM, but surrounded by explicit solvent, treated by molecular mechanics (MM). However, this is still in the perspective of surface reaction energies, rather than the assessment of adsorption/desorption events.

An explicit solvent molecular dynamics simulation coupled with Free Energy Perturbation, FEP,<sup>25</sup> is a “logical” improvement along these lines, as it describes the physics of hydrogen bonds, hydrophobic and cavitation effects and is equally well adapted for “isolated” molecules in solution and periodic surfaces. FEP is popular in bio-molecular simulations to compute free energy differences in order to obtain binding or solvation free energies of drugs.<sup>26</sup> Furthermore, enzyme catalysis<sup>27</sup> and solvation effects for organic reactions have been extensively studied within the framework of QM/MM-FEP, where reactions are described in the QM subsystem, while solvation is treated by MM.<sup>28</sup> The size (both in lateral and out of plane direction) of a solid–liquid interface limits the usefulness of “brute force” *ab initio* molecular dynamics. Furthermore, the reliable description of the evolution of the solvation shell requires extensive sampling that is clearly out of reach at a first principles level. Hence, we herein compare two more approximate methods to include the bulk solvent effect on any adsorption or surface reaction energy.

Our present development computes solvation energies in an ONIOM like<sup>29</sup> approximation avoiding any cluster computations and the associated problems of how to choose the size of these clusters or how to correct for the limited cluster size. More importantly, the periodicity allows us, in principle, to assess coverage effects, which is beyond the scope of eSMS. The system consists of two parts: the quantum mechanical subsystem (QM) and the solvent, which is treated by molecular mechanics (MM). The QM subsystem describes the interaction of the molecule with the surface or, in the case of molecules, describes relative energies of different conformations in vacuum. The interaction between the QM and the MM subsystem is evaluated at the MM level. We call this scheme, which is fully detailed in the next section, MM-FEP. We reserve the acronym QM/MM-FEP for a (self-consistent) electrostatic embedding approach, which is beyond the scope of the current paper. An implicit solvent is compared to the MM-FEP scheme. In particular, a polarized continuum model (PCM) has been implemented in the periodic boundary DFT code VASP under the name VASPsol by the group of Hennig.<sup>16</sup> The implicit

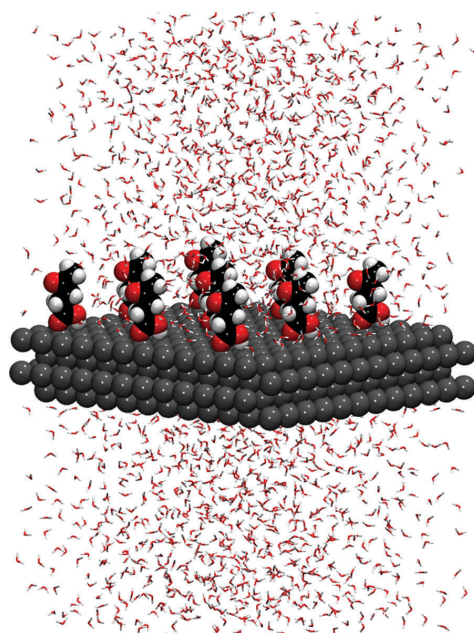


Fig. 1 Model of levulinic acid chemisorbed at the water/Ru(0001) interface. The solute (levulinic acid and the Ru atoms) is represented by van der Waals spheres and the water solvent molecules with lines. The depicted system corresponds to the unit cell for MM computations. The solute is kept in its PBE-dDsC chemisorption geometry; water is described with the TIP3P force field; the water/solute interaction is provided by a mixed TIP3P–QM–UFF description: the electrostatic interactions are TIP3P–QM and the Lennard–Jones interactions are TIP3P–UFF.

solvent also allows to incorporate bulk solvent effects on the QM geometry and electronic structure, which should improve the quality of the MM-FEP estimates.

After setting the stage by describing in detail the approximations involved in the assessed schemes, we first benchmark the implicit solvent (PCM) and our MM-FEP for hydration energies of small molecules. Then we assess the influence of solvation on the adsorption energy of an organic molecule on a metallic surface. We have chosen the adsorption of a bi-functional molecule, levulinic acid (LA), at the water/Ru(0001) interface as a typical test case (see Fig. 1). Levulinic acid is an essential platform molecule in cellulosic biomass valorization that can be converted to molecules of interest using Ru supported catalysts in water such as  $\gamma$ -valerolactone.<sup>30</sup> Two chemical functions can interact with either the solvent or the metal catalyst, namely a ketone and a carboxylic acid and the preferred adsorption mode might be impacted by the presence of water.

## 2 Theory

### 2.1 Decomposition of energies in solvent

In the context of continuum solvation models, it is customary to divide the influence of the solvent into two effects:<sup>18–20</sup> direct

participation in the reaction (or cooperative co-adsorption) and indirect influences. Hence, the Gibbs free energy of solvation ( $\Delta_s G$ ) is divided into two terms

$$\Delta_s G = \Delta_s G_{\text{direct}} + \Delta_s G_{\text{indirect}} \quad (1)$$

where we only introduce the approximation that solvent molecules can be classified as “strongly” or “weakly” bound. This distinction is not always obvious. However, a well defined scheme has been put forward that minimizes the introduced error by assessing the differential solvation energy induced by including each additional explicit solvent molecule.<sup>18</sup>

The direct participation occurs, for instance, in proton-shuttling mechanisms and requires explicit water molecules to be simulated on equal footing with the reactant, *i.e.*, at the explicit QM level. Care has to be taken in order to obtain meaningful results, first because of the number of solvent molecules needs to be chosen carefully<sup>18</sup> and second because the same standard state needs to be applied to the explicit and implicit solvent contributions.<sup>20</sup>

$\Delta_s G_{\text{indirect}}$  accounts for the remaining “indirect”, bulk solvation effects in the context of solvent embedded QM methods, this term can be further decomposed:

$$\Delta_s G_{\text{indirect}} = \Delta_s E_{\text{pol}} + \Delta_s G_{\text{inter}} + \Delta_s G_{\text{sps}} \quad (2)$$

where  $\Delta_s E_{\text{pol}}$  accounts for the polarization of the electronic wave function in the presence of a solvent.  $\Delta_s G_{\text{inter}}$ , on the other hand, represents the interaction energy between the (polarized) solute and the solvent and includes the solvent re-organization energy. Finally,  $\Delta_s G_{\text{sps}}$  accounts for non-trivial entropic terms due to translation, rotation and vibrations of the solute that differ between the gas- and solution-phase.

## 2.2 Polarizable continuum model

PCM refers here to the VASPsol implementation, where

$$\Delta_s G_{\text{inter}}^{\text{PCM}} = - \int dr \varepsilon(\vec{r}) \frac{|\nabla \phi(\vec{r})|^2}{8\pi} + \tau \int dr |\nabla S(\vec{r})| \quad (3)$$

The first term is a generalized Poisson equation for the electrostatic interaction and the second term accounts for cavitation energy.  $\varepsilon(\vec{r})$  represents the relative permittivity which depends on the electron density and  $\phi(\vec{r})$  is the total electrostatic potential.  $\tau$  is the surface tension and  $S(\vec{r})$  the cavity shape function, which is given by

$$S(r) = \frac{1}{2} \text{erfc} \left\{ \frac{\ln(\rho(r)/\rho_c)}{\sigma\sqrt{2}} \right\} \quad (4)$$

where  $\rho$  is the electron density and  $\rho_c$  is the isodensity value around which the cavity is created.  $\sigma$  modulates the diffuseness of the cavity around  $\rho_c$ , *i.e.*, how fast “inside” switches to “outside” as a function of the electron density. Due to the derivative of the cavity shape function, the cavitation energy is at the origin of significant numerical instabilities, especially when uniform grids are used which is the case for VASP. Since the cavitation energy usually only gives a small contribution (in the order of 0.05 eV), it is often neglected.<sup>16,31</sup> The model contains three empirical parameters ( $\rho_c$ ,  $\sigma$ ,  $\tau$ ) that have been

fitted to reproduce the reference data,<sup>32</sup> comparing the computed  $\Delta_s G_{\text{indirect}} = \Delta_s E_{\text{pol}} + \Delta_s G_{\text{inter}}$  with the experimental solvation Gibbs free energy. However, the last term in eqn (2), *i.e.*, the modification of the phase-space accessible to the solute when immersed in a solvent, is inaccessible within PCM.

## 2.3 Free energy perturbation

The aim of the presented MM-FEP scheme is to describe the same physics as the PCM but in a way that allows to systematically improve the scheme. Furthermore, the MM-FEP scheme can be applied to a wider range of systems with a similar expected accuracy, in particular also to (counter-)ion effects on interfacial reactions such as electrocatalysis and corrosion, which are tricky to describe by a PCM. At the end of this section we also discuss extensions for the present FEP that will improve its predictive power.

Free energy perturbation is a well established method and the interested reader is encouraged to consult the excellent reviews on the topic.<sup>26–28</sup> However, for sake of completeness, we give the most important equations in the following. The basic idea of the free energy perturbation methods is to obtain the free energy difference between state A and state B as a Boltzmann-weighted average between two potential energy functions  $U_0$  and  $U_0 + \Delta U$ , evaluated for a representative ensemble of system configurations. In practice, the size of the perturbation is reduced by doing the transformation step-wise, *i.e.*, the interval from 0 to 1 is divided into  $n$  “windows” and the difference between state A and B becomes a function of the coupling parameter  $\lambda$ :

$$U(\lambda) = U_0 + \Delta U(\lambda) \quad (5)$$

The coupling parameter runs from 0 (initial/reference state) to 1 (final state). Since molecules interacting with the environment at  $\lambda = 0$  and non-interacting at  $\lambda = 1$  fully contribute to the initial state but not to the final state, we refer to them as “disappearing”, while “appearing” molecules have the opposite characteristics. Typically, one assesses a free energy difference of solvation between two closely related molecules by gradually replacing the interactions of molecule A with the solvent by the interactions of molecule B with the solvent.

The free energy difference between the two states is computed as<sup>25</sup>

$$\Delta G = -k_B T \sum_i \ln \left\langle \exp \left[ -\frac{\Delta U(\lambda_{i+1}) - \Delta U(\lambda_i)}{k_B T} \right] \right\rangle_{\lambda_i} \quad (6)$$

where  $k_B$  is Boltzmann’s constant and the brackets indicate thermodynamic averages obtained from molecular dynamics or Monte Carlo simulations. In order to improve statistical accuracy, the simple-overlap sampling formula allows to combine two trajectories, one in the “forward” (fw) direction ( $0 \rightarrow 1$ ) and on in the “backward” (bw) direction ( $1 \rightarrow 0$ ). The corresponding free energy estimate is given by:

$$\Delta G = -k_B T \sum_i \ln \frac{\left\langle \exp \left[ -\frac{U(\lambda_{i_{\text{fw}}+1}) - U(\lambda_{i_{\text{fw}}})}{2k_B T} \right] \right\rangle_{\lambda_{i_{\text{fw}}}}}{\left\langle \exp \left[ -\frac{U(\lambda_{i_{\text{bw}}}) - U(\lambda_{i_{\text{bw}}-1})}{2k_B T} \right] \right\rangle_{\lambda_{i_{\text{bw}}}}} \quad (7)$$

where  $i$  goes from 1 to the total number of windows ( $N$ ),  $i_{fw}$  the  $i$ th window of the forward and  $i_{bw}$  is the  $(N - i + 1)$ th window of the backward run.

The key question for our simulations is the definition of  $U(\lambda)$ . To enable an efficient sampling of solvent phase-space, we describe the solvent by the classical TIP3P water model.<sup>33</sup> In all our simulations, this corresponds to  $U_0$  of eqn (5). The solute is described through the combination of QM derived point charges<sup>34</sup> and UFF Lennard-Jones parameters,<sup>35</sup> which are, to the best of our knowledge, the only ones available for most elements in the periodic table. Hence, the interaction between the solute and the solvent is provided by a mixed TIP3P-QM-UFF description: the electrostatic interactions are TIP3P-QM and the Lennard-Jones interactions are TIP3P-UFF. Following the study of Jorgensen and co-workers, the point charges for the QM regions are derived from slightly modified CM5 charges,<sup>34,36</sup> which initially have been developed to yield accurate gas-phase dipole moments and are used in the SM12 implicit solvation model.<sup>37</sup> Please note that the Lennard-Jones parameters for water are similar for TIP3P and UFF: the O–O equilibrium distance is virtually the same. The well depth of the O–O interaction in TIP3P includes the vdW interaction with the hydrogens, while UFF assigns individual contributions that sum up to about the same interaction energy. For the hydration energy of water we obtained similar values for a TIP3P water molecule and our UFF-CM5 water molecule: 0.26 and 0.24 eV in comparison to 0.27 eV, its experimental value.

A certain degree of “(self-)consistency” between the computation of the solute and the solvation free energy is desirable in order to capture the subtle coupling between  $\Delta_s E_{\text{pol}}$  and  $\Delta_s G_{\text{inter}}$ . However, only the dominant term ( $\Delta_s G_{\text{inter}}$ ) can be approximated by MM-FEP. On the other hand, the polarization component  $\Delta_s E_{\text{pol}}$  is naturally included in the self-consistent implementations of implicit solvent models. Hence, the two approaches can be combined, to benefit from the strengths of each method.

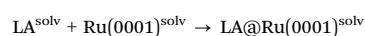
In contrast to the situation for organic molecules,<sup>38</sup> to the best of our knowledge no reliable, extremely fast semi-empirical electronic structure method is available for transition metal surfaces. Furthermore, in contrast to attempts to characterize the structural properties of interfacial water by classical molecular mechanics simulations,<sup>39</sup> low-cost force-field methods are generally not available for reactive adsorption events on metal surfaces, which are the main systems of interest herein. Therefore, the QM region is kept frozen during all our MM computations, very similar to what has been done for reactions in solution.<sup>33</sup>

Although our MM-FEP scheme relies on several approximations, it has the same merit as the PCM: it can be applied to all kinds of systems and, as we demonstrate hereafter, it provides a similar accuracy as the implicit solvent. The advantage is, however, that MM-FEP can be systematically improved and can “easily” account for all the relevant physics, especially when other solvents than pure water are involved. In particular, MM-FEP naturally accounts for the size of solvent molecules and ions (rather than an infinitesimal small point charges), which need to be included for more realistic simulations of

processes at electrode surfaces.<sup>40,41</sup> The improvements we are envisioning are, on the one hand, self-consistency between the QM and the MM computations (especially the polarization of the solute) and on the other hand an improved MM description, which ultimately would allow to include the changes in accessible phase-space of the solute, but for which reasonably accurate force fields are required.

## 2.4 Impact of the solvation on adsorption energies

Our target in this work is to assess the impact of the water solvent on the adsorption reaction of a given substrate (here levulinic acid, named LA in the following) on a surface (here Ru(0001)). This process can be described by the following reaction:



Since the free energy of adsorption in vacuum is much more accessible than the one in solvent, it is customary to write the Gibbs free energy of adsorption in solution  $\Delta_a G^{\text{solv}}$  as the following sum

$$\Delta_a G^{\text{solv}} = \Delta_a G^{\text{vac}} + \Delta_s \Delta_a G \quad (8)$$

where  $\Delta_a G^{\text{vac}}$  is the Gibbs free energy of adsorption in vacuum and  $\Delta_s \Delta_a G$  corresponds to the variation of the solvation Gibbs free energy ( $\Delta_s G$ ) along the adsorption process ( $\Delta_a$ ), *i.e.*, the solvation energy of the surface with the adsorbed molecule, minus the solvation energy of the separated molecule and surface (see Fig. 2). Note that we use the index “s” and “a” to symbol for a reaction energy ( $\Delta$ ) for the “solvation” and “adsorption” process, respectively.

Since we have no experimental benchmark data for the solvation effect on adsorption energies, we do not include any terms that affect PCM and MM-FEP to the same extent such as estimates for the modified available phase space ( $\Delta_s G_{\text{sps}}$ ). This implies that thermal effects (*e.g.*, entropy of adsorption) are neglected in the present approach, but could be included at least approximately by “standard” statistical mechanics formulas. More rigorous treatments than the ideal gas, harmonic oscillators exist, but necessitate significantly higher computational resources.<sup>42,43</sup> In short, in our study, we consider the approximation  $\Delta_a G^{\text{vac}} \approx \Delta_a E^{\text{vac}}$ .

In addition, as discussed in Section 2.1,  $\Delta_s G$  can be decomposed in direct and indirect terms, leading to

$$\Delta_s \Delta_a G = \Delta_s \Delta_a G_{\text{direct}} + \Delta_s \Delta_a G_{\text{indirect}} \quad (9)$$

We do not expect any significant direct solvent effects for the adsorption of levulinic acid on Ru(0001) and therefore do not include any explicit water molecules in the QM subsystem. In other words,  $\Delta_s \Delta_a G_{\text{direct}}$  is neglected. Hence, the Gibbs free energy of adsorption in solution considered in this article reads

$$\Delta_a G^{\text{solv}} = \Delta_a G^{\text{vac}} + \Delta_s \Delta_a G_{\text{indirect}} = \Delta_a E^{\text{vac}} + \Delta_s \Delta_a E_{\text{pol}} + \Delta_s \Delta_a G_{\text{inter}} \quad (10)$$

The first term can be easily computed based on periodic DFT computations and the strategies of refinements are well-known. In particular, we are using a dispersion corrected GGA functional, which has been shown to provide robust results.<sup>44</sup> The second

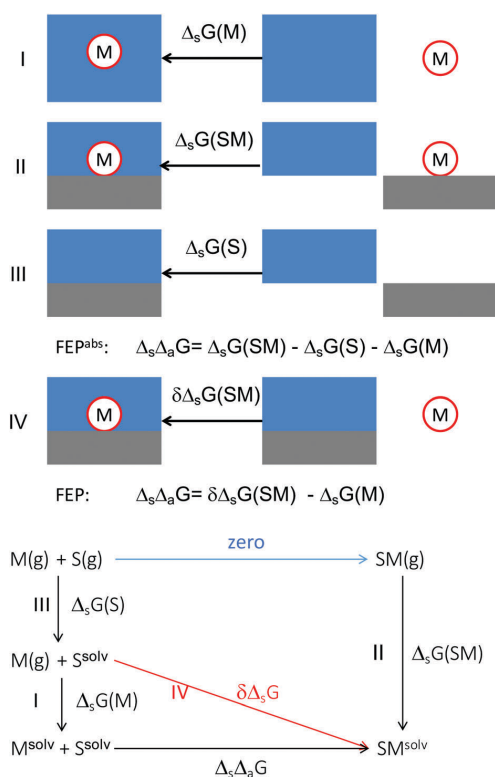


**Fig. 2** Schematic of the two possibilities to assess  $\Delta_s \Delta_a G$ , evaluated by FEP, which only accounts for the variation of the solvation free energy upon adsorption of the molecule on the surface. (top) “M” and “S” refer to the molecule (red circle) and surface (gray rectangle), respectively, while the solvent is depicted by the blue rectangle. Steps II–I–III define the scheme dubbed  $\text{FEP}^{\text{abs}}$ , where the solvation energy for each species needs to be computed separately. Alternatively, steps IV–I directly give the solvation energy contribution to adsorption. (bottom) Corresponding thermodynamic cycles, with roman letters indicating the corresponding processes depicted in the top scheme. The FEP contribution to the adsorption process in vacuum evaluates to strictly zero (horizontal blue line in the thermodynamic cycle) and its value is evaluated at the DFT level. The rectangle represents the “standard” cycle ( $\text{FEP}^{\text{abs}}$ ), while the triangle avoids the absolute solvation free energies for metallic slabs by assessing process IV, in red.

term,  $\Delta_s \Delta_a E_{\text{pol}}$  will be shown to be a rather small contribution in the PCM. As detailed above, it is not re-evaluated within the FEP scheme. However, it could be included in a computationally significantly more expensive QM/MM-FEP scheme, which is beyond the scope of the present paper, but parallels the approach that has been published during the revision of this paper.<sup>45</sup> Herein, we focus on different approximations for the dominant  $\Delta_s \Delta_a G_{\text{inter}}$  term, which describes the intermolecular solvent–solute contribution to the free energy of solvation, including the solvent re-organization energy.

Evaluating the solvation energy contribution to the adsorption energy,  $\Delta_s \Delta_a G_{\text{inter}}$ , within the PCM framework is straight forward:

$$\Delta_s \Delta_a G = \Delta_s G(\text{SM}) - \Delta_s G(\text{S}) - \Delta_s G(\text{M}) \quad (11)$$

where S, M and SM represent the individual surface, molecule and the surface with the adsorbed molecule, respectively. The same scheme can be applied to the FEP computations, where we call it  $\text{FEP}^{\text{abs}}$  (see processes I–III in Fig. 2). However, the absolute solvation free energies for extended systems ( $\Delta_s G(\text{SM}), \Delta_s G(\text{S})$ ) are difficult to converge. Hence, we have devised an alternative, avoiding these two terms: when the initial state is defined as metal surface in the solvent and the molecule in the gas-phase and the final state is the molecule adsorbed on the solvated surface, we can directly assess  $\delta \Delta_s G = \Delta_s G(\text{S}) - \Delta_s G(\text{SM})$  (see process IV in Fig. 2 and the corresponding triangular thermodynamic cycle). This perturbation is, obviously, much smaller than completely desolvating an entire metal surface and hence converges rather easily.

### 3 Methods and computational details

The presented computational strategy consists of three distinct phases: (i) DFT computations, (ii) setting up the molecular mechanics computations, (iii) running the free energy perturbation computations. These steps are described in the following subsections.

#### 3.1 DFT computations

All DFT computations are performed with a locally modified version of VASP 5.3.5,<sup>46,47</sup> patched to include the implicit solvent module VASPsol<sup>16</sup> and including the recently implemented<sup>44</sup> dispersion correction dDSC<sup>48</sup> that has become available to the public in version VASP 5.4.1. The electronic structure is described at the PBE level,<sup>49</sup> with an energy cut-off of at least 400 eV for the plane-wave basis set. The electron-ion interactions are described by the PAW formalism.<sup>50,51</sup>

The metal surface is modeled as a  $p(4 \times 4)$  Ru(0001) slab with a lattice constant of 2.70 Å and a thickness of 4 layers, with the two lowest ones fixed in the bulk position. One levulinic acid molecule is chemisorbed on this slab, which corresponds to a low coverage situation. Such a coverage appears reasonable considering the modest chemisorption energy, but determination of optimal coverage is beyond the scope of this paper. The vacuum layer completes the z-direction to reach 40.5 Å. Dipole corrections in z-direction are included in some computations during the SCF procedure, which is indicated by a subscript “dip” when appropriate. Molecules are computed in a cubic box of a length of 20 Å. All computations are performed at the gamma point. Integrating the Brillouin zone more accurately or using thicker, symmetric slabs changes the DFT contribution (relative energy changes of  $\sim 0.1$  eV), but leaves the solvation energy unchanged compared to the dipole corrected results (see ESI†).

All geometries are optimized to reach a gradient smaller than 0.02 eV Å<sup>-1</sup> with wave functions converged to  $1 \times 10^{-6}$  eV. In most of the computations the precision setting of VASP is set to “normal”. For testing purposes, we have also performed computations with more stringent accuracy settings, particularly, the FFT grids are improved from  $54 \times 54 \times 98$  to  $90 \times 90 \times 160$



grid points for the surface model by using “accurate” precision settings, and a plane-wave cut-off of 600 eV is used. The automatic optimization of the real-space projection operators is used. If not stated otherwise, the default implicit solvent settings are used, except that the cavitation energy is not included, *i.e.*, the cavity surface tension  $\tau$  is set to zero to increase the numerical robustness. A 2nd order Methfessel–Paxton smearing is applied to the metallic surfaces (width of 0.2 eV). Reported charges are based on a Hirshfeld analysis,<sup>52</sup> which is a by-product of the dDsC dispersion correction.

### 3.2 Setting up the MM force field

The CM5 charges, which have been developed for the SMD implicit solvent model,<sup>36</sup> are evaluated based on the Hirshfeld charges given by VASP, transformed by the cm5pack utility available from the University of Minnesota,<sup>53</sup> and modified to take into account the recommended scaling factor of 1.27 for explicit solvent computations.<sup>34</sup> This scaling value is similar to the one suggested by Grimme for his QM derived force field.<sup>54</sup> The transformation from Hirshfeld to CM5 charges depends on the geometry. However, cm5pack is not a periodic code. Therefore, the DFT cell is first replicated in all 3 directions in order to minimize finite size effects and then only the results of the central unit are exploited, resulting in charges for all atoms in the QM region.

For the MM computations of surface bound species, the relatively small DFT unit-cell has been replicated to a  $3 \times 3$  super super-cell, corresponding to a formally  $p(12 \times 12)$ . This allows for a better description of the bulk solvent region due to less “enforced” periodicity, increases the statistical averaging and avoids technical issues with MM programs that are intended for large unit cells. The Lennard-Jones (LJ) parameters are taken from UFF.<sup>35</sup> The initial solvent distribution is obtained from the predefined TIP3P<sup>33</sup> box with about 35 Å of water surrounding the system. § This generates an orthorhombic box that does not account for the periodicity of the surface, since the QM system was treated like a molecule, resulting in water surrounding the entire system. From the thus generated orthorhombic box with in plane angles of 90 degrees, the “original”, hexagonal (rhombus of length 32.4 Å with 60/120 degrees in-plane angles) cell is cut out by removing all the solvent which is not on top of the metal surface. This restores the correct periodicity of the entire system. Typically, there are about 1900 water molecules surrounding the metal surface. The final unit cell for one of the adsorption modes is represented in Fig. 1.

### 3.3 Free energy perturbation

All MM computations are performed with NAMD 2.9.<sup>55</sup> In addition to being highly efficient, NAMD allows us to fix the QM region in its starting position during the entire FEP computation and to still apply a barostat in the out-of-plane direction. In other words, the QM region is kept frozen during the evaluation of the solvation free energy, a strategy well known from applications to molecular systems.<sup>56</sup> This also avoids the necessity of periodic

bonded interactions, which would be necessary otherwise in order to reliably describe a metal surface.

The electrostatics are evaluated according to the Particle Mesh Ewald summation, with a 4th order interpolation scheme and a grid spacing of 1 Å. The temperature (300 K) is controlled by a Langevin thermostat with a damping coefficient of  $1 \text{ ps}^{-1}$ . The Langevin barostat for keeping the pressure constant to 1 bar is used with a piston period of 100 fs and a decay of 150 fs. The LJ terms are cut off at 11 Å, after having been switched to zero, starting from 9 Å. The water geometry is kept fixed and a time step of 2 fs is applied. To fully exploit the efficiency of NAMD and its multiple-time step algorithm,<sup>57</sup> the full electrostatics are evaluated every second time step, while the LJ interactions are evaluated every time step. Tests have shown that evaluating the full electrostatics every time step barely affects the results (see ESI†).

Prior to the FEP simulation, the system is minimized for 2000 steps, then heated from 100 K to 300 K within 10 ps and then equilibrated during 200 ps.

The FEP computations are performed with a variable number of equally spaced windows (at least 10), each of the length of 200 ps, of which the first 100 ps are used to equilibrate. Data presented in the ESI† for windows of 500 ps with 250 ps equilibration each, yield the same results, demonstrating a well converged setup. Note, that this is especially true for the surfaces, since the “primitive” system is repeated 9 times, yielding statistics that are roughly equivalent to 0.9 ns per window. To avoid the “end-point catastrophe” (diverging interactions) in the FEP computations, the default settings are applied, *i.e.*, a soft-core potential is used for the LJ potential.<sup>58,59</sup> The electrostatic interactions are scaled twice as fast than the LJ parameters (*e.g.*, “incoming” particles have partial charges starting from  $\lambda = 0.5$ ).<sup>60</sup> Furthermore, the internal interactions of the solute do not contribute to the MM-FEP free energy estimates, which is achieved through “decoupling”.<sup>61</sup> Note, that these “internal” energy differences are fully accounted for in the QM computations and therefore included in the final energy.

The free energy difference is obtained from joining the forward and backward run through the simple overlap sampling,<sup>62</sup> with outputs written every 50 fs.

The error estimates were obtained through the ParseFEP toolkit.<sup>63</sup> Since these errors were found to be below 0.01 eV for all species, we do not report them herein. For hydration energies of individual molecules the errors are, however, given in the ESI.†

## 4 Results and discussion

We will discuss two distinct problems: first, the computation of free energy of solvation  $\Delta_s G$  for small molecules, for which we have compared the PCM solvation energies to results of our straight forward MM-FEP scheme. Second, we present the adsorption Gibbs energies  $\Delta_a G^{\text{sol}}$  of levulinic acid on Ru(0001) and the impact of the inclusion of the solvation free energies contributions  $\Delta_s \Delta_a G$ , first as obtained from PCM and then FEP. We discuss the numerical precision and the sensitivity of these

§ The system setup is performed using tleap of the AmberTools.

quantities to the geometry and to the polarization of the QM system by an implicit solvent. We conclude by discussing some shortcomings of the presented method.

#### 4.1 Molecules

In Fig. 3, we compare the hydration energies  $\Delta_s G$  obtained with six methods to experiment for 17 molecules. The set of molecules (see ESI† for detailed information) includes typical polar organic molecules such as alcohols, amines and carboxylic acids.

Two different PCM setups are tested: PCM <sup>$\tau=0$</sup>  (to which we will also simply refer as “PCM”, as it is the stable, default variant as implemented in VASPsol<sup>16</sup>) uses default parameters, except that the cavitation energy is neglected ( $\tau = 0$ ), which is needed in some applications for sake of numerical stability.<sup>16,31</sup> As clearly seen, PCM <sup>$\tau=0$</sup>  overestimates the solvation free energy rather dramatically (mean absolute deviation, MAD of 0.14 eV ( $>3$  kcal mol<sup>-1</sup>)).<sup>¶</sup> The cavitation energy is, by definition, positive and its inclusion reduces the solvent affinity. Indeed, including this contribution in PCM<sup>acc</sup> yields somewhat better results (MAD = 0.08 eV). Nevertheless, both schemes do not compare well with experiment. However, as discussed above, the parametrization of the PCM was done taking into account the energetic cost of polarizing the electronic wave function. Hence, a fair comparison assesses rather polPCM ( $\Delta_s E_{\text{pol}}^{\text{PCM}} + \Delta_s G_{\text{inter}}^{\text{PCM}}$ ). Indeed, the MAD drops from 0.14 to 0.07 eV for PCM <sup>$\tau=0$</sup>  and becomes, with 0.04 eV, excellent for polPCM<sup>acc</sup>. Jorgensen and co-workers reported a MAD of around 0.04 eV for their FEP computations that are based on the sophisticated OPLS-AA force field to describe the Lennard-Jones interactions and the dynamics of the molecules.<sup>34</sup> Let us, nevertheless emphasize that the physics captured by the two schemes (PCM and Jorgensen’s FEP) is somewhat different, as the PCM does not account for any dynamic properties (e.g., conformational changes), while the FEP is missing  $\Delta_s E_{\text{pol}}$ . Hence, we conclude that both schemes are accurate due to some error cancellation based on parameter fitting. This error cancellation implies that functional groups or types of molecules (e.g., transition metal complexes) require some benchmarking prior to being confident that predictions are in line with experiments. Very similar conclusions have been drawn from an earlier comparison.<sup>64</sup>

Alternatively, the hydration energies are computed by our MM-FEP approach. As a first approach we use vacuum charges to evaluate the FEP free energy of solvation. The MAD of 0.08 eV indicates that the scheme is reasonable, but not very accurate. Using atomic charges which have been evaluated from a DFT computation that includes an implicit solvent (PCM <sup>$\tau=0$</sup> ), the performance is improved, yielding a MAD of 0.06 eV. This performance is remarkable considering that the LJ parameters for the FEP computations have not been “tuned” for this application and that in general the LJ parameters need to depend on the

<sup>¶</sup> The histogram of the errors around the mean error is shown in the ESI† to represent the scattering of the data. For all the methods, about half of the errors are located within  $\pm 25$  meV of the mean error, with the remaining errors being quite similarly distributed. Hence, the trend of the MAD is a reasonable descriptor to compare these different methods.

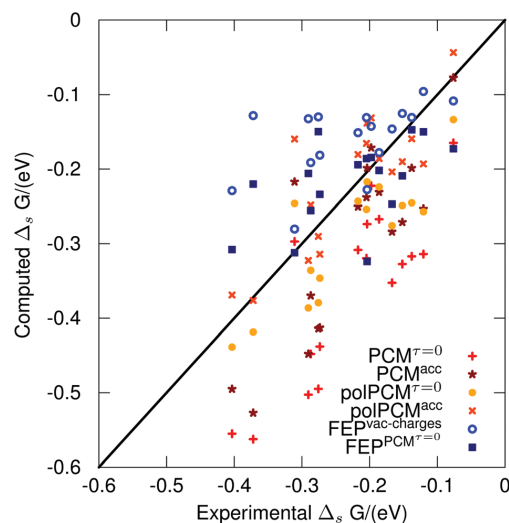


Fig. 3 Computed solvation free energies  $\Delta_s G$  of small molecules compared to experimental data (see ESI† for their distributions in form of a histogram around the average error). Two settings are tested for the PCM: PCM <sup>$\tau=0$</sup>  refers to the use of standard parameters, except that the cavity surface tension  $\tau$  is set to zero to improve numerical stability and PCM<sup>acc</sup> uses the default parameters for the PCM, but with increased numerical precision (600 eV plane-wave basis set and more accurate FFT grids). polPCM includes the polarization contribution to the solvation energy, i.e.,  $\Delta_s E_{\text{pol}}^{\text{PCM}}$ . FEP computations are either based on vacuum charges (FEP<sup>vac-charges</sup>) or on an electronic structure surrounded by an implicit solvent (PCM <sup>$\tau=0$</sup> ).

chemical environment of the atom.<sup>65</sup> Furthermore, this accuracy is sufficient for most applications we target, i.e., adsorption and reactions on metal surfaces, where other sources of errors (density functional approximation, thermal contributions, surface coverage and direct solvent effects) give much larger uncertainties.

In conclusion, our approach of keeping the DFT geometry fixed during the FEP computation and the application of UFF Lennard-Jones parameters together with atomic charges derived from PCM computations yields reasonably accurate results. Our molecule of interest (levulinic acid) has a solvation energy of about  $-0.7$  eV and  $-0.5$  eV at the PCM <sup>$\tau=0$</sup>  and FEP level, respectively.

#### 4.2 LA@Ru(0001)

We now turn to our system of interest, the adsorption of levulinic acid (LA) at a liquid water/Ru(0001) interface. For such a system, reference experimental data is, unfortunately, not available. In this part, we assess the impact of numerical settings on the results we obtain with the PCM and MM-FEP approaches and analyze their consistency. We focus on four adsorption modes (see Fig. 4 for their representations). In the most stable mode, LA forms a loop, so that the two chemical functions interact with the metallic surface (labeled **ket\*-COOH\***): the ketone is adsorbed on top of a Ru atom through its O atom and the carboxyl group is chemisorbed on a neighboring site in a similar configuration. In the other configurations we considered,



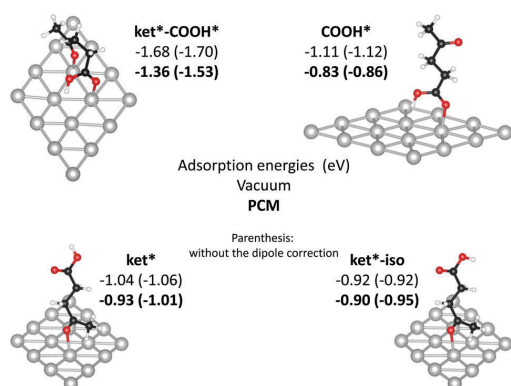


Fig. 4 Representation of the four adsorption modes studied of levulinic acid and the adsorption energies computed by different schemes; numbers in parenthesis refer to the absence of the dipole correction. The first row gives the adsorption energies in vacuum ( $\Delta_a E^{\text{vac}}$ ). The second row (bold) gives the adsorption energy when including an implicit solvent ( $\Delta_a G^{\text{PCM}}$ ), which naturally includes the polarization contribution  $\Delta_s \Delta_a E_{\text{pol}}$ .

the levulinic acid is oriented perpendicular to the surface. In **COOH\***, the carboxylic acid is chemisorbed while the ketone is not interacting with the metallic surface. In **ket\*** and **ket\*-iso**, it is the carbonyl that is chemisorbed, and they differ only by the orientation of the OH bond of the carboxylic acid.

**4.2.1 PCM.** Fig. 4 depicts the adsorption modes of levulinic acid on Ru(0001) and the associated adsorption energies  $\Delta_a G$  as computed by DFT in vacuum and in implicit solvent (PCM<sup>z=0</sup>). The components of the adsorption energy ( $\Delta_a E^{\text{vac}} + \Delta_s \Delta_a E_{\text{pol}}^{\text{PCM}}$ ,  $\Delta_s \Delta_a G_{\text{inter}}^{\text{PCM}}$ ) are reported in Table 1.

Comparing the adsorption energies in vacuum with and without the dipole correction (numbers without/within parenthesis on the first lines in Fig. 4), we could conclude that this correction is not necessary. However, in implicit solvent, we find a significant difference upon including the dipole correction. Inspecting the solvation free energy (Table 1), we find that  $\Delta_s \Delta_a G^{\text{PCM}}$  (**ket\*-COOH\***) changes by more than 0.5 eV due to the use of the dipole correction. Computing the dipole moment of the system reveals that it is 1.1 e Å in vacuum and 1.6 e Å in PCM when using the dipole correction, but in the absence of this correction, the dipole moment increases to 1.5 and 4.8 e Å in vacuum and PCM, respectively. The latter value clearly indicates a spurious, macroscopic dipole moment. This statement is confirmed by both, increasing the number of metallic layers (which increases the spurious dipole moment) and the lack of a reasonable convergence as a function of the void separating two slabs, even at box sizes around 100 Å. From these tests (documented in the ESI<sup>†</sup>) we conclude that the origin of the problem is not a dipole–dipole interaction between cells, but the polarizability of the metallic slab. The artificial polarization occurs because the “bottom” of the slab is supposed to mimic a bulk material that cannot be polarized at all, but the solvent is on both sides of the slab and thus favors a polarization across the metallic slab. The negative

$\Delta_s \Delta_a G^{\text{PCM}}$  nicely illustrate how the PCM solvates this macroscopic dipole, leading to heavily biased estimates of solvent effects. In order to verify the reliability of the dipole correction for the chosen box size, we have performed simulations with symmetric slabs (see ESI<sup>†</sup>). The use of symmetric slabs precludes the artificial polarization of the “bottom” slab. These computations have evidenced that the dipole correction is, despite its magnitude, highly accurate. Hence, we conclude that the dipole correction (or the use of symmetric slabs) is absolutely necessary when dealing with metallic (and thus highly polarizable) slabs on which polar molecules are adsorbed, surrounded by a continuum model. In addition, tests (see ESI<sup>†</sup>) have revealed that the geometry (optimized in vacuum or implicit solvent) does not influence these results, suggesting that re-optimization in solvent would not be necessary.

To gain chemical insights, we consider now the dipole corrected results. Based on the adsorption energies in vacuum, we find that **ket\*-COOH\*** is by far the most and **ket\*-iso** the least stable adsorption mode. Accounting implicitly for the solvent overall weakens the adsorption free energies  $\Delta_a G$  compared to vacuum, since the isolated molecule is more stabilized by the solvent than when adsorbed on the surface. This reduction strongly depends on the adsorption mode and is particularly small in the **ket\*** structures. Therefore, the implicit solvent reduces the range of relative energies between different adsorption modes from 0.76 to 0.53 eV. This can easily be rationalized considering that desolvating COOH implies a significant destabilization compared to adsorption modes where the acid is still solvated (**ket\*** and **ket\*-iso**). Furthermore, the **ket\*-iso** conformation is particularly stabilized by the solvent, because the O–H proton is more exposed to the solvent and therefore more strongly solvated (see Table 1). We also observe that the bi-adsorbed structure **ket\*-COOH\*** is slightly better solvated than **COOH\***. At first sight, this may seem surprising since the ketone function is desolvated during the **ket\*-COOH\*** adsorption and not for **COOH\***. However, the dipoles generated by the two oxygenated functions are parallel in the loop-like adsorption mode **ket\*-COOH\*** and not in the straight ones. Since the metallic surface is highly polarizable, this leads to an enhanced charge transfer between the surface (negative) and the molecule (positive) in **ket\*-COOH\*** (0.28 e) compared with **COOH\*** (0.14 e). This is also reflected in the overall (out-of-plane) dipole moment of 1.6 and 0.7 e Å<sup>-1</sup>, respectively. In a nutshell, the larger surface dipole generated in **ket\*-COOH\*** compensates the desolvation of the ketone function.

**4.2.2 FEP.** As outlined in the Theory section, we apply two different approaches to assess the solvation energy contribution to adsorption  $\Delta_s \Delta_a G$ : the straight forward scheme (FEP<sup>abs</sup>), which assesses the solvation energy of each system individually and the scheme simply dubbed “FEP”, which takes a short-cut by determining the change in solvation energy of the surface when adding a molecule  $\delta \Delta_a G$ . Of course, the two approaches are expected to converge to the same  $\Delta_s \Delta_a G$  result, especially taking into account error compensation when annihilating the interactions with the entire metal slab. Note, however, that following

**Table 1** Components of the PCM $^{\tau=0}$  adsorption free energies in eV:  $\Delta_a G^{\text{PCM}} = \Delta_a E^{\text{vac}} + \Delta_s \Delta_a E_{\text{pol}}^{\text{PCM}} + \Delta_s \Delta_a G_{\text{inter}}^{\text{PCM}} = \Delta_a E^{\text{PCM}} + \Delta_s \Delta_a G_{\text{inter}}^{\text{PCM}}$  and the surface dipole moment ( $\mu$ , in e Å). The “dip” superscript refers to the use of the dipole correction during the SCF procedure. Note that the energy cost to polarize the wave function in the PCM is responsible for  $\Delta_a E^{\text{PCM}} > \Delta_a E^{\text{vac}}$ . Hence, even a negative  $\Delta_s \Delta_a G_{\text{inter}}^{\text{PCM}}$  can lead to a more weakly adsorbed molecule in implicit solvent than in vacuum. For ease of comparisons,  $\Delta_a E^{\text{vac}}$  is given as well

	$\Delta_a E^{\text{vac}}$	$\mu^{\text{vac,dip}}$	$\Delta_a E^{\text{PCM}}$	$\Delta_s \Delta_a G_{\text{inter}}^{\text{PCM}}$	$\mu^{\text{PCM}}$	$\Delta_a E^{\text{PCM,dip}}$	$\Delta_s \Delta_a G_{\text{inter}}^{\text{PCM,dip}}$	$\mu^{\text{PCM,dip}}$
<b>ket*-COOH*</b>	-1.70	-1.08	-1.11	-0.42	-4.84	-1.60	0.24	-1.55
<b>COOH*</b>	-1.12	-0.58	-1.05	0.19	-2.22	-1.13	0.31	-0.69
<b>ket*</b>	-1.06	-0.77	-0.76	-0.25	-3.36	-0.97	0.04	-1.05
<b>ket*-iso</b>	-0.92	-0.32	-0.42	-0.54	-2.66	-0.64	-0.26	-0.83

an ONIOM-like approach,<sup>29</sup> in both cases FEP is only used to assess the difference in adsorption energy between vacuum and solution (second term in eqn (10)) and that the major energetic contribution is described at the DFT level (first term in eqn (10)).

Let us now turn to the solvation free energy computed by FEP. Our first concern is precision, before we can assess the accuracy of the proposed scheme. In order to address this point, we systematically increase the number of windows from 10 to 50 for the perturbation where only the adsorbate (dis)appears (denoted FEP) and from 25 to 100 for the absolute free energy of solvation (denoted FEP<sup>abs</sup>), *i.e.*, the slab and the adsorbate disappear and the solvation energy of the empty slab is assessed independently by a similar computation. We would like to use 10 windows (FEP<sub>10</sub>), which worked well for the isolated molecules. Therefore, in Fig. 5 we put FEP<sub>10</sub> in between FEP<sub>50</sub> and FEP<sup>abs</sup><sub>100</sub>, to compare it to the best converged results. As expected,  $\Delta_s \Delta_a G^{\text{FEP}}$  converges very slowly with respect to the number of windows when the perturbation is large (*i.e.*, the entire system is solvated, FEP<sup>abs</sup>), while with 10 windows we already get results accurate within 0.05 eV when the perturbation is only the adsorbate. This demonstrates the efficiency of our scheme.

**4.2.3 Comparison of PCM and FEP for surfaces.** After having discussed the PCM and FEP results individually, we now compare the two approaches, both in term of overall results and the contribution of the solvation energy. The comparison of the adsorption energies in vacuum, PCM $^{\tau=0}$  and FEP are presented in Fig. 6. The major result is that the

most stable conformation is **ket\*-COOH\***, independently on the environment, which rationalizes the observation that vacuum conditions (with micro-solvation) are often enough to gain valuable insight from DFT. The implicit solvent affords one of the “expected” qualitative results, *i.e.* that **ket\*** is more stable than **COOH\***, since the carboxylic acid does not need to be completely desolvated. The FEP adsorption free energies, on the other hand, are closer to the trends in vacuum than to the PCM. These differences are small and might depend significantly on the adsorption strength of water on the metal surface, which is inaccurately described by both methods.

While the total adsorption energies are the ultimately relevant quantities, the comparison of  $\Delta_s \Delta_a G_{\text{inter}}$ , *i.e.*, the modification of the adsorption energy due to the solvation energy allows a more detailed comparison of the two methods. The comparison between the PCM and FEP results for  $\Delta_s \Delta_a G_{\text{inter}}$  is given in Fig. 7, *i.e.*, we compare the balance of solvation energy between the adsorbed state on the one hand and the isolated molecule and a clean surface on the other hand (see Fig. 2). The positive sign of most of these contributions indicates that accounting for the solvation free energy weakens the adsorption free energy, *i.e.*, that the solvent interacts less strongly with the adsorbed state than with the isolated molecule and the clean surface. This is rather intuitive, keeping in mind that the fraction of the molecule interacting directly with the surface is inaccessible for the solvent and assuming that chemisorption does not induce a large polarization of the solvent accessible surface area. As discussed above, this assumption is not valid in the

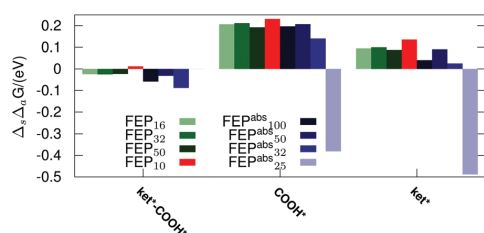


**Fig. 5** Computed solvation free energy contributions  $\Delta_s \Delta_a G^{\text{FEP}}$  to the adsorption of levulinic acid in three distinct adsorption modes according to different FEP setups: the index gives the number of “windows” used, while the superscript “abs” refers to the computation of the free energy of adsorption by two separate computations: one for the naked metal surface and one for the surface with the molecule adsorbed. In the absence of this superscript, the FEP is computed between surface with the molecule adsorbed as the end state and the naked metal surface as the initial state.

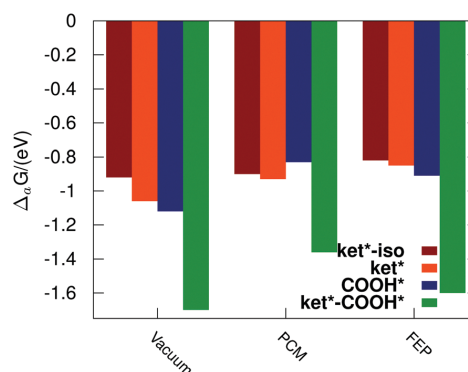


**Fig. 6** Comparison of the adsorption free energy in vacuum, an implicit solvent (PCM $^{\tau=0}$ ) and in explicit solvent (FEP).

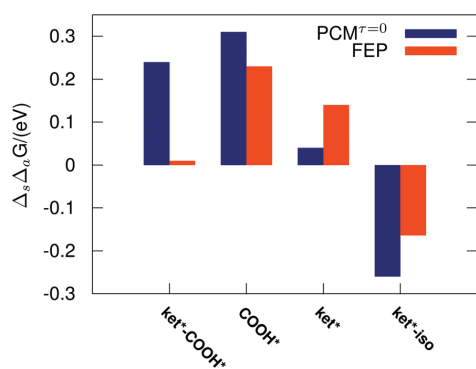


Fig. 7 Comparison of the solvation free energy contribution to adsorption  $\Delta_s\Delta_aG$  as computed by the PCM<sup>r=0</sup> and FEP approaches.

absence of the dipole correction, leading to spurious results. There is only one exception to this “expected” behavior, which is **ket\*-iso**, where the proton is better exposed to the solvent than in the other orientations and in solution: the lowest energy solution conformation is derived from the **COOH\*** adsorption mode. PCM and FEP give a negative contribution to the adsorption free energy of **ket\*-iso**, which results in a relative stabilization of this adsorption mode compared to the vacuum results.¶

Probably the most important message of Fig. 7 is that both approaches give the same sign for the solvation energy contribution for each adsorption mode. This gives credence that the dominating physics captured by the two methods is, as expected, similar. However, there is one rather significant difference: MM-FEP solvates **ket\*-COOH\*** better than **COOH\*** to a larger extent than PCM. This increased relative solvation can be rationalized as follows: in the **COOH\*** adsorption mode, a hydrophobic zone close to the metal surface is created (see ESI‡ for average water distributions). This reduces the access of the solvent to the (polarized) metal surface as measured by the radial distribution function between Ru and the water molecules, which is lower for **COOH\*** than for **ket\*-COOH\***, thereby weakening the solvation energy. For **ket\*-COOH\***, on the other hand, the molecule adsorbs rather flatly on the surface, which exposes roughly half of the molecular surface to the solvent. Furthermore, this flat adsorption allows the water molecules to better solvate the large surface dipole (*vide supra*). As discussed in the ESI‡, the creation of a hydrophobic zone in the “upright standing” conformations could be overestimated in our current model, mostly because water adsorbs too weakly on Ru(0001) with the default UFF LJ parameters (physisorption of  $-0.03$  eV compared to the chemisorption of  $-0.7$  eV according to DFT). However, even when increasing the interaction between water and Ru, the stability ordering of the four conformations

¶ The same observation applies to isolated levulinic acid, but the effect is not strong enough to change the preferred conformation: the energy difference is reduced from 0.18 to 0.05 eV when going from vacuum to PCM<sup>r=0</sup>.

remains the same although the difference between **ket\*-COOH\*** and **COOH\*** decreases from 0.7 eV to 0.4 eV (see ESI‡). The failure of the UFF Lennard-Jones parameters to capture the chemisorption of water on Ru(0001) cannot come as a surprise, since these parameters are only able to account for weakly bound water molecules (*i.e.*, the “indirect” contributions). Here, the “direct” solvent contributions would mainly describe the chemisorption of water molecules. However, both the FEP and the PCM model neglect this chemisorption of water molecules, providing a fair comparison between the two approaches. In other words, a more complete model would need to consider chemisorbed water molecules on the Ru surface in the QM subsystem in order to capture the “direct” solvent effect.

Our work highlights two points that warrant further studies: first, the impact of the strong adsorption of water on the Ru(0001) surface might change the solvation free energies significantly, given that this effect is basically absent in PCM and the present MM-FEP approach. Second, the solvation free energy might strongly depend on the coverage. MM-FEP is ideally suited for elucidating the coverage effect, as it takes the finite size and chemical shape of the solvent fully into account. Furthermore, the entropy of adsorption is neglected in the present approach, which might introduce a slight imbalance in disfavor of the more flexible adsorption modes **ket\*** and **COOH\*** compared to the roughly immobile, bi-dentate **ket\*-COOH\***. These questions can be addressed by straightforward improvements of the current MM-FEP scheme along two axes: on the one hand, improved force fields for the interface would allow for approximations of the adsorption entropy and on the other hand (self-)consistent coupling between QM and MM, with eventually a full QM resampling<sup>66,67</sup> would improve the energetics.

## 5 Conclusion

Solvent effects for adsorption free energies of organic molecules on (metal) surfaces are a great challenge to assess both experimentally and theoretically. Our target is to evaluate the solvation free energy contribution to chemisorption of organic molecules chemisorbed at the liquid–metal interface. To this end, we describe the chemisorption on a periodic surface by DFT. To assess the solvation free energy, we have compared two schemes: implicit solvation and molecular mechanics based free energy perturbation (MM-FEP). Our results demonstrate the benefit of polarizing the QM subsystem by an implicit solvent prior to MM-FEP, but also the need for dipole corrections or symmetric slabs in order to avoid artificial polarization of the metallic slab. We have shown that the MM-FEP relative solvation energies converge at low to modest computational cost to an acceptable precision, given the approximations involved in the overall scheme. The method is validated for bulk solutions on a set of 17 standard “organic” molecules, delivering accurate results (MAD = 0.06 eV). In the test case of the chemisorption of the bifunctional molecule levulinic acid at the Ru–water interface, the comparison of MM-FEP with an implicit solvent model shows that trends are often similar.

Most notably, the bulk solvation effect is not strong enough to desorb the carboxylic acid from the surface, despite its desolvation being necessary upon chemisorption. The demonstration that even such a simplistic MM-FEP approach yields valuable results is encouraging, since, in contrast to PCM, the MM-FEP approach can be systematically improved and is well adapted to assess coverage effects and to model solvation effects in ionic liquids and electrolytes as well as solvents at high temperature and pressure.

## References

- B. S. Akpa, C. D'Agostino, L. F. Gladden, K. Hindle, H. Manyar, J. McGregor, R. Li, M. Neurock, N. Sinha, E. H. Stitt, D. Weber, J. A. Zeitler and D. W. Rooney, *J. Catal.*, 2012, **289**, 30.
- C. Michel, J. Zaffran, A. M. Ruppert, J. Matras-Michalska, M. Jedrzejczyk, J. Grams and P. Sautet, *Chem. Commun.*, 2014, **50**, 12450.
- C. Michel and P. Gallezot, *ACS Catal.*, 2015, **5**, 4130.
- S. K. Desai, V. Pallassana and M. Neurock, *J. Phys. Chem. B*, 2001, **105**, 9171.
- C. Michel, F. Auneau, F. Delbecq and P. Sautet, *ACS Catal.*, 2011, **1**, 1430.
- L. Arnadottir, E. M. Stuve and H. Jonsson, *Chem. Phys. Lett.*, 2012, **541**, 32.
- D. Cao, G. Q. Lu, A. Wieckowski, S. A. Wasileski and M. Neurock, *J. Phys. Chem. B*, 2005, **109**, 11622.
- S. A. Wasileski and M. J. Janik, *Phys. Chem. Chem. Phys.*, 2008, **10**, 3613.
- B. N. Zope, D. D. Hibbitts, M. Neurock and R. J. Davis, *Science*, 2010, **330**, 74.
- D. D. Hibbitts and M. Neurock, *J. Catal.*, 2013, **299**, 261.
- J. Liu, X.-M. Cao and P. Hu, *Phys. Chem. Chem. Phys.*, 2014, **16**, 4176.
- M. Faheem, S. Suthirakun and A. Heyden, *J. Phys. Chem. C*, 2012, **116**, 22458.
- C. J. Cramer and D. G. Truhlar, *Chem. Rev.*, 1999, **99**, 2161.
- S. A. Petrosyan, A. A. Rigos and T. A. Arias, *J. Phys. Chem. B*, 2005, **109**, 15436.
- O. Andreussi, I. Dabo and N. Marzari, *J. Chem. Phys.*, 2012, **136**, 064102.
- K. Mathew, R. Sundararaman, K. Letchworth-Weaver, T. A. Arias and R. G. Hennig, *J. Chem. Phys.*, 2014, **140**, 084106.
- G. König and S. Boresch, *J. Phys. Chem. B*, 2009, **113**, 8967.
- J. R. Pliego and J. M. Riveros, *J. Phys. Chem. A*, 2001, **105**, 7241–7247.
- D. Asthagiri, L. R. Pratt and H. S. Ashbaugh, *J. Chem. Phys.*, 2003, **119**, 2702–2708.
- V. S. Bryantsev, M. S. Diallo and W. A. Goddard III, *J. Phys. Chem. B*, 2008, **112**, 9709–9719.
- H.-F. Wang and Z.-P. Liu, *J. Phys. Chem. C*, 2009, **113**, 17502.
- B. Mennucci, J. Tomasi, R. Cammi, J. R. Cheeseman, M. J. Frisch, F. J. Devlin, S. Gabriel and P. J. Stephens, *J. Phys. Chem. A*, 2002, **106**, 6102.
- M. Faheem and A. Heyden, *J. Chem. Theory Comput.*, 2014, **10**, 3354.
- H. Hu, Z. Lu and W. Yang, *J. Chem. Theory Comput.*, 2007, **3**, 390.
- R. W. Zwanzig, *J. Chem. Phys.*, 1954, **22**, 1420.
- P. Kollman, *Chem. Rev.*, 1993, **93**, 2395.
- J. Aqvist and A. Warshel, *Chem. Rev.*, 1993, **93**, 2523.
- O. Acevedo and W. L. Jorgensen, *Acc. Chem. Res.*, 2010, **43**, 142.
- M. Svensson, S. Humbel, R. D. J. Froese, T. Matsubara, S. Sieber and K. Morokuma, *J. Phys. Chem.*, 1996, **100**, 19357.
- W. R. H. Wright and R. Palkovits, *ChemSusChem*, 2012, **5**, 1657.
- S. N. Steinmann, C. Michel, R. Schwiedernoch and P. Sautet, *Phys. Chem. Chem. Phys.*, 2015, **17**, 13949.
- D. Gunceler, K. Letchworth-Weaver, R. Sundararaman, K. A. Schwarz and T. A. Arias, *Modell. Simul. Mater. Sci. Eng.*, 2013, **21**, 074005.
- W. L. Jorgensen, J. Chandrasekhar, J. D. Madura, R. W. Impey and M. L. Klein, *J. Chem. Phys.*, 1983, **79**, 926.
- J. Z. Vilseck, J. Tirado-Rives and W. L. Jorgensen, *J. Chem. Theory Comput.*, 2014, **10**, 2802.
- A. K. Rappe, C. J. Casewit, K. S. Colwell, W. A. Goddard and W. M. Skiff, *J. Am. Chem. Soc.*, 1992, **114**, 10024.
- A. V. Marenich, S. V. Jerome, C. J. Cramer and D. G. Truhlar, *J. Chem. Theory Comput.*, 2012, **8**, 527.
- A. V. Marenich, C. J. Cramer and D. G. Truhlar, *J. Chem. Theory Comput.*, 2013, **9**, 609.
- M. P. Repasky, C. R. W. Guimaraes, J. Chandrasekhar, J. Tirado-Rives and W. L. Jorgensen, *J. Am. Chem. Soc.*, 2003, **125**, 6663.
- D. T. Limmer, A. P. Willard, P. Madden and D. Chandler, *Proc. Natl. Acad. Sci. U. S. A.*, 2013, **110**, 4200.
- S. N. Steinmann and P. Sautet, *J. Phys. Chem. C*, 2016, **120**, 5619.
- S. Ringe, H. Oberhofer, C. Hille, S. Matera and K. Reuter, *J. Chem. Theory Comput.*, 2016, **12**, 4052–4066.
- T. P. Straatsma and J. A. McCammon, *J. Chem. Phys.*, 1989, **90**, 3300.
- M. Strajbl, Y. Y. Sham, J. Villa, Z.-T. Chu and A. Warshel, *J. Phys. Chem. B*, 2000, **104**, 4578.
- S. Gautier, S. N. Steinmann, C. Michel, P. Fleurat-Lessard and P. Sautet, *Phys. Chem. Chem. Phys.*, 2015, **17**, 28921.
- H.-K. Lim, H. Lee and H. Kim, *J. Chem. Theory Comput.*, 2016, **12**, 5088–5099.
- G. Kresse and J. Hafner, *Phys. Rev. B: Condens. Matter Mater. Phys.*, 1993, **47**, 558.
- G. Kresse and J. Furthmüller, *Phys. Rev. B: Condens. Matter Mater. Phys.*, 1996, **54**, 11169.
- S. N. Steinmann and C. Corminboeuf, *J. Chem. Theory Comput.*, 2011, **7**, 3567.
- J. P. Perdew, K. Burke and M. Ernzerhof, *Phys. Rev. Lett.*, 1996, **77**, 3865.
- P. E. Blochl, *Phys. Rev. B: Condens. Matter Mater. Phys.*, 1994, **50**, 17953.
- G. Kresse and D. Joubert, *Phys. Rev. B: Condens. Matter Mater. Phys.*, 1999, **59**, 1758.

## Chapter 6. Solvation free energies for periodic surfaces: comparison of implicit and explicit solvation models

---

[View Article Online](#)

Paper

PCCP

- 52 F. L. Hirshfeld, *Theor. Chem. Acc.*, 1977, **44**, 129.
- 53 A. V. Marenich, C. J. Cramer and D. G. Truhlar, *CM5PAC, version 2011*, University of Minnesota, Minneapolis, MN, 2011.
- 54 S. Grimme, *J. Chem. Theory Comput.*, 2014, **10**, 4497.
- 55 J. C. Phillips, R. Braun, W. Wang, J. Gumbart, E. Tajkhorshid, E. Villa, C. Chipot, R. D. Skeel, L. Kalé and K. Schulten, *J. Comput. Chem.*, 2005, **26**, 1781.
- 56 W. L. Jorgensen and J. K. Buckner, *J. Phys. Chem.*, 1986, **90**, 4651.
- 57 M. Tuckerman, B. J. Berne and G. J. Martyna, *J. Chem. Phys.*, 1992, **97**, 1990.
- 58 T. C. Beutler, A. E. Mark, R. C. van Schaik, P. R. Gerber and W. F. van Gunsteren, *Chem. Phys. Lett.*, 1994, **222**, 529.
- 59 M. Zacharias, T. P. Straatsma and J. A. McCammon, *J. Chem. Phys.*, 1994, **100**, 9025.
- 60 A. Pohorille, C. Jarzynski and C. Chipot, *J. Phys. Chem. B*, 2010, **114**, 10235.
- 61 S. Boresch and M. Karplus, *J. Phys. Chem. A*, 1999, **103**, 103.
- 62 N. Lu, D. A. Kofke and T. B. Woolf, *J. Comput. Chem.*, 2004, **25**, 28.
- 63 P. Liu, F. Dehez, W. Cai and C. Chipot, *J. Chem. Theory Comput.*, 2012, **8**, 2606.
- 64 M. Orozco, W. L. Jorgensen and F. J. Luque, *J. Comput. Chem.*, 1993, **14**, 1498–1503.
- 65 D. Casanova, S. Gusarov, A. Kovalenko and T. Ziegler, *J. Chem. Theory Comput.*, 2007, **3**, 458–476.
- 66 M. Retegan, M. Martins-Costa and M. F. Ruiz-Lopez, *J. Chem. Phys.*, 2010, **133**, 064103.
- 67 G. König, P. S. Hudson, S. Boresch and H. L. Woodcock, *J. Chem. Theory Comput.*, 2014, **10**, 1406.



## **7 Force Field for Water over Pt(111): Development, Assessment, and Comparison**

As seen in chapter 6, the force field description of water with a metal surface is a critical part of the accuracy of the prediction of solvation free energies at the solid/liquid interface. However, even for the most investigated metal/water interface, Pt(111), the existing force fields turned out to suffer from severe limitations when applied to the cases for which accurate DFT computations are feasible, i.e., a single water molecule or ice-like layers. Therefore, we developed a novel functional form for the Pt(111)/H<sub>2</sub>O force field, reproducing extensive DFT data. Since the structuration of water at the interface depends on the delicate balance between water–water and water–platinum interactions, the “true” structure at the interface remains inaccessible to current simulations. Furthermore, significant many-body effects for water–water and water–Pt interactions at the interface have been observed. Hence, more involved force fields would need to be developed in order to confidently describe the Pt/water interface. Also, compared to the force field used in chapter 6, the dynamics of water at the interface is much slower, which is due to the much stronger interaction between the solvent and the surface. Therefore, the equilibration time is significantly longer (~ 500 ps).





## Force Field for Water over Pt(111): Development, Assessment, and Comparison

Stephan N. Steinmann,<sup>\*,†</sup> Rodrigo Ferreira De Morais,<sup>†</sup> Andreas W. Götz,<sup>\*,‡</sup> Paul Fleurat-Lessard,<sup>¶</sup> Marcella Iannuzzi,<sup>§</sup> Philippe Sautet,<sup>||,⊥</sup> and Carine Michel<sup>†</sup>

<sup>†</sup>Univ Lyon, Ecole Normale Supérieure de Lyon, CNRS Université Lyon 1, Laboratoire de Chimie UMR 5182, 46 allée d'Italie, F-69364 Lyon, France

<sup>‡</sup>San Diego Supercomputer Center, University of California San Diego, La Jolla, California 92093, United States

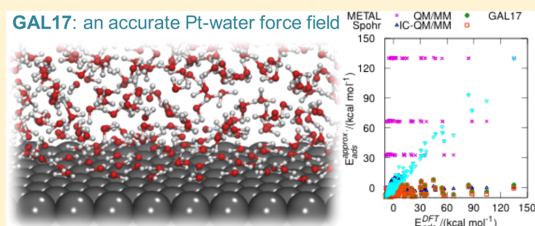
<sup>¶</sup>Institut de Chimie Moléculaire de l'Université de Bourgogne (ICMUB, UMR 6302, CNRS), Université de Bourgogne Franche-Comté, 9 Avenue Alain Savary, 21078 Dijon, France

<sup>§</sup>Institut für Chemie, University of Zurich, Winterthurerstrasse 190, CH-8057 Zurich, Switzerland

<sup>||</sup>Department of Chemical and Biomolecular Engineering, and <sup>⊥</sup>Department of Chemistry and Biochemistry, University of California Los Angeles, Los Angeles, California 90095, United States

### Supporting Information

**ABSTRACT:** Metal/water interfaces are key in many natural and industrial processes, such as corrosion, atmospheric, or environmental chemistry. Even today, the only practical approach to simulate large interfaces between a metal and water is to perform force-field simulations. In this work, we propose a novel force field, GAL17, to describe the interaction of water and a Pt(111) surface. GAL17 builds on three terms: (i) a standard Lennard-Jones potential for the bonding interaction between the surface and water, (ii) a Gaussian term to improve the surface corrugation, and (iii) two terms describing the angular dependence of the interaction energy. The 12 parameters of this force field are fitted against a set of 210 adsorption geometries of water on Pt(111). The performance of GAL17 is compared to several other approaches that have not been validated against extensive first-principles computations yet. Their respective accuracy is evaluated on an extended set of 802 adsorption geometries of H<sub>2</sub>O on Pt(111), 52 geometries derived from icelike layers, and an MD simulation of an interface between a c(4 × 6) Pt(111) surface and a water layer of 14 Å thickness. The newly developed GAL17 force field provides a significant improvement over previously existing force fields for Pt(111)/H<sub>2</sub>O interactions. Its well-balanced performance suggests that it is an ideal candidate to generate relevant geometries for the metal/water interface, paving the way to a representative sampling of the equilibrium distribution at the interface and to predict solvation free energies at the solid/liquid interface.



## 1. INTRODUCTION

In the last 10 years, molecular modeling has matured to become a valuable tool during catalyst screening and development.<sup>1–3</sup> With the advent of biomass conversion, where water is almost omnipresent and for which metal catalysts are key for hydrogenations, reforming, and many other transformations,<sup>4,5</sup> the demand for atomistic understanding of reactions at the aqueous/metal interface has soared. There are also many other important processes that occur at the metal/liquid interface, such as corrosion, electrochemistry, lubrication, and biomedical applications as for example cancer phototherapy by gold nanoparticles.<sup>6,7</sup> Experimentally and computationally it has been shown that, depending on the catalyst, water can play a noninnocent role during heterogeneous catalysis.<sup>8–11</sup> However, the computational approaches that are well suited to describe reactions at the solid–gas-phase interface are not necessarily suitable to describe the solid–liquid interface: the amorphous

character of these interfaces make static computations questionable, while ab initio molecular dynamics (AIMD) simulations are too costly to be routinely applied<sup>12–16</sup> and also the cost of adaptive QM/MM is prohibitive for metal surfaces.<sup>17,18</sup> Therefore, approximate methods have been developed aiming at representing the solid–liquid interface. Implicit solvent models, well established for molecular computations already in the 1990s,<sup>19</sup> have been developed lately for periodic systems<sup>20–22</sup> and made publicly available only very recently, first in VASP<sup>23</sup> and by now also in CP2K,<sup>24</sup> jDFTx,<sup>25</sup> and Quantum-Espresso.<sup>26</sup> However, the accuracy of these models remains largely unknown for metal/water interfaces.<sup>27</sup> Microsolvation, where a small number of crucial water molecules are included explicitly, has been applied since

Received: November 21, 2017

Published: April 16, 2018



## Chapter 7. Force Field for Water over Pt(111): Development, Assessment, and Comparison

the pioneering work by Neurock and co-workers<sup>28</sup> to capture the direct effect of water on reaction pathways.<sup>29,30</sup> Hybrid methods, where the microsolvation is complemented by an implicit solvent, are particularly attractive in terms of computational efficiency, but consistent treatment of the explicit water molecules remains a significant challenge.<sup>9,31–34</sup> Another approach is based on icelike structures,<sup>35–39</sup> which are motivated by low-temperature surface science studies which have evidenced the existence of these arrangements over many transition metal surfaces.<sup>40–42</sup> However, these rigid networks are unlikely to be representative at ambient temperature and even less so at the elevated temperatures applied, for instance, in aqueous-phase reforming.<sup>43</sup> Reoptimizing structures obtained from short AIMD simulations is yet another strategy,<sup>8,44</sup> but it remains unclear to which extent these basically arbitrarily selected water arrangements are representative of the properties at the solid–liquid interface.

While implicit solvation methods are, without any doubt, the most convenient and efficient ones for large-scale applications,<sup>45,46</sup> several approaches have been devised to replace the implicit solvent by an effective field (or solvation energy) obtained from molecular mechanics based molecular dynamics (MMMD) simulations or related methods.<sup>47–51</sup> In contrast to AIMD, the MMMD simulations can easily access the necessary time scales (nanosecond range for equilibration) and length scales that are required to equilibrate these interfaces and to avoid spurious effects due to 2D periodic repetitions of water configurations. Furthermore, these approaches allow, at least in principle, to assess also the subtle change in entropy upon adsorption, which, due to the competition between the solvent and the adsorbate for adsorption on the surface and the associated solvent reorganization at the interface, is far from trivial to assess.<sup>52–54</sup> Note that already for reactions in solution, the situation is significantly more complicated than in the gas phase, which explains the use of rough approximations in the literature, approximating solution-phase entropy changes as half of the values obtained in the gas phase.<sup>55,56</sup>

However, methods that rely on molecular mechanics introduce a different problem: the accuracy of the force field. The success of force fields for biological systems heavily relies on two pillars: First, there exist many experimentally resolved crystal or NMR solution structures which allow to validate a given force field. Second, the functional form has reached a certain consensus, with a clear distinction of bonded and nonbonded parameters describing bonds/angles and Coulomb and Lennard-Jones interactions, respectively. The problem of water/metal interfaces is that the experiments (in particular averaged information from X-ray scattering<sup>57</sup> or local information from spectroscopy<sup>58,59</sup>) do not yield nearly enough information to (in-)validate any proposed force field. Therefore, the “constraints” from experiment are very few and largely insufficient to validate a given theoretical model. This might explain why the last 30 years have seen numerous and contradictory force fields and simulations for metal–water interfaces.<sup>60–69</sup> Furthermore, not even the functional form is obvious: Water adsorption on metals has often at least some degree of directional covalency, without creating well-defined covalent bonds. The most successful recent water models have been parametrized against large data sets of high-level correlated electronic structure computations.<sup>70,71</sup> Unfortunately, for the size and nature of metal/liquid interfaces, the highest achievable level for a sufficient number of distinct geometries is density functional theory (DFT) in the

dispersion-corrected generalized gradient approximation. Our level of theory (PBE-dDsC<sup>72,73</sup>) has been benchmarked against various experimental adsorption energies from single-crystal microcalorimetry and found to perform very well.<sup>74</sup> As shown below, the preference of water to adsorb on top sites is also well reproduced. This level is significantly more reliable than the extended Huckel computations<sup>75</sup> used for some of the older (but still popular) parametrizations.<sup>62,64</sup> Among previous works, only the neural network model by Behler and co-workers<sup>68</sup> and the very recent work by Johnston and co-workers<sup>69</sup> have made extensive use of first-principles computations for training and validation. However, as best illustrated by the repeated discussion on the “best suitable functional”, the choice of the particular flavor remains debatable,<sup>14</sup> and the sensitivity of the final result on this choice is, similar to the true structure of the water/metal interface, unknown.

Herein we propose a functional form for the metal–water interaction that is designed to capture the major effects, in particular the directional chemisorption interaction as well as the short-range repulsion and long-range attraction. Furthermore, in the interest of being able to combine the interaction potential with well-established force fields for solutes, our functional form is rather simple (compared to a neural network), with few parameters that do not depend on the water model. Hence, our water–metal force field can be complemented with diverse water–water interaction potentials, thus assessing the sensitivity of the interface structuring on the competition between water–water and water–surface interaction, a question which has not been addressed frequently in the literature (see ref 76 for an exception).

Our force field is implemented in the publicly available *sander* program, from the AmberTools package (available in version 18).<sup>77</sup> Furthermore, we introduce a training and validation set to assess the quality of a metal/water force field. On the one hand, we extensively sample the adsorption energy as a function of adsorption site (hollow, bridge, and top), rotational angles, and distance from the surface. On the other hand, we also try to reproduce the adsorption energy for (partial) icelike layers. This benchmark data has also been used to assess previously proposed schemes, in particular the METAL force field by Heinz et al.<sup>78</sup> and the IC-QM/MM (and QM/MM) by Golze et al.<sup>79</sup> where the water–water interaction is treated at the DFT level, while the water–surface interaction is given by the potential of Siepmann and Sprik,<sup>64</sup> which has been used extensively in MMMD studies.<sup>66</sup> The potential by Spohr and Heinzinger<sup>61,62</sup> has been among the first atomistic potentials trying to describe the interaction between water and a platinum surface. The Spohr–Heinzinger potential is an interesting contender among the Pt–H<sub>2</sub>O force fields, last but not least since it includes an explicit term for H–Pt interaction. Therefore, we herein also test this potential in its original form, although it has been parametrized for Pt(100). Finally, from MD simulations we demonstrate the sensitivity of the orientational preference of H<sub>2</sub>O at the interface not only to the water–metal interaction potential but also to the water–water interaction. Furthermore, the time scale for equilibration of the interfacial water is around 0.5 ns in agreement with previous studies.<sup>66,80</sup> This is far beyond the scope of AIMD for an interface with a suitable size.

## 2. FUNCTIONAL FORM OF THE FORCE FIELD

The functional form for the force field between water and metallic surfaces has been the subject of several previous publications, with a wide range of sophistication proposed: from simple Lennard-Jones potentials (like the METAL force field of Heinz et al.)<sup>78</sup> to ReaxFF<sup>81</sup> or neural networks<sup>68</sup> for the case of copper surfaces. After extensive testing, we herein propose a pairwise potential that is completely independent of the chosen model for the water–water interactions. This has the advantage that the effect of the water model on the interface structure can be assessed straight forwardly, and in the future, QM/MM simulations in analogy to what has been done for the Siepmann–Sprick potential<sup>64,79</sup> are in reach. Additionally, we have developed the functional form in view of a possible generalization to other molecules, in particular alcohols and polyols, which are important species in biomass processing.

A united atom like approach was chosen in which the water–Pt interaction depends on the distance between the water and the metallic surface and on the orientation of the water molecule with respect to the surface normal. The basic terms of our force field are a standard Lennard-Jones potential ( $V_{\text{LJ}}$ ) between the surface and the oxygen atom, which takes care of the long-range dispersion and the short-range repulsion. The surface corrugation is improved by a Gaussian potential ( $V_{\text{Gauss}}$ ). Since water and its interaction with a surface are not spherically symmetric, we also introduce two terms that improve the description of the angular dependence of the interaction energy ( $V_{\text{Ang}}$ ). This force field will thus be called GAL17.

$$V_{\text{GAL17}}(\text{Pt}, \text{H}_2\text{O}) = V_{\text{Gauss}} + V_{\text{Ang}} + V_{\text{LJ}} \quad (1)$$

We have considered including electrostatic interactions via the image charge rod model.<sup>82</sup> However, we found that the corresponding contributions are comparatively small and therefore do not justify the significantly larger computational cost associated with the thermalization of the dipoles.<sup>83,84</sup> Hence we decided not to include an explicit image charge term. In agreement with previous reports,<sup>85–87</sup> water–water interactions are significantly modified by the presence of the metal surface. This is likely to be a combination of charge-transfer and many-body polarization effects. Many-body terms between water molecules are,<sup>88,89</sup> just like the interactions between the platinum surface and more than one water molecule, beyond the scope of the current force field, which is neither polarizable nor based on fluctuating charges, in order to keep the computational cost down and allow its implementation with minimal modification of classical MD codes. The following subsections detail the three terms of eq 1.

**2.1. Chemisorption and Lennard-Jones Potential.** A Lennard-Jones potential between the Pt and O atoms leads to a preferred adsorption of water on hollow sites (i.e., in the triangle between neighboring Pt atoms), while DFT computations<sup>41</sup> and experiments<sup>90</sup> unambiguously identify the adsorption site on top position as most stable. To correct this, Corni and co-workers have proposed to introduce LJ potentials between water and “virtual sites” (VS) located at the hollow sites of the outermost metal layer. By simple geometry, these interactions reverse the situation, allowing to retrieve the preference for top adsorption.<sup>65</sup> However, the functional form of the Lennard-Jones potential does not allow to consistently reproduce the correct magnitude of the energy difference between top and hollow sites on platinum. Therefore, we

herein introduce an anisotropic Gaussian function to correct the surface corrugation, i.e., the difference in adsorption energy between top and hollow sites. Such a potential might be reminiscent of the famous Morse potential or its modern extensions.<sup>91</sup>

The combination of Lennard-Jones and a Gaussian potential opens up two possibilities: (1) The Lennard-Jones potential is centered on the virtual sites to get the minimum at the top sites. In this case, the attraction at the VS is too strong, requiring a repulsive Gaussian centered on VS. (2) The Lennard-Jones potential can be based on Pt atoms, governing the attraction observed at the hollow sites. In this case, the Gaussian potential needs to be attractive and also centered at the Pt atoms in order to account for the stronger (chemisorption) interaction on top sites compared to the hollow sites. The first possibility is inspired by the work of Corni and co-workers, and its results are discussed in the Supporting Information under the name vsGAL17. It suffices here to say that the results are quite similar to the second possibility, GAL17. We prefer to avoid the virtual sites, also because it allows us to give a physical meaning to the two terms of the following equation: physisorption and chemisorption for the first and second term, respectively.

$$V_{\text{LJ}} + V_{\text{Gauss}} = \sum_{i \in [\text{O}]} \sum_{j \in [\text{Pt}]} \varepsilon_{ij} \left[ \left( \frac{r_{\text{min}}}{r_{ij}} \right)^{12} - 2 \left( \frac{r_{\text{min}}}{r_{ij}} \right)^6 \right] - \sum_{i \in [\text{O}]} \sum_{j \in [\text{Pt}]} \varepsilon_{\text{att}} e^{-b_{\parallel}((x_j-x_i)^2 + (y_j-y_i)^2)} e^{-b_{\perp}(z_j-z_i)^2} \quad (2)$$

where  $r_{ij}$  is the distance between atoms  $i$  and  $j$  and  $\varepsilon_{ij}$  is the minimum of the LJ energy well which is located at  $r_{\text{min}}$ .  $\varepsilon_{\text{att}}$  is the magnitude of the Gaussian attraction. The Gaussian function itself is anisotropic in the out-of-plane direction (here assumed to be the  $z$  axis), with the two in-plane directions ( $x, y$ ) being equivalent due to symmetry:  $b_{\parallel}$  and  $b_{\perp}$  are constants that define the width of the Gaussian in the surface plane and out-of-plane directions, respectively.

**2.2. Angular Correction.** According to our tests, two angles are key: the cartwheel angle  $\theta$  and the propeller angle  $\varphi$ , which are depicted in Figure 1. The helicopter motion  $\omega$  has

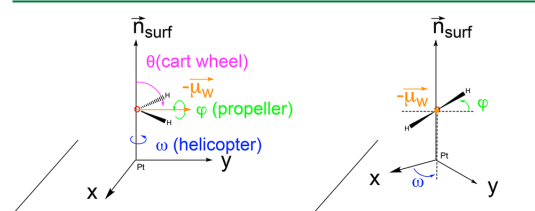


**Figure 1.** Definition of angles between a water molecule and a platinum surface in the  $xy$  plane.  $\vec{\mu}_w$  and  $\vec{n}$  are the water dipole (i.e., the bisector of the H–O–H angle) and surface normal vectors, respectively.

been found to lead to very small energy variations and is, therefore, not investigated in detail. Fortunately for us, to a good approximation, the effects of the two angles are separable, avoiding complex expressions and making the functional form physically more transparent. In fact, it turns out that only the cartwheel angle  $\theta$ , which describes the orientation of the dipole

moment with respect to the surface normal, requires a potential that depends explicitly on this angle. It can be approximated as a truncated Fourier expansion, switched off smoothly at a certain distance away from the surface by multiplying with a Fermi function. The position of the surface is defined as the plane going through the topmost layer of Pt atoms. The latter are held fixed in all our simulations. The  $\varphi$  dependence is well reproduced by a repulsive term between the surface and the hydrogens, decaying as  $1/r^5$ , with the power 5 being adjusted empirically on DFT data.

In summary, for each water molecule the angular correction potential takes the form

$$V_{\text{ang}} = \left( 1 - \frac{1}{e^{-s_{\text{ang}}(r_{\text{O,surf}}/r_{\text{ang}}-1)} + 1} \right) \sum_{n=1}^4 a_n \cos(n\theta) + \sum_{i=1}^2 \frac{A_{\text{Hsurf}}}{r_{\text{H}_i,\text{surf}}^5} \quad (3)$$

where  $r_{\text{O,surf}}$ ,  $r_{\text{H}_1,\text{surf}}$  and  $r_{\text{H}_2,\text{surf}}$  are the distances between the oxygen atom and the two hydrogen atoms, respectively, and the platinum surface, while  $s_{\text{ang}}$  defines the steepness and  $r_{\text{ang}}$  the location of the midpoint of the Fermi function.  $a_n$  are the coefficients in the Fourier series, while  $A_{\text{Hsurf}}$  is the repulsion parameter between the hydrogen atoms and the surface.

Given the above expressions, we have the following 12 parameters: two for the LJ potential ( $\epsilon_{ij}$ ,  $r_{\text{min}}$ ) and three for the anisotropic Gaussian ( $\epsilon_{\text{att}}$ ,  $b_{\parallel}$ ,  $b_{\perp}$ ) from eq 2, six for the distance dependent  $\theta$  dependence ( $s_{\text{ang}}$ ,  $r_{\text{ang}}$ ,  $a_n$  ( $n = [1,4]$ )), and one for the repulsion between the hydrogen atoms and the surface ( $A_{\text{Hsurf}}$ ) from eq 3.

### 3. COMPUTATIONAL DETAILS

**3.1. DFT Computations.** All static DFT computations have been carried out using VASP 5.4.1<sup>92,93</sup> using periodic boundary conditions, the PBE<sup>72</sup> generalized gradient approximation (GGA) exchange-correlation functional with dDsC dispersion correction,<sup>73,74</sup> and an energy cutoff of 400 eV for the expansion of the plane-wave basis set. The electron-ion interactions are described by the PAW formalism.<sup>94,95</sup> We have constructed a series of 802 configurations of a single water molecule adsorbed on a  $p(3 \times 3)$  Pt(111) unit cell with 4 metallic layers (Figure 2a). The Pt–Pt distance was optimized for the bulk and found to be 2.812 Å. The slabs are separated by a vacuum of 20 Å in order to minimize interactions between periodic images. The Brillouin zone was sampled by a  $\Gamma$ -centered  $3 \times 3 \times 1$  Monkhorst–Pack K-point grid. An idealized geometry (as cut from bulk Pt) was adopted for the metallic layers, while the water molecule was taken from a DFT optimization (O–H: 0.98 Å and a H–O–H angle of 105.32°). Thirteen values for  $\theta$  were picked spaced by 30°, except for the “end points” which were taken to be 10° and 340°. These  $\theta$  values were combined with  $\varphi = 0$  and 12 distances (from 2.1 to 6.0 Å above the surface for the top site), leading to a set of 156 configurations. Similarly, 11 distances (2.3–6.0 Å) were selected to assess the same set of orientations above the bridge and hcp site, summing up to 286 configurations. To study the  $\varphi$  dependence, 10 values between 20° and 180° were selected and combined with 3 values for  $\theta$  (30, 90 and 120°) at the same 12 distances above the top site generating 360 configurations.

We also built two validation sets: the first one is based on the two main structures proposed for an icelike layer on Pt(111):  $H_{\text{up}}$  and  $H_{\text{down}}$ , which are both hexagonal structures. In this

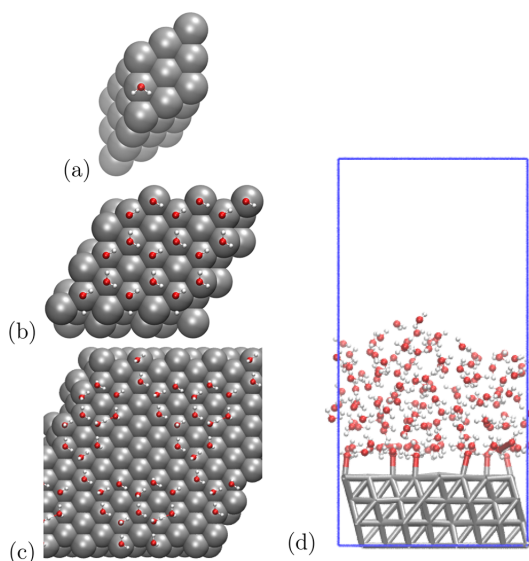


**Figure 2.** Systems used in this study. Fitting set: (a) One configuration of a single molecule adsorbed on the Pt(111) surface. Validation sets: (b) full ice layer, (c) defective ice layer, (d) snapshot of the MD simulation. The blue frame corresponds to the unit cell. The water layer thickness is approximately 14 Å.

structure, water molecules are alternating between a “flat” chemisorption mode and water molecules that are H-bonded to the chemisorbed water molecules, with the second hydrogen molecule either pointing up or down. All these geometries are fully optimized at the DFT level on a 3 layer Pt(111) (18 water molecules on a  $3\sqrt{3} \times 3\sqrt{3} R30^\circ$  unit cell), for which the Brillouin zone was sampled by a  $\Gamma$ -centered  $3 \times 3 \times 1$  Monkhorst–Pack K-point grid. From the two full icelike layers (Figure 2b), 52 configurations were constructed and optimized by removing 1–6 molecules (Figure 2c) or by keeping only 1–6 molecules. The DFT optimization induced significant reorganizations in several instances. Therefore, this validation set will be discussed as a whole, without distinguishing between  $H_{\text{up}}$  and  $H_{\text{down}}$  derived structures.

For the second set, we have performed extensive ab initio molecular dynamics simulations on a  $c(4 \times 6)$  unit cell of four metallic layers with 151 water molecules on top of it (Figure 2d). This leads to a water layer of approximately 14 Å on top of the surface. This thickness is sufficient to recover bulk water above the surface.<sup>12</sup> All these MD simulations were performed with CP2K<sup>24</sup> and the Brillouin zone was probed at the  $\Gamma$  point only. The initial configuration was provided by D. Golze and corresponds to the equilibrated IC-QM/MM simulation presented in ref 79. The Pt layer was, however, reoptimized at the PBE-D3<sup>72,96</sup> level since the molecular mechanics generated structure corresponds to a (hot) configuration far from equilibrium at the DFT level. After this preparatory adjustment for the change of the level of theory, the system was subjected to 10 ps of Born–Oppenheimer molecular dynamics using a 1 fs time step, while simulating protons as deuterium at 300 K and keeping the bottom two layers of Pt frozen. The wave function was expanded in a polarized double- $\zeta$  basis set and the charge density computed on a grid characterized by a 400 au cutoff. The wave function was converged to  $10^{-6}$  au,

applying a Fermi smearing of 300 K and diagonalizing the Kohn–Sham Hamiltonian.

**3.2. MM Computations.** All MM computations were performed with a locally modified version of *sander* of the AmberTools simulation package.<sup>77</sup> The GAL17 implementation is publicly available in AmberTools 18. Except for the MD simulation of the Pt/H<sub>2</sub>O interface, all MM computations were single-point energies. The nonbonded cutoff distance was set to 8 Å, which required to set the safety distance parameter (*skinnb*) to 0.4 Å due to the size of the unit cell for the Pt/H<sub>2</sub>O interface. For all other computations we simply replicated the original DFT unit cell by 4 in each in-plane direction and divided the resulting adsorption energy by 16. Standard settings were used for the particle mesh Ewald treatment of the long-range electrostatics.<sup>97</sup> During MD simulations, the surface atoms were held fixed at their initial position by applying “belly” dynamics, i.e., zeroing out their velocities at each time step. The temperature was maintained at 298.15 K through the weak coupling thermostat by Berendsen,<sup>98</sup> and the water models were held rigid with a tolerance of 10<sup>-7</sup> Å applying the default algorithms in AMBER.<sup>99</sup> For the 10 ps simulations, a time step of 1 fs was used, while longer simulations were performed with a 2 fs time step.

**3.3. IC-QM/MM Computations.** All (IC-)QM/MM computations were performed with CP2K, v 4.0. A typical input is provided in the [Supporting Information](#). In these simulations, the water–water interaction is modeled at the PBE-D3<sup>72,96</sup> level, while the metallic surface is described by EAM and the water–surface interaction is accounted for by the Siepmann–Sprik potential with or without including the image charge (IC) effect. All other technical settings were equivalent to the ones used for the *ab initio* MD simulations mentioned above, except that the highly efficient orbital transformation<sup>100</sup> was applied for the wave function optimization instead of the diagonalization and that all Pt atoms were kept fixed during the simulation. For the single-point computations on the p(3 × 3) unit cell, it was necessary to double the in-plane repetitions, similar to the AMBER simulations, in order to properly account for the atoms within the cutoff distance of 8 Å.

**3.4. Fitting of the Parameters.** The parameters of our force field could have been determined in a force matching scheme to the DFT MD simulations.<sup>101</sup> However, such a strategy would make the fit specific to a given water model. Furthermore, the discrepancy in water–water description between DFT and a given force field is likely to skew the fit for the H<sub>2</sub>O–Pt interaction. Therefore, we prefer to optimize the parameters only on the training set described below. This optimization was achieved through a Nelder–Mead “amoeba/simplex” algorithm as implemented by A. Garcia and distributed within the SIESTA simulation package,<sup>102</sup> targeting a minimal root-mean-square deviation (rmsd) over the training set.

Of the 802 water orientations, only 210 configurations were used as a training set. In particular, the 22 adsorptions for  $\theta = 90^\circ$ ,  $\varphi = 0^\circ$  above the hcp and bridge site were included, as well as the  $\theta$  dependence on the top site for the 8 smallest distances. The  $\varphi$  dependence was probed for the 4 smallest distances. However, configurations leading to adsorption energies above 1 eV (23 kcal mol<sup>-1</sup>) have been excluded, leading to 210 instead of the “full” 246 configurations.

The functional form of our force field is rather general and should, therefore, be suitable for various metals, from surfaces that interact strongly, e.g., Ru(0001), or weakly, e.g., Au(111),

with water molecules. The parameters determined for Pt(111) are unlikely to be transferable to these materials: we expect them to depend on the radius of the metal atoms and on the oxophilic character of the metal. However, with the protocol established, other metal surfaces can be parametrized at a relatively low complexity. These extensions are currently underway.

## 4. RESULTS AND DISCUSSION

**4.1. Water Adsorption and Rotation.** The 12 characteristic parameters of our force field have been fitted to minimize the rmsd and are given in [Table 1](#). As a first test, we present the

**Table 1. Optimized Parameters and Root Mean Square Deviation (rmsd) for the GAL17 Force Field<sup>a</sup>**

parameter	GAL17	units
$\epsilon_{ij}$	6.410	kcal mol <sup>-1</sup>
$r_{\min}$	1.136	Å
$\epsilon_{\text{att}}$	8.901	kcal mol <sup>-1</sup>
$b_{\parallel}$	9.331	Å <sup>-2</sup>
$b_{\perp}$	0.102	Å <sup>-2</sup>
$s_{\text{ang}}$	11.135	
$r_{\text{ang}}$	2.441	Å
$a_1$	15.768	kcal mol <sup>-1</sup>
$a_2$	1.594	kcal mol <sup>-1</sup>
$a_3$	1.922	kcal mol <sup>-1</sup>
$a_4$	2.838	kcal mol <sup>-1</sup>
$A_{\text{Hsurf}}$	304.081	kcal mol <sup>-1</sup> Å <sup>5</sup>
rmsd <sup>tot</sup>	2.44	kcal mol <sup>-1</sup>
rmsd <sup>validation</sup>	2.68	kcal mol <sup>-1</sup>
rmsd <sup>bound</sup>	1.67	kcal mol <sup>-1</sup>

<sup>a</sup>The superscripts “tot”, “validation”, and “bound” refer to the full set of 802 configurations, the 592 configurations outside the training set, and the 700 configurations with negative adsorption energies, respectively.

adsorption energies of all 802 adsorption energies of a single water molecule on a p(3 × 3) Pt(111) surface as a parity plot in [Figure 3](#). Since GAL17 has been trained on 210 configurations, [Figure S1](#) shows the corresponding graph for the validation set (592 configurations), and [Table 1](#) gives the rmsd for the full and the validation set. Both figures convey the same conclusions, but [Figure 3](#) shows also the low-lying and thus most important configurations. We conclude that GAL17 correlates quite well with the DFT data, which is also reflected in the relatively small rmsd over the entire set of 2.44 kcal mol<sup>-1</sup>. As can be expected, restricting the rmsd computation to the 592 configuration outside of the training set leads to a small increase. However, with 2.68 kcal mol<sup>-1</sup>, GAL17 still performs very well. Furthermore, if we consider only the geometries in which the water molecule is bound (negative adsorption energy), the rmsd drops to 1.67 kcal mol<sup>-1</sup>. Focusing on the region of negative adsorption energies (right panel), we see that GAL17 tends to underestimate the stability of configurations which have a DFT adsorption energy of -5 to -2 kcal mol<sup>-1</sup>. While GAL17 is clearly not perfect, the comparison with the other force fields shows a significant improvement, be it the seminal force field of Spohr and Heinzinger (also known as Spohr potential)<sup>61,62</sup> or compared to “state of the art” methods, i.e., the Siepmann–Sprik potential<sup>64</sup> coupled to a DFT description for water with or without image charge effects ((IC-)QM/MM)<sup>79</sup> or the much simpler, but popular, Lennard-



# Chapter 7. Force Field for Water over Pt(111): Development, Assessment, and Comparison

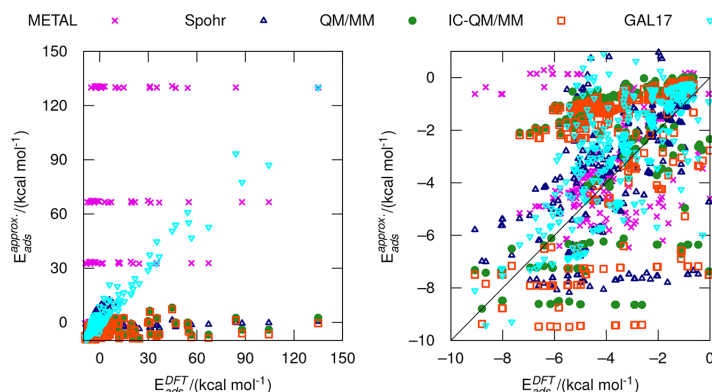


**Figure 3.** Correlation between DFT data and various approximate methods for the adsorption of a water molecule on a  $p(3 \times 3)$  unit cell for various adsorption sites and combinations of  $\theta$  and  $\phi$ . Left: overall correlation. Right: correlation for geometries with negative DFT adsorption energies.

Jones only potential called METAL by Heinz et al.<sup>78</sup> The most characteristic differences between our force field and these predecessors are the “horizontal lines” observed for the latter: for these series of configurations, the force fields do not show any significant variation in the adsorption energy, while DFT assigns energy differences up to 150 kcal mol<sup>-1</sup>. The second immediate observation is that the METAL force field binds water molecules rather weakly. A more detailed analysis (see Figure 6) shows that the interaction on top is too weak, while hollow sites are overstabilized. Indeed, when comparing the simple pairwise attractive/repulsive terms of the three different force fields, we find that the METAL force field is not very attractive (see the Supporting Information).

Upon investigating the origin of the horizontal lines observed in Figure 3 for the force fields from the literature, the  $\varphi$  dependence is quickly identified as the culprit: Figure 4 illustrates the energy evolution as a function of  $\varphi$  at an oxygen position of 2.6 Å above a Pt atom and a value of 90° for  $\theta$ . Along this rotation around the dipole moment of the molecule, the hydrogen atoms get closer to the surface, effectively “bumping” into it, leading to an increase of up to 14 kcal mol<sup>-1</sup>

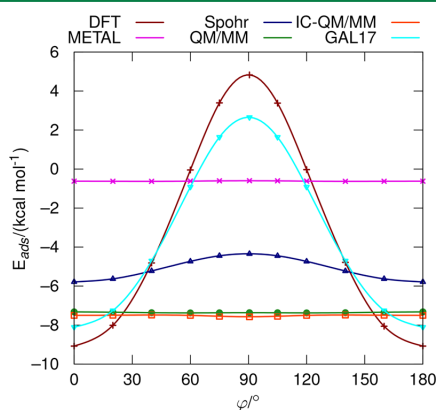


**Figure 4.** Adsorption of a water molecule on a  $p(3 \times 3)$  unit cell on a top site (2.6 Å above a Pt atom), as a function of  $\varphi$ , the angle describing the rotation of the water molecular plane around the dipole moment at  $\theta = 90^\circ$ , computed with various methods.

according to DFT. This increase is quite faithfully reproduced by the  $r^{-5}$  repulsion included in our force field but is totally absent in most of the force fields of the literature (Figure 4). The exception is the Spohr potential, which includes a Pt–H repulsive term that improves the  $\varphi$  dependence. However, this repulsion is too weak compared to the DFT results, demonstrating the need for a more balanced description and careful parametrization. This strongly suggests that our force field is likely to sample a more relevant configurational space than previous approaches, which is particularly important in QM/MM resampling approaches, where configurations are extracted from MM simulations and their energies reweighted at the QM level.<sup>103,104</sup>

Next, we turn to the rotation of the dipole moment with respect to the surface normal ( $\theta$ ). At 90° the water molecule is parallel to the platinum surface (for  $\varphi = 0$ ), and the lowest interaction energy is obtained (see Figure 5). Rotating it to 0° moves the hydrogen atoms up, which is associated with a loss of roughly 3 kcal mol<sup>-1</sup> according to DFT. Rotating in the other direction is strongly disfavored (+12 kcal mol<sup>-1</sup>) since the hydrogen atoms get too close to the surface. These variations are well reproduced by the GAL17 force field. As can be

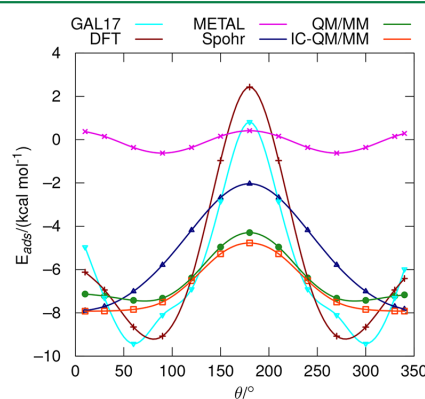


**Figure 5.** Adsorption of a water molecule on a  $p(3 \times 3)$  unit cell on a top site (2.6 Å above a Pt atom), as a function of  $\theta$ , the angle between the dipole moment and the out-of-plane axis at  $\varphi = 0$ , computed with various methods.

expected, the METAL force field, where hydrogens are just described by point charges, cannot resolve this  $\theta$  dependence either. The small variation observed in Figure 5 is electrostatic in nature and comes from the finite coverage used in these computations. The potential of Spohr and Heinzinger predicts a reasonable maximum around  $180^\circ$ , but it fails to identify  $90^\circ$  as the minimum. The force field of Siepmann and Sprik, on the other hand, depends explicitly on  $\theta$ . Indeed, the variation has roughly the right shape for QM/MM although the magnitude of the differences is underestimated by more than a factor of 2, which is most likely due to the outdated benchmark data used 20 years ago. When accounting for the image charge effect, however, the curve gets less satisfying, with a flat potential energy for angles between  $0$  and  $90^\circ$  (and, by symmetry,  $270$  and  $360^\circ$ ).

Finally, we assess the interaction energy as a function of the water–surface distance for a water molecule adsorbed with its molecular plane parallel to the surface plane at three different sites: top, bridge sites, and hollow sites in Figure 6. At the DFT

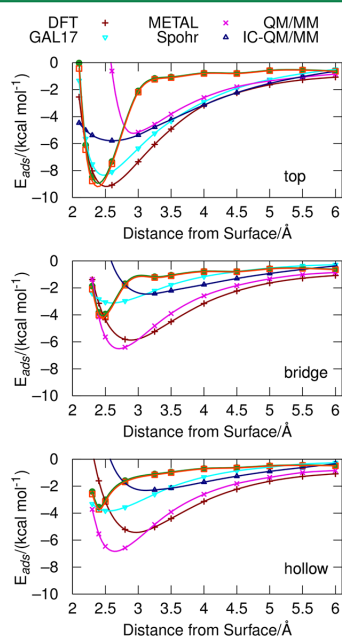


**Figure 6.** Adsorption of a water molecule on a  $p(3 \times 3)$  unit cell on top (top), bridge (middle), and hollow (bottom) sites with  $\theta = 90^\circ$  and  $\varphi = 0^\circ$ .

level, the top adsorption is clearly preferred by at least  $3 \text{ kcal mol}^{-1}$  with respect to the adsorption on a bridge site, which is only slightly more stable than the adsorption on the hollow site. Interestingly, at distances above  $3.5 \text{ \AA}$ , the difference between the sites is disappearing quickly, which we see as a strong indication that the top site is stabilized by chemisorption, while the adsorption on bridge and hollow sites is due to physisorption. Regarding our force field, the agreement with DFT data is reasonable, although GAL17 underestimates the stability of the hollow and bridge sites. Also the difference in adsorption height for the minimum energy of the three sites ( $2.6 \text{ \AA}$  on top, but roughly  $2.8 \text{ \AA}$  on bridge and hollow sites) is washed out. METAL, a pure LJ potential, predicts the hollow

site to be most stable, while the top site is least stable, with an error of  $4 \text{ kcal mol}^{-1}$ , at the minimum energy positions. This is qualitatively wrong, since all DFT data indicate that the minimum should be at the top site, not the hollow site. Unfortunately, no pairwise, atom-centered potential is able to reproduce this preference, as also shown by Berg et al.<sup>69</sup> Note, however, that the long-range physisorption potential is quite well reproduced by the LJ potential, indicating that only the chemisorption energy is missing. The Spohr and Heinzinger potential accurately reproduces the site preference, but the interaction profile is too shallow compared to the reference DFT potential. The potential of Siepmann and Sprik is quite different. In this case, the use of a small training set with old, inaccurate benchmark data<sup>75</sup> is most likely to be at the origin of the issue: the long-range part is severely underestimated (see also Figure S2 in the Supporting Information), and the minimum at the hollow and bridge sites is very narrow. The minimum at the top site, on the other hand, is quite well reproduced.

In summary, the analysis of 800 adsorption geometries of a water molecule on a  $p(3 \times 3)$  unit cell has highlighted the challenges of capturing the orientational preferences of a water molecule over a platinum surface. In particular, the introduction of a repulsion between the surface and the hydrogen atoms was key for the rotation around the axis of the dipole moment, a term that is missing in most of the tested force fields from the literature, although it was present in some of the older parametrizations,<sup>63,105</sup> including the one by Spohr and Heinzinger tested herein.<sup>61</sup> Additionally, reproducing the position and depth of the minima at top, bridge, and hollow positions turned out to be less than trivial. Despite these small shortcomings, our force field still shows the best correlation against the reference data, capturing the essential physics of the orientation-dependent adsorption energy of water on Pt(111), including a non-negligible contribution from chemisorption, which is notoriously difficult to be captured at the force-field level.<sup>106</sup>

**4.2. Water Aggregates: From Monomer to an Ice Layer.** Having established a reasonable accuracy for the interaction between a single water molecule and a platinum surface, the question is to which extent the potential is transferable to configurations with more than one water molecule. For this purpose, we have constructed a validation set based on icelike layers on Pt(111) (see Computational Details).

Assessing structures with water–water and water–surface interactions also requires to choose a water model. Since the developed force field is completely independent of the water model, we decided to test several models, i.e., the TIPxP family with  $x = 3, 4$ , and  $5$ ,<sup>107–109</sup> the popular SPC/E,<sup>110</sup> and the recent OPC model.<sup>111</sup> All of these models use a fixed water geometry and are nonpolarizable. As for the reference of the water molecule, we consider that the least biased choice is an isolated water molecule. Hence, the  $-280 \text{ kcal mol}^{-1}$  adsorption energy for 18 water molecules (in a full  $\text{H}_{\text{down}}$  layer) at the DFT level corresponds to an average adsorption/interaction energy of  $15 \text{ kcal mol}^{-1}$ , compared to the  $9 \text{ kcal mol}^{-1}$  at the DFT minimum for a single water molecule, stressing the importance of the interaction between water molecules, including many-body effects,<sup>88,89</sup> which are not explicitly included in the pairwise additive force fields tested here.

# Chapter 7. Force Field for Water over Pt(111): Development, Assessment, and Comparison

Figure 7 presents the correlation between the DFT data and the force-field predictions of GAL17 combined with the five

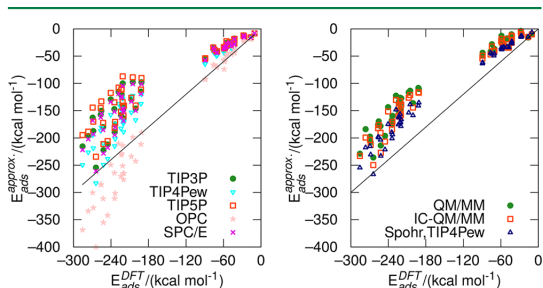


**Figure 7.** Correlation between DFT data and approximate methods for the adsorption energy of (defective) icelike layers. Left: GAL17 using various water models. Right: IC-QM/MM and QM/MM using DFT for water–water interactions (from ref 79) and the Spohr–Heinzinger potential with the TIP4Pew water model.

different water models, while Table 2 provides statistical measures for this set. The graph on the right shows the same data for the QM/MM and IC-QM/MM approaches, in which the many-body effects within the water layer are described at the DFT level, while the ones with the platinum surface are still not captured. Note that the METAL force field of Heinz and co-workers has been excluded in this figure since the adsorption energies are very repulsive due to the use of DFT geometries and the shift to longer Pt–O distances of the minimum around the top sites evidenced in Figure 6.

The first observation is that the OPC water model is quite different compared to the other water models, overestimating the water–water interactions significantly. The other four water models yield rather similar results, with  $R^2$  of 0.89–0.96. While the rmsd is lowest for OPC (3 kcal mol<sup>-1</sup> per H<sub>2</sub>O or 40 kcal mol<sup>-1</sup> per system), it is TIP4Pew that fares overall best, with an rmsd of only 1 and 4 kcal mol<sup>-1</sup> larger (per H<sub>2</sub>O and per system, respectively), but with the smallest maximum error per system (94 kcal mol<sup>-1</sup>, compared to 136 kcal mol<sup>-1</sup> for OPC) and the slope of the linear regression that is closest to 1.0. On the other hand, TIP5P is clearly the worst performer, with an rmsd<sup>tot</sup> of 70 kcal mol<sup>-1</sup>, a maximum error of 143 kcal mol<sup>-1</sup>, and a slope of only 0.66. With an error of 4 kcal mol<sup>-1</sup> per water molecule (for an interaction of about 15 kcal mol<sup>-1</sup>), our approach is short from reaching the 5% accuracy obtained by an empirical scheme for the adsorption energy of icelike structures.<sup>39</sup> However, this approach contains explicit parameters for the strength of hydrogen bonds and the extra stabilization energy in a two-dimensional ice layer. Remarkably,

for nearly complete ice layers, all models predict two distinct families of structures, one being more strongly bound than the other for the same DFT interaction. Since the same applies to the QM/MM and IC-QM/MM simulations, we suggest that it is due to (many-body) charge transfer effects between the icelike layer and the surface, which happen to be more pronounced in the H<sub>down</sub> than the H<sub>up</sub> conformations.

Given the approximations involved in the force field, the overall performance (error of ~4 kcal mol<sup>-1</sup> per H<sub>2</sub>O) for the defective water layers and water clusters on Pt(111) is rather encouraging. This validation set is also well described (albeit at higher computational cost) by the potential of Siepmann and Sprik in combination with a DFT treatment for the water–water interaction. This is partially due to the fact that the water molecules are all located close to the surface where the chemisorption potential is still active and not in the zone beyond 3.0 Å where the interaction is, erroneously, very weak (see Figure 6). By comparing the results for IC-QM/MM with QM/MM, we conclude that the image charge effect, which slightly improves the statistical measures (see Table 2), remains rather small, even for these more complex systems. This further confirms our choice of neglecting this effect in GAL17. Somewhat surprisingly, the Spohr and Heinzinger potential in combination with TIP4Pew consistently outperforms all the other methods for this set.

In summary, water clusters and layers on Pt(111) are challenging test cases for pairwise additive force fields. The combination of our force field with TIP4Pew seems to be a reasonably accurate option, rivaling the more expensive QM/MM methods, while being more accurate for nonequilibrium configurations and the longer-range surface–water interaction (vide supra).

**4.3. Pt(111)/Water Interface.** Characterizing the liquid–solid interface can be seen as the holy grail for interfacial sciences from lubricants and corrosion inhibition to catalysts and batteries, up to nanoparticles in biomedical contexts.<sup>6,7,42</sup>

Several characteristics have been proposed to describe the metal/liquid interface, with density profiles and histograms of characteristic angles being most popular. Therefore, we herein also present results for these quantities, in addition to the ratio of molecules that are on top of a Pt atom. Here, following our previous work on the recognition of adsorption modes on graphical lattices,<sup>112</sup> we define top, bridge, and hollow sites as nonoverlapping circles with a radius of 0.4 Å, covering roughly 37% of the entire surface. Due to symmetry, the ratio top:bridge:hollow is 1:2:2. Hence, for a random distribution we expect 20% of the water molecules assigned to top sites.

Our best estimates come from 10 ps of AIMD for a 192 Pt atoms system with 151 water molecules on top of it, followed

**Table 2.** Statistical Measures for the Accuracy of the Description of (Defective) Icelike Layers<sup>44</sup>

method	rmsd <sup>mol</sup> /kcal mol <sup>-1</sup>	rmsd <sup>tot</sup> /kcal mol <sup>-1</sup>	max. error/kcal mol <sup>-1</sup>	R <sup>2</sup>	slope	intercept/kcal mol <sup>-1</sup>
GAL17-TIP3P	6	63	121	0.90	0.71	9
GAL17-TIP4Pew	4	44	94	0.93	0.83	10
GAL17-TIP5P	6	70	143	0.89	0.66	6
GAL17-OPC	3	40	136	0.96	1.25	16
GAL17-SPC/E	6	60	117	0.91	0.73	9
Spohr-TIP4Pew	3	23	58	0.98	0.97	14
QM/MM	7	61	105	0.95	0.76	17
IC-QM/MM	6	54	97	0.95	0.79	16

<sup>44</sup>The root mean square deviation is reported per molecule rmsd<sup>mol</sup> and for the full system rmsd<sup>tot</sup>.

by a sufficient empty space to avoid confinement effects<sup>12</sup> at the cost of a liquid/vacuum interface. The interface was pre-equilibrated at the IC-QM/MM level of theory as explained in the [Computational Details](#). The AIMD simulations are computationally extremely demanding: a single time step took, on average, 520 s (on 96 CPU cores), totaling to about 140 000 CPU core hours (or 60 days real time) for the 10 ps trajectory. To produce a fair comparison with the force-field methods, the same simulation time has been applied, starting from the same initial configuration, except that the water molecules have been moved away from the surface by 1 Å for the setup using the METAL force field by Heinz in order to avoid the extremely repulsive distances with this force field when starting from DFT geometries. If not stated explicitly, the METAL force field is combined with the SPC/E water model as originally proposed,<sup>78</sup> while the Spohr–Heinzinger and GAL17 force fields rely on the TIP4Pew model, since it gave the best agreement for the icelike water layers (vide supra). The IC-QM/MM simulations can be considered to be better converged, since at least the initial structure is obtained from equilibrating at this level. However, it is not given that accumulating statistics of 10 ps is sufficient even for equilibration. Note that the IC-QM/MM simulations are around 50 times more efficient than pure AIMD, requiring approximately 60 s per time step on 16 CPU cores or roughly 2600 CPU core hours for a 10 ps trajectory. Since the force-field computations are again 4–5 orders of magnitude faster (15 ms per time step on a single CPU core or 2.5 min for 10 ps), we were easily able to assess the equilibration time which turned out to be on the order of 100 ps, with trajectories of 500 ps generally providing converged statistics (see Supporting Information, [Figure S4](#)).

Having these limitations in mind, we can now discuss the results obtained from the 10 ps of simulations for each method. [Figure 8](#) presents the density as a function of the distance from

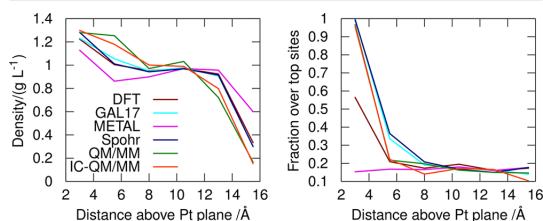


**Figure 8.** Density (left) and fraction of water molecules on top sites (right) as a function of the surface–solution distance for various methods as obtained from a 10 ps MD simulation.

the platinum nuclear plane. Generally, the density at the interface is 20–30% higher than in the bulk, which can be traced back to the significant chemisorption energy and is in qualitative agreement with experimental results for an electrified Ag/H<sub>2</sub>O interface.<sup>57</sup> The density in the bulk region (which here is found to start roughly 8 Å above the surface) corresponds to the expected 1 g L<sup>-1</sup> and is followed by the liquid/vapor (or vacuum) interface. Overall, we find that our water layer is probably somewhat slightly too thin, i.e., that the region that is affected by neither of the interfaces is small to nonexistent, as evidenced by the single point around 10 Å for which all force fields roughly agree. Hence, we suggest that future investigations should have at least 20 Å of solvent on top of the platinum surface. Since running reliable isobaric

simulations for these kind of systems is out of reach for any QM-based method today, we do not recommend to use “filled” unit cells, i.e., two solid/liquid interfaces, in order to avoid artifacts due to confinement effects.<sup>12</sup>

The right-hand side of [Figure 8](#) measures the in-plane ordering of the water layers. In agreement with previous reports, the potential by Siepmann and Sprik used in QM/MM and IC-QM/MM pushes all water molecules on top sites in the first hydration layer, so that hollow and bridge sites are not occupied at all. The same observation applies to the simulations based on the potential by Spohr and Heinzinger. The 10 ps of simulations at the AIMD level were sufficient to reduce the percentage of water on top positions to roughly 0.6. Hence, the bridge and hollow sites become also important at the DFT level, suggesting a less ordered interface than predicted previously.<sup>66</sup> Regarding the GAL17 force field, which underestimates the stability of bridge and hollow adsorption sites (see [Figure 6](#)), the ordering extends to the second layer of water molecules (see [Supporting Information](#) for vsGAL17 results, in which this problem is absent because the bridge and hollow sites are overly stabilized). The METAL force field, on the other hand, is incapable of reproducing the expected ordering, lowering the ratio of top sites below 0.2, the ratio characteristic for a random distribution. This, again, could have been predicted simply by looking at [Figure 6](#), where the hollow and bridge sites are most stable for this force field.

In order to have a more detailed appreciation of the ordering at the first water layer over Pt(111) and how it varies with the different methods, [Figure S7](#) represents typical structures. In all simulations, a significant degree of disordering is observed, although various sizes of ring structures can be recognized. Compared to DFT, the force fields predict somewhat more ordered interfaces with a tendency of mixing six- and four-membered rings, rather than the five- and six-membered rings that dominate the DFT interface. This strongly suggests that these various motives, which can also be found in ice,<sup>113</sup> would need to be included in a force-field fit that aims at a balanced description of water–water and water–metal interactions at the interface due to the inclusion of many-body effects.

Having seen that 10 ps is sufficient to modify the site preference significantly and in agreement with the predictions for a single water molecule, we now investigate the angular preference within the first hydration layer in [Figure 9](#) (for the corresponding results for the “bulklike” layer around 8 Å, see [Figure S6](#) in the Supporting Information). When compared to the random distributions, both angles ( $\theta$ , the orientation of the dipole moment with respect to the surface normal, and  $\varphi$ , the angle describing the rotation of the water molecular plane around the dipole moment) show clear preferences. Regarding the nature of the preference, the different models agree that having the water dipole perpendicular to the surface ( $\theta \approx 0$  or  $180^\circ$ ) is unfavorable. Where the models disagree is regarding the question if inclining the dipole moment up ( $60^\circ$ , GAL17 and IC-QM/MM) or down ( $120^\circ$ , DFT) is energetically preferable compared to the “flat” ( $90^\circ$ , METAL) adsorption mode. Both the QM/MM and the Spohr–Heinzinger potential predict a degeneracy of the “up” and “flat” lying dipole moments. Note that this is the first time within this paper that we can evidence a significant difference between QM/MM and IC-QM/MM. While this is analogous to the findings of Tarmyshov et al. for isopropyl alcohol/water mixtures at the Pt(111) interface,<sup>114</sup> we cannot exclude an artifact due to nonconverged configurational sampling: Extending the GAL17



## Chapter 7. Force Field for Water over Pt(111): Development, Assessment, and Comparison

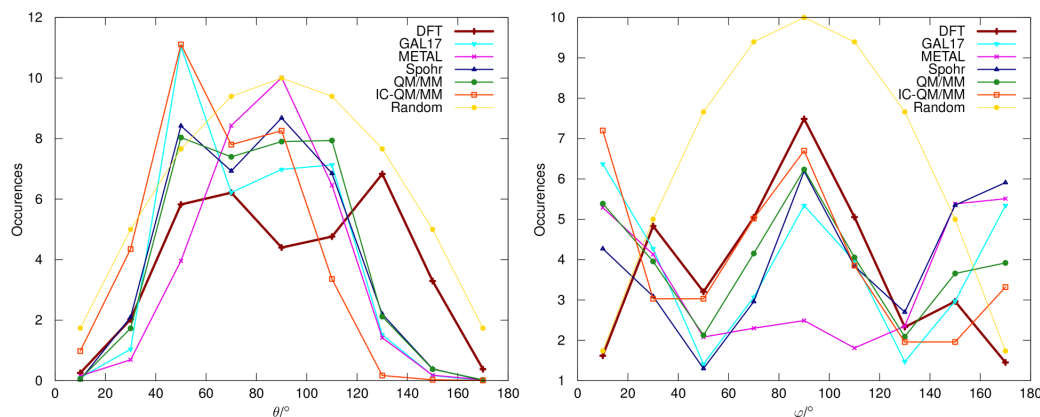


Figure 9. Distributions of  $\theta$  (left) and  $\varphi$  (right) for the first solvation layer for various methods as obtained from a 10 ps MD simulation.

simulations to 500 ps, the interval between 60 and 120 becomes very flat (see Figure S4 in the Supporting Information). The situation is even worse for  $\varphi$ , where the convergence issues with respect to the sampling are enhanced. To conclude, there is no agreement between the methods regarding the balance between  $\varphi = 90^\circ$  and  $\varphi = 0^\circ$ : depending on the method,  $\varphi = 90^\circ$  is a dominant maximum (DFT and random distribution) or a maximum that is almost degenerate with  $\varphi = 0^\circ$  (all other methods, except METAL). At first sight, we have been a bit puzzled that GAL17, which introduces a  $\varphi$  preference, is not significantly different from METAL or the Siepmann and Sprik potential, where this dependence is missing for a single molecule. At second thought, however, this can be explained as follows: the hydrogen repulsion introduced in eq 3 serves to push the hydrogen “up”, away from the surface. At the Pt/H<sub>2</sub>O interface, the same effect can be obtained through the interaction with other water molecules: the hydrogen atoms are charged and will therefore interact with water molecules from the second layer and/or water molecules within the same layer. Hence, hydrogens will be dissuaded from pointing toward the surface due to competition. Nevertheless, we anticipate that the fine structures, such as corrugation and correlations between  $\theta$  and  $\varphi$ , are affected by the physically motivated repulsion between hydrogen atoms and the surface.

Having mentioned the competition between water–water and water–surface interaction, we would like to emphasize the importance of the uncertainty associated with the water model: since the interfacial structure is due to a balance between the energy of a water molecule at the interface and its energy in the bulk solution, it is an open question as to which extent this difference is significant enough to be robust with respect to changes in the water model that mainly affect the water–water interactions. Hence, we have performed additional computations (see Figure S5 in the Supporting Information) by replacing the TIP4Pew water model with TIPSP and OPC, which are, according to Figure 7, the two extremes for weak and strong water–water interactions, respectively. We show in the Supporting Information that even though GAL17 and vsGAL17 are fairly similar for the single-water molecule adsorption modes and for the icelike layers, the results varying the water model and the water–surface interactions fail to provide fully consistent results for the angular distributions.

Hence, we conclude that the greatest caution should be applied when deriving conclusions about the “real” water/metal interfacial structure from either short AIMD or long MM simulations: The relaxation times at the Pt(111)/water interface are high,<sup>66</sup> and the energetic balance between water at the interface and water in bulk solution seems to be too subtle to produce clear-cut and robust interfacial characteristics.

### 5. CONCLUSION

We have presented a novel force-field form for the interaction of water with Pt(111) to capture the angular dependence and surface corrugation. The 12 parameters of the GAL17 force field have been fitted to 210 DFT adsorption energies of water on a Pt(111) surface. The accuracies of GAL17 and several force fields from the literature have been compared for 802 adsorption energies on Pt(111), 52 geometries derived from icelike layers, and an MD simulation of a Pt(111)/water interface, for which we have also presented a 10 ps first-principles trajectory. In all cases, GAL17 shows a better agreement with the DFT results than its predecessors. In particular, the adsorption energies of a single water molecule are reproduced with an rmsd of only 2 kcal mol<sup>-1</sup>, while defective icelike layers are within 4 kcal mol<sup>-1</sup> per H<sub>2</sub>O of the DFT reference energies. Using this force field, we confirm that the equilibration time of the interfacial water is much slower (up to 2 orders of magnitude) than that of bulk water. Moreover, by assessing the combination of GAL17 with different water models, we demonstrate that the fine structure of the interface is very sensitive to the competition between platinum–water and water–water interactions. Hence, we suggest that force fields should only be used to generate relevant configurations that are, subsequently, reassessed at the DFT level in order to gain insight into the “true” nature of the interface, while also keeping in mind the shortcomings of DFT. However, since GAL17 is more accurate than other published force fields, it is a very promising step toward the assessment of MM-based solvation free energies at the interface, which are particularly relevant in heterogeneous catalysis.

### ■ ASSOCIATED CONTENT

#### Supporting Information

The Supporting Information is available free of charge on the ACS Publications website at DOI: 10.1021/acs.jctc.7b01177.

Figures illustrating the Pt–O LJ interaction for various models and the evolution of the histograms of different angles with simulation time and as a function of the water model (PDF)

Archive of geometries, including the 802 water configurations on a  $p(3 \times 3)$  unit cell and the 52 geometries derived from the icelike water layers (ZIP)

Initial structure for the Pt(111)/H<sub>2</sub>O interface, together with a list of PBE-dDsC reference adsorption energies (ZIP)

Input files for IC-QM/MM simulations in cp2k (ZIP)

## AUTHOR INFORMATION

### Corresponding Authors

\*E-mail: [stephan.steinmann@ens-lyon.fr](mailto:stephan.steinmann@ens-lyon.fr).

\*E-mail: [agoetz@sdsu.edu](mailto:agoetz@sdsu.edu).

### ORCID

Stephan N. Steinmann: 0000-0002-2777-356X

Andreas W. Götz: 0000-0002-8048-6906

Paul Fleurat-Lessard: 0000-0003-3114-2522

Marcella Iannuzzi: 0000-0001-9717-2527

Philippe Sautet: 0000-0002-8444-3348

Carine Michel: 0000-0002-4501-7194

### Notes

The authors declare no competing financial interest.

## ACKNOWLEDGMENTS

The authors thank D. Golze for providing input files and equilibrated structures of the IC-QM/MM simulations and T. Jiang for some analysis scripts for the interface. Computational resources were generously provided by the mesocenter PSMN. This work was also granted access to the HPC resources of CINES and IDRIS under the allocation 2014-080609 and A0010810119 made by GENCI. The PHC Germaine de Staël program “Reactivity at the solid/liquid interface: Better simulation for a better comprehension”, number 30617PA, is acknowledged for supporting the collaboration between CM and MI. This work benefited from the support of the project MuSic ANR-14-CE06-0030 of the French National Research Agency (ANR). This research was also supported by the National Science Foundation (grant number CHE-1416571) and used resources at the San Diego Supercomputer Center through the Extreme Science and Engineering Discovery Environment (XSEDE), which is supported by the National Science Foundation (Grant No. ACI-1053575, allocation TG-CHE130010).

## REFERENCES

- (1) Norskov, J. K.; Bligaard, T.; Rossmeisl, J.; Christensen, C. H. Towards the computational design of solid catalysts. *Nat. Chem.* **2009**, *1*, 37.
- (2) van Santen, R. A.; Sautet, P. Conclusion: Challenges to Computational Catalysis. *Computational Methods in Catalysis and Materials Science: An Introduction for Scientists and Engineers* **2009**, 441.
- (3) Calle-Vallejo, F.; Tymoczko, J.; Colic, V.; Vu, Q. H.; Pohl, M. D.; Morgenstern, K.; Loffreda, D.; Sautet, P.; Schuhmann, W.; Bandarenka, A. S. Finding optimal surface sites on heterogeneous catalysts by counting nearest neighbors. *Science* **2015**, *350*, 185.
- (4) Alonso, D. M.; Wettstein, S. G.; Dumesic, J. A. Gamma-valerolactone, a sustainable platform molecule derived from lignocellulosic biomass. *Green Chem.* **2013**, *15*, 584.
- (5) Besson, M.; Gallezot, P.; Pinel, C. Conversion of Biomass into Chemicals over Metal Catalysts. *Chem. Rev.* **2014**, *114*, 1827.
- (6) Benjamin, I. Chemical Reactions and Solvation at Liquid Interfaces: A Microscopic Perspective. *Chem. Rev.* **1996**, *96*, 1449.
- (7) Hakkinen, H. The gold-sulfur interface at the nanoscale. *Nat. Chem.* **2012**, *4*, 443.
- (8) Akpa, B. S.; D'Agostino, C.; Gladden, L. F.; Hindle, K.; Manyar, H.; McGregor, J.; Li, R.; Neurock, M.; Sinha, N.; Stitt, E. H.; Weber, D.; Zeitler, J. A.; Rooney, D. W. Solvent effects in the hydrogenation of 2-butanone. *J. Catal.* **2012**, *289*, 30.
- (9) Michel, C.; Zaffran, J.; Ruppert, A. M.; Matras-Michalska, J.; Jedrzejczyk, M.; Grams, J.; Sautet, P. Role of water on metal catalyst performance for ketone hydrogenation. A joint experimental and theoretical study on levulinic acid conversion into gamma-valerolactone. *Chem. Commun.* **2014**, *50*, 12450.
- (10) Michel, C.; Gallezot, P. Why Is Ruthenium an Efficient Catalyst for the Aqueous-Phase Hydrogenation of Biosourced Carbonyl Compounds? *ACS Catal.* **2015**, *5*, 4130.
- (11) Zaffran, J.; Michel, C.; Delbecq, F.; Sautet, P. Towards more accurate prediction of activation energies for polyalcohol dehydrogenation on transition metal catalysts in water. *Catal. Sci. Technol.* **2016**, *6*, 6615.
- (12) Bellarosa, L.; Garcia-Muelas, R.; Revilla-Lopez, G.; Lopez, N. Diversity at the Water-Metal Interface: Metal, Water Thickness, and Confinement Effects. *ACS Cent. Sci.* **2016**, *2*, 109.
- (13) Ferreira de Moraes, R.; Kerber, T.; Calle-Vallejo, F.; Sautet, P.; Loffreda, D. Capturing Solvation Effects at a Liquid/Nanoparticle Interface by Ab Initio Molecular Dynamics: Pt201 Immersed in Water. *Small* **2016**, *12*, 5312.
- (14) Sakong, S.; Forster-Tonigold, K.; Gross, A. The structure of water at a Pt(111) electrode and the potential of zero charge studied from first principles. *J. Chem. Phys.* **2016**, *144*, 194701.
- (15) Cheng, T.; Xiao, H.; Goddard, W. A. Full atomistic reaction mechanism with kinetics for CO reduction on Cu(100) from ab initio molecular dynamics free-energy calculations at 298 K. *Proc. Natl. Acad. Sci. U. S. A.* **2017**, *114*, 1795.
- (16) Le, J.; Iannuzzi, M.; Cuesta, A.; Cheng, J. Determining Potentials of Zero Charge of Metal Electrodes versus the Standard Hydrogen Electrode from Density-Functional-Theory-Based Molecular Dynamics. *Phys. Rev. Lett.* **2017**, *119*, 016801.
- (17) Bulo, R. E.; Michel, C.; Fleurat-Lessard, P.; Sautet, P. Multiscale Modeling of Chemistry in Water: Are We There Yet? *J. Chem. Theory Comput.* **2013**, *9*, 5567.
- (18) Boereboom, J. M.; Fleurat-Lessard, P.; Bulo, R. E. Explicit Solvation Matters: Performance of QM/MM Solvation Models in Nucleophilic Addition. *J. Chem. Theory Comput.* **2018**, *14*, 1841.
- (19) Tomasi, J.; Persico, M. Molecular Interactions in Solution: An Overview of Methods Based on Continuous Distributions of the Solvent. *Chem. Rev.* **1994**, *94*, 2027.
- (20) Petrosyan, S. A.; Rigos, A. A.; Arias, T. A. Joint Density-Functional Theory: Ab Initio Study of Cr<sub>2</sub>O<sub>3</sub> Surface Chemistry in Solution. *J. Phys. Chem. B* **2005**, *109*, 15436.
- (21) Andreussi, O.; Dabo, I.; Marzari, N. Revised self-consistent continuum solvation in electronic-structure calculations. *J. Chem. Phys.* **2012**, *136*, 064102.
- (22) Ringe, S.; Oberhofer, H.; Hille, C.; Matera, S.; Reuter, K. Function-Space-Based Solution Scheme for the Size-Modified Poisson-Boltzmann Equation in Full-Potential DFT. *J. Chem. Theory Comput.* **2016**, *12*, 4052.
- (23) Mathew, K.; Sundararaman, R.; Letchworth-Weaver, K.; Arias, T. A.; Hennig, R. G. Implicit solvation model for density-functional study of nanocrystal surfaces and reaction pathways. *J. Chem. Phys.* **2014**, *140*, 084106.
- (24) Hutter, J.; Iannuzzi, M.; Schiffmann, F.; VandeVondele, J. CP2K: atomistic simulations of condensed matter systems. *WIREs Comput. Mol. Sci.* **2014**, *4*, 15.
- (25) Sundararaman, R. G.; Letchworth-Weaver, K.; Schwarz, K. A.; Gunceler, D.; Ozhabes, Y.; Arias, T. JDFTx: software for joint density-functional theory. *ArXiv e-prints* **2017**, *1708*, 03621.
- (26) Andreussi, O.; Nattino, F. ENVIRON. <http://www.quantum-environment.org/releases.html>, 2017.

# Chapter 7. Force Field for Water over Pt(111): Development, Assessment, and Comparison

- (27) Saleheen, M.; Heyden, A. Liquid-Phase Modeling in Heterogeneous Catalysis. *ACS Catal.* **2018**, *8*, 2188.
- (28) Desai, S. K.; Pallassana, V.; Neurock, M. A Periodic Density Functional Theory Analysis of the Effect of Water Molecules on Deprotonation of Acetic Acid over Pd(111). *J. Phys. Chem. B* **2001**, *105*, 9171.
- (29) Michel, C.; Auneau, F.; Delbecq, F.; Sautet, P. C-H versus O-H Bond Dissociation for Alcohols on a Rh(111) Surface: A Strong Assistance from Hydrogen Bonded Neighbors. *ACS Catal.* **2011**, *1*, 1430.
- (30) Arnadottir, L.; Stuve, E. M.; Jonsson, H. The effect of coadsorbed water on the stability, configuration and interconversion of formyl (HCO) and hydroxymethylidyne (COH) on platinum (111). *Chem. Phys. Lett.* **2012**, *541*, 32.
- (31) Pliego, J. R.; Riveros, J. M. The Cluster-Continuum Model for the Calculation of the Solvation Free Energy of Ionic Species. *J. Phys. Chem. A* **2001**, *105*, 7241.
- (32) Asthagiri, D.; Pratt, L. R.; Ashbaugh, H. S. Absolute hydration free energies of ions, ion-water clusters, and quasichemical theory. *J. Chem. Phys.* **2003**, *119*, 2702.
- (33) Bryantsev, V. S.; Diallo, M. S.; Goddard, W. A., III Calculation of Solvation Free Energies of Charged Solutes Using Mixed Cluster/Continuum Models. *J. Phys. Chem. B* **2008**, *112*, 9709.
- (34) Wang, H.-F.; Liu, Z.-P. Formic Acid Oxidation at Pt/H<sub>2</sub>O Interface from Periodic DFT Calculations Integrated with a Continuum Solvation Model. *J. Phys. Chem. C* **2009**, *113*, 17502.
- (35) Cao, D.; Lu, G. Q.; Wieckowski, A.; Wasileski, S. A.; Neurock, M. Mechanisms of methanol decomposition on platinum: A combined experimental and ab initio approach. *J. Phys. Chem. B* **2005**, *109*, 11622.
- (36) Wasileski, S. A.; Janik, M. J. A first-principles study of molecular oxygen dissociation at an electrode surface: a comparison of potential variation and coadsorption effects. *Phys. Chem. Chem. Phys.* **2008**, *10*, 3613.
- (37) Zope, B. N.; Hibbitts, D. D.; Neurock, M.; Davis, R. J. Reactivity of the Gold/Water Interface During Selective Oxidation Catalysis. *Science* **2010**, *330*, 74.
- (38) Hibbitts, D. D.; Neurock, M. Influence of oxygen and pH on the selective oxidation of ethanol on Pd catalysts. *J. Catal.* **2013**, *299*, 261.
- (39) Revilla-Lopez, G.; Lopez, N. A unified study for water adsorption on metals: meaningful models from structural motifs. *Phys. Chem. Chem. Phys.* **2014**, *16*, 18933.
- (40) Ogasawara, H.; Brena, B.; Nordlund, D.; Nyberg, M.; Pelmenchikov, A.; Pettersson, L. G. M.; Nilsson, A. Structure and Bonding of Water on Pt(111). *Phys. Rev. Lett.* **2002**, *89*, 276102.
- (41) Michaelides, A.; Ranea, V. A.; de Andres, P. L.; King, D. A. General Model for Water Monomer Adsorption on Close-Packed Transition and Noble Metal Surfaces. *Phys. Rev. Lett.* **2003**, *90*, 216102.
- (42) Bjorneholm, O.; Hansen, M. H.; Hodgson, A.; Liu, L.-M.; Limmer, D. T.; Michaelides, A.; Pedevilla, P.; Rossmel, J.; Shen, H.; Tocci, G.; Tyrode, E.; Walz, M.-M.; Werner, J.; Bluhm, H. Water at Interfaces. *Chem. Rev.* **2016**, *116*, 7698.
- (43) Davda, R. R.; Shabaker, J. W.; Huber, G. W.; Cortright, R. D.; Dumesic, J. A. A review of catalytic issues and process conditions for renewable hydrogen and alkanes by aqueous-phase reforming of oxygenated hydrocarbons over supported metal catalysts. *Appl. Catal., B* **2005**, *56*, 171.
- (44) Liu, J.; Cao, X.-M.; Hu, P. Density functional theory study on the activation of molecular oxygen on a stepped gold surface in an aqueous environment: a new approach for simulating reactions in solution. *Phys. Chem. Chem. Phys.* **2014**, *16*, 4176.
- (45) Gu, G. H.; Schweitzer, B.; Michel, C.; Steinmann, S. N.; Sautet, P.; Vlachos, D. G. Group Additivity for Aqueous Phase Thermochemical Properties of Alcohols on Pt(111). *J. Phys. Chem. C* **2017**, *121*, 21510.
- (46) Iyemperumal, S. K.; Deskins, N. A. Evaluating Solvent Effects at the Aqueous/Pt(111) Interface. *ChemPhysChem* **2017**, *18*, 2171–2190.
- (47) Kovalenko, A.; Hirata, F. Self-consistent description of a metal-water interface by the Kohn-Sham density functional theory and the three-dimensional reference interaction site model. *J. Chem. Phys.* **1999**, *110*, 10095.
- (48) Faheem, M.; Heyden, A. Hybrid Quantum Mechanics/Molecular Mechanics Solvation Scheme for Computing Free Energies of Reactions at Metal-Water Interfaces. *J. Chem. Theory Comput.* **2014**, *10*, 3354.
- (49) Bodenschatz, C. J.; Sarupria, S.; Getman, R. B. Molecular-Level Details about Liquid H<sub>2</sub>O Interactions with CO and Sugar Alcohol Adsorbates on Pt(111) Calculated Using Density Functional Theory and Molecular Dynamics. *J. Phys. Chem. C* **2015**, *119*, 13642.
- (50) Lim, H.-K.; Lee, H.; Kim, H. A Seamless Grid-Based Interface for Mean-Field QM/MM Coupled with Efficient Solvation Free Energy Calculations. *J. Chem. Theory Comput.* **2016**, *12*, 5088.
- (51) Steinmann, S. N.; Sautet, P.; Michel, C. Solvation free energies for periodic surfaces: comparison of implicit and explicit solvation models. *Phys. Chem. Chem. Phys.* **2016**, *18*, 31850.
- (52) Schravendijk, P.; van der Vegt, N.; Delle Site, L.; Kremer, K. Dual-Scale Modeling of Benzene Adsorption onto Ni(111) and Au(111) Surfaces in Explicit Water. *ChemPhysChem* **2005**, *6*, 1866.
- (53) Lee, M.-S.; Peter McGrail, B.; Rousseau, R.; Glezakou, V.-A. Structure, dynamics and stability of water/scCO<sub>2</sub>/mineral interfaces from ab initio molecular dynamics simulations. *Sci. Rep.* **2015**, *5*, 14857.
- (54) Cantu, D. C.; Wang, Y.-G.; Yoon, Y.; Glezakou, V.-A.; Rousseau, R.; Weber, R. S. Heterogeneous catalysis in complex, condensed reaction media. *Catal. Today* **2017**, *289*, 231.
- (55) Wertz, D. H. Relationship between the gas-phase entropies of molecules and their entropies of solvation in water and 1-octanol. *J. Am. Chem. Soc.* **1980**, *102*, 5316.
- (56) Kelly, E.; Seth, M.; Ziegler, T. Calculation of Free Energy Profiles for Elementary Bimolecular Reactions by ab Initio Molecular Dynamics: Sampling Methods and Thermostat Considerations. *J. Phys. Chem. A* **2004**, *108*, 2167.
- (57) Toney, M. F.; Howard, J. N.; Richer, J.; Borges, G. L.; Gordon, J. G.; Melroy, O. R.; Wiesler, D. G.; Yee, D.; Sorensen, L. B. Voltage-dependent ordering of water molecules at an electrode-electrolyte interface. *Nature* **1994**, *368*, 444.
- (58) Schiros, T.; Andersson, K. J.; Pettersson, L. G. M.; Nilsson, A.; Ogasawara, H. Chemical bonding of water to metal surfaces studied with core-level spectroscopies. *J. Electron Spectrosc. Relat. Phenom.* **2010**, *177*, 85.
- (59) Velasco-Velez, J.-J.; Wu, C. H.; Pascal, T. A.; Wan, L. F.; Guo, J.; Prendergast, D.; Salmeron, M. The structure of interfacial water on gold electrodes studied by x-ray absorption spectroscopy. *Science* **2014**, *346*, 831.
- (60) Spohr, E.; Heinzinger, K. Molecular dynamics simulation of a water/metal interface. *Chem. Phys. Lett.* **1986**, *123*, 218.
- (61) Spohr, E.; Heinzinger, K. A Molecular Dynamics Study on the Water/Metal Interfacial Potential. *Ber. Bunsenges Phys. Chem.* **1988**, *92*, 1358.
- (62) Spohr, E. Computer simulation of the water/platinum interface. *J. Phys. Chem.* **1989**, *93*, 6171.
- (63) Zhu, S.; Philpott, M. R. Interaction of water with metal surfaces. *J. Chem. Phys.* **1994**, *100*, 6961.
- (64) Siepmann, J. I.; Sprik, M. Influence of surface topology and electrostatic potential on water/electrode systems. *J. Chem. Phys.* **1995**, *102*, 511.
- (65) Iori, F.; Di Felice, R.; Molinari, E.; Corni, S. GoIP: An atomistic force-field to describe the interaction of proteins with Au(111) surfaces in water. *J. Comput. Chem.* **2009**, *30*, 1465.
- (66) Limmer, D. T.; Willard, A. P.; Madden, P.; Chandler, D. Hydration of metal surfaces can be dynamically heterogeneous and hydrophobic. *Proc. Natl. Acad. Sci. U. S. A.* **2013**, *110*, 4200.
- (67) Li, X.; Agren, H. Molecular Dynamics Simulations Using a Capacitance-Polarizability Force Field. *J. Phys. Chem. C* **2015**, *119*, 19430.



- (68) Natarajan, S. K.; Behler, J. Neural network molecular dynamics simulations of solid-liquid interfaces: water at low-index copper surfaces. *Phys. Chem. Chem. Phys.* **2016**, *18*, 28704.
- (69) Berg, A.; Peter, C.; Johnston, K. Evaluation and Optimization of Interface Force Fields for Water on Gold Surfaces. *J. Chem. Theory Comput.* **2017**, *13*, 5610–5623.
- (70) Wang, Y.; Bowman, J. M. Ab initio potential and dipole moment surfaces for water. II. Local-monomer calculations of the infrared spectra of water clusters. *J. Chem. Phys.* **2011**, *134*, 154510.
- (71) Medders, G. R.; Babin, V.; Paesani, F. Development of a "First-Principles" Water Potential with Flexible Monomers. III. Liquid Phase Properties. *J. Chem. Theory Comput.* **2014**, *10*, 2906.
- (72) Perdew, J. P.; Burke, K.; Ernzerhof, M. Generalized Gradient Approximation Made Simple. *Phys. Rev. Lett.* **1996**, *77*, 3865.
- (73) Steinmann, S. N.; Corminboeuf, C. Comprehensive Benchmarking of a Density-Dependent Dispersion Correction. *J. Chem. Theory Comput.* **2011**, *7*, 3567.
- (74) Gautier, S.; Steinmann, S. N.; Michel, C.; Fleurat-Lessard, P.; Sautet, P. Molecular adsorption at Pt(111). How accurate are DFT functionals? *Phys. Chem. Chem. Phys.* **2015**, *17*, 28921.
- (75) Holloway, S.; Bennemann, K. H. *Surf. Sci.* **1980**, *101*, 327.
- (76) Yeh, K.-Y.; Janik, M. J.; Maranas, J. K. *Electrochim. Acta* **2013**, *101*, 308.
- (77) Case, D. A.; Cerutti, D. S.; Cheatham, T. E., III; Darden, T. A.; Duke, R. E.; Giese, T. J.; Gohlke, H.; Goetz, A. W.; Greene, D.; Homeyer, N.; Izadi, S.; Kovalenko, A.; Lee, T. S.; LeGrand, S.; Li, P.; Lin, C.; Liu, J.; Luchko, T.; Luo, R.; Mermelstein, D.; Merz, K. M.; Monard, G.; Nguyen, H.; Omelyan, I.; Onufriev, A.; Pan, F.; Qi, R.; Roe, D.R.; Roitberg, A.; Sagui, C.; Simmerling, C. L.; Botello-Smith, W. M.; Swails, J.; Walker, R. C.; Wang, J.; Wolf, R. M.; Wu, X.; Xiao, L.; York, D. M.; Kollman, P. A. *AMBER 2017*; University of California: San Francisco, CA, 2017.
- (78) Heinz, H.; Vaia, R. A.; Farmer, B. L.; Naik, R. R. Accurate Simulation of Surfaces and Interfaces of Face-Centered Cubic Metals Using 12–6 and 9–6 Lennard-Jones Potentials. *J. Phys. Chem. C* **2008**, *112*, 17281.
- (79) Golze, D.; Iannuzzi, M.; Nguyen, M.-T.; Passerone, D.; Hutter, J. Simulation of Adsorption Processes at Metallic Interfaces: An Image Charge Augmented QM/MM Approach. *J. Chem. Theory Comput.* **2013**, *9*, 5086.
- (80) Willard, A. P.; Limmer, D. T.; Madden, P. A.; Chandler, D. Characterizing heterogeneous dynamics at hydrated electrode surfaces. *J. Chem. Phys.* **2013**, *138*, 184702.
- (81) van Duin, A. C. T.; Bryantsev, V. S.; Diallo, M. S.; Goddard, W. A.; Rahaman, O.; Doren, D. J.; Raymand, D.; Hermansson, K. Development and Validation of a ReaxFF Reactive Force Field for Cu Cation/Water Interactions and Copper Metal/Metal Oxide/Metal Hydroxide Condensed Phases. *J. Phys. Chem. A* **2010**, *114*, 9507.
- (82) Iori, F.; Corni, S. Including image charge effects in the molecular dynamics simulations of molecules on metal surfaces. *J. Comput. Chem.* **2008**, *29*, 1656.
- (83) Steinmann, S. N.; Fleurat-Lessard, P.; Götz, A. W.; Michel, C.; Ferreira de Morais, R.; Sautet, P. Molecular mechanics models for the image charge, a comment on "including image charge effects in the molecular dynamics simulations of molecules on metal surfaces". *J. Comput. Chem.* **2017**, *38*, 2127.
- (84) Corni, S. Reply to "Molecular mechanics models for the image charge". *J. Comput. Chem.* **2017**, *38*, 2130.
- (85) Meng, S.; Wang, E. G.; Gao, S. Water adsorption on metal surfaces: A general picture from density functional theory studies. *Phys. Rev. B: Condens. Matter Mater. Phys.* **2004**, *69*, 195404.
- (86) Cicero, G.; Calzolari, A.; Corni, S.; Catellani, A. Anomalous Wetting Layer at the Au(111) Surface. *J. Phys. Chem. Lett.* **2011**, *2*, 2582.
- (87) Michel, C.; Gold, F.; Sautet, P. Early stages of water/hydroxyl phase generation at transition metal surfaces - synergetic adsorption and O-H bond dissociation assistance. *Phys. Chem. Chem. Phys.* **2012**, *14*, 15286.
- (88) Medders, G. R.; Götz, A. W.; Morales, M. A.; Bajaj, P.; Paesani, F. On the representation of many-body interactions in water. *J. Chem. Phys.* **2015**, *143*, 104102.
- (89) Reddy, S. K.; Straight, S. C.; Bajaj, P.; Pham, C. H.; Riera, M.; Moberg, D. R.; Morales, M. A.; Knight, C.; Götz, A. W.; Paesani, F. On the accuracy of the MB-pol many-body potential for water: Interaction energies, vibrational frequencies, and classical thermodynamic and dynamical properties from clusters to liquid water and ice. *J. Chem. Phys.* **2016**, *145*, 194504.
- (90) Mitsui, T.; Rose, M. K.; Fomin, E.; Ogletree, D. F.; Salmeron, M. Water Diffusion and Clustering on Pd(111). *Science* **2002**, *297*, 1850.
- (91) Le Roy, R. J.; Dattani, N. S.; Coxon, J. A.; Ross, A. J.; Crozet, P.; Linton, C. Accurate analytic potentials for  $\text{Li}_2(X^1\Sigma_g^+)$  and  $\text{Li}_2(A^1\Sigma_u^+)$  from 2 to 90 Å, and the radiative lifetime of  $\text{Li}(2p)$ . *J. Chem. Phys.* **2009**, *131*, 204309.
- (92) Kresse, G.; Hafner, J. Ab initio molecular dynamics for liquid metals. *Phys. Rev. B: Condens. Matter Mater. Phys.* **1993**, *47*, 558.
- (93) Kresse, G.; Furthmüller, J. Efficient iterative schemes for ab initio total-energy calculations using a plane-wave basis set. *Phys. Rev. B: Condens. Matter Mater. Phys.* **1996**, *54*, 11169.
- (94) Blochl, P. E. Projector augmented-wave method. *Phys. Rev. B: Condens. Matter Mater. Phys.* **1994**, *50*, 17953.
- (95) Kresse, G.; Joubert, D. From ultrasoft pseudopotentials to the projector augmented-wave method. *Phys. Rev. B: Condens. Matter Mater. Phys.* **1999**, *59*, 1758.
- (96) Grimme, S.; Antony, J.; Ehrlich, S.; Krieg, H. A consistent and accurate ab initio parametrization of density functional dispersion correction (DFT-D) for the 94 elements H-Pu. *J. Chem. Phys.* **2010**, *132*, 154104.
- (97) Darden, T.; York, D.; Pedersen, L. Particle mesh Ewald: An Nlog(N) method for Ewald sums in large systems. *J. Chem. Phys.* **1993**, *98*, 10089.
- (98) Berendsen, H. J. C.; Postma, J. P. M.; van Gunsteren, W. F.; DiNola, A.; Haak, J. R. Molecular dynamics with coupling to an external bath. *J. Chem. Phys.* **1984**, *81*, 3684.
- (99) Miyamoto, S.; Kollman, P. A. Settle: An analytical version of the SHAKE and RATTLE algorithm for rigid water models. *J. Comput. Chem.* **1992**, *13*, 952.
- (100) Vandevondele, J.; Hutter, J. An efficient orbital transformation method for electronic structure calculations. *J. Chem. Phys.* **2003**, *118*, 4365.
- (101) Izvekov, S.; Parrinello, M.; Burnham, C. J.; Voth, G. A. Effective force fields for condensed phase systems from ab initio molecular dynamics simulation: A new method for force-matching. *J. Chem. Phys.* **2004**, *120*, 10896.
- (102) Soler, J. M.; Artacho, E.; Gale, J. D.; García, A.; Junquera, J.; Ordejon, P.; Sánchez-Portal, D. The SIESTA method for ab initio order-*N* materials simulation. *J. Phys.: Condens. Matter* **2002**, *14*, 2745.
- (103) König, G.; Hudson, P. S.; Boreesch, S.; Woodcock, H. L. Multiscale Free Energy Simulations: An Efficient Method for Connecting Classical MD Simulations to QM or QM/MM Free Energies Using Non-Boltzmann Bennett Reweighting Schemes. *J. Chem. Theory Comput.* **2014**, *10*, 1406.
- (104) Cave-Ayland, C.; Skylaris, C.-K.; Essex, J. W. A Monte Carlo Resampling Approach for the Calculation of Hybrid Classical and Quantum Free Energies. *J. Chem. Theory Comput.* **2017**, *13*, 415.
- (105) Raghavan, K.; Foster, K.; Motakabbir, K.; Berkowitz, M. Structure and dynamics of water at the Pt(111) interface: Molecular dynamics study. *J. Chem. Phys.* **1991**, *94*, 2110.
- (106) van Duin, A. C. T.; Dasgupta, S.; Lorant, F.; Goddard, W. A. ReaxFF: A Reactive Force Field for Hydrocarbons. *J. Phys. Chem. A* **2001**, *105*, 9396.
- (107) Jorgensen, W. L.; Chandrasekhar, J.; Madura, J. D.; Impey, R. W.; Klein, M. L. Comparison of simple potential functions for simulating liquid water. *J. Chem. Phys.* **1983**, *79*, 926.
- (108) Horn, H. W.; Swope, W. C.; Pitera, J. W.; Madura, J. D.; Dick, T. J.; Hura, G. L.; Head-Gordon, T. Development of an improved

## Chapter 7. Force Field for Water over Pt(111): Development, Assessment, and Comparison

four-site water model for biomolecular simulations: TIP4P-Ew. *J. Chem. Phys.* **2004**, *120*, 9665.

(109) Mahoney, M. W.; Jorgensen, W. L. A five-site model for liquid water and the reproduction of the density anomaly by rigid, nonpolarizable potential functions. *J. Chem. Phys.* **2000**, *112*, 8910.

(110) Berendsen, H. J. C.; Grigera, J. R.; Straatsma, T. P. The missing term in effective pair potentials. *J. Phys. Chem.* **1987**, *91*, 6269.

(111) Izadi, S.; Anandakrishnan, R.; Onufriev, A. V. Building Water Models: A Different Approach. *J. Phys. Chem. Lett.* **2014**, *5*, 3863.

(112) Vignola, E.; Steinmann, S. N.; Vandegheuchte, B. D.; Curulla, D.; Stamatakis, M.; Sautet, P. A machine learning approach to graph-theoretical cluster expansions of the energy of adsorbate layers. *J. Chem. Phys.* **2017**, *147*, 054106.

(113) Chen, J.; Zen, A.; Brandenburg, J. G.; Alfe, D.; Michaelides, A. Evidence for stable square ice from quantum Monte Carlo. *Phys. Rev. B: Condens. Matter Mater. Phys.* **2016**, *94*, 220102.

(114) Tarmyshov, K. B.; Mueller-Plathe, F. Interface between platinum(111) and liquid isopropanol (2-propanol): A model for molecular dynamics studies. *J. Chem. Phys.* **2007**, *126*, 074702.

## 8 Impacts of electrode potentials and solvents on the electroreduction of CO<sub>2</sub>: a comparison of theoretical approaches

The previous chapters (5-7) have highlighted the challenges of modelling the metal/liquid interface in the context of heterogeneous catalysis. The next two chapters are dealing with an even harder problem: heterogeneous electro-catalysis. The electrochemical potential is not straight forward to control in atomistic simulations and the impact of the solvent and the electrolyte can by no means be neglected in electro-catalysis. In computational chemistry, modifying potential, i.e., the workfunction, implies modifying the surface charge. For modifying the surface charge, two approaches exist: Either, ion/electron pairs are explicitly simulated or only the number of electrons is adapted, while the countercharge is provided by an implicit description. Technically, the easiest way of introducing a countercharge is a homogeneous background charge. This is the approach that we exploited in combination with an implicit solvent for the electro-reduction of CO<sub>2</sub> over a nickel surface. Compared to water, the aprotic solvent used experimentally (DMF) is less specifically interacting with the surface. Therefore, approximating the solvent effect by electrostatic interactions is better justified for DMF than for aqueous solutions over oxophilic metals such as Pt or Ni. Moreover, since DMF is expected to form a liquid, i.e., random add-layer, evaluating electrochemical reactions with explicit DMF molecules would have been very cumbersome. To assess the suitability of this simplified method, where the combination of an implicit solvent with a homogeneous background charge serves as a model for the double layer, we have assessed the qualitative features of CO<sub>2</sub> electroreduction under aprotic conditions, investigating the difference between the preferred steps in solution and the influence of the catalyst surface for modifying the preference between the two simplest products, CO and oxalate. We found that the adsorption behavior of CO<sub>2</sub> follows the expected behavior when explicitly including the electrochemical potential, i.e., at reducing potentials it becomes an exothermic process.





Cite this: *Phys. Chem. Chem. Phys.*, 2015, 17, 13949

## Impacts of electrode potentials and solvents on the electroreduction of CO<sub>2</sub>: a comparison of theoretical approaches†

Stephan N. Steinmann,<sup>a</sup> Carine Michel,<sup>ab</sup> Renate Schwiedernoch<sup>c</sup> and Philippe Sautet<sup>\*ab</sup>

Since CO<sub>2</sub> is a readily available feedstock throughout the world, the utilization of CO<sub>2</sub> as a C1 building block for the synthesis of valuable chemicals is a highly attractive concept. However, due to its very nature of energy depleted “carbon sink”, CO<sub>2</sub> has a very low reactivity. Electrocatalysis offers the most attractive means to activate CO<sub>2</sub> through reduction: the electron is the “cleanest” reducing agent whose energy can be tuned to the thermodynamic optimum. Under protic conditions, the reduction of CO<sub>2</sub> over many metal electrodes results in formic acid. Thus, to open the road to its utilization as a C1 building block, the presence of water should be avoided to allow a more diverse chemistry, in particular for C–C bond formation with alkenes. Under those conditions, the intrinsic reactivity of CO<sub>2</sub> can generate carbonates and oxalates by C–O and C–C bond formation, respectively. On Ni(111), almost exclusively carbonates and carbon monoxide are evidenced experimentally. Despite recent progress in modelling electrocatalytic reactions, determining the actual mechanism and selectivities between competing reaction pathways is still not straight forward. As a simple but important example of the intrinsic reactivity of CO<sub>2</sub> under aprotic conditions, we highlight the shortcomings of the popular linear free energy relationship for electrode potentials (LFER-EP). Going beyond this zeroth order approximation by charging the surface and thus explicitly including the electrochemical potential into the electronic structure computations allows us to access more detailed insights, shedding light on coverage effects and on the influence of counterions.

Received 13th February 2015,  
Accepted 21st April 2015

DOI: 10.1039/c5cp00946d

www.rsc.org/pccp

### 1 Introduction

Heterogeneous electrocatalysis is at the heart of advanced energy technologies such as hydrogen production<sup>1</sup> and fuel-cells.<sup>2</sup> Furthermore, electrochemistry, in combination with photovoltaic cells, promises access to “green” and “mild” redox chemistry.<sup>3–5</sup> In particular, the electroreduction of CO<sub>2</sub> is a conceptually attractive avenue: electrochemistry activates the intrinsically rather inert green-house gas under mild conditions (*i.e.*, low pressure and temperature), enabling us to utilize CO<sub>2</sub> as a C1 building block in C–C coupling reactions<sup>6–9</sup> or to generate

small, energy rich molecules such as CO, methanol or formic acid.<sup>10–13</sup>

In protic media, the reduction of CO<sub>2</sub> competes with H<sub>2</sub> evolution and mixtures of CO + H<sub>2</sub>O, formic acid and very small amounts of hydrocarbons are observed in general.<sup>14,15</sup> Hence, the efficient use of CO<sub>2</sub> as a C1 building block precludes the presence of water and protons. For instance the electroreduction of CO<sub>2</sub> in DMF in the presence of a diene over Ni has been reported to yield C–C coupled products, in particular the dicarboxylates.<sup>6,7,16–18</sup> However, the existing procedure is not very efficient in terms of yield and selectivity and the mechanism is poorly understood. In addition, in aprotic solvents, CO<sub>2</sub> has an intrinsic reactivity, potentially yielding oxalate and a combination of CO and carbonate,<sup>11,19</sup> opening additional reaction paths.

Electrocatalysis is carried out in a complex environment, *i.e.*, an electrolyte is required to increase the conductivity of the solution and the interface between the catalyst and the solvent is thin compared to the solution, making experimental characterization challenging.<sup>20–25</sup> Despite considerable efforts, we lack, therefore, a detailed mechanistic understanding at the atomic level, hampering the rational design of novel catalysts. For all these reasons, research and development have still huge

<sup>a</sup> Université de Lyon, Laboratoire de Chimie, Ecole Normale Supérieure de Lyon 46 allée d'Italie, Lyon, France

<sup>b</sup> CNRS, Laboratoire de Chimie, UMR 5182, 46 allée d'Italie, Lyon, France.

E-mail: philippe.sautet@ens-lyon.fr; Fax: +334 7272 8080; Tel: +334 7272 8155

<sup>c</sup> Eco-Efficient Products and Processes Laboratory (E2P2L), UMI 3464 Solvay/CNRS, Shanghai, P. R. China

† Electronic supplementary information (ESI) available: Bader charges for selected adsorbates as a function of potential, all geometries optimized at zero-charge in a vacuum and a shell-script to post-process VASP computations according to the correction proposed by Filhol and Neurock. See DOI: 10.1039/c5cp00946d

## Chapter 8. Impacts of electrode potentials and solvents on the electroreduction of CO<sub>2</sub>: a comparison of theoretical approaches

View Article Online

Paper

PCCP

challenges to overcome in order to efficiently use CO<sub>2</sub> as a C1 building block.

Atomic scale modelling is a powerful tool for complementing the experimental effort and providing detailed information under very well controlled conditions (catalyst surface, applied potential). However, computations are usually performed on simplified models and the influences of the electrolyte and of the solvent on the catalyst interfacial properties are rarely considered,<sup>26</sup> although their importance is well known from more empirical approaches.<sup>27,28</sup> The classical description of electrochemical systems typically relies on “empirical” or at least drastically simplified equations<sup>29</sup> (e.g., Marcus–Hush for electron transfer, Gouy–Chapman for the double layer properties or the Fokker–Planck equation for mass transport). These mesoscopic equations require system averaged parameters which can either be obtained by fitting to experiment or approximately extracted from first principles data. Although such multi-scale models<sup>30,31</sup> may correctly describe the relevant physics, the fundamental issue is that the central ingredient in electrocatalysis, the electrochemical potential, is far from being straight forward to include explicitly in a first principles approach at the atomic level.

The present study investigates the electroreduction of CO<sub>2</sub> in an aprotic solvent as a prerequisite for further investigations of the CO<sub>2</sub> coupling with alkenes.<sup>6,7,16–18</sup> Oxalate is the major product of CO<sub>2</sub> electrolysis under aprotic conditions on “inert” electrodes, in particular over Pb.<sup>32,33</sup> The proposed reaction mechanism, which is in good agreement with the high overpotentials required for this reaction, goes through CO<sub>2</sub><sup>•-</sup>. The radical anion is supposed to be slightly stabilized by the surface at potentials below –1.8 V (vs. Ag/AgCl) and then undergo a fast surface assisted coupling.<sup>34</sup> On more reactive electrodes, and in particular over nickel, CO formation is frequently reported.<sup>11,14</sup>

The large majority of simulations of heterogeneous electrocatalysis rely on a simple model proposed in the seminal work reported by Norskov and coworkers under the name of the computational hydrogen electrode (CHE),<sup>35</sup> and its extension to other cations than H<sup>+</sup>, e.g., Li<sup>+</sup><sup>36</sup> or Na<sup>+</sup>, which we call linear free energy relationship for electrode potentials (LFER-EP). In this model, the electrochemical potential is assumed to affect only the chemical potential of the exchanged electrons and solvent effects are generally neglected. In a nutshell, this approach is an *a posteriori* correction of first principles studies of neutral metal surfaces in a vacuum that are routine computations for some decades.<sup>37</sup> The CHE model leads to highly exploitable results,<sup>38–44</sup> despite its known limitations: the absence of polarisation of adsorbed molecules and electron transfer strictly coupled to cation transfer. This implies, for example, that this method cannot grasp the transient anionic species CO<sub>2</sub><sup>•-</sup>.

The comparison by Rossmeisl *et al.*<sup>45</sup> of the zeroth order approach CHE and the more advanced surface charge (SC) method of Filhol and Neurock<sup>46</sup> (*vide infra*) concluded that for adsorbates with large dipole moments and for kinetic studies the more sophisticated SC method should be applied.<sup>45</sup> However, to go beyond the CHE approach, one needs to explicitly integrate the electrochemical potential into the first principles calculations. Applying an electrochemical potential is equivalent to tune the

workfunction, which is simulated by adding or subtracting electrons from the neutral system. Hence, charged systems are necessary to explicitly investigate the effect of an electrochemical potential on surface adsorbed species. Unfortunately, charged systems cannot be simulated under periodic boundary conditions, which most efficiently simulate extended metallic systems: a periodically charged system is infinitely charged and hence the Coulomb potential diverges. Therefore, when changing the number of electrons in periodic computations a countercharge is required. Several schemes have been proposed in the literature.<sup>26,46–53</sup> The technically simplest way to deal with the situation is to include a homogeneous background charge.<sup>46</sup> The technical simplicity leads to a major drawback: the uniform background charge interacts with the system, even within the metallic slab. Filhol and Neurock have proposed a correction, leading to the surface charging (SC) method, in order to mitigate the issue.<sup>46,52</sup> The SC model provides, despite the approximations, excellent agreement with experiment when a water bilayer is used to solvate the surfaces, as exemplified by the phase diagram of H<sub>2</sub>O over Pt<sup>45,54</sup> and Ni,<sup>55</sup> CO electro-oxidation over Pt<sup>56</sup> and the borohydride oxidation.<sup>57</sup>

In addition to the electrochemical potential, electrochemistry depends critically on the solvent because the dielectric constant of the solvent governs the capability of a system to stabilize and “store” charges, *i.e.*, the capacitance of the system. Therefore, solvent effects are especially important for charged systems. So far, the water solvent was modeled using an explicit bilayer of water.<sup>45,54–59</sup> In our case, we aim at modelling an aprotic solvent such as DMF. However, just like including an electrochemical potential into the simulations, accounting for solvent effects in electronic structure computations of extended systems is still in its infancy,<sup>60–63</sup> with implicit solvent models becoming publicly available only very recently.<sup>64</sup> This is in contrast with the situation of molecular chemistry where several solvent models have been developed and applied for many years.<sup>65</sup>

The aim of this study is two-fold. On the one hand, we will provide some insight into the selectivity towards the formation of carbonates upon CO<sub>2</sub> electrolysis over nickel under aprotic conditions. On the other hand, we will elucidate the influence of the applied electrochemical potential on species adsorbed on a metal surface in order to clarify two aspects of the modelling of heterogeneous electrocatalysis: first, the importance to account explicitly for the electrochemical potential, going beyond the simplest consideration of the electrochemical potential and second the role of modelling the solvent.

The following section reminds the reader of the basics of modelling electrochemistry, before discussing the advantages and limitations of the two schemes applied herein: the simple linear free energy relationship for the electron chemical potential (LFER-EP), popularized by Norskov and coworkers and the explicit change of the electrochemical potential through charging the surface and neutralizing the simulation cell with a homogeneous background charge (SC) as developed by Filhol and Neurock. After this methodological discussion, the results for aprotic CO<sub>2</sub> reduction as described by the two approaches are presented to illustrate the influence of the applied electrochemical potential

and the solvation effects simultaneously. With the SC method, we investigate the origin of the selectivity of Ni(111) to produce carbon monoxide and carbonates rather than oxalates.

## 2 Methods

Computational modelling of electrochemistry is hampered by the simple fact that the electrode potential is not a natural variable in quantum chemical computations. Most chemists are used to think in the “constant charge” picture, *i.e.*, the number of electrons is not fluctuating during a reaction. Since each species with a given number of electrons corresponds to a different electrochemical potential, the “constant charge” picture is inadequate for electrochemistry, where all the intermediates should be treated at the same potential. For example, CO<sub>2</sub> adsorbed on a metal surface corresponds to a different potential than CO and O co-adsorbed on the same surface. Hence, to get the correct reaction energy, the charge on the surface for adsorbed CO<sub>2</sub> and CO, O needs to be adapted individually to reach the desired potential. Therefore, an electrochemical half-cell is effectively a grand-canonical ensemble where the number of electrons is adapted according to the electrochemical potential in a different way for different intermediates of an electrochemical reaction. The most realistic approach would be to account for solvent molecules and explicit counterions, but this approach is computationally very demanding, requiring large unit cells together with statistically meaningful sampling of the solvent and counterion positions. To overcome this challenge, more approximate schemes have been developed, where the countercharge is introduced as some idealized distribution in the unit cell (*vide infra*).

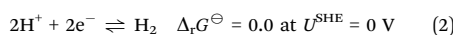
### 2.1 Basics of electrochemistry

To set the stage, this section gives a brief reminder of the basic text book equations in electrochemistry, starting with the standard Gibbs energy of reaction  $\Delta_r G^\ominus$

$$\Delta_r G^\ominus = -nFU^{\text{SHE},\ominus} \quad (1)$$

where  $n$  is the number of electrons transferred,  $F$  the Faraday constant and  $U^{\text{SHE},\ominus}$  the standard reduction potential referenced to the standard hydrogen electrode (SHE).

The SHE is an ideal electrode which is immersed in an aqueous solution with a H<sub>2</sub> and H<sup>+</sup> activity of unity and a zero overpotential for hydrogen evolution, which corresponds to the following definition



It is with respect to this idealized electrode reaction that formal “half-cell” potentials are commonly defined.

By definition, the reduction occurs at the cathode and the oxidation at the anode, yielding the cell potential  $U_{\text{cell}}^\ominus$

$$U_{\text{cell}}^\ominus = U_{\text{cathode}}^\ominus - U_{\text{anode}}^\ominus \quad (3)$$

Away from standard conditions, it is most straight forward to compute first  $\Delta_r G$  of the reaction and then convert it back

into a potential, also known as electromotive force, using the universal equation

$$U_{\text{cell}} = -\frac{\Delta_r G}{nF} \quad (4)$$

For spontaneous reactions,  $\Delta_r G$  is negative and hence  $U_{\text{cell}}$  is positive.

When applying an electrochemical potential, it is helpful to work with the following equation

$$\Delta_r G(U^{\text{SHE}}) = -nF(U^{\text{SHE},\ominus} - U^{\text{SHE}}) = \Delta_r G^\ominus + nFU^{\text{SHE}} \quad (5)$$

where  $U^{\text{SHE}}$  is the imposed potential and  $U^{\text{SHE},\ominus} - U^{\text{SHE}}$  is, in general, the over- or underpotential.

The SHE is inconvenient for computational purposes, as simulating the hydrogen evolution under realistic conditions and measuring potentials relative to this half-cell are extremely cumbersome. Therefore, the common computational reference state is vacuum: on the “vacuum scale”, the energy of an electron in vacuum is defined as zero and all the attractive energy comes from interactions with the nuclei. This scale is often called the “absolute” scale for redox potentials; we will stick to the unambiguous term “vacuum scale”.<sup>66</sup>

A concept closely related to the electrode potential on the vacuum scale is the workfunction  $W$ . The workfunction is the energy required to remove one electron from a surface, *i.e.*, we can understand the workfunction as the ionization energy. For metals, the electron affinity and the ionization energy have the same value with opposite signs. Since the vacuum scale sets the energy of the electron in a vacuum to zero, the chemical potential of the electron ( $\mu_e$ ) in the electrode is equal to minus the workfunction, whereas the workfunction is identical to the electrochemical potential,  $U^{\text{vac}}$ . Hence we might write

$$W = U^{\text{vac}} = -\mu_e \quad (6)$$

Of course, the “experimental scale”,  $U^{\text{SHE}}$ , and the vacuum scale,  $U^{\text{vac}}$ , are related. IUPAC recommends<sup>67</sup> to assign a value of  $U^{\text{vac}} = 4.44 \text{ V}$  to the standard hydrogen electrode.<sup>70</sup> Accordingly, we easily switch from one scale to the other using  $U^{\text{vac}} = U^{\text{SHE}} + 4.44 \text{ V}$  as illustrated in Fig. 1. The remaining question is how a given computation is connected to one or the other scale.

### 2.2 Linear free energy relationship for electrochemical potentials

The linear free energy relationship for accounting for the electrochemical potential, LFER-EP, is the zeroth order level to treat electrochemical reactions, since it accounts exclusively for the energy of the transferred electron. The premise is that elementary reaction steps can be divided into chemical steps (where the composition of the system remains constant) and electrochemical steps, where the number of electrons changes due to adding/removing an electron and its cation (*e.g.*,  $\text{Na}^+ + \text{e}^- \rightleftharpoons \text{Na}_{(\text{s})}$  or the more typical  $\text{H}^+ + \text{e}^- \rightleftharpoons \frac{1}{2}\text{H}_2$ ). The LFER-EP has been introduced by Norskov and coworkers in the formulation of the computational hydrogen electrode (CHE).<sup>35</sup> Throughout this article, we will use LFER-EP for the generalization of the CHE to other cations than the proton.<sup>36</sup> However, in this section,

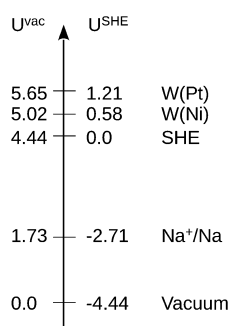


Fig. 1 Scales of the electrochemical potential in volts with respect to the vacuum (left) and to the standard hydrogen electrode (right). The experimental Na/Na<sup>+</sup> redox couple and the computed workfunction of Ni(111) and Pt(111) are given as examples.

the characteristics of the LFER-EP are discussed with the example of the CHE.

The model and assumptions of the CHE are summarized in the following:

1. Electronic energies are only required for electroneutral entities and thus do not depend on the electrochemical potential. When evaluating the potential dependence of reaction energies, these “zero charge” results give the reaction energy at 0 V vs. SHE.<sup>71</sup>

2. Electron transfers are always coupled to proton transfers and no charged systems are involved. Therefore, processes that have no direct involvement of counterions (e.g., Fe<sup>3+</sup>(cp)<sub>2</sub> + e<sup>-</sup> → Fe<sup>2+</sup>(cp)<sub>2</sub> with cp = cyclopentadienyl) cannot be studied straightforwardly.

3. The applied electrochemical potential only affects the electrochemical steps, i.e., the proton coupled electron transfers.

4. The correction for the applied potential is derived from:

$$\Delta G_{\text{H}^+ + \text{e}^-}(U^{\text{SHE}}) = \frac{1}{2} \Delta G_{\text{H}_2}^\ominus - qU^{\text{SHE}}.$$

In other words, the energy of the electron in the electrode is equal to  $-qU^{\text{SHE}}$ , where  $q$  is the fundamental charge involved in the electrochemical step.

5. The choice of the reference electrode and how it is coupled to the system under consideration imply that the solvent is water and that the hydration energy of a proton is neither influenced by the electrochemical potential nor by the electrolyte.

To summarize, the computational hydrogen electrode allows us to account for the nominal potential dependence of an electrochemical reaction, i.e., to account for the last term of eqn (5),  $nFU$ . However, it disregards any influence of the interaction between species and the electrode itself at a specific potential, i.e., it describes the correct physics for solution phase electrochemistry, but it is an approximation for the elementary reaction steps on an electrified interface where the number of electrons is variable in order to keep the potential constant. Despite these limitations, the LFER-EP is not only extremely simple to apply (being an *a posteriori* correction to “standard” computations), but also the first step in any scheme improving on the LFER-EP.

## 2.3 Beyond the linear free energy relationship: the surface charging method

Any method aiming to improve over the LFER-EP has to take the specific interactions between adsorbates and the electrified electrode explicitly into account, lifting assumptions 1–3 in the CHE (*vide supra*) by introducing  $\Delta G_{\text{r}}^{\text{elec}}(U)$ . The superscript “elec” indicates that the electronic contribution, originating in polarization and charge-transfer, to the free energy is included. The simplest approach to assess the importance of the applied electrochemical potential on the energies of adsorbates would be to apply an electrical field in the simulation cell.<sup>72–74</sup> However, the surface charge density  $q_{\text{surf}}$  needed for obtaining the electrochemical free energy, is tricky to evaluate.<sup>75</sup>

Schemes that account for all relevant free energy changes alter, therefore, the number of electrons in the system explicitly<sup>46,48,49,51–53,76</sup> and work with the grand-canonical energy expression for all the surface adsorbed species. The potential dependent free energy of the surface  $G_{\text{surf}}(U^{\text{vac}})$  is given by

$$\begin{aligned} \Delta G_{\text{surf}}(U^{\text{vac}}) &= \Delta E_{\text{surf}}^{\text{elec}}(U^{\text{vac}}) - q_{\text{surf}}(U^{\text{vac}})FU^{\text{vac}} \\ &\approx \Delta E_{\text{surf}}^{\text{elec}}(U_0) - \frac{1}{2}C(U^{\text{vac}} - U_0^{\text{vac}})^2 \end{aligned} \quad (7)$$

with  $\Delta E_{\text{surf}}^{\text{elec}}(U^{\text{vac}})$  being the electronic energy at potential  $U^{\text{vac}}$  and  $q_{\text{surf}}$  is positive if electrons are removed and negative when electrons are added, i.e.,  $q_{\text{surf}}$  is the surface charge density of the system and  $U^{\text{vac}}$  is the vacuum scale potential of the electrode. The reasoning behind eqn (7) is that electrons removed from the system are transferred to the electrode which serves as the reservoir of electrons at the potential  $U^{\text{vac}}$ . Similarly, adding an electron from the electrode is associated with the energetic cost of removing the electron from the reservoir. The approximate equality refers to the quadratic development of the electronic free energy,<sup>76,77</sup> which can serve to introduce the notion of the capacitance  $C$  of the surface and simplifies the link between SC and LFER-EP results. Assuming a constant capacitance for a given surface (which is often a reasonable first order approximation<sup>78</sup>) the results of LFER-EP and eqn (7) are identical at the potential which corresponds to the average of the zero charge potentials ( $U_0$ ), i.e., the workfunctions. Note that in the SC model the capacitance  $C$  is not an “external” constant: its value, which corresponds to the curvature of the parabola (*vide infra*), is determined for each system independently and is thus quite different in a vacuum than in implicit DMF. Furthermore, as can be seen in Fig. 6, the capacitance weakly depends on the adsorbate: the binding energy difference between two adsorbates (e.g., 2CO<sub>2</sub> vs. CO, CO<sub>3</sub>) is not simply a straight line as would be the case if the capacitances of the implicated systems were equal.

The different surface charging schemes (e.g., neutralization with a homogeneous background-charge as developed by Filhol and Neurock<sup>46,52,76</sup> or Otani’s implicit counterelectrode<sup>48,53</sup>) have a different way to obtain the first term of eqn (7), i.e.,  $\Delta E_{\text{surf}}^{\text{elec}}(U^{\text{vac}})$ , while the second term is, essentially, the same as the one needed for the nominal potential dependence, introduced in the previous section. Here, we will apply the surface charging method in the formulation by Filhol and Neurock which we abbreviate by SC.<sup>76</sup>

The two main advantages of these general approaches are (a) Proper potential alignment: since these methods work with the vacuum scale potential, assessed through workfunctions, the potential of all the systems is referenced to vacuum and properly aligned, *i.e.*, changes in the workfunction due to adsorptions and reactions are fully taken into account. (b) Decoupling of electrons and counterion transfer: eqn (7) does not make use of any counterion. Hence a potential dependence of a system where only an electron transfer has occurred is easily accessible. For example, the potential dependence of CO<sub>2</sub> adsorption is readily evaluated with such a scheme, while it is a constant within the LFER-EP framework. To be explicit, the clear distinction between “chemical” and “electrochemical” steps makes place for a “gradual, nuanced” description, where the electrochemical potential fixes an electrode polarization, which requires a specific surface charge density,  $q_{\text{surf}}$ . Hence, the coupled electron cation transfer, which could be reasonably described by LFER-EP and be a good approximation in the case of covalent bond formation (*e.g.*, C–H), becomes a special case, while in general the surface charge changes by a characteristic value for a given elementary reaction.

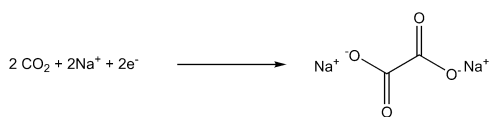
The energy of the reactants in the formally electrochemical steps are obtained like in the LFER-EP approach, *i.e.*,

$$\Delta G_{X'e^-}(U^{\text{vac}}) = \Delta G_X + q(U_X^{\text{vac},\ominus} - U^{\text{vac}}) \quad (8)$$

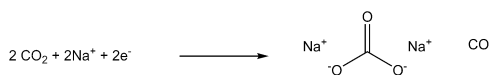
where,  $U_X^{\text{vac},\ominus}$  can be either obtained from the experiment (*e.g.*, 4.44 V for  $\frac{1}{2}\text{H}_2$ ) or from the computed workfunction (*e.g.*, 2.74 V for Na(100) in a vacuum). The advantage of the later approach is that the workfunction of an uncharged sodium surface can be computed under the specific computational conditions, *e.g.*, using the same solvent model, giving a “consistent” description. Of course, this standard redox-potential can also be applied in the LFER-EP.

### 3 Model

The electroreduction of CO<sub>2</sub> under aprotic conditions opens up several reaction channels. Herein, we investigate the C–C coupling of CO<sub>2</sub>, leading to oxalate



and the dissociation reaction of CO<sub>2</sub> into CO and adsorbed oxygen. Under electrochemical conditions, the surface bound oxygen may further be reduced to carbonate



Both products are, in principle, competitors in any reaction where CO<sub>2</sub> is reduced electrochemically, *e.g.*, formic acid or hydrocarbon formation<sup>8,9,11,12,14,15</sup> and are therefore worth studying in order to, subsequently, assess the selectivity of

the target reactions. However, under the studied aprotic conditions, no formic acid or hydrocarbons can be formed.

As far as simulations are concerned, the aprotic solvent DMF has the advantage compared to water that it is non-reactive and that no specific interactions (H-bonds) are expected between the solvent and the solute, but the disadvantage that its size is considerably larger, pushing simulations with meaningful explicit layers of DMF beyond our present capabilities. However, the average effect of the solvent, *i.e.*, increased capacitance, might be captured well enough by an implicit solvent model, which avoids the ambiguities in choosing a structure for the static solvent layers as usually proposed when including solvent effects.<sup>46</sup> Therefore, our study investigates the combination of implicit solvent treatment and explicit accounting of the electrochemical potential. Although this model is far from perfect (the double layer is grossly approximated by the homogeneous background charge and there are no explicit solvent molecules), to the best of our knowledge, it is the state of the art that can be done with publicly available, well established, periodic DFT codes.

We model the catalyst surface by the Ni(111) facet and the solvent by a continuum with a relative dielectric constant ( $\epsilon$ ) of 37.2, characteristic of DMF. The latter is also very close to the one of another typical aprotic solvent for electrochemistry, acetonitrile ( $\epsilon = 37.7$ ). The results will hence be generally applicable to aprotic solvents with a high dielectric constant. Vlachos and co-workers concluded that the water gas shift reaction, which involves chemisorbed CO<sub>2</sub> and co-adsorbed CO and O, similarly to systems reported herein, yields overall similar results at the Ni(111) surface or the Ni(211) facet.<sup>79</sup> Therefore, we have limited ourselves to the ideal Ni(111) surface. In order to gain a more complete understanding, simulations over different surfaces and the determination of activation barriers should be considered, but these investigations are beyond the scope of this study.

Experimentally, the electroreductive coupling of CO<sub>2</sub> to alkenes is carried out with a sacrificing aluminum or magnesium electrode.<sup>16–18</sup> Computationally, the monovalent sodium cation is more convenient than the di- or trivalent cations and the redox potential is comparable. Therefore, we model the counterion by Na<sup>+</sup>. For example, carbonate is simulated as Na<sub>2</sub>CO<sub>3</sub> instead of Al<sub>2</sub>(CO<sub>3</sub>)<sub>3</sub>. The solvation energy of Na<sup>+</sup> is predicted to be –3.14 eV by the implicit solvation model. At the equilibrium potential, the energy of Na<sup>+</sup> in solution is equal to the energy of Na on the metallic sodium surface, *i.e.*, the solvation energy is roughly compensated by the workfunction. The solvation energy provided by the implicit solvent model is, thus, fairly consistent with the workfunction of sodium metal (2.7 V) but underestimated compared to the 4–4.5 eV expected based on experimental data and cluster-continuum data in a similar solvent.<sup>80</sup> Considering that Na<sup>+</sup> is co-adsorbed on the surface (or embedded in the salt solid) and therefore never “fully solvated” and its energy is obtained from the workfunction of solid sodium, we did not try to improve the description of Na<sup>+</sup> by including explicit solvent molecules. Furthermore, the incurred error has an undetermined sign and magnitude compared to the experimentally relevant Al<sup>3+</sup> or Mg<sup>2+</sup>.



The salts (Na<sub>2</sub>CO<sub>3</sub> and Na<sub>2</sub>C<sub>2</sub>O<sub>4</sub>) are modelled as crystals with two chemical formulas per unit cell. These models are derived from experimental crystal structures<sup>81,82</sup> and are fully optimized.

To assess the window of the electrochemical stability of Na<sup>+</sup> under our conditions, there is, on the one hand, a workfunction of sodium (~2.7 V), which assures the formal stability of Na<sup>+</sup> down to about -1.8 V vs. SHE with respect to the formation of solid sodium. On the other hand, Na<sup>+</sup> adsorption on Ni(111) is positive (*i.e.*, unstable) within this potential window (*vide infra*, Fig. 2). Hence, Na<sup>+</sup> is, indeed, the relevant chemical species under the simulated conditions.

## 4 Computational details

The metal surface is modeled as a symmetric  $p(3 \times 3)$  Ni(111) slab with a lattice constant of 3.52 Å and a thickness of 5 layers (the middle layer is frozen in its bulk position), in a periodic box of 37.35 Å. The spin-polarized electronic structure is described at the PBE level,<sup>83</sup> with an energy cut-off of 400 eV for the plane-wave basis set. The electron-ion interactions are described by the PAW formalism.<sup>84,85</sup> All computations are performed with VASP 5.3.3.<sup>86,87</sup> Accounting for solvation effects is achieved by exploiting the implicit solvation model<sup>26,88</sup> as implemented by Hennig and co-workers under the name VASPsol.<sup>64</sup> In this model, the electrostatic interaction with the implicit solvent is computed based on a linear polarization model, where the relative permittivity of the medium is a continuous function of the electron density. A switching function around a specified isodensity value is used to vary the relative permittivity from 1 (well “inside” the surface metal atoms) to the solvent bulk value far away from the surface. This modified Hartree potential is obtained by solving the modified Poisson equation. Hence, the polarization of the system due to the solvent is included self-consistently. In order to get numerically stable results for the potential in empty space, the surface tension was set to zero (no cavitation energy) and the critical density value was reduced to  $2.5 \times 10^{-4} \text{ e \AA}^{-3}$ . The dielectric constant of DMF was set to 37.2. Note that when we started this study, VASPsol was incompatible with non-local van der Waals density functionals and we did therefore not apply them. Since we are mainly comparing two electrochemical approaches, we do not expect to obtain qualitatively different conclusions upon accounting for weak non-bonded interactions. All geometries were optimized to reach a gradient smaller than  $0.05 \text{ eV \AA}^{-1}$  with wave functions converged to  $5 \times 10^{-5} \text{ eV}$ . The precision setting of VASP is set to “normal” and the automatic optimization of the real-space projection operators is used.

The energy of the sodium cation is obtained according to eqn (7) with the energy of an atom in bulk sodium ( $\Delta G_{\text{Na}}$ ) and the workfunction of the Na(100) surface ( $U_{\text{Na}}^{\text{acc}, \ominus}$  is 2.74 V in a vacuum and 2.67 V in implicit DMF).

In the SC method, the system is charged and  $N_e$  electrons are present in total instead of the neutral  $N_0$  number. In order to reach an overall neutral cell, a uniform background charge of the opposite sign is applied. This uniform charge is also

present in the metal slab itself, where it is screened by the metal. Hence, the “effective” applied charge is reduced and the DFT energy must be corrected accordingly. The correction suggested by Filhol and Neurock<sup>46,52,76</sup> reads

$$G^{\text{elec}}(U^{\text{abs}}) = E_{\text{DFT}}(N_0) + \frac{z_0}{Z}(E_{\text{DFT}}(N_e) - E_{\text{DFT}}(N_0)) + \frac{z_0}{Z}q \int_{N_0}^{N_e} V_a(N_e) dN_e + U^{\text{abs}}(N_e - N_0) \quad (9)$$

where  $U^{\text{abs}}$  is the workfunction for the system with  $N_e$  electrons and  $N_0$  is the number of electrons for the neutral system.  $Z$  is the interslab repeat vector of one supercell ( $z$ -direction) and  $z_0$  is the segment along this direction not occupied by the metal slab (the radius of the atoms is derived from the lattice constant), therefore  $\frac{z_0}{Z}$  (in our setup  $\frac{z_0}{Z} = 0.703$ ) gives the ratio of the space in which the homogeneous back-ground charge is “active”, *i.e.*, not screened by the metallicity of the slab. This “screening” concerns  $(N_e - N_0) \left(1 - \frac{z_0}{Z}\right)$  electrons.  $q$  is the elementary charge and the integral approximates the interaction energy of the homogeneous background with the system in order to remove this spurious interaction. The interaction is estimated from the electrostatic potential  $V_a$ , in the middle between the two symmetric surfaces, which is taken to be the energy of the “vacuum”, *i.e.*, it is also used to compute the workfunction. Note that even though we are using the symbol  $G$  for the free energy (to emphasize that the free energy change due to electron transfer is taken into account) eqn (9) would need to be supplemented by the standard terms accounting for translational, rotational and vibrational degrees of freedom in order to be a “proper” Gibbs energy. When discussing the results, we will thus refer to “adsorption energies” and not “adsorption free energies”, although they are “electronic free energies”.

Energies were obtained for at least 5 different charges for each system. Subsequently, a parabolic fit was used for accessing arbitrary potentials. The same procedure is applied to get the effective charge  $q_{\text{surf}}(U)$  at an arbitrary potential. These data are used to evaluate the charge injection  $\Delta^{\text{ads}} q(U) = (q_{\text{surf}}^{\text{slab}}(U) + N^{\text{mol}}) - q_{\text{surf}}^{\text{system}}(U)$  for a given reaction, where  $N^{\text{mol}}$  is the sum of the electrons in the isolated molecules (the counterion, Na<sup>+</sup>, is considered as a charged species) adsorbed on the surface. A script for automating these tasks is available in the supplementary information. Whenever technically possible, the charges were chosen to obtain an interpolating parabola between -2 and 1 V (vs. SHE). Depending on the system this was not possible, as in the highly (negatively) charged systems the required electrons are not bound on the surface anymore but spilling out into the “vacuum”, filled with the background charge. In these situations, eqn (9) is not applicable anymore, which is seen as strong deviations from the parabolic behavior.

## 5 Results and discussion

CO<sub>2</sub> electrolysis under aprotic conditions is reported to yield CO and carbonate or the C-C coupling product, oxalate, depending

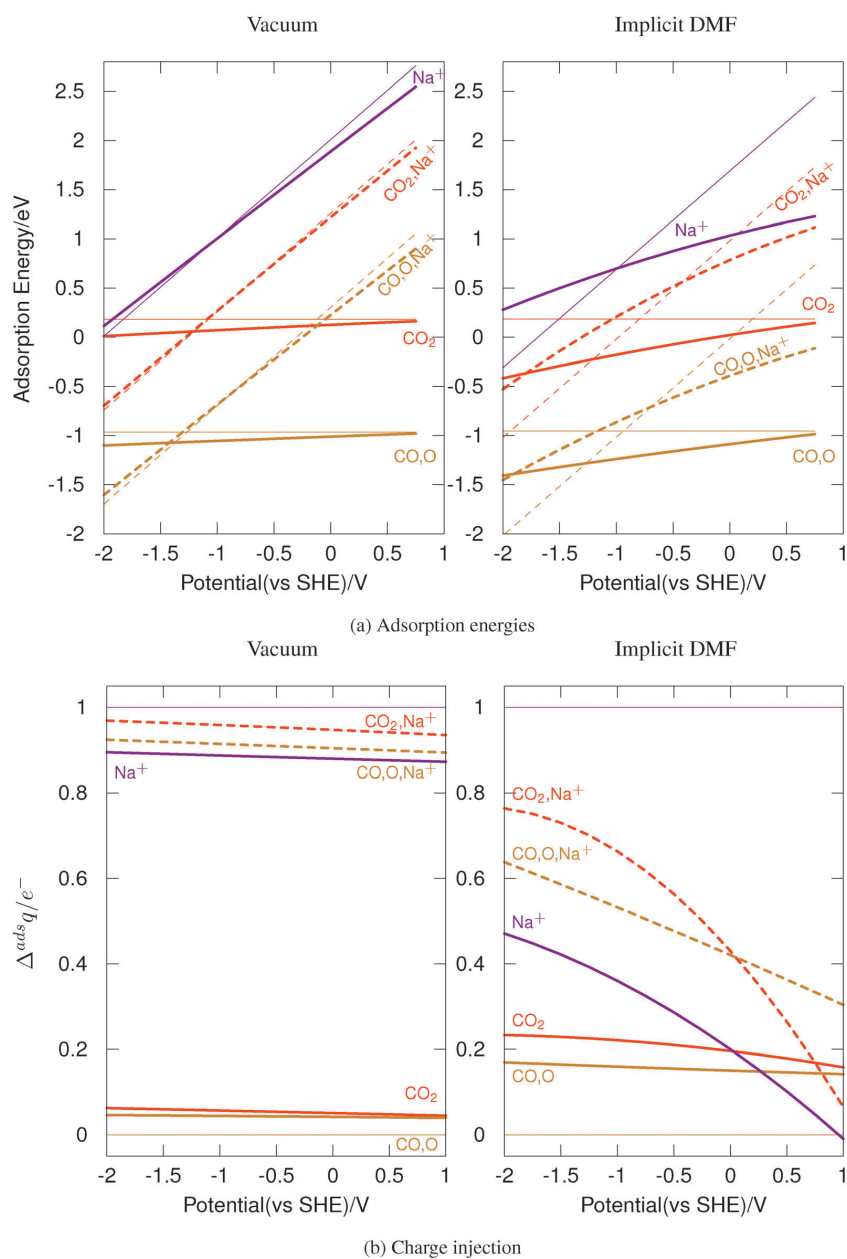


**Fig. 2** Adsorption (top) and associated charge injection (bottom) upon adsorption of Na<sup>+</sup> (purple) and of CO<sub>2</sub> on Ni(111) as a function of electrochemical potential in a vacuum (left) and implicit DMF (right). Two adsorption modes are compared for CO<sub>2</sub>: the intact chemisorption (red) and the dissociative adsorption (*i.e.*, CO and O co-adsorption, brown). Broken lines indicate the co-adsorption with Na<sup>+</sup>. The thin lines refer to the LFER-EP, while the thick lines are computed with the SC method.

on the electrode material. We therefore start by investigating the adsorption of the reactant, CO<sub>2</sub>, and its dissociation into co-adsorbed CO and O. Then we consider the influence of CO<sub>2</sub>

coverage and the formation of oxalate, competing with the one of carbonate and carbon monoxide. Investigating this intrinsic reactivity of CO<sub>2</sub> under aprotic, reductive conditions will not



## Chapter 8. Impacts of electrode potentials and solvents on the electroreduction of CO<sub>2</sub>: a comparison of theoretical approaches

View Article Online

Paper

PCCP

only be helpful to understand the mechanism and selectivity of the carboxylation reaction of alkenes under similar conditions, but serves equally well to determine the level of modelling necessary to conduct such mechanistic studies for reactions where experimental results are scarce.

We compare the simple linear free energy relationship for the electrochemical potential (LFER-EP) to the more advanced surface charging (SC) method. As explained above, LFER-EP does not describe the polarization of the surface and imposes a strict coupling of the Na<sup>+</sup> and e<sup>-</sup> transfer. In contrast, the SC model polarizes the surface according to the electrochemical potential and electron transfer occurs also in the absence of a cation transfer. Hence, under strongly reducing conditions SC and LFER-EP may differ significantly and SC is potentially more convenient: the cation (Na<sup>+</sup>) has no well defined place in the reduced species (in contrast to the proton which forms regular C-H and O-H bonds), but has to be introduced in LFER-EP, while it might not be necessary in SC.

The adsorption of CO<sub>2</sub> together with the preferred adsorption mode of oxalate on Ni(111) as a function of potential will be used to assess the limitations of LFER-EP in practice and the role of the solvent. Having established the consequences of the improved description of SC compared to LFER-EP, we investigate the coverage effect on CO<sub>2</sub> dissociative adsorption and elucidate the origin of the selectivity of CO and carbonate rather than oxalate formation over Ni(111).

### 5.1 Comparison of the potential dependence of adsorption energies in a vacuum and an implicit solvent

Fig. 2 shows the energetics and associated charge injection  $\Delta^{\text{ads}}q$  in the case of CO<sub>2</sub> and Na<sup>+</sup> adsorption on Ni(111) as a function of electrochemical potential in a vacuum (left) and when accounting for solvent effects through an implicit solvent (right). The charge injection is defined as the net charge applied for the considered potential for the chemisorbed system minus that of the bare Ni(111) surface. It hence corresponds to the extra charge that needs to be injected in the presence of adsorbed species to maintain the potential constant. The LFER-EP framework is characterized by the distinction of elementary steps into “chemical” and “electrochemical” steps. The former are rearrangements of nuclear coordinates, while the latter involve addition/subtraction of an electron and its counterion, e.g., Na<sup>+</sup> + e<sup>-</sup>. Since electron and cation transfer are strictly coupled, the injected charge is simply 1 e<sup>-</sup> for electrochemical steps and 0 for chemical steps. As a consequence, only the reaction energies of electrochemical steps depend on the potential within the LFER-EP approach. Furthermore, all systems are electroneutral. Within the SC model, however, the number of electrons in the system is individually adapted to every intermediate to tune the work-function to the specified level. Therefore, the chemical and electrochemical steps are no longer formally separated from each other. In the text we will frequently refer to “oxalate” or “carbonate” for species adsorbed on the surface. These adsorbates do not necessarily have the “net” charge of the corresponding solution species: the adsorbate and the electrode form one system and

the (surface) charge is a continuous function of the electrochemical potential.

We start the comparison of the two methods for including the electrochemical potential first in a vacuum and only in a second stage when accounting for solvent effects.

As a first example for a chemical step, consider the adsorption of CO<sub>2</sub> in the absence of Na<sup>+</sup> co-adsorption: by construction, LFER-EP yields an adsorption energy which is independent of the potential and the injected charge is strictly 0. However, when co-adsorbing CO<sub>2</sub> with Na<sup>+</sup>, we are confronted with an electrochemical step within the LFER-EP framework, since cation and electron transfer are coupled. The adsorption energy as a function of potential has a slope of one, corresponding to the coupled electron transfer. In the case of the SC model, the surface charge adapts to the potential. However, since charges are not well stabilized in a vacuum, the charge variations compared to LFER-EP (strict coupling of electron and cation transfer), obtained with the surface charging method, are almost negligible (Fig. 2b): the maximum difference occurs for Na<sup>+</sup> where the charge injection is  $\sim 0.9$  instead of 1. The number of injected electrons is the main factor determining the potential dependence: according to eqn (5) the slope of  $\Delta G(U)$  is, to first order, proportional to the number of electrons injected. The inability of vacuum to stabilize charges implies that minor charge variations change the potential considerably, leading to very small free energy changes due to potential alignment effects. Since at the same time the electrons are only marginally better stabilized in one system than in the other (e.g., on CO<sub>2</sub>@Ni(111) compared to the bare surface), the adsorption energies barely change compared to the zero charge (LFER-EP) results. In a vacuum, the systems are thus effectively electroneutral and introducing a counterion is strongly coupled to an electron transfer. Hence, the potential dependence for the more detailed SC method is very similar to the simple LFER-EP method, i.e., adsorptions in the absence of Na<sup>+</sup> are basically horizontal lines, while the reductive Na<sup>+</sup> adsorption or co-adsorption leads to a strong potential dependence with a slope of  $\sim 1$ . Therefore, in a vacuum, where charge accumulation at metals is small, the LFER-EP is a very reliable approximation.

Accounting for solvent effects leads to a very different picture when explicitly tuning the electrode potential, while the LFER-EP lines are quite similar to the ones in a vacuum: on Fig. 2a (right) slopes of the thin lines are unchanged by construction, while intercepts are only affected in the case of Na<sup>+</sup> adsorption where the charge distribution is somewhat stabilized by the polarizable solvent. When applying the surface charging method, the dielectric medium stabilizes charges at the interface, especially in the presence of adsorbates and as a result the injected charge significantly deviates from the ideal values of zero or 1. Equivalently one might say that the dielectric medium increases the capacitance of the system. For chemisorbed CO<sub>2</sub> or CO, O, the injected charge is significantly enhanced by the solvent, up to a value of  $\sim 0.2e^-$ , and hence the adsorption energy depends on the potential with a marked stabilization at negative potentials, where CO<sub>2</sub> or CO accumulates a negative charge, which is stabilized by the solvent (Bader charges on the

adsorbate as a function of potential and the solvent can be found in the  $\text{ESI}^\dagger$ ). Such a potential dependence is obviously absent in the LFER-EP. Hence, the two methods considerably deviate in the presence of a solvent. For example, at  $U = -1$  V  $\text{CO}_2$  is underbound by 0.4 eV compared to the SC method, which gives an exothermic reaction for  $\text{CO}_2$  adsorption below 0 V.

Assuming a constant capacitance ( $C$ , see eqn (7)), lines for SC and LFER-EP cross at the average zero charge potential, *i.e.*, at the potential that corresponds to the average of the workfunction of the neutral systems. Note that such an assumption is not involved in the SC model, but might be made for interpretative purposes. For example, the workfunction of  $\text{Ni}(111)$  and  $\text{CO}_2@ \text{Ni}(111)$  is 0.58 and 1.39 V *vs.* SHE in implicit DMF, respectively (see  $\text{ESI}^\dagger$ ). Hence, the thin and thick full orange-red lines in the graph on the right of Fig. 2a are expected to cross at 0.99 V. Indeed, at 0.75 V (the limit of the  $x$ -axis in Fig. 2a), the two lines almost cross. The good agreement between the constant  $C$  prediction and the actual crossing point gives credibility to the approximation of constant capacity when comparing similar systems. Furthermore, this observation justifies to call the potential at the crossing point the effective potential to which the LFER-EP results of non-electrochemical steps correspond to. Hence, the LFER-EP results for  $\text{CO}_2$  adsorption in the absence of  $\text{Na}^+$  co-adsorption correspond to an effective potential of almost 1 V, which is very far from the reducing conditions of interest herein.

The potential dependence of the  $\text{Na}^+$  assisted adsorptions is also considerably modified by the solvent. The injected charge is markedly lower than 1 for  $\text{Na}^+$  adsorption since the polar solvent stabilizes the partial positive charge on Na. This can be easily explained considering a particular case. Neutral  $\text{Na}@ \text{Ni}(111)$  corresponds to a potential of  $-2.6$  V. At this potential, the bare surface is, however, not neutral, but effectively charged by  $0.5 e^-$  for a  $p(3 \times 3)$  super cell. Hence, the injected charge to reach the neutral  $\text{Na}@ \text{Ni}(111)$  is only  $0.5 e^-$ . The co-adsorption of  $\text{Na}^+$  and  $\text{CO}_2$  combines the effects described above and the charge injection (although not complete to  $-1$ ) reaches  $\sim 0.75 e^-$  at strongly reducing potentials. In other words,  $\text{Na}^+$  adsorption is not coupled anymore with a full electron transfer and we are dealing with a somehow solvated  $\text{Na}^+$  and partially reduced carbon dioxide. Similarly, in the case of  $\text{CO}_2$  dissociation, there is only a rather weak potential dependence. Nevertheless, in both competing reactions, we clearly obtain a stronger potential dependence in the presence of the counterion than in its absence, demonstrating the stabilizing capabilities of counterions without imposing counterion-coupled electron transfers, provided that ionic species are stabilized in a dielectric medium. The partially injected charge under realistic solvent conditions and its deviation from the ideal values of 0 or 1 have strong consequences on the slope of the adsorption energy as a function of potential energy, which markedly differs between the two methods as seen on Fig. 2a right. Obviously, in the presence of a high dielectric constant solvent, the LFER-EP is not anymore a reliable approximation to evaluate adsorption energies.

## 5.2 Preferred surface species and coverage dependence of $\text{CO}_2$ adsorption

In the following section, we will focus more closely on the nature of the preferred surface species as a function of electrochemical potential. Independent of the scheme and conditions, the dissociative adsorption of  $\text{CO}_2$  into CO and O is favored by at least 1 eV at low coverage (1/9 ML), motivating us to investigate higher coverages. Increasing the coverage also allows us to model carbonate and oxalate formation since they require at least two  $\text{CO}_2$  molecules in the unit cell, which corresponds, in our case to a coverage of 2/9 ML.

As seen in the previous section, SC delivers a more general description of the electrochemical systems than LFER-EP, provided solvation is included. Here, we are discussing the extreme case of dissociative adsorption of  $\text{CO}_2$  in the absence of  $\text{Na}^+$  co-adsorption as a function of surface coverage. By construction, LFER-EP gives constant adsorption energies for these reactions. Furthermore, CO, O co-adsorption at zero charge has a workfunction of 1.37 V *vs.* SHE. Hence, the LFER-EP results for the dissociative adsorption correspond to an effective potential of about 1 V, just like  $\text{CO}_2@ \text{Ni}(111)$  (*vide supra*). This oxidative potential is far from the potentials of interest herein and we will thus not consider LFER-EP any further in this section. In the SC model, we can compute the Bader charges as a function of potential (see  $\text{ESI}^\dagger$ ). This analysis reveals that the charge on the surface bound oxygen varies less than the charge on CO when lowering the potential: the oxygen is already negatively charged like in a surface oxide and does not accept significantly more electrons.  $\text{CO}_3$  is, on the other hand, a rather powerful electron acceptor and hence the injected charge is significantly higher when a  $\text{CO}_2$  is coupled to a surface oxygen atom instead of being dissociated into CO, O (blue compared to brown lines in Fig. 3b). With the solvent taken into account, the charge injection reaches up to 0.5 electrons for carbonate at the highest coverage considered. This significant charge injection goes along with a dramatic stabilization of the species at reducing potentials, not only compared to the LFER-EP results, but also compared to other surface bound species. For example carbonate and CO at high coverages (full, blue line in Fig. 3b) get more stable than dissociated  $\text{CO}_2$  at 2/9 ML (broken, brown line) at potentials  $< -1.2$  V.

This comparison shows that solvent effects are crucial for the prediction of relative stabilities under electrochemical conditions and for allowing rather decoupled electron transfers. Hence, for chemical conclusions only SC results with a solvent description are discussed.

Increasing the  $\text{CO}_2$  coverage from 1/9 to 3/9 ML (see Fig. 3a) goes along with a reduced tendency (per  $\text{CO}_2$  molecule) to dissociate  $\text{CO}_2$ . Dissociative  $\text{CO}_2$  adsorption is even endothermic at a coverage of 3/9 ML for potential  $> -0.5$  V, while at 2/9 ML the  $\text{CO}_2$  dissociation is exothermic, but already less than twice the value for 1/9 ML. Comparing the dissociated systems with the ones where carbonate is formed ( $\text{CO}_2 + \text{O} \rightarrow \text{CO}_3$ ), a contrasting picture emerges. At a coverage of 2/9 ML carbonate formation (without counterions) is still disfavored at all potentials considered,

## Chapter 8. Impacts of electrode potentials and solvents on the electroreduction of CO<sub>2</sub>: a comparison of theoretical approaches

View Article Online

Paper

PCCP

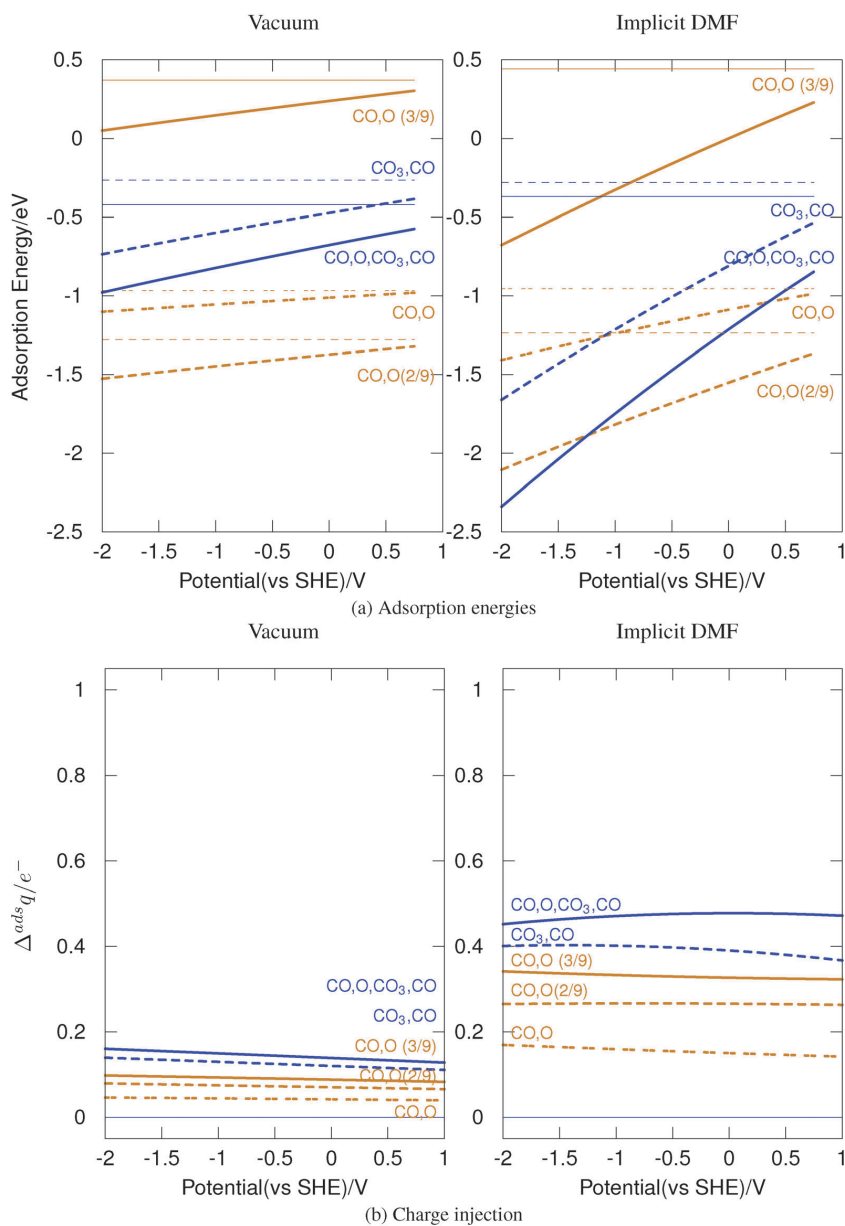


**Fig. 3** Total adsorption energies (top) and associated charge injection (bottom) of one, two and three CO<sub>2</sub> on Ni(111) as a function of electrochemical potential. The adsorbed species are derived from dissociated CO<sub>2</sub>, i.e., CO and O (in brown), and at higher coverages, CO and CO<sub>3</sub>. Three coverages are considered: 1/9 ML (spaced broken lines), 2/9 ML (broken lines) and 3/9 ML (full lines) in a vacuum (left) and implicit DMF (right). The lines in blue correspond to systems where one CO<sub>2</sub> has reacted with a surface adsorbed oxygen atom to give CO<sub>3</sub>. Thin lines refer to LFER-EP and thick lines to the SC method.

but if a coverage of 3/9 ML is imposed, carbonate formation is expected even at mildly positive potentials. Furthermore, since the full blue line crosses the broken brown line in Fig. 3a right,

the thermodynamically preferred state switches with the potential: from dissociated CO<sub>2</sub> at an intermediate coverage (2/9 ML) for potentials > -1.2 V to carbonate and dissociated CO<sub>2</sub>,

yielding higher coverages (3/9 ML), for potentials  $< -1.2$  V. The latter is in fair agreement with the report of carbonate formation starting around  $-1.5$  V.<sup>15,19,89</sup> Nevertheless, even at 3/9 ML coverage, the dissociative adsorption of CO<sub>2</sub> is exothermic at potentials below  $-0.5$  V in solution, suggesting that CO might generally be a relevant intermediate in CO<sub>2</sub> reduction over Ni, *e.g.*, even for C–C bond formation with alkenes.

From a chemical point of view we have learned two lessons: first, CO<sub>2</sub> has a strong thermodynamic tendency to dissociate on Ni(111) at any potential considered. Nevertheless, strongly reducing conditions are required to desorb reduced products (*vide infra*), *i.e.*, the dissociation at anodic potentials is not catalytic but just poisoning the catalyst surface. This tendency to dissociate CO<sub>2</sub> is well in line with the frequently reported CO production during CO<sub>2</sub> electroreduction over Ni<sup>15,19,89</sup> and the use of Ni as a catalyst at the cathode of solid oxide electrolyzers of CO<sub>2</sub>.<sup>90</sup> Second, thermodynamically, the surface bound oxygen can be coupled to a second CO<sub>2</sub> molecule yielding carbonates – and carbonate formation is favored at reducing potentials and high surface coverage.

**5.2.1 Adsorption mode of oxalate.** Above, we have focused on CO<sub>2</sub> dissociation and the formation of a C–O bond. As an alternative, the reductive dimerization, *i.e.*, the C–C bond formation yielding oxalate, has to be considered. When comparing the relative stability of C<sub>2</sub>O<sub>4</sub> with CO<sub>3</sub>, CO on Ni(111) one finds that oxalates are much higher in energy than carbonates, which is largely due to the important CO adsorption energy. Nevertheless, the adsorption mode of oxalates serves as an example for a switch in the preferred adsorption mode (as opposed to a switch in the preferred surface species) as a function of electrochemical potential. Such a switch is, by definition, absent in the LFER-EP and thus illustrates the truly atomic, detailed understanding which is obtained with the SC method.

Fig. 4 displays the geometries of oxalates either adsorbed “flat”, parallel, to the Ni(111) surface or slightly twisted, “perpendicular”, creating a strong surface dipole and Fig. 5 shows their adsorption energies. The different magnitude of the surface dipole is also reflected by the workfunction, which is 1.52 and 1.78 V *vs.* SHE for the parallel and perpendicular adsorption mode, respectively. The first observation is that with or without implicit solvent, the parallel adsorption mode is favored in the zero charge picture, which is what would be discussed in the context of the LFER-EP. However, when accounting for the potential dependence of the two adsorption modes, a crossing is obtained: in a vacuum, quite reducing potentials ( $< -1.1$  V) are necessary to stabilize the perpendicular mode. However, when accounting for the solvent, the situation is completely reversed: for potentials as high as 0.5 V the “perpendicular” mode is more stable, as now the charge accumulation “far” from the surface is stabilized by the solvent. In addition, the energy of the adsorbed species is markedly modified. For example, the surface charging method stabilizes oxalate by 0.7 eV at  $-1$  V compared to the zero charge picture.

Unfortunately, this implies that the “zero charge” relative stabilities (here a difference of about 0.2 eV) are not necessarily representative for the relative stabilities under electrochemical

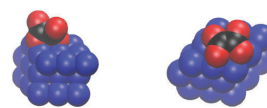


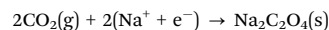
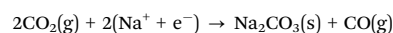
Fig. 4 “Perpendicular” and “parallel” adsorption modes of oxalate (C<sub>2</sub>O<sub>4</sub>) on Ni(111) on the left and right, respectively.

conditions. Therefore, even for the “conformational search” the potential dependence would need to be accounted for. However, since this is associated with substantial effort, we have limited ourselves herein to the lowest adsorption energy at zero charge. Further studies will try to establish a rapid pre-screening or a “predictive” scheme which exploits the work-function differences between competing adsorption modes in order to identify the structures for which computing the potential dependence is warranted.

### 5.3 Reaction energies for carbonate and oxalate formation

Carbonates are possibly formed at high coverages, even in the absence of counterions. On the other hand, the simplest C–C coupling product, oxalate, seems to lie at considerably higher energy. These findings raise the question: with the possibility of stabilizing counterions, would carbonate form quantitatively or could oxalate be dramatically stabilized?

To start with, we consider the reaction energy of the overall reactions starting from CO<sub>2</sub> in the gas-phase



yielding the Na<sub>2</sub>CO<sub>3</sub>(s) and Na<sub>2</sub>C<sub>2</sub>O<sub>4</sub>(s) salts, which are, for computational efficiency, modelled by perfect periodic crystals (see section Models). These salts are dissolved by high dielectric solvents such as DMF. Hence, their true energy (*e.g.*, as ion pairs in solution) is lower than assumed herein. These reaction energies are given as a function of potential in thin broken lines in Fig. 6. For the sake of consistency with the adsorption energies discussed above, reaction energies are “electronic” energies, *i.e.*, neglecting zero-point and thermal corrections.

If the overall reaction is uphill at potential  $U$ , then the reaction is unlikely to proceed at room temperature. Hence, we first investigate the overall thermodynamics of the quantitative formation of crystalline sodium carbonate and sodium oxalate starting from CO<sub>2</sub>, Na<sup>+</sup> and electrons at a potential  $U$  that is sufficiently reductive (see broken lines in Fig. 6). In the case of carbonates, the side product is carbon monoxide, which has to be desorbed from the surface in order to close the catalytic cycle. This step is endothermic by about 1.9 eV and therefore the formation of crystalline sodium carbonate requires a minimal potential of  $-1.25$  V for the combined reaction to be exothermic, in reasonable agreement with the reported onset potential around  $-1.5$  V.<sup>15</sup> Oxalate formation, on the other hand, is thermodynamically much more accessible: already at potentials lower than  $-0.6$  V, the formation of sodium oxalate is thermodynamically feasible.

## Chapter 8. Impacts of electrode potentials and solvents on the electroreduction of CO<sub>2</sub>: a comparison of theoretical approaches

Paper

View Article Online

PCCP

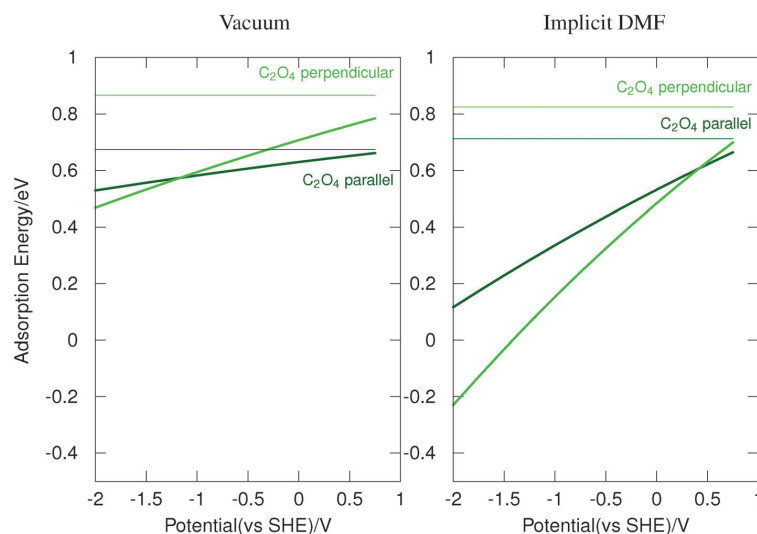


Fig. 5 Adsorption energies of two CO<sub>2</sub> molecules, in the form of oxalate as a function of electrochemical potential. The oxalate can be adsorbed “parallel” to the nickel surface (dark green) or perpendicular (green). Thin lines refer to the zero charge picture while broken lines refer to the surface charging method. The graph on the left and right corresponds to vacuum and implicit DMF, respectively.

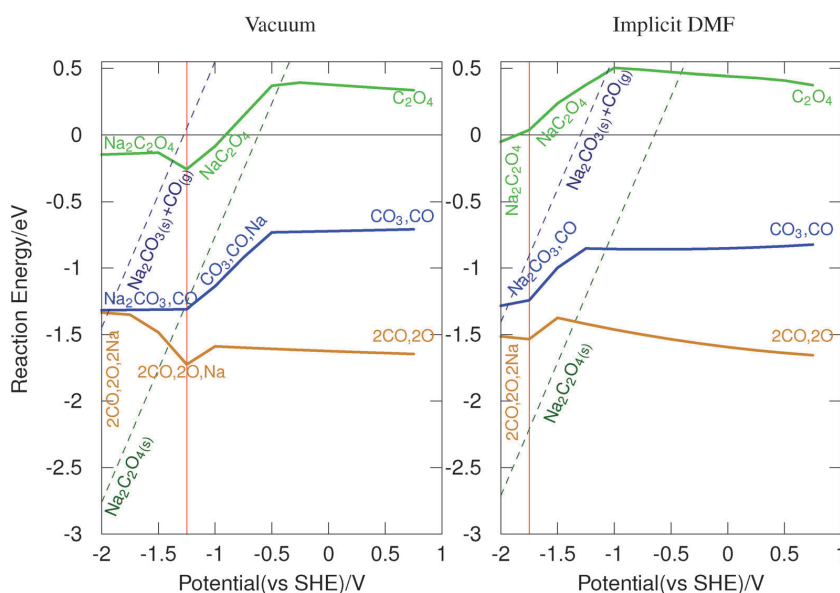


Fig. 6 Reaction energies of two CO<sub>2</sub> as a function of electrochemical potential in a vacuum (left) and implicit DMF (right). Thick lines refer to reactions starting from chemisorbed CO<sub>2</sub> yielding adsorbed products, e.g., CO<sub>3</sub>, CO (blue): 2CO<sub>2</sub><sup>ads</sup> → CO, CO<sub>3</sub><sup>ads</sup>, with the number of co-adsorbed Na<sup>+</sup> adapted according to the potential. Thin lines refer to the overall reaction: isolated CO<sub>2</sub> reacts with electrons and counterions to yield precipitated salts, e.g., Na<sub>2</sub>C<sub>2</sub>O<sub>4</sub>(s) (dark-green): 2CO<sub>2</sub>(g) + 2Na<sup>+</sup> + 2e<sup>-</sup> → Na<sub>2</sub>C<sub>2</sub>O<sub>4</sub>(s). The vertical red lines indicate the point where the reactant changes from CO<sub>2</sub>, Na@Ni(111) to CO<sub>2</sub>@Ni(111).

Since both carbonate and oxalate formation are surface assisted processes, the second relevant question is if these reactions are feasible on the surface. Hence, we investigate

the transformation of chemisorbed CO<sub>2</sub> into adsorbed products. Depending on the potential, the reactant and/or the products are co-adsorbed with Na<sup>+</sup> and the corresponding SC

reaction energies are represented in thick lines in Fig. 6. Concerning the reactant, the co-adsorption of  $\text{CO}_2$  with  $\text{Na}^+$  is favored at strongly reducing potentials. This change in the energy reference leads to a discontinuity in the reaction energies and is indicated by a vertical line. Similarly, for each segment, the most stable product is indicated in Fig. 6 at the given coverage (*i.e.* 2/9 ML): the number of co-adsorbed  $\text{Na}^+$  increases with more and more reducing (more negative) potentials. These changes in the number of cations lead to the other discontinuities in the reaction energy. Since we are considering reaction energies, the reference energy is different from that of the preceding figures, which modifies the aspect of the potential dependence. The potential dependence of relative energies is directly related to workfunction differences. The change in workfunction (potential of zero charge) is often larger for an adsorption process than for a surface reaction. Therefore, the potential dependence of reaction energies is often less pronounced than for adsorption energies. Nevertheless, since the workfunction still changes during a reaction, the SC method delivers more reliable results in general and we are only showing and discussing these results.

The oxalate formation is shown as a green line in Fig. 6: at potentials  $> -0.5$  V,  $\text{Na}^+$  does neither co-adsorb with the reactant nor with the product in vacuum and the formation of oxalate on the surface is endothermic. For lower potentials, one counterion is co-adsorbed with oxalate, but not with  $\text{CO}_2$ , giving rise to the noticeable potential dependence of the reaction energy. Furthermore, at potentials lower than  $-0.9$  V, the surface catalyzed reaction could take place at a reasonable rate since it is exothermic, provided that there is chemisorbed  $\text{CO}_2$  available and not only CO and O. At potentials lower than  $-1.25$  V, the reactant is  $\text{CO}_2$ , co-adsorbed with  $\text{Na}^+$  that yields surface adsorbed sodium oxalate ( $\text{Na}_2\text{C}_2\text{O}_4$ ). However, the potential dependence of the elementary reaction is almost negligible in the absence of  $\text{Na}^+$  co-adsorption, *i.e.*, the capacitance and workfunction of  $\text{C}_2\text{O}_4@Ni(111)$  are not significantly larger than those of  $\text{CO}_2@Ni(111)$ . The situation for carbonate formation is similar to that for oxalate formation, except that thermodynamically it is much more accessible on the surface, not the least because of the  $\text{CO}@Ni(111)$  byproduct. Hence, carbonate formation is preferred over oxalate formation on the  $Ni(111)$  surface, although the overall reaction energy is less favorable. Nevertheless, the dominating surface species down to  $-1.75$  V is CO, O, which itself might react with additional  $\text{CO}_2$  to yield carbonate, but is not expected to form oxalates.

$\text{Na}^+$  co-adsorption provides less stability under solvent conditions than in a vacuum. For instance, surface adsorbed oxalate is stabilized by  $\text{Na}^+$  at potentials below  $-0.5$  V in vacuum, but only below  $-1.0$  V in implicit DMF. As a consequence, the surface reaction forming  $\text{C}_2\text{O}_4$  is isoenergetic at  $\sim -0.9$  V in a vacuum, but it takes  $-1.9$  V when solvating the systems. Hence, oxalate formation on  $Ni(111)$  is even less expected under solvent conditions than in a vacuum. Furthermore, adsorbed oxalate is more compact and thus less accessible to the solvent than two chemisorbed  $\text{CO}_2$  molecules, resulting in a loss of solvation energy for oxalate formation. Although similar remarks apply to carbonate formation, the details differ

slightly, mostly because the solvent effect is enhanced for carbonate compared to oxalate. Finally, the relative stability of CO, O (2/9 ML) compared to carbonate in solvent varies less with the potential than in vacuum. Nevertheless, at very reducing potentials carbonate formation becomes competitive with the poisoning of the catalyst by the CO, O surface layer, just like in vacuum. Hence, the combination of unfavorable oxalate formation on the surface with the overwhelming competition of  $\text{CO}_2$  dissociation and carbonate formation makes oxalate formation unlikely over a nickel catalyst despite a favorable overall reaction energy. In contrast, carbonate and carbon monoxide formation is likely at low potentials. This selectivity between the two possible products of  $\text{CO}_2$  electroreduction under aprotic conditions over Ni is in excellent agreement with experimental observations: oxalate formation accounts for less than 10% of the current density, while CO formation is the major product observed under aprotic conditions.<sup>11,14,15</sup>

## 6 Conclusion

Investigating by first principles the intrinsic reactivity of  $\text{CO}_2$  on  $Ni(111)$  under electrochemically reducing conditions in aprotic media, we have compared two approaches that take the electrochemical potential into account. Furthermore, the comparison exploits a recently implemented implicit solvent model<sup>64</sup> to move towards more realistic conditions than vacuum.

The present study evidences that the zeroth order method for including the electrochemical potential (LFER-EP) is a valuable tool for quickly assessing the thermodynamic aspects of electrocatalysis in vacuum, which often gives a good indication of the processes under more realistic conditions. For example, this highly efficient approach correctly identifies the dissociative adsorption of  $\text{CO}_2$  yielding CO and O as exothermic at all relevant potentials and predicts the formation of carbonates, rather than oxalates, over  $Ni(111)$ . This preference is due to an insufficiently stabilizing interaction of oxalate with the surface. The surface charging method (SC) allows us to vary the charge on the adsorbates as a function of potential. Therefore, in contrast to the LFER-EP, which is limited to cation coupled electron transfers, the SC method stabilizes the chemisorption of  $\text{CO}_2$  at reducing potentials even in the absence of counterions. While the LFER-EP results are insensitive to the inclusion of an implicit solvent description, the situation is dramatically modified when explicitly accounting for the electrochemical potential by charging the electrode. The solvent strongly increases the capacitance of the surface and hence the surface charge for a given bias potential. Even the rather simplistic solvation model applied herein gives rise to marked changes in electrochemical reactivity compared to vacuum. Most strikingly, the charge injection is system dependent and differs significantly from the ideal values of 0 and 1. As a consequence, adsorption energies are potential dependent when accounting for solvent effects. This results, even in the absence of counterion co-adsorption, in a potential dependence of the most stable surface species, *e.g.*, the formation of carbonates rather than



## Chapter 8. Impacts of electrode potentials and solvents on the electroreduction of CO<sub>2</sub>: a comparison of theoretical approaches

View Article Online

Paper

PCCP

just CO and O for coverages above 2/9 ML, and the preferred adsorption mode of oxalate, while such a dependency is inherently absent in LFER-EP. In summary, the SC method coupled with an implicit solvent model gives access to a wealth of detailed information beyond the LFER-EP. Therefore, we recommend this more advanced, but still quite efficient, model when seeking an understanding of the fundamental processes in an electrochemical interfacial system.

### Acknowledgements

The authors acknowledge Solvay for financial support. J.-S. Filhol and N. Lespes are thanked for help in setting up the surface charging method and for fruitful discussions in the early stage of composing the manuscript. The authors acknowledge computational resources generously provided by the mesocenter PSMN. This work was granted access to the HPC resources of CINES and IDRIS under the allocation 2014-080609 made by GENCI.

### References

- 1 K. S. Joya, Y. F. Joya, K. Ocakoglu and R. van de Krol, *Angew. Chem., Int. Ed.*, 2013, **52**, 10426.
- 2 A. J. Appleby, *Catal. Rev.*, 1971, **4**, 221.
- 3 J. Bockris, *Int. J. Hydrogen Energy*, 1999, **24**, 1.
- 4 N. S. Lewis and D. G. Nocera, *Proc. Natl. Acad. Sci. U. S. A.*, 2006, **103**, 15729.
- 5 J. O. Bockris, *Int. J. Hydrogen Energy*, 2008, **33**, 2129.
- 6 D. Pletcher and J. Girault, *J. Appl. Electrochem.*, 1986, **16**, 791.
- 7 J. Bringmann and E. Dinjus, *Appl. Organomet. Chem.*, 2001, **15**, 135.
- 8 M. Gattrell, N. Gupta and A. Co, *J. Electroanal. Chem.*, 2006, **594**, 1.
- 9 Y. Hori, *Modern Aspects of Electrochemistry*, Springer, New York, Gaithersburg MD, 2008, ch. 3, p. 89.
- 10 D. Canfield and K. W. Frese, *J. Electrochem. Soc.*, 1983, **130**, 1772.
- 11 S. Ikeda, T. Takagi and K. Ito, *Bull. Chem. Soc. Jpn.*, 1987, **60**, 2517.
- 12 D. T. Whipple and P. J. A. Kenis, *J. Phys. Chem. Lett.*, 2010, **1**, 3451.
- 13 I. Ganesh, *Renewable Sustainable Energy Rev.*, 2014, **31**, 221.
- 14 M. Jitaru, D. Lowy, M. Toma, B. Toma and L. Oniciu, *J. Appl. Electrochem.*, 1997, **27**, 875.
- 15 J.-P. Jones, G. K. S. Prakash and G. A. Olah, *Isr. J. Chem.*, 2014, **54**, 1451.
- 16 G.-Q. Yuan, H.-F. Jiang, C. Lin and S.-J. Liao, *Electrochim. Acta*, 2008, **53**, 2170.
- 17 C.-H. Li, G.-Q. Yuan, X.-C. Ji, X.-J. Wang, J.-S. Ye and H.-F. Jiang, *Electrochim. Acta*, 2011, **56**, 1529.
- 18 R. Mattheessen, J. Fransaer, K. Binnemans and D. E. D. Vos, *RSC Adv.*, 2013, **3**, 4634.
- 19 T. Yamamoto, D. A. Tryk, K. Hashimoto, A. Fujishima and M. Okawa, *J. Electrochem. Soc.*, 2000, **147**, 3393.
- 20 O. M. Magnussen, J. Hotlos, R. J. Nichols, D. M. Kolb and R. J. Behm, *Phys. Rev. Lett.*, 1990, **64**, 2929.
- 21 T. Iwasita and F. Nart, *Prog. Surf. Sci.*, 1997, **55**, 271.
- 22 K. Jambunathan and A. C. Hillier, *J. Electrochem. Soc.*, 2003, **150**, E312.
- 23 K. Jambunathan, S. Jayaraman and A. C. Hillier, *Langmuir*, 2004, **20**, 1856.
- 24 Y. X. Chen, M. Heinen, Z. Jusys and R. J. Behm, *Angew. Chem., Int. Ed.*, 2006, **45**, 981.
- 25 Y. Gorlin, B. Lassalle-Kaiser, J. D. Benck, S. Gul, S. M. Webb, V. K. Yachandra, J. Yano and T. F. Jaramillo, *J. Am. Chem. Soc.*, 2013, **135**, 8525.
- 26 K. Letchworth-Weaver and T. A. Arias, *Phys. Rev. B: Condens. Matter Mater. Phys.*, 2012, **86**, 075140.
- 27 J. I. Siepmann and M. Sprik, *J. Chem. Phys.*, 1995, **102**, 511.
- 28 S. Tazi, M. Salanne, C. Simon, P. Turq, M. Pounds and P. A. Madden, *J. Phys. Chem. B*, 2010, **114**, 8453.
- 29 D. M. Bernardi and M. W. Verbrugge, *J. Electrochem. Soc.*, 1992, **139**, 2477.
- 30 W. Goddard, B. Merinov, A. van Duin, T. Jacob, M. Blanco, V. Molinero, S. Jang and Y. Jang, *Mol. Simul.*, 2006, **32**, 251.
- 31 R. Ferreira de Morais, P. Sautet, D. Loffreda and A. A. Franco, *Electrochim. Acta*, 2011, **56**, 10842.
- 32 K. Ito, S. Ikeda, N. Yamauchi, T. Iida and T. Takagi, *Bull. Chem. Soc. Jpn.*, 1985, **58**, 3027.
- 33 L. Sun, G. K. Ramesha, P. V. Kamat and J. F. Brennecke, *Langmuir*, 2014, **30**, 6302.
- 34 B. Eneau-Innocent, D. Pasquier, F. Ropital, J.-M. Leger and K. B. Kokoh, *Appl. Catal., B*, 2010, **98**, 65.
- 35 J. K. Norskov, J. Rossmeisl, A. Logadottir, L. Lindqvist, J. R. Kitchin, T. Bligaard and H. Jonsson, *J. Phys. Chem. B*, 2004, **108**, 17886.
- 36 J. S. Hummelshoj, J. Blomqvist, S. Datta, T. Vegge, J. Rossmeisl, K. S. Thygesen, A. C. Luntz, K. W. Jacobsen and J. K. Norskov, *J. Chem. Phys.*, 2010, **132**, 071101.
- 37 J. Greeley, J. K. Norskov and M. Mavrikakis, *Annu. Rev. Phys. Chem.*, 2002, **53**, 319.
- 38 V. Stamenkovic, B. S. Mun, K. J. J. Mayrhofer, P. N. Ross, N. M. Markovic, J. Rossmeisl, J. Greeley and J. K. Norskov, *Angew. Chem., Int. Ed.*, 2006, **45**, 2897.
- 39 J. Rossmeisl, Z.-W. Qu, H. Zhu, G.-J. Kroes and J. Norskov, *J. Electroanal. Chem.*, 2007, **607**, 83.
- 40 P. Ferrin, A. U. Nilekar, J. Greeley, M. Mavrikakis and J. Rossmeisl, *Surf. Sci.*, 2008, **602**, 3424.
- 41 J. Greeley, I. E. Stephens, A. S. Bondarenko, T. P. Johansson, H. A. Hansen, T. F. Jaramillo, J. Rossmeisl, I. Chorkendorff and J. K. Norskov, *Nat. Chem.*, 2009, **1**, 552.
- 42 J. A. Keith, G. Jerkiewicz and T. Jacob, *ChemPhysChem*, 2010, **11**, 2779.
- 43 I. C. Man, H.-Y. Su, F. Calle-Vallejo, H. A. Hansen, J. I. Martinez, N. G. Inoglu, J. Kitchin, T. F. Jaramillo, J. K. Norskov and J. Rossmeisl, *ChemCatChem*, 2011, **3**, 1159.
- 44 A. S. Bandarenka, A. S. Varela, M. Karamad, F. Calle-Vallejo, L. Bech, F. J. Perez-Alonso, J. Rossmeisl, I. E. L. Stephens and I. Chorkendorff, *Angew. Chem., Int. Ed.*, 2012, **51**, 11845.

- 45 J. Rossmeisl, J. K. Norskov, C. D. Taylor, M. J. Janik and M. Neurock, *J. Phys. Chem. B*, 2006, **110**, 21833.
- 46 C. D. Taylor, S. A. Wasileski, J.-S. Filhol and M. Neurock, *Phys. Rev. B: Condens. Matter Mater. Phys.*, 2006, **73**, 165402.
- 47 A. Y. Lozovoi and A. Alavi, *Phys. Rev. B: Condens. Matter Mater. Phys.*, 2003, **68**, 245416.
- 48 M. Otani and O. Sugino, *Phys. Rev. B: Condens. Matter Mater. Phys.*, 2006, **73**, 115407.
- 49 R. Jinnouchi and A. B. Anderson, *Phys. Rev. B: Condens. Matter Mater. Phys.*, 2008, **77**, 245417.
- 50 I. Dabo, B. Kozinsky, N. E. Singh-Miller and N. Marzari, *Phys. Rev. B: Condens. Matter Mater. Phys.*, 2008, **77**, 115139.
- 51 Y.-H. Fang and Z.-P. Liu, *J. Phys. Chem. C*, 2009, **113**, 9765.
- 52 M. Mamatkulov and J.-S. Filhol, *Phys. Chem. Chem. Phys.*, 2011, **13**, 7675.
- 53 I. Hamada, O. Sugino, N. Bonnet and M. Otani, *Phys. Rev. B: Condens. Matter Mater. Phys.*, 2013, **88**, 155427.
- 54 J.-S. Filhol and M. Neurock, *Angew. Chem., Int. Ed.*, 2006, **45**, 402.
- 55 C. Taylor, R. G. Kelly and M. Neurock, *J. Electrochem. Soc.*, 2006, **153**, E207.
- 56 M. J. Janik and M. Neurock, *Electrochim. Acta*, 2007, **52**, 5517.
- 57 G. Rostamikia and M. J. Janik, *Energy Environ. Sci.*, 2010, **3**, 1262.
- 58 S. A. Wasileski and M. J. Janik, *Phys. Chem. Chem. Phys.*, 2008, **10**, 3613.
- 59 K.-Y. Yeh and M. J. Janik, *J. Comput. Chem.*, 2011, **32**, 3399.
- 60 J.-L. Fattebert and F. Gygi, *Int. J. Quantum Chem.*, 2003, **93**, 139.
- 61 S. A. Petrosyan, A. A. Rigos and T. A. Arias, *J. Phys. Chem. B*, 2005, **109**, 15436.
- 62 Y.-H. Fang and Z.-P. Liu, *J. Am. Chem. Soc.*, 2010, **132**, 18214.
- 63 O. Andreussi, I. Dabo and N. Marzari, *J. Chem. Phys.*, 2012, **136**, 064102.
- 64 K. Mathew, R. Sundararaman, K. Letchworth-Weaver, T. A. Arias and R. G. Hennig, *J. Chem. Phys.*, 2014, **140**, 084106.
- 65 C. J. Cramer and D. G. Truhlar, *Chem. Rev.*, 1999, **99**, 2161.
- 66 J. O. Bockris, A. K. N. Reddy and M. Gamboa-Aldeco, *Modern Electrochemistry 2A, Fundamental of Electrodeics*, Kluwer Academic Publishers, New York, 2002.
- 67 *GoldBook*, Standard Hydrogen electrode, <http://goldbook.iupac.org/S05917.html>.
- 68 C. P. Kelly, C. J. Cramer and D. G. Truhlar, *J. Phys. Chem. B*, 2006, **110**, 16066.
- 69 Y. P. Zhang, C. H. Cheng, J. T. Kim, J. Stanojevic and E. E. Eyler, *Phys. Rev. Lett.*, 2004, **92**, 203003.
- 70 If we use  $2\text{H}^+ + 2\text{e}^- \rightarrow \text{H}_2$  to estimate the energy of  $\text{H}_2$  at standard conditions, we need the energy of the solvated proton and the energy of the electrons. The hydration free energy of the proton is estimated to be about  $-11.5 \text{ eV}$ .<sup>68</sup> Together with the electron potential of  $-4.44 \text{ V}$  vs. vacuum, we get  $-31.88 \text{ eV}$ , which is in good agreement with the “quantum chemical estimate” of  $2 \times -13.6 \text{ eV}$  (energy of a hydrogen atom) +  $-4.5 \text{ eV}$  (binding energy of the hydrogen molecule<sup>69</sup>) =  $-31.7 \text{ eV}$ .
- 71 In the generalization of the CHE to an arbitrary reference couple (see ref. 36) the severeness of this approximation is most clearly visible: the zero charge energy of a system always corresponds to the reversible potential of the reference redox couple. For example the zero charge energy of  $\text{CO}_2@\text{Ni}$  corresponds to  $0 \text{ V}$ , if we consider a hydrogenation, but to  $-2.7 \text{ V}$  if we consider a reduction with sodium.
- 72 S. A. Wasileski, M. T. M. Koper and M. J. Weaver, *J. Am. Chem. Soc.*, 2002, **124**, 2796.
- 73 A. Panchenko, M. T. M. Koper, T. E. Shubina, S. J. Mitchell and E. Roduner, *J. Electrochem. Soc.*, 2004, **151**, A2016.
- 74 M. P. Hyman and J. W. Medlin, *J. Phys. Chem. B*, 2005, **109**, 6304.
- 75 S. A. Wasileski and M. J. Weaver, *J. Phys. Chem. B*, 2002, **106**, 4782.
- 76 J.-S. Filhol and M.-L. Doublet, *Catal. Today*, 2013, **202**, 87.
- 77 J.-S. Filhol and M.-L. Doublet, *J. Phys. Chem. C*, 2014, **118**, 19023.
- 78 Y.-H. Fang, G.-F. Wei and Z.-P. Liu, *J. Phys. Chem. C*, 2014, **118**, 3629.
- 79 R. C. Catapan, A. A. M. Oliveira, Y. Chen and D. G. Vlachos, *J. Phys. Chem. C*, 2012, **116**, 20281.
- 80 E. Westphal and J. R. Pliego, *J. Chem. Phys.*, 2005, **123**, 074508.
- 81 M. Dusek, G. Chapuis, M. Meyer and V. Petricek, *Acta Crystallogr., Sect. B: Struct. Sci.*, 2003, **59**, 337.
- 82 D. A. Reed and M. M. Olmstead, *Acta Crystallogr., Sect. B: Struct. Crystallogr. Cryst. Chem.*, 1981, **37**, 938.
- 83 J. P. Perdew, K. Burke and M. Ernzerhof, *Phys. Rev. Lett.*, 1996, **77**, 3865.
- 84 P. E. Blochl, *Phys. Rev. B: Condens. Matter Mater. Phys.*, 1994, **50**, 17953.
- 85 G. Kresse and D. Joubert, *Phys. Rev. B: Condens. Matter Mater. Phys.*, 1999, **59**, 1758.
- 86 G. Kresse and J. Hafner, *Phys. Rev. B: Condens. Matter Mater. Phys.*, 1993, **47**, 558.
- 87 G. Kresse and J. Furthmuller, *Phys. Rev. B: Condens. Matter Mater. Phys.*, 1996, **54**, 11169.
- 88 D. Gunceler, K. Letchworth-Weaver, R. Sundararaman, K. A. Schwarz and T. A. Arias, *Modell. Simul. Mater. Sci. Eng.*, 2013, **21**, 074005.
- 89 K. Hara, A. Kudo and T. Sakata, *J. Electroanal. Chem.*, 1995, **391**, 141.
- 90 R. J. Lim, M. Xie, M. A. Sk, J.-M. Lee, A. Fisher, X. Wang and K. H. Lim, *Catal. Today*, 2014, **233**, 169.



## 9 Electro-carboxylation of butadiene and ethene over Pt and Ni catalysts

Having assessed the suitability of the explicit inclusion of the electrochemical potential in combination with an implicit solvent for CO<sub>2</sub> reduction under aprotic conditions in chapter 8, we turned to the experimentally relevant question of the carboxylation of alkenes. Indeed, our industrial partner, Solvay, was investigating the feasibility of a sustainable process for adipic acid production based on the electro-carboxylation of butadiene. Applying the surface charging method to the carboxylation reaction over nickel and platinum, we rationalized the experimentally observed features: (1) platinum is a very poor catalyst for electro-carboxylation since it does not stabilize the C–C bond forming transition state very well. (2) The overpotential is excessively high over common catalysts, since it is an almost desorbed CO<sub>2</sub><sup>•-</sup> radical anion which is the reactive species for C–C bond formation. (3) It is the first C–C bond formation which is rate and potential determining, while the second one leads to a stable product. In summary, this chapter illustrates the capabilities of state-of-the-art modelling techniques for the rationalization and guiding of experiments, even though in the present case the perspectives for an improved catalyst were dire in view of the reaction mechanism that, finally, involved the catalyst surface only weakly in the critical step. Concomitantly, given the relative prices of butadiene and adipic acid, the economic analysis done by Solvay indicated that the process would not be favorable.





Contents lists available at ScienceDirect

Journal of Catalysis

journal homepage: [www.elsevier.com/locate/jcat](http://www.elsevier.com/locate/jcat)

## Electro-carboxylation of butadiene and ethene over Pt and Ni catalysts



Stephan N. Steinmann<sup>a</sup>, Carine Michel<sup>a,b</sup>, Renate Schwiedernoch<sup>c</sup>, Mengjia Wu<sup>c</sup>, Philippe Sautet<sup>a,b,\*</sup>

<sup>a</sup> Univ Lyon, Ecole Normale Supérieure de Lyon, Université Lyon 1, Laboratoire de Chimie, 46 allée d'Italie, F69364 Lyon, France

<sup>b</sup> CNRS, Laboratoire de Chimie UMR 5182, 46 allée d'Italie, F69364 Lyon, France

<sup>c</sup> Eco-Efficient Products and Processes Laboratory (E2P2L), UMI 3464 Solvay/CNRS, Shanghai, PR China

### ARTICLE INFO

#### Article history:

Received 22 September 2015

Revised 8 January 2016

Accepted 13 January 2016

Available online 15 February 2016

#### Keywords:

Electrochemistry

Carbon dioxide

Nickel

Density functional theory

Mechanism

### ABSTRACT

Electrochemical synthesis could provide an elegant and efficient means to exploit the largely available C1 building block CO<sub>2</sub>. The electrocarboxylation of dienes is, in particular, an attractive goal. However, the presently known electrocatalysts are inefficient and not very selective since they work around  $-2.3$  V vs. SHE. In order to identify more active catalysts, we need to better understand the reaction mechanism. In this contribution, we present prototypical experimental results for the electrocarboxylation of 2,3-dimethyl-butadiene on a Ni catalyst and quantify the side-products, namely carbonates, oxalic and formic acid. Together with the extensive, state of the art, first principles investigation of the mechanism at the atomic scale, we reveal a highly activated process around the onset potential of  $-1.3$  V and a change in mechanism at the peak potential of  $-2.3$  V, suggesting that a more active catalyst could be engineered by modifying the morphology in order to facilitate the “chemical” C–C coupling step.

© 2016 Elsevier Inc. All rights reserved.

### 1. Introduction

Electrochemical synthesis could become an attractive means to exploit the largely available and thus cheap C1 building block, CO<sub>2</sub>. However, before society might benefit from this carbon source, major developments in the identification of (energy) efficient catalysts are still required. The main issue to overcome is that CO<sub>2</sub> is a rather inert molecule and its activation is, therefore, an energy intensive process, limiting the industrial interest.

The electrocatalyst can either be molecular (see [1] and references therein) or the surface of the cathode itself. It is on this second option that we focus on in the following: Due to easier separation, metallic electrodes are more attractive for large scale industrial applications than molecular catalysts.

The C–C bond formation between an unsaturated hydrocarbon (typically butadiene, see Fig. 1) and CO<sub>2</sub> is an elegant synthetic process to form dicarboxylated species [2–7]. The reaction is carried out in a polar, aprotic solvent (DMF) and requires high electrochemical potentials ( $-2$  to  $-2.5$  V vs SHE) for practical current densities. Furthermore, tolerance to heteroatom-substituents is, unfortunately, rather limited [8]. In particular the necessary very reducing potential is the main drawback of the

method, as it implies very low selectivity, since highly reactive species are generated. Therefore, a more active catalyst should be identified that allows to reduce the overpotentials dramatically.

Nickel is the favorite catalyst for carboxylation reactions of di-alkenes [9,10,7] and alkynes [11]. Platinum, on the other hand, leads to low yields for carboxylation of butadiene, cyclohexadiene and phenylacetylene substrates [11,10,7], while styrene could be carboxylated in equal yields over Ni and Pt [9]. Hence, we conclude that overall, Pt should lead to lower yields for carboxylations of alkenes.

The aim of this contribution is to elucidate the reaction mechanism of this reaction under electrochemical conditions in order to identify the rate limiting step.

Theoretical studies under aprotic conditions in the presence of an electrochemical potential are still rather scarce, since the description of the electrochemical potential from first principles is challenging and the solvent also needs to be accounted for, which, again, is a rather recent undertaking in periodic electronic structure codes. We have recently extensively studied the intrinsic reactivity of CO<sub>2</sub> under reducing conditions over Ni(111) [12] combining an established method for the electrochemical potential [13,14] with an implicit solvent [15]. The same methodology has been applied to the electro-oxidation of formic acid and has evidenced the importance of accounting for the electrochemical potential for “chemical” steps and their activation energies [16].

\* Corresponding author at: Univ Lyon, Ecole Normale Supérieure de Lyon, CNRS Université Lyon 1, Laboratoire de Chimie UMR 5182, 46 allée d'Italie, F-69364, Lyon, France.

E-mail address: [philippe.sautet@ens-lyon.fr](mailto:philippe.sautet@ens-lyon.fr) (P. Sautet).

<http://dx.doi.org/10.1016/j.jcat.2016.01.008>

0021-9517/© 2016 Elsevier Inc. All rights reserved.



## Chapter 9. Electro-carboxylation of butadiene and ethene over Pt and Ni catalysts

S.N. Steinmann et al./Journal of Catalysis 343 (2016) 240–247

241

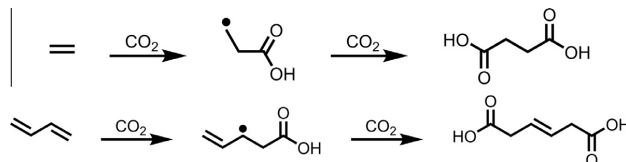


Fig. 1. Reaction schemes for carboxylation of ethene and butadiene. Charges are omitted for clarity. Formal radicals, indicated by dots, are strongly bound to the metal surface, which quenches the spin-polarization.

After the presentation of prototypical experimental results using a Ni catalyst that also quantify side products, we discuss in detail the reactivity on Ni(111) (best catalyst identified) and Pt (111) (poor catalyst for this reaction according to the literature [11,10,7]) model surfaces, in the presence of an electrochemical potential as determined by density functional theory (DFT) computations. Combining the experimental and theoretical insight we draw conclusions on the mechanism and on the prospects for improved electrocatalysts for this reaction.

### 2. Experimental details

#### 2.1. Chemicals and materials

Dry DMF and 2,3-dimethyl-1,3-butadiene (J&K Chemicals) were used as received. Tetrabutylammonium bromide ( $n\text{-Bu}_4\text{NBr}$ ) was dried in vacuum at 60 °C for 24 h. In order to minimize the introduction of water to the system a 0.24 mg/ml  $n\text{-Bu}_4\text{NBr}$  stock solution in DMF was prepared. Electrodes: Ni foam (battery grade, Shandong Heze Tianyu Technology Development Co., Ltd.), Al foil (99.9%, Shenzheng Kejing Star Technology Company), Pt wire (99.99%, Goodfellow Cambridge Limited).

#### 2.2. Instrumentation

A custom made high pressure stainless steel electrochemical reactor allows to run electrochemical synthesis under inert conditions. The electrochemical measurements and synthesis were carried out with Gamry Reference 3000 potentiostat/galvanostat. NMR spectra were measured with a BRUKER 300 MHz instrument. IC measurements were carried out in a DIONEX ICS-3000 with AS11-HC column. The carbonate content of the reaction residue was determined using a buret apparatus for  $\text{CO}_2$  capture as described in Pile et al. [17]. Before the setup is used, the apparatus is calibrated with calcium carbonate.

#### 2.3. Electrochemical procedure

In all experiments a single compartment high pressure stainless steel reactor was used and equipped with nickel foam cathode, aluminum sacrificing anode and platinum wire as reference electrode. Before the chemicals are filled in, the reactor is sealed and dried at 50 °C in vacuum for 12 h. 67 ml DMF and 13 ml N4444Br solution are added and degassed with Ar. Then 2,3-dimethyl-1,3-butadiene is introduced, the reactor is closed and

the pressure is increased by adding  $\text{CO}_2$ . Once the pressure is stable and the reactor cooled down to 25 °C, the electrodes are connected to a Gamry potentiostat. Cyclic voltammetry experiments were carried out before and after electrochemical synthesis. Scan rate was 50 mV/s.

Chronopotentiometric experiments were carried out for the synthesis of the diacids (see Fig. 2). The current density was set in a range between 5 and 10  $\text{mA}/\text{cm}^2$  in order to achieve the desired potential range. After synthesis, DMF was removed under vacuum and the carbonate content was determined by a buret apparatus for  $\text{CO}_2$  capture. The residue was acidified with 2 M HCl for 6 h. Oxalic acid and formic acid were measured by IC measurements before the product was extracted with dimethyl ether and dried over  $\text{Na}_2\text{SO}_4$ . After isolation of the hexadienoic acid,  $^1\text{H}$  and  $^{13}\text{C}$  NMR in DMSO were performed to validate the product.

### 3. Computational details

All computations are carried out using the surface charging method and include an implicit DMF solvent. For more details on the methodology, see Ref. [12]. The electronic structure is described by the PBE density functional and the valence electrons expanded in a 400 eV cutoff basis set. Note, that when we started this study, VASPsol [15] was incompatible with non-local van der Waals density functionals and we did therefore not apply them. Dispersion is expected to lead to stronger adsorption energies, but reaction energies should be less affected and in particular the comparison between Ni and Pt should barely change upon inclusion of these non-bonded interactions. Symmetric slabs of 5 metallic layers were used to model catalyst surfaces by the (111) facet. Ethene carboxylation is studied in a  $p(3 \times 3)$  unit cell with a  $3 \times 3 \times 1$  K point mesh, while butadiene carboxylation is assessed in a  $p(5 \times 5)$  unit cell and a  $2 \times 2 \times 1$  K point mesh. These K-point grids were checked to give well converged results for the chemisorption of  $\text{CO}_2$ . All geometries were optimized to reach a gradient smaller than 0.05 eV/Å with wave functions converged to  $5 \cdot 10^{-5}$  eV. The precision setting of VASP is set to “normal” and the automatic optimization of the real-space projection operators is used.

We model the  $\text{Al}^{3+}$  or  $\text{Mg}^{2+}$  counterions as  $\text{Na}^+$  in analogy to our previous work. In reality, these salts are solvated in the polar DMF solvent. Hence, their true energy (e.g., as ion pairs in solution) is lower than assumed herein, where the ion pair is just surrounded by an implicit solvent.

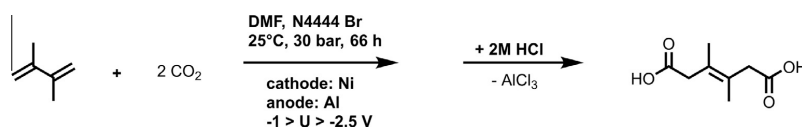
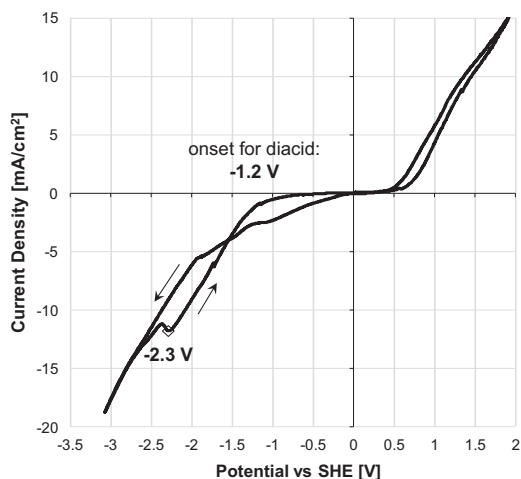


Fig. 2. Experimental reaction scheme.



**Fig. 3.** CV diagram (Scan rate: 50 mV/s) of 2,3-dimethyl-1,3-butadiene in 12 mM of tetrabutylammonium bromide in DMF, under a pressure of 30 bar CO<sub>2</sub> for a rotating nickel anode.

#### 4. Results and discussion

Electrosynthesis promises an efficient route towards CO<sub>2</sub> valorization, where the electron activates the rather inert molecule to yield a useful C1 building block. One of the conceptually simplest applications of this strategy is the electrocarboxylation of unsaturated hydrocarbons. This reaction is well documented in the literature [3,7], with butadiene being the prototype substrate [10]. Nevertheless, the process is far from being economically efficient, mostly due to the substantial associated overpotentials and low yields. Herein, we strive to shed light on the origin of these overpotentials in the hope that the detailed understanding might provide hints about the design of improved catalysts. All the electrochemical potentials of the experimental and theoretical studies are referenced to the standard hydrogen electrode (SHE).

##### 4.1. Experimental results

The selectivity between different products can be controlled by changing the potential and is affected by the current. Generally speaking, the potential determines which products are possible to obtain, i.e., the thermodynamics, and the current reflects the reaction rate, i.e., the kinetics. In addition to the C–C coupling reaction of the diene with CO<sub>2</sub>, formic acid is formed due to traces of water that provide protons for CO<sub>2</sub> reduction.

We focused our experimental study on a Ni electrode. Fig. 3 shows a typical CV measurement, which allows us to identify the onset and peak potential of the C–C coupling reaction. We obtain an onset potential of –1.2 V vs. SHE for the reaction of CO<sub>2</sub> with

2,3-dimethyl-1,3-butadiene and a peak potential around –2.3 V. The large difference between the two potentials indicates that the reaction has a considerable (chemical) activation energy. Note that the peak potential is in the range of potentials (–2.3 to –2.6 V vs SHE depending on the electrolyte) reported for CO<sub>2</sub> reduction to (almost) free CO<sub>2</sub> radicals [3].

Electrolysis experiments were carried out to characterize the product selectivity and efficiency of the electroreductive C–C coupling between the diene and CO<sub>2</sub>.

In order to assess the efficiency and selectivity of the process, Table 1 reports the selectivities of the four main products as derived from their measured mole fractions, i.e., the percentage of reduced CO<sub>2</sub> found in one of the four identified products. Since we are mainly interested in the production of the diacid, we also quantified the conversion of the diene by measuring the remaining reactant in the reaction mixture, the yield of the diacid with respect to the reactant (diene) and the Faraday yield, i.e. the yield of diacid with respect to the total amount of charge passed through the system.

In the experiments that were carried out at a high reduction potential of about –2.5 V and current densities between 5 and 8 mA/cm<sup>2</sup>, the diacid could be achieved with a Faraday yield of about 32% and about 65% yield with respect to the reacted diene (see Table 1). The diene missing from mass balance is either lost by leaks in the systems or polymerizes under these strongly reducing conditions [3]. Inorganic carbonate accounts for 3% of the reacting CO<sub>2</sub> under such conditions, while formate formation is responsible for about 60%. At these strongly reducing potentials even oxalates could be obtained with about 15% selectivity.

When the potential and current density were decreased to –1.8 V and below 1 mA/cm<sup>2</sup>, respectively, the applied reduction potential remains beyond the onset potential of diacid formation (–1.3 V). Despite prolonged reaction time, the chemical and Faraday yield for the diacid were decreased dramatically (below 0.5%). The same observation is true for oxalate, for which the selectivity drops to 0.2%. Carbonates and formate, however, are produced with about 10% and 90% selectivity, respectively. The pronounced difference in potential dependence of the formation of the two groups of products (formate and carbonate on one hand, oxalate and diacid on the other) suggests that different rate limiting intermediates are involved.

##### 4.2. Alkene vs. dialkene carboxylation

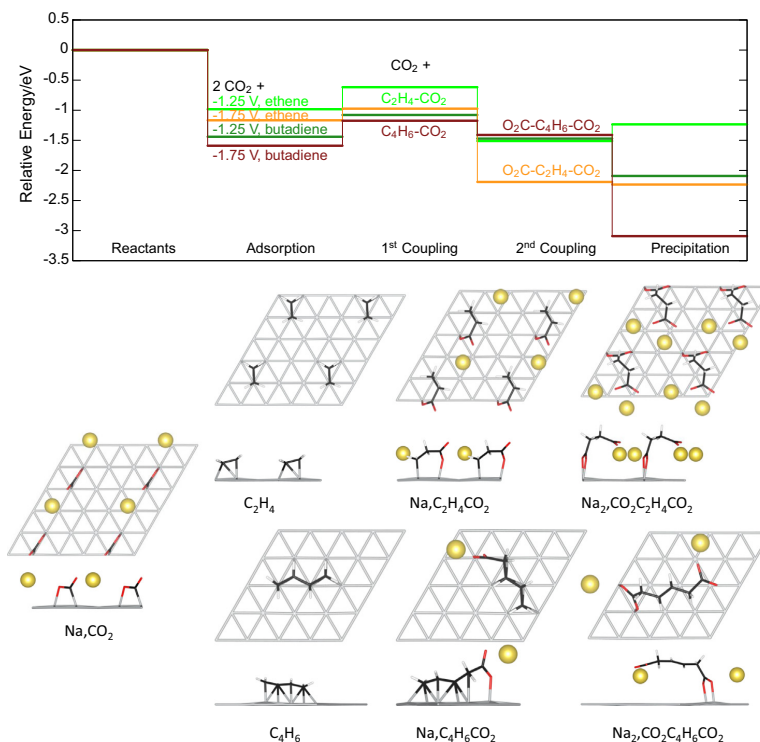
To gain more insights in the visibly challenging selectivity issues and the origin of the slow kinetics, we performed a detailed computational analysis of the electro-carboxylation reaction at the atomic level.

Fig. 4 gives the thermodynamic profile for the carboxylation of butadiene on Ni, the best catalyst identified to date [11,10,7]. Additionally, we present the corresponding results for the carboxylation of ethene, which serves as a convenient computational model for the computational most demanding steps (transition states). Following the general scheme outlined in Fig. 1, the thermodynamic profile starts with the chemisorption of the reactants, which is followed by the first C–C coupling step. After the second

**Table 1**

Current density, selectivities of reacting CO<sub>2</sub> yielding the diacid, inorganic carbonate, formic and oxalic acid, conversion of the diene, yield of the diacid and current efficiency (Faraday yield) for the diacid, for two different average potentials vs. SHE on a Ni electrode.

U [V]	j [mA/cm <sup>2</sup> ]	Selectivities [%]			Conv. of diene [%]	Diacid yield [%]	Faraday yield [%]
		Diacid	CO <sub>3</sub> <sup>2-</sup>	Formic acid			
–2.5	5	21	3	59	17	51	32
–1.8	0.8	0.4	8.6	90.8	0.2	53.5	0.8



**Fig. 4.** (top) Thermodynamic energy profile for carboxylation of ethene (light green/orange) compared to butadiene (dark green/dark red) on Ni(111) at  $-1.25$ – $-1.75$  V vs. SHE. (bottom) Geometries relevant to the carboxylation of ethene and butadiene on Ni(111) (see SI for ethene on Pt(111)). The  $3 \times 3$  unit cell for ethene is repeated in each direction parallel to the surface to show close contacts, while the  $5 \times 5$  cell for butadiene is not repeated. The Ni atoms are colored gray and Na<sup>+</sup> yellow, while carbon, hydrogen and oxygen are colored black, white and red, respectively. (For interpretation of the references to color in this figure legend, the reader is referred to the web version of this article.)

carboxylation, the product can desorb, which is modeled by the precipitation of the sodium salt.

Ethene adsorbs on Ni(111) in a C(top),C'(hcp) mode, with the typical out of plane bending of the hydrogen atoms in order to rehybridize the carbon atoms to optimize the energy match to the d-band of the metal. CO<sub>2</sub> is adsorbed on a bridge site. The molecule is bent, with one oxygen atom pointing away from the surface (angle of about 125°) and at sufficiently negative potentials ( $< -1.75$  V vs. SHE), a Na<sup>+</sup> cation co-adsorbs in the vicinity (2.26 Å) of this oxygen atom and in close contact with the negatively charged surface (2.90 Å). After the first coupling, the singly carboxylated species is adsorbed in a similar way to ethene: the new C–C bond is formed at the C'(hcp) carbon atom. In the case of co-adsorption with Na<sup>+</sup>, one of the oxygen atoms is found in a top position, while the other one is pointing away from the surface and is strongly interacting with the co-adsorbed Na<sup>+</sup> ion (distance 2.29 Å). The second coupling goes along with a significant rearrangement, since no carbon atom is adsorbed strongly on the surface anymore. The adsorption mode is, furthermore, asymmetric: one carboxylate group is adsorbed directly to the Ni surface (2.12 Å), while the second group is almost 2 Å further away and more directly surrounded by the Na<sup>+</sup> counterions.

Although the initial adsorption of ethene is, as expected, weaker than of butadiene, the overall reaction profile is quite similar (Fig. 4). The first carboxylation is somewhat endothermic, while the second carboxylation is exothermic. These features are essen-

tially independent on the chosen potential: as will be shown in the following, the adsorption and the first C–C coupling do not markedly depend on the electrochemical potential. Indeed, considering the difference between the red ( $-1.75$  V) and the green ( $-1.25$  V) lines, the adsorption and the first coupling are only slightly affected by the electrochemical potential. It is the second coupling (for ethene) and the precipitation (for butadiene) which are most affected by the potential. In addition, the impact of the potential on the precipitation illustrates the significance of the electrochemical potential for the overall reaction: it is required to drive the reaction. These results indicate that at least for butadiene the precipitation is the key electrochemical step, although the slowest step is expected to be the formation of the first C–C bond. From this thermodynamic analysis, we identify ethene as a reasonable computational model for the carboxylation of di-alkenes over metal electrodes.

#### 4.3. Comparison of Pt(111) and Ni(111)

Having established the similarities between ethene and butadiene carboxylation, we investigate the ethene carboxylation over a good catalyst (Ni, *vide supra*) with a poor one (Pt) [11,10,7] in order to deepen our understanding of the limitations of the electrocarboxylation of unsaturated hydrocarbons. The insights from this comparison might lead us to identify the critical parameters for an improved catalyst.

#### 4.3.1. Adsorption of reactants

Fig. 5 traces the interaction energy between the reactant and the electrified surface as a function of the electrochemical potential over Ni (solid lines) and Pt (broken lines). Ethene adsorption is identical for the two catalysts and weakened at reducing potentials and the same is expected to hold for butadiene, which is only given for Ni(111). Carbon dioxide adsorption, on the other hand, is stabilized by reducing potentials. The major difference between the two metal electrodes consists in the stabilization of the formally reduced  $\text{CO}_2$ , i.e., the co-adsorption of  $\text{CO}_2$  and  $\text{Na}^+$ . This co-adsorption is energetically favorable over Pt at potentials below  $-1.0$  V vs. SHE, while the same process starts to occur over Ni only at potentials below  $-1.75$  V. This stabilization of  $\text{CO}_2$  co-adsorbed with  $\text{Na}^+$  might considerably influence the reactivity:  $\text{CO}_2$  is basically reduced on Pt, while this is not the case over Ni at the considered potentials. However, for all the reactions considered herein, no evidence for a marked difference due to the co-adsorption with  $\text{Na}^+$  is found.

As shown previously [12],  $\text{CO}_2$  has a strong tendency to dissociate into CO and O on Ni(111). This behavior is not paralleled by Pt(111), where the dissociative adsorption (light blue, broken lines in Fig. 5) is clearly unfavorable at all potentials considered compared to the chemisorption of  $\text{CO}_2$  (red lines). Hence, we may conclude that at the relevant potentials and  $\text{CO}_2$  pressure, the surface of Ni(111) has a dominant coverage of CO, O, while over Pt a co-adsorption of  $\text{CO}_2$  and  $\text{Na}^+$  should be expected. In terms of the competitive alkene adsorption, the situation is quite similar over both electrodes: ethene adsorption is less strong than either the dissociative adsorption of  $\text{CO}_2$  over Ni(111) or the  $\text{CO}_2/\text{Na}^+$  co-adsorption over Pt(111). Butadiene, featuring two C=C bonds,

on the other hand, adsorbs significantly stronger to the metal surface than ethene. The competition between butadiene and CO, O is, therefore more fierce on Ni(111), especially when considering the site requirements: 2/9 mono layer (ML) CO, O need 4 hollow sites, while butadiene is more “compact” occupying at least two adjacent three fold sites (see Fig. 4). A more advanced study of the coverage effects in CO, O or  $\text{CO}_2$  and  $\text{Na}^+$  on alkene adsorption in electrochemical conditions is extremely demanding computationally and hence out of the scope of this study.

To assess the nature of the surface species derived from  $\text{CO}_2/\text{Ni}$  (111), Fig. 6 investigates the coverage effect on the dissociation (activation) energy of  $\text{CO}_2$  on Ni(111). Since this reaction barely depends on the potential (see SI), the profile is shown for a typical potential of  $-1.75$  V vs SHE. In other words, the dissociation of  $\text{CO}_2$  is best described as a “chemical” step and not as a formal reduction of  $\text{CO}_2$  to CO, as could be thought at first sight. At low coverage (1/9 ML)  $\text{CO}_2$  dissociation requires an activation energy of around 0.5 eV, leading to the considerably more stable (around 1 eV) CO, O co-adsorbed state. While adsorbing (and dissociating) a second  $\text{CO}_2$  is still exothermic, the activation energy is increased to almost 1 eV and the exothermicity reduced significantly. In other words, the second dissociation of  $\text{CO}_2$  is a rather slow step and could be in competition with the C–C direct bond formation between  $\text{CO}_2$  and an alkene. The diminished exothermicity and increased activation barrier can be understood by the site requirements of the reaction: while the reactant ( $\text{CO}_2$ ) occupies a bridge position, the product (CO, O) is most stable in two dis-joint hollow sites. In other words, steric hindrance on the surface due to other strong adsorbates (e.g. alkenes) reduces the probability of  $\text{CO}_2$  dissociation. Due to the presence of CO on the surface, a carbonylation pathway

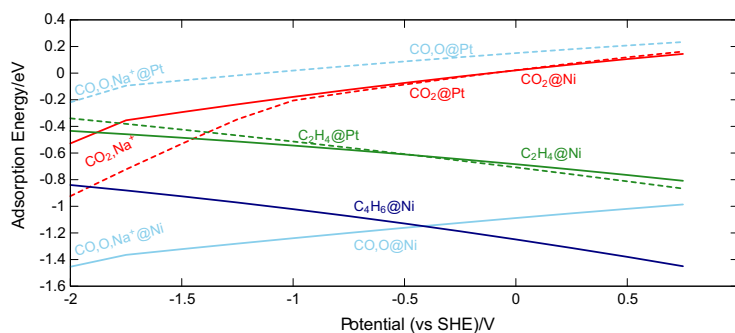


Fig. 5. Comparison of adsorption energies on Pt and Ni for  $\text{CO}_2$  and  $\text{C}_2\text{H}_4$  as a function of the electrochemical potential vs. SHE. Kinks indicate the onset of  $\text{Na}^+$  co-adsorption.  $\text{CO}_2$  chemisorption and dissociative adsorption are shown in red and light blue, respectively. Ethene and butadiene adsorption is given in dark green and blue, respectively. Full and broken lines refer to Ni(111) and Pt(111), respectively. (For interpretation of the references to color in this figure legend, the reader is referred to the web version of this article.)

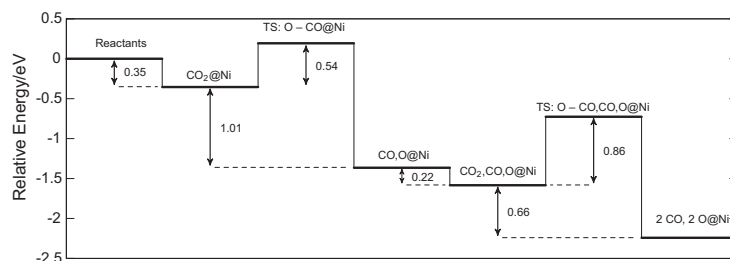


Fig. 6.  $\text{CO}_2$  dissociation over Ni(111) at 1/9 ML and 2/9 ML coverage at  $-1.75$  V vs SHE. Arrows indicate adsorption, activation and reaction energies.

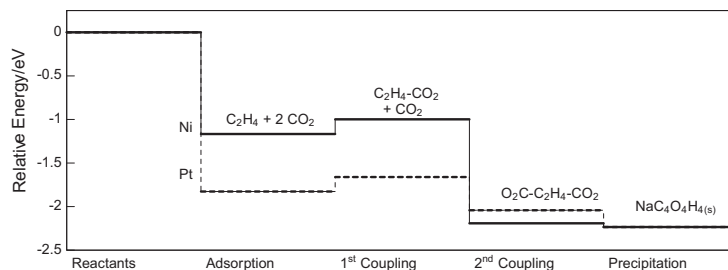


Fig. 7. Comparison of the energy profile for the carboxylation of ethene on Pt (broken lines) and Ni (full lines) at  $-1.75$  V vs. SHE.

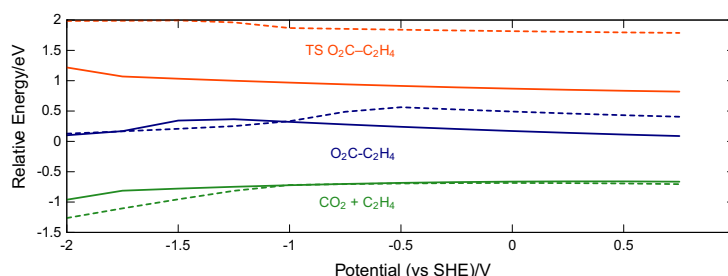


Fig. 8. C–C bond formation over Ni(111) (full lines) and Pt(111) (broken lines) as a function of the electrochemical potential. The energies are given with respect to isolated  $\text{CO}_2$  and  $\text{C}_2\text{H}_4$ .

could be in competition with a carboxylation pathway. However, a thermodynamic analysis of such a stepwise coupling of  $\text{CO}$ , followed by  $\text{O}$  to butadiene on Ni(111) goes through higher energy intermediates (see SI). Furthermore, the oxidation of the carboxylated intermediate is also expected to be a strongly activated process, since atomic oxygen is almost “buried” in the surface due to its strong interactions in the hollow sites.

#### 4.3.2. Origin of the superior activity of Ni(111) compared to Pt(111)

Experimentally, it is reported that the activity (yields) of Ni is significantly superior to Pt for the electro-carboxylation of dialkenes [11,10,7]. There are two possible scenarios to explain the higher yields over Ni than over Pt: Either the carboxylation is more facile over Ni than over Pt, or a competing reaction is more interfering over Pt than over Ni.

**C–C Bond formation.** The thermodynamics of the adsorption and carboxylation steps of ethene over Pt follows the Ni results (see Fig. 7) quite closely, except for a shift to lower energies for the first two steps, where  $\text{CO}_2, \text{Na}^+$  co-adsorption on Pt(111) is considerably more exothermic than  $\text{CO}_2$  chemisorption over Ni. While the second carboxylation is slightly less exothermic over Pt than over Ni, this does not change the predicted activity, which hinges on the first, endothermic, carboxylation. Hence, on thermodynamic grounds the reaction is found to be as difficult over Ni as over Pt.

The kinetics for the first C–C coupling, however, yields more insight (Fig. 8): For both the reactant (green) and singly coupled intermediate (blue)<sup>1</sup>, the adsorption energy with respect to isolated  $\text{CO}_2$  and ethene is very similar for Ni (full lines) and Pt (broken lines) over the entire potential range. As seen before, the coupling is endothermic by roughly 1 eV, with very little variation with the

potential, reflecting that the C–C coupling process is a chemical step. Since, however, the reactant (chemisorbed  $\text{CO}_2$ ) is not yet reduced by  $1 e^-$ , further electron transfer takes place in later reaction steps (second coupling and precipitation). The activation energy for the coupling process is, with 1.5–2 eV on Ni(111) high, but accessible, considering the approximate nature of the treatment of the electrochemical environment. Over Pt, however, the transition state is roughly 0.75 eV higher than over Ni(111). This high activation energy explains the low activity of Pt described in the literature. Note, that the barrier for the reverse reaction (C–C breaking) is low over Ni(111) (0.75 eV), while it is 1.5 eV for Pt(111), both values being in the expected range for C–C ruptures over Ni and Pt, respectively [18]. From the limiting transition state one might conclude that stepped surfaces should be much more active, since  $\text{CO}_2$  could more easily “slide under” the adsorbed alkene. Furthermore, C–C bonds are reported to be easier to form on steps (e.g. 211 [19] or 554 [20]) than on the 111 plane, anyway. Nevertheless, the relative activity of Pt and Ni is not expected to change qualitatively [21]. The reason for the substantial difference between Ni and Pt is suggested to lie in the difference of oxophilicity of the two metals: Ni is more oxophilic than Pt and can, therefore, better stabilize the  $\text{CO}_2$  fragment: the bent molecule lies flat on Ni(111) while on Pt(111) a rather unfavorable adsorption mode is adopted with one of the two oxygen atoms pointing away from the surface (see Fig. 9).

**Competing Reactions.** Considering the competing reactions of  $\text{CO}_2$  reduction under aprotic conditions, the main contributor is the formation of  $\text{CO}$  and its carbonate byproduct:



In agreement with earlier reports [22], the reductive dimerization of  $\text{CO}_2$  to oxalate ( $\text{C}_2\text{O}_4^{2-}$ ) is thermodynamically not competitive, neither over Ni, nor over Pt (see SI).

<sup>1</sup> For interpretation of color in Fig. 8, the reader is referred to the web version of this article.

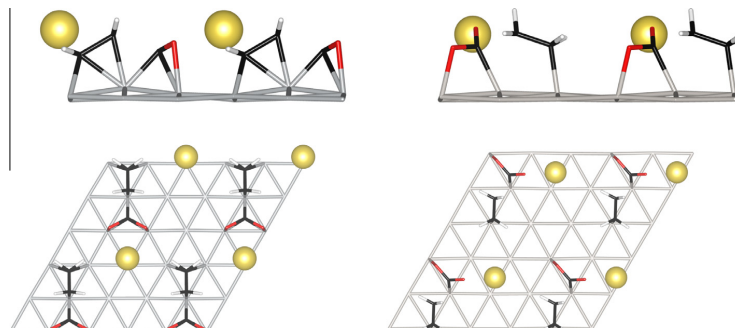


**Fig. 9.** Representation of the transition state for the first C–C bond coupling over Ni(111) (left) and Pt(111) (right). The  $3 \times 3$  unit cell is repeated in each direction parallel to the surface to show close contacts. The forming C–C bond distance is 1.93 and 1.90 Å for Ni and Pt, respectively. The metal atoms are colored gray, while sodium, carbon, hydrogen and oxygen are colored yellow, black, white and red, respectively. (For interpretation of the references to color in this figure legend, the reader is referred to the web version of this article.)

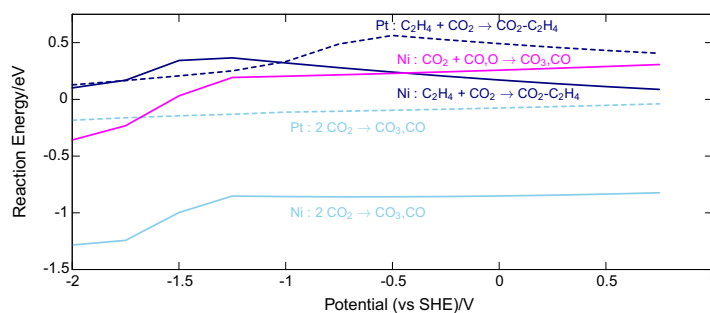


**Fig. 10.** Competing reactions on Ni and Pt during aprotic  $\text{CO}_2$  reduction in the presence of ethene as a function of the electrochemical potential vs. SHE. The first carboxylation step of ethene is given in dark blue (broken and solid line for Pt and Ni, respectively). Carbonate formation on Pt is given in pale blue broken line, while for Ni we consider two different scenarios: two chemisorbed  $\text{CO}_2$  yielding carbonates in pale blue line, or one chemisorbed  $\text{CO}_2$  and one  $\text{CO}, \text{O}$  (dissociated  $\text{CO}_2$ ) reacting to carbonates by the pink full line. (For interpretation of the references to color in this figure legend, the reader is referred to the web version of this article.)

**Fig. 10** analyzes the competition between the “productive”, but kinetically hindered, first carboxylation reaction and the main side-reaction (carbon monoxide/carbonate formation) over Ni and Pt. As already seen in **Fig. 7**, the first carboxylation of ethene has roughly the same thermodynamic characteristics over Pt as over Ni, i.e., it is endothermic by 0.2–0.5 eV at the relevant, highly reducing potentials ( $< -1.5$  V) and overall does not show a pronounced potential dependence. Nevertheless, over Ni the C–C bond formation can be coupled to a  $\text{Na}^+$  co-adsorption at potential between  $-1.25$  V and  $-2$  V, which results in a less endothermic process.

$\text{CO}$  and  $\text{CO}_3$  formation may occur through one of two “simple” mechanisms. The reaction can proceed along a two-step mechanism, starting with the dissociation of  $\text{CO}_2$ , followed by the C–O bond formation between surface adsorbed oxygen and a second carbon dioxide molecule. The alternative goes through the direct transformation of two chemisorbed  $\text{CO}_2$  into  $\text{CO}$  and  $\text{CO}_3$ , which can be described as a surface-assisted disproportionation, partially, coupled to an electron transfer in order to form actual carbonate ( $\text{CO}_3^{2-}$ ). In this mechanism, one oxygen atom migrates from one  $\text{CO}_2$  to the other.

The mechanisms are analyzed in **Fig. 10** for Ni(111) and Pt(111) by tracing the reaction energy as a function of the electrochemical potential. Compared to the relative energy considered so far, the reaction energy allows to quickly assess whether a given reaction step is exo- or endothermic. The pink line represents reac-

tion energy for the coupling of  $\text{CO}_2$  to the surface oxygen of  $\text{CO}, \text{O}@Ni(111)$ . This process is endothermic by about 0.2 eV at most potentials and athermic if the second  $\text{CO}_2$  molecule came from the solution instead of the chemisorbed precursor state. The alternative transformation of two  $\text{CO}_2$  into carbonates and  $\text{CO}$  (light blue) is highly exothermic (about 1.0 eV). Nevertheless, since  $\text{CO}_2$  has a high probability to dissociate over Ni(111) (*vide supra*), this path is unlikely to be dominant.<sup>2</sup>  $\text{CO}_2$  dissociation is endothermic over Pt(111), which precludes the first mechanism. However, the second mechanism is exothermic by about 0.2 eV. In other words, over Pt, the C–O bond formation is more favorable than the C–C bond formation at all potentials considered. Hence, based on thermodynamic criteria, the electroreduction of  $\text{CO}_2$  in presence of an alkene over Pt is expected to yield more of the carbonate side product (C–O bond formation) than of the carboxylated alkene (C–C bond formation).

Therefore, the C–C formation is outcompeted by the C–O formation on Pt over the entire potential range, while for Ni(111) the competition between the two products (carbonates or carboxylation) is more subtle, which is in line with our experimental results that carbonate formation is possible, but can be suppressed by the carboxylation reaction under suitable conditions.

<sup>2</sup> A mechanism that would transform two  $\text{CO}, \text{O}$  ( $2 \times \text{CO}_2$ ) into  $\text{CO}, \text{CO}_3$  is unlikely to proceed without going through a  $\text{CO}_2$  like intermediate and is, therefore, not represented in **Fig. 10**. Anyway, the process would be highly endothermic (see SI).



#### 4.4. Insight from the combination of theory and experiment

At the peak of the CV (around  $-2.3$  V), corresponding to the electrolysis experiment at  $-2.5$  V, the mechanism is likely to be different from what we have presented herein:  $-2.5$  V vs. SHE is around the reduction potential of  $\text{CO}_2$  to yield “free”  $\text{CO}_2^-$  radical anions [3]. These free radicals have a very short life time and stay at least loosely bound to the catalytic surface until they react. According to the experimental results, they have two main fates: either they dimerize with a second  $\text{CO}_2$  molecule to form oxalates or they couple to the diene which is activated by the catalyst. The reaction under such conditions has not been modeled, as these loosely bound  $\text{CO}_2^-$  radical anions are difficult to describe accurately, even with our state of the art electrochemical models that include the effect of the electrochemical potential in the electronic structure computations in combination with an implicit solvent model. Nevertheless, the first C–C coupling reaction is, based on thermodynamical grounds, predicted to remain the rate limiting step. However, the C–C coupling is dramatically accelerated, most likely since the re-orientation of  $\text{CO}_2$ , necessary to make the carbon atom accessible for the C–C bond formation, is much easier for a loosely bound  $\text{CO}_2^-$  than for a chemisorbed  $\text{CO}_2$  molecule.

The onset potential of about  $-1.3$  V vs. SHE for the carboxylation of butadiene on Ni is in reasonable agreement with our computations that find that at the potential of  $-1.0$  V the precipitation step becomes exothermic on Ni(111). Note, that the difference between the experimental and theoretical “onset potential” can have numerous reasons, such as the approximate nature of the density functional applied, the model for the electrochemical interface, the hypothesis that Ni(111) is a relevant model for the actual catalytic active surface, that the experiments were carried out with the much safer 2,3-dimethylbutadiene instead of butadiene and the fact that we only consider electronic energies and not the experimentally relevant Gibbs free energies. Despite all these approximations, the C–C coupling reaction is likely to occur along a reaction path very similar to the one proposed herein. Our previous theoretical studies on Ni(111) [12,16] have already evidenced that the formation of formic acid (in presence of a proton donor such as water) and carbonates occurs to a large extent at  $-1.8$  V. The carboxylation reaction, on the other hand, does not involve a proton transfer and is, therefore, not expected to be significantly accelerated by a proton donor such as water. Even worse, the presence of water opens the competitive (and kinetically dominant) routes of  $\text{CO}_2$  to formic acid reduction, thereby suppressing the carboxylation reaction which features high activation barriers.

#### 5. Conclusion

We have investigated the electro-carboxylation reaction of alkenes over a nickel catalyst. The experimental results confirm a feasible, but energy-inefficient process. Although the onset potential is obtained at a practical  $-1.3$  V, the kinetics are sluggish and it is only around  $-2.5$  V that the reaction occurs readily. Our extensive computational investigation identifies the first carboxylation reaction as the rate limiting step. In the vicinity of the onset potential this step is, unfortunately, a chemical step and the overpotential does, therefore, not substantially accelerate the production of the diacid. The generation of almost “free”  $\text{CO}_2^-$  radicals at potentials around  $-2.5$  V opens a more facile reaction path, explaining the relatively fast reaction. The side products of the reaction depend on the potential: formic acid is formed due to traces of water at all considered potentials, while oxalates are only accessible from “free”  $\text{CO}_2^-$  radicals at strongly reducing potentials.

Carbonates and CO are interfering at modest potentials, but their formation is suppressed at higher potentials, as they are mostly formed on the metal surface and not through “free”  $\text{CO}_2^-$  radicals.

Our computations have, furthermore, elucidated that the activation energies for the first carboxylation reaction are significantly lower over Ni(111) than over Pt(111), explaining the superior catalytic activity of Ni compared to Pt. In addition, the competing CO and carbonate formation is faster over Pt than over Ni, since the later strongly stabilizes the atomic oxygen intermediate. This decreases the selectivity of carboxylate formation on Pt. For the design of an improved catalyst one would need to lower the activation energy for the C–C coupling reaction while suppressing carbonates, which might be achieved by modifying the morphology of the electrode.

#### Acknowledgments

The authors acknowledge Solvay for financial support. Computational resources were generously provided by the mesocenter PSMN. This work was granted access to the HPC resources of CINES and IDRIS under the allocation 2014-080609 made by GENCI.

#### Appendix A. Supplementary material

Supplementary data associated with this article can be found, in the online version, at <http://dx.doi.org/10.1016/j.jcat.2016.01.008>.

#### References

- [1] A. Jutand, *Chem. Rev.* 108 (2008) 2300, <http://dx.doi.org/10.1021/cr068072h>.
- [2] J.W. Loveland, *Us patent* 3032489, 1962.
- [3] D. Pletcher, J. Girault, *J. Appl. Electrochem.* 16 (1986) 791, <http://dx.doi.org/10.1007/BF01006524>.
- [4] J. Bringmann, E. Dinjus, *Appl. Organometal. Chem.* 15 (2001) 135, [http://dx.doi.org/10.1002/1099-0739\(200102\)15:23.0.CO;2-L](http://dx.doi.org/10.1002/1099-0739(200102)15:23.0.CO;2-L).
- [5] M. Gattrell, N. Gupta, A. Co, *J. Electroanal. Chem.* 594 (2006) 1, <<http://www.sciencedirect.com/science/article/pii/S0022072806002853>>.
- [6] Y. Hori, in: *Modern Aspects of Electrochemistry*, Springer, New York, Gaithersburg MD, 2008, p. 89, 20899.
- [7] R. Matthesen, J. Fransaer, K. Binnemans, D.E.D. Vos, *RSC Adv.* 3 (2013) 4634, <http://dx.doi.org/10.1039/C3RA00129F>.
- [8] K. Zhang, Y. Xiao, Y. Lan, M. Zhu, H. Wang, J. Lu, *Electrochem. Commun.* 12 (2010) 1698, <<http://www.sciencedirect.com/science/article/pii/S1388248110004248>>.
- [9] G.-Q. Yuan, H.-F. Jiang, C. Lin, S.-J. Liao, *Electrochim. Acta* 53 (2008) 2170, <<http://www.sciencedirect.com/science/article/pii/S0013468607011656>>.
- [10] C.-H. Li, G.-Q. Yuan, X.-C. Ji, X.-J. Wang, J.-S. Ye, H.-F. Jiang, *Electrochim. Acta* 56 (2011) 1529, <<http://www.sciencedirect.com/science/article/pii/S001346861000873X>>.
- [11] G.-Q. Yuan, H.-F. Jiang, C. Lin, *Tetrahedron* 64 (2008) 5866, <<http://www.sciencedirect.com/science/article/pii/S0040402008007618>>.
- [12] S.N. Steinmann, C. Michel, R. Schwiedernoch, P. Sautet, *Phys. Chem. Chem. Phys.* 17 (2015) 13949, <http://dx.doi.org/10.1039/C5CP00946D>.
- [13] C.D. Taylor, S.A. Wasileski, J.-S. Filhol, M. Neurock, *Phys. Rev. B* 73 (2006) 165402, <http://dx.doi.org/10.1103/PhysRevB.73.165402>.
- [14] M. Mamatkulov, J.-S. Filhol, *Phys. Chem. Chem. Phys.* 13 (2011) 7675, <http://dx.doi.org/10.1039/C0CP01444C>.
- [15] K. Mathew, R. Sundararaman, K. Letchworth-Weaver, T.A. Arias, R.G. Hennig, *J. Chem. Phys.* 140 (2014) 084106, <http://dx.doi.org/10.1063/1.4865107>.
- [16] S.N. Steinmann, C. Michel, R. Schwiedernoch, J.-S. Filhol, P. Sautet, *ChemPhysChem* 16 (2015) 2307, <http://dx.doi.org/10.1002/cphc.201500187>.
- [17] D.L. Pile, A.S. Benjamin, K.S. Lackner, C.H. Wendt, D.P. Butt, *J. Chem. Educ.* 75 (1998) 1610, <http://dx.doi.org/10.1021/ed075p1610>.
- [18] J.E. Sutton, D.G. Vlachos, *Ind. Eng. Chem. Res.* 54 (2015) 4213, <http://dx.doi.org/10.1021/ie5043374>.
- [19] R.T. Vang, K. Honkala, S. Dahl, E.K. Vestergaard, J. Schnadt, E. Laegsgaard, B.S. Clausen, J.K. Nørskov, F. Besenbacher, *Nat. Mater.* 4 (2005) 160, <http://dx.doi.org/10.1038/nmat1311>.
- [20] V. Del Colle, A. Berna, G. Tremiliosi-Filho, E. Herrero, J.M. Feliu, *Phys. Chem. Chem. Phys.* 10 (2008) 3766, <http://dx.doi.org/10.1039/B802683A>.
- [21] F. Calle-Vallejo, D. Loffreda, M.T.M. Koper, P. Sautet, *Nat. Chem.* 7 (2015) 403, <http://dx.doi.org/10.1038/nchem.2226>.
- [22] S. Ikeda, T. Takagi, K. Ito, *Bull. Chem. Soc. Jpn.* 60 (1987) 2517.





# 10 Projects

As might have transpired in the “introduction” to the various chapters, we are not quite “there” yet! Indeed, significant developments still lie ahead in order to truly exploit computational chemistry for gaining insight into the interface of metals and accelerating catalyst design.

In the following, I will outline the main ideas of projects that are either on-going or at least clearly defined in terms of submitted proposals. Despite the rather diverse nature of the projects, they share two characteristics: they all concern the solid (mostly metal) interface and they all require method development to *efficiently* model the complex, reactive, interfaces.

## 10.1 Tools for Automatically Generate Lattice Based Cluster Expansions (2017–2020)

The thesis project of Ruben Staub is to develop tools that allow an efficient establishment of model Hamiltonians. As introduced in chapter 2, model Hamiltonians are extremely efficient to explore the surface chemistry in complex mixtures. In this context, we choose to work with a two-dimensional graphical lattice, leading to the expansion of the total energy in terms of “clusters”, i.e., a set of vertices of a graph. While chapter 2 was dealing with only one species (acetylene) on a complex surface (rearrangements of the Pd-Ag alloy), the aim here is to describe the adsorption and lateral interaction of various species as observed, for instance, in the hydrogenation of acetylene, also studied in chapter 3. Based on the work by Emanuele Vignola,<sup>1</sup> we know that many intermediates are necessary in the model Hamiltonian. Emanuele also started designing the corresponding training set to establish a model Hamiltonian which would allow to run kinetic Monte Carlo simulations at realistic coverages. However, the roughly 300 configurations, constructed by hand, revealed to be too complex to be directly used to fit a cluster expansion. This highlighted the need to automatically

generate relevant configurations (instead of constructing them by hand) and to fit the corresponding cluster expansion. Indeed, in the literature most examples relying on kinetic Monte Carlo either use very simple adsorbates (atoms and di-atomics)<sup>2</sup> and/or largely neglect lateral interactions,<sup>3</sup> leading to uncontrolled approximations. Here, we propose a general iterative approach based on a revisited Monte-Carlo Tree Search (MCTS) optimizer. The construction of the training set is optimized using a constantly updated model Hamiltonian with the aim to reduce the number of necessary, costly, DFT computations. The algorithm uses a MCTS minimizer to find the next configuration that should be included, defining a score based on chemical relevance (from predicted energy) and a priori usefulness regarding model update (from model sensitivity). Particular care is taken to update the model Hamiltonian at each iteration with low computational cost and using an initial guess. This initial guess serves to reduce fluctuations in parameters and to keep physically relevant parameters for better transferability even in the presence of linear dependencies between different orders of the cluster expansion (i.e., between single molecule adsorption energy and lateral interactions). Designing such an algorithm will enable to explore the kinetics of complex mixtures under realistic conditions at the solid/gas interface with a minimal human effort, while containing the computational cost.

### 10.2 Force Fields for Metal/Water Interactions (2018–2021)

The aim of the PhD thesis of Paul Clabaut is two fold: (a) establish an easy to use bundle of scripts to interface a quantum mechanical code (VASP) with a molecular mechanics code (AMBER) to facilitate the assessment of the solvation free energy at the metal/liquid interface according to the protocol outlined in chapter 6. (b) As highlighted in the conclusion of chapter 6, the accuracy of the force field which treats the metal/solvent interaction remains to be improved. A first step towards this goal was achieved in chapter 7, but so far we did not yet successfully exploit this force field for determining the solvation free energy at the interface. Indeed, several small functionalities needed to be implemented in AMBER in order to make GAL17 compatible with alchemical transformations. Furthermore, the equilibration time depends on the interaction strength between the solvent and the surface: the weak interaction of water with the surface of chapter 6 was quite quick ( $\sim 50$  ps) to equilibrate, while the improved GAL17 force field leads to at least ten times longer equilibration times as seen in chapter 7. Therefore, we are currently establishing a robust protocol to avoid artificial results originating from non-equilibrated simulations.

The next step, on which we are working in parallel, is the parametrization of metal/water force fields for other metals (Cu, Ag, Pd, Au) and the second most common surface for these fcc metals, i.e., the 100 facet. These parameterizations have evidenced the possibility to improve the functional form and to increase its flexibility without increasing the number of parameters. This increased flexibility will enable us to include

### **10.3. Towards an Atomistic Understanding of Wettability for Industrial Lubricants (2018–2021)**

---

geometric information (i.e., coordination number<sup>4</sup>) in the force field parameters in order to obtain a “general” metal/water force field that would accurately describe the water solvation of nanoparticles.

An other aspect that has caught our attention are the many-body effects at the metal/liquid interface. As seen in chapter 7, having an accurate force field for the interaction of a single water molecule with a given surface does not ensure a highly accurate description of ice-like layers and is unlikely to represent the “truth” for the metal/liquid water interface. The missing physics is an intricate mixture of many-body effects, with charge-transfer and polarization being non-negligible. In the framework of a Masters project, we are assessing these contributions in detail using the method of chapter 4. Based on these insights, we are expecting to be able to devise either simple corrections (i.e., similar to hydrogen bond corrections<sup>5</sup>) or recognize the necessity to include polarization effects in the force field.<sup>6</sup> If, however, we learn that the physics is too complex for corrections, we will explore the use of semi-empirical methods, such as PM6 or PM7, where the parameters could be tuned to improve the accuracy.

All these improvements will need to be validated against benchmark data. In collaboration with Philippe Sautet, we are currently planning to exploit DFT computations to train a neural network which will correct the “simple” force field.<sup>7</sup> The combination between the force field, the neural network and (if necessary) DFT resampling<sup>8–11</sup> will allow us to establish how the Pt(111)/water interface “really” looks like and which “low-cost” methods can be devised to reproduce similar properties in terms of the structure of the interface (coverage, relative orientation) and interaction strength.

### **10.3 Towards an Atomistic Understanding of Wettability for Industrial Lubricants (2018–2021)**

In this project, which is carried out in the framework of the PhD thesis of Sarah Blanck with Total (thèse CIFRE), we are investigating the mechanism of action of lubrication additives in the context of industrial aluminum shaping. When aluminium is put into its final form, a lubricant consisting of a “base oil” (mostly long-chain hydrocarbons and/or esters) and various additives is applied to reduce friction. The focus of the present study is to understand the influence of various additives on the wettability properties, i.e., if the lubricant spreads out quickly on the metal surface, and its capability to stay on the surface. These additives are generally composed of a polar head-group which adsorbes on the metal surface (in our case  $\gamma$ -alumina) and an apolar tail, which solubilizes the molecule in the base oil.

The working hypothesis of the thesis is that the competition between adsorption of an additive molecule and its loss of solvation is a key parameter for the effectiveness of the additive. However, the adsorption might occur as a (disordered) film, and not

only at low coverage. Efficiently modelling the film formation is the (technically) most challenging aim of this project. We are planning to build a bottom-up model by first studying the adsorption of head-group model compounds to screen the various adsorption modes. In a second step, we are establishing a protocol to automatically determine the adsorption mode of multi-functional molecules. Last but not least, we will combine the conformational search of single molecules (which contain long alkyl chains) with the adsorption conformation modes in order to generate candidates for film formation. We envision two possible approaches to achieve this goal. Either, we rely on model Hamiltonians for the adsorption mode, which allows to rapidly generate various coverages of adsorbed head-groups. These head-group films can then be combined with independently determined configurations of the apolar tail. Or else, we develop an approximate force-field which could be used to directly perform a conformational search of the films, subjecting the thus generated geometries to quantitative DFT energy assessment in a second step.

### 10.4 Genesis of supported MoS<sub>2</sub> on $\gamma$ -alumina (2018–2021)

Molybdenum disulfide supported on  $\gamma$ -alumina is the archetypical hydrodesulfurization catalyst, used to reduce the sulfur content in fuels.<sup>12</sup> IFP Énergie nouvelles (IFPEN) develops and commercializes MoS<sub>2</sub> based hydrodesulfurization catalysts. In order to meet the ever stricter regulations on the sulfur content in fuels, IFPEN aims at a fundamental understanding of the entire catalyst lifetime, from synthesis to deactivation. As part of the joint IFPEN-IDEX Lyon project Road4Cat of Pascal Raybaud, the thesis project of Amit Sahu is focusing on one of the key steps during the industrial synthesis of this catalyst: the activation of  $\gamma$ -alumina supported molybdenum oxide precursor under reductive sulfurization conditions. Experimental studies have shown that this process involves various intermediate species which only partially disappear, leading to incompletely sulfided catalysts.<sup>13</sup> Our study will be based on a combination of thermodynamical and kinetic information obtained from DFT computations. To compare to experiment, we will heavily rely on spectroscopic data (XPS, EXAFS, Raman) which is available in the literature or is currently acquired by other projects of IFPEN.

To begin with, we are elucidating the local molecular structure of the intermediate phase observed experimentally which has the approximate stoichiometry of MoS<sub>3</sub>.<sup>13</sup> Bulk MoS<sub>3</sub> is known to be amorphous, but even its building blocks are not very well known.<sup>14–16</sup> Hence, relying on extensive DFT studies, we explore the relative stability of the different propositions and their relations to small MoS<sub>2</sub> sheets, which are ultimately formed on the support. In a second step, we will assess the ease with which various molybdenum oxide and oxysulfide species are sulfided and reduced and how the thermodynamics and kinetics of these processes depend on the alumina anchoring sites.

### 10.5 Use of MoS<sub>2</sub> in Electrocatalysis for Hydrogen Evolution (2019–2023)

The project MoSHy, awarded to me in 2018 by the region Auvergne-Rhône-Alpes, is carried out in strong collaboration with IFPEN (Audrey Bonduelle) for catalyst synthesis and with LEPMI (Eric Sibert) for the electrochemical characterization of the catalysts.

The shift from an oil-dependent economy to a green economy using renewable energy sources requires innovations in terms of energy production and storage. IFPEN is one of the leaders in the development of supported molybdenum disulfide (MoS<sub>2</sub>) on an industrial scale, used as a hydrodesulfurization catalyst. MoSHy aims at exploring further economic opportunities for this recognized expertise. For example, supported molybdenum disulfides are good candidates for replacing platinum in acidic electrolyzers, producing hydrogen efficiently from green electricity and water.<sup>17</sup> Hydrogen is a key reagent in petrochemistry and ammonia synthesis which is currently mostly obtained by reforming of natural gas or coal, co-generating CO<sub>2</sub>. It is estimated that the production of “green” hydrogen via electrocatalysis would reduce the yearly CO<sub>2</sub> emissions by 1-2%. Within MoSHy, we rely on computational chemistry to provide detailed, atomistic understanding in order to accelerate innovation by overcoming a strategy based solely on experimental trial-and-error.

This project will address several key challenges on the way from the proof-of-principle of a viable MoS<sub>2</sub>-based electrocatalyst to an industrially relevant demonstrator. First, the catalytically active sites will be identified under realistic conditions, i.e., at a given electrochemical potential, to determine the best polymorph of MoS<sub>2</sub>, the best morphology of platelets and the best dopants for electrochemical reactions. Second, in one of my previous studies we have shown that the conductivity of the MoS<sub>2</sub> catalyst can limit its activity,<sup>18</sup> the conductivity of the (semi-conducting) catalyst-support system needs to be optimized. One solution is to deposit the MoS<sub>2</sub> sheets on a conductive support. Suitable anchoring groups should ensure a low barrier for electron transport between the support and the catalytically active material. Finally, renewable electricity resources are often intermittent, so it is essential to consider the effect of repeated charge/discharge cycles on aging of the catalyst. These three aspects will mainly be investigated theoretically within the PhD thesis of Nawras Abidi, which starts in november 2019. The main method used in the project consists in combining density functional theory (DFT) with a continuum solvent model, while taking into account the influence of the applied electrical potential.<sup>19–21</sup> Frequent feedbacks between theory and experiments will maximize the impact of this project, providing on the one hand validation of the theoretical approach and, on the other hand, proposals for improvements in the electrocatalyst.

### 10.6 Evaluating Soot–Surface and Detergent–Surface Interactions for the Efficiency of Fuel Additives (2019–2020)

Detergent additives in diesel and gasoline keep the engine clean, either by reducing (or cleaning-up) soot adsorption or by inhibiting the agglomeration of soot particles in order to minimize the soot deposit. The complex processes and structural details involved in the working principles of the detergents is challenging to capture by experimental techniques alone. Molecular modelling can, however, provide complementary atomistic detail of the process and thus accelerate the design of the next-generation detergents.

During the post-Doc of Elias Azne Gebremedhn (2016–2017), a soot model has been developed and a screening procedure has been established to evaluate the detergent–soot interaction. In the continuation of this project, Carles Marti, a post-Doc sponsored by Total, is evaluating the interaction of soot with the metal surface of the engine as well as the interaction of the detergent with the metal surface. Hematite has been shown to be a suitable model<sup>22</sup>, even though other surface states have also been observed in the engine.<sup>23</sup> Knowing the relative strength of the different components (soot–detergent, soot–engine and detergent–engine) will yield a molecular understanding of the mode of action of the detergent and bring insights on how to design better additives.

In order to rapidly assess these interactions, we will apply or adapt semi-empirical methods such as PM6,<sup>24</sup> PM7<sup>25</sup> or DFTB.<sup>26</sup> While these methods work well for organic molecules, their accuracy for the interaction between hematite and organic molecules (soot and detergent models) needs to be benchmarked and, if unacceptable, improved by tuning the corresponding parameters.

### 10.7 Transition-metal Chalcogenides for Electrochemical CO<sub>2</sub> Reduction (2020?)

This collaboration has been proposed to me by Zhi Wei Seh from A\*STAR (Singapore) and we have submitted the project to the joint call of the French and Singaporean agency for research (ANR and NRF, respectively) under the acronym ECONCat. Previously, Zhi Wei Seh has demonstrated that copper sulfide catalysts are capable of reducing CO<sub>2</sub> to formate, albeit at a moderate Faradaic efficiency of 75% at -0.9 V vs. RHE.<sup>27</sup>

In ECONCat we aim to enhance the activity and selectivity of transition metal chalcogenide (TMC) electrocatalysts in aqueous solution. In the framework of theory-driven materials design, we will establish a close collaboration between experiment and theory in order to accelerate the discovery of advanced electrocatalysts. We will explore



## 10.8. Embedded Wave Function Approaches at the Metal Interface (2020?)

---

the tuning of binary and multinary TMC compositions and engineering of polymorphs. By combining operando measurements and theoretical computations, we aim to elucidate reaction mechanisms and perform *in silico* catalyst screening under realistic conditions. The specific objectives, to be achieved in the context of a three years post-Doc at A\*STAR and a PhD thesis under my direction consist of 3 milestones: (1) Validation of volcano plots by correlating experimental results and theoretical predictions of known TMC materials. (2) Atomistic understanding of active sites based on operando surface characterization and advanced DFT modelling, including the effect of electrochemical potential and electrolyte. (3) Design, synthesis and optimization of conditions to obtain optimal TMC catalysts. To investigate the importance of polymorph in reducing the overpotential and accelerating the kinetics of CO<sub>2</sub> reduction, we will rely on machine learning, i.e., cluster expansions similar to what is presented in chapter 2, to screen the activity of multinary TMCs.

This project fits well into my current research portfolio, given that I am working on the genesis of MoS<sub>2</sub> in collaboration with Pascal Raybaud (see section 10.4) and on the use of MoS<sub>2</sub> for the hydrogen evolution reaction (see section 10.5).

## 10.8 Embedded Wave Function Approaches at the Metal Interface (2020?)

The block localized wave function (BLW) defines “local” effective Hamiltonians. My working hypothesis is that these effective Hamiltonians can be used in wave function techniques (WFT), such as MRCI or CCSD and, for systems with non-vanishing gap, perturbative methods such as MP2.

The combination of DFT+WFT has been developed by Carter through self-consistent embedding<sup>28;29</sup> and by Wesolowski<sup>30</sup> and Visscher<sup>31</sup> by perturbative means. This topic has been very recently reviewed by Gagliardi and co-workers for the context of heterogeneous catalysis.<sup>32</sup> Exploiting the BLW local Hamiltonian has not been explored so far, but represents an intriguing possibility. As also shown in chapter 4, BLW couples the different blocks by projecting the system Hamiltonian onto the local basis set and then solves these local, but coupled SCF problems.<sup>33</sup> The main advantage of BLW compared to other embedding techniques is that no approximate kinetic energy functional is needed during the determination of the effective potential for the WFT subsystem.

As a proof of principle, I have a pilot implementation of CCSD@BLW, where the BLW is determined according to the algorithm of Gianinetti.<sup>34</sup> Preliminary tests on the modification of the hydrogen bond between H<sub>2</sub>O and NH<sub>3</sub> by binding BH<sub>3</sub> to NH<sub>3</sub> show that CCSD@BLW with H<sub>2</sub>O-NH<sub>3</sub> as one and BH<sub>3</sub> as the other block reproduces the full result within 10% (1 kcal/mol), while the use of simple point charges to polarize

NH<sub>3</sub> (the typical electrostatic embedding strategy) leads to an error of 50%. This suggests, that accurate results can be obtained even when formally breaking bonds between subsystems.

However, several questions remain to be clarified: On the one hand, the theoretical link is missing, i.e., at present it is an ad hoc approximation, but the connection with an exact theory needs to be established. On the other hand, several kinds of BLW local Hamiltonians exist,<sup>33–35</sup> but it is unclear if they would provide the same result when used for embedding. Last but not least, an efficient coupling of CP2K for BLW with CCSD-F12 as implemented in Molpro<sup>36</sup> or Orca<sup>37</sup> would allow to benefit from the efficiency for the full system of CP2K and for approaching the basis set limit for CCSD via the explicitly correlated methods.

CCSD@BLW is probably the most challenging part of my projects, but if successful, it would also represent a major breakthrough: the strategy could be applied to embedded metal clusters for obtaining adsorption energies with beyond DFT accuracy and could also be extended to excited states in solids and solution. This project is part of the submitted proposal TErRASSE, an ANR project lead by E. Sibert of the LEPMI (Grenoble), who is a collaborator of MoSHy (see section 10.5) and involving the team of Emmanuel Maisonhaute at the LISE in Paris for in situ Raman spectroscopy.

## Bibliography

- [1] Vignola, E.; Steinmann, S. N.; Al Farra, A.; Vandegehuchte, B. D.; Curulla, D.; Sautet, P. *ACS Catal.* **2018**, *8*, 1662.
- [2] Piccinin, S.; Stamatakis, M. *ACS Catal.* **2014**, *4*, 2143.
- [3] Falcinelli, S.; Capriccioli, A.; Pirani, F.; Vecchiocattivi, F.; Stranges, S.; Martì, C.; Nicoziani, A.; Topini, E.; Laganà, A. *Fuel* **2017**, *209*, 802.
- [4] Calle-Vallejo, F.; Martínez, J. I.; García-Lastra, J. M.; Sautet, P.; Loffreda, D. *Angew. Chem., Int. Ed.* **2014**, *53*, 8316.
- [5] Řezáč, J. *J. Chem. Theory Comput.* **2017**, *13*, 4804.
- [6] Tazi, S.; Molina, J. J.; Rotenberg, B.; Turq, P.; Vuilleumier, R.; Salanne, M. *J. Chem. Phys.* **2012**, *136*, 114507.
- [7] Sun, G.; Sautet, P. *J. Chem. Theory Comput.* **2019**,
- [8] König, G.; Hudson, P. S.; Boresch, S.; Woodcock, H. L. *J. Chem. Theory Comput.* **2014**, *10*, 1406.
- [9] Cave-Ayland, C.; Skylaris, C.-K.; Essex, J. W. *J. Chem. Theory Comput.* **2017**, *13*, 415.

- [10] Kearns, F. L.; Hudson, P. S.; Woodcock, H. L.; Boresch, S. *J. Comput. Chem.* **2017**, *38*, 1376.
- [11] Hudson, P. S.; Woodcock, H. L.; Boresch, S. *J. Chem. Theory Comput.* **2019**, *15*, 4632.
- [12] Toulhoat, H.; Raybaud, P.; (translator), L. *Catalysis by transition metal sulfides : from molecular theory to industrial application*; Paris Éditions TECHNIP, 2013.
- [13] Payen, E.; Kasztelan, S.; Houssenbay, S.; Szymanski, R.; Grimblot, J. *J. Phys. Chem.* **1989**, *93*, 6501.
- [14] Weber, T.; Muijsers, J. C.; Niemantsverdriet, J. W. *J. Phys. Chem.* **1995**, *99*, 9194.
- [15] Hibble, S. J.; Wood, G. B. *J. Am. Chem. Soc.* **2004**, *126*, 959.
- [16] Tran, P. D.; Tran, T. V.; Orio, M.; Torelli, S.; Truong, Q. D.; Nayuki, K.; Sasaki, Y.; Chiam, S. Y.; Yi, R.; Honma, I.; Barber, J.; Artero, V. *Nature Mater* **2016**, *15*, 640.
- [17] Benck, J. D.; Hellstern, T. R.; Kibsgaard, J.; Chakthranont, P.; Jaramillo, T. F. *ACS Catal.* **2014**, *4*, 3957.
- [18] Yu, Y.; Huang, S.-Y.; Li, Y.; Steinmann, S. N.; Yang, W.; Cao, L. *Nano Lett.* **2014**, *14*, 553.
- [19] Letchworth-Weaver, K.; Arias, T. A. *Phys. Rev. B* **2012**, *86*, 075140.
- [20] Steinmann, S. N.; Sautet, P. *J. Phys. Chem. C* **2016**, *120*, 5619.
- [21] Sundararaman, R.; Goddard, W. A.; Arias, T. A. *J. Chem. Phys.* **2017**, *146*, 114104.
- [22] Pan, T.; van Duin, A. C. T. *Mater. Lett.* **2011**, *65*, 3223.
- [23] Guan, Y. C.; Ng, G. K. L.; Zheng, H. Y.; Hong, M. H.; Hong, X.; Zhang, Z. *Appl. Surf. Sci.* **2013**, *270*, 526.
- [24] Stewart, J. J. P. *J. Mol. Model.* **2007**, *13*, 1173.
- [25] Stewart, J. J. P. *J. Mol. Model.* **2013**, *19*, 1.
- [26] Liu, H.; Seifert, G.; Di Valentin, C. *J. Chem. Phys.* **2019**, *150*, 094703.
- [27] Deng, Y.; Huang, Y.; Ren, D.; Handoko, A. D.; Seh, Z. W.; Hirunsit, P.; Yeo, B. S. *ACS Appl. Mater. Interfaces* **2018**, *10*, 28572.
- [28] Huang, C.; Pavone, M.; Carter, E. A. *J. Chem. Phys.* **2011**, *134*, 154110.
- [29] Xia, J.; Carter, E. A. *Phys. Rev. B* **2012**, *86*, 235109.
- [30] Wesolowski, T. A. *Phys. Rev. A* **2008**, *77*, 012504.

## Chapter 10. Projects

---

- [31] Hofener, S.; Visscher, L. *J. Chem. Phys.* **2012**, *137*, 204120.
- [32] Gaggioli, C. A.; Stoneburner, S. J.; Cramer, C. J.; Gagliardi, L. *ACS Catal.* **2019**, *9*, 8481.
- [33] Stoll, H.; Wagenblast, G.; Preuss, H. *Theor. Chem. Acc.* **1980**, *57*, 169.
- [34] Famulari, A.; Gianinetti, E.; Raimondi, M.; Sironi, M. *Int. J. Quantum Chem.* **1998**, *69*, 151.
- [35] Nagata, T.; Takahashi, O.; Saito, K.; Iwata, S. *J. Chem. Phys.* **2001**, *115*, 3553.
- [36] Adler, T. B.; Knizia, G.; Werner, H.-J. *J. Chem. Phys.* **2007**, *127*, 221106.
- [37] Neese, F.; Valeev, E. F. *J. Chem. Theory Comput.* **2011**, *7*, 33.



# 11 General Conclusions

In this habilitation thesis I have given an overview on what I personally identify as the most pressing methodological issues in heterogeneous (electro-)catalysis and how improved methods could not only improve our understanding of the solid/gas and solid/liquid interface, but also serve to accelerate the development of novel catalysts.

In short, at the solid/gas interface an automatic generation of lattice based model Hamiltonians is necessary in order to treat complex reaction mixtures and enable kinetic Monte Carlo simulations, which take the site requirements of each adsorbate and the lateral interactions seamlessly into account. At the solid/liquid interface, we face two major issues: first, the development of accurate force fields for the interaction between the metal surface and the solvent and second an efficient sampling of the solvent phase-space together with the feedback of the electrostatic potential into the DFT computations. Both interfaces share the common challenge to go beyond the semi-local DFT level of theory.

After this introductory point of view, a selection of articles illustrating my research directions, from method developments to applications within collaborations between theory and experiment, has been presented. These works have been realized during my second post-Doc and my first years as independent CNRS researcher (“chargé de recherche”). Even though these last ~5 years have brought progress, much effort is still required to reach a toolbox of methods that can be confidently applied to various metallic interfaces.

The last part of this thesis has been devoted to my current projects and the planned research projects, which I expect to realize within the next five years or so.

The first key project which is at its very beginning is MoSHy, aiming at a fundamental understanding of the hydrogen evolution reaction over MoS<sub>2</sub> in collaboration with IFP Énergies Nouvelles, which is funded by the Region Auvergne Rhône Alpes. More advanced are the projects of the two PhD students sponsored by the French Government,

## Chapter 11. General Conclusions

---

i.e., the one of P. Clabaut and R. Staub. Since almost two years, P. Clabaut is working hard on generalizing the force field development from Pt(111) to general metallic surfaces, i.e., different metals and different surface facets. R. Staub, on the other hand, is working on method developments towards the automatization of the determination of lattice based cluster expansions. In contrast to MoSHy, which is rather “applied” and in collaboration with experimental partners, these two students allow me to advance in the development of novel simulation tools, which will have a long-term impact. Last but not least, the PhD thesis of S. Blanck is devoted to the atomistic understanding of wettability in the context of industrial metal working. This thesis is carried out in collaboration with Total and joins developments to achieve a robust description of the functionalized surfaces with theory/experiment collaborations in order to rationalize experimentally observed trends.

The main projects which are currently being submitted for funding are (i) related to method developments for embedded wave function computations at the metal interface and (ii) the use of DFT and cluster expansions to screen catalyst materials for more efficient CO<sub>2</sub> electro-reduction catalysts in strong collaboration with experiments.

These on-going and planned research projects reflect my commitment to combine method development with collaborations with experimental chemists.



# Curriculum Vitae

## Personal Data

Full name	Stephan Niklaus Steinmann
Date of birth	21 February 1985
Nationality	Swiss
Languages	German (mother tongue), English (fluent), French (fluent)
E-mail	stephan.steinmann@ens-lyon.fr

## Education and Professional Situation

Since Oct. 2016	Chargé de Recherche, CNRS, at the Ecole Normale Supérieure de Lyon
Oct. 2014 - Sept. 2016	Post-Doc with P. Sautet at the Ecole Normale Supérieure de Lyon
Oct. 2013 - Sept. 2014	Post-Doc with P. Sautet at the Ecole Normale Supérieure de Lyon in collaboration with Solvay and E2P2L (Shanghai)
Nov. 2012 - Sept. 2013	Post-Doc with Prof. W. Yang at Duke University
Nov. 2008 - Oct. 2012	Ph.D. studies in the Laboratory for Computational Molecular Design (LCMD) at the Ecole Polytechnique Fédérale de Lausanne; Advisor: Prof. C. Corminboeuf Thesis Title: "Understanding and Minimizing Density Functional Failures Using Dispersion Corrections"
Mar. 2008 - Sept. 2008	Master's Thesis "Investigation of Allostery and Cooperativity by Molecular Dynamics Simulation" Supervisor: Prof. M. Meuwly, University of Basel
Oct. 2004 - Sept. 2007	Bachelor of Science in Chemistry, University of Basel



### Track Record

Number of publications	<b>58</b>
Number of citations	<b>2014 (1852 without self-citations)</b>
H-index	<b>24</b>
First author publications	<b>22</b>
Corresponding author publications	<b>12</b>
Invited talks	<b>6</b>
Contributed talks	<b>24</b>
Poster presentations	<b>14</b>

### Supervision of Master Students, Graduate Students and Post-doctoral Fellows

2019 - 2020	Post-Doc (C. Marti) Co-supervision (50%) with C. Michel
2019	Master student (N. Abidi)
2018 - 2021	PhD student (A. Sahu) Co-supervision (30%) with P. Raybaud
2018 - 2021	PhD student (S. Blanck) Co-supervision (50%) with C. Michel
2017 - 2020	PhD student (R. Staub)
2016 - 2018	PhD student (B. Schweitzer) Co-supervision (40%) with C. Michel
2015 - 2017	PhD student (E. Vignola) Co-supervision (80%) with P. Sautet
2016 - 2017	Post-Doc (E. Azne) Co-supervision (50%) with C. Michel
2017	Master student (R. Staub)
2017	Master student (L. Treps) Co-supervision (50%) with C. Michel
2017	Master student (P. Colinet) Co-supervision (40%) with T. Le Bahers
2016	Post-Doc (R. Ferreira de Morais) Co-supervision (30%) with P. Fleurat-Lessard and C. Michel
2015	Master student (K. Li) Co-supervision (60%) with C. Michel
2015	2 visiting PhD students (P. Wang and E. Monyoncho)
2012	Master student (S. Gex) Co-supervision (90%) with C. Corminboeuf

## Project Funding

8. *H<sub>2</sub>-Lignin: H<sub>2</sub> production by ligninelectrolysis: Proof of concept and First Principles Calculations*  
 Institut de chimie de Lyon (2 Master students)  
 2019            Co-PI
7. *MoSHy: Developpement of an economical electrocatalyst for efficient hydrogen evolution by coupling experiments and theoretical modelling*  
 Région Auvergne-Rhône-Alpes (PhD grant)  
 2018 - 2023    PI
6. *Wettability parameters by multi-scale modelling approach*  
 Total (PhD grant)  
 2018 - 2021    Co-PI
5. *MUSIC: Multiscale Simulations of Bifunctional Catalysts: Application to the Hydrodeoxygenation of Molecules Extracted From Biomass*  
 ANR (PhD & post-Doc)  
 2016 - 2019    PI
4. *Multi-scale modelling approach for Lubrication*  
 Total  
 2016 - 2019    Consultant
3. *Molecular simulation to better understand clean-up process of detergent molecules with soot*  
 Total (post-Doc)  
 2016 - 2017    Co-PI
2. *Modelling hydrogenations on alloy surfaces*  
 Total (PhD grant)  
 2015 - 2017    Co-PI
1. *Towards Fundamentally Improved Approximations in Density Functional Theory*  
 Schweizerischer Nationalfonds zur Förderung der Wissenschaftlichen Forschung  
 2015 - 2017    Personal post-Doc grant; PBELP2-143559

## Teaching Activities

- |             |  |
|-------------|--|
| 2014 -      | Molecular modelling, practical sessions for chemists (10 h per year),<br>ENS de Lyon, France |
| 2014 - 2016 | Wet chemistry for physicists (70 h), ENS de Lyon, France                                     |
| 2008 - 2012 | Supervision of projects in computational chemistry (60 h), EPFL,<br>Switzerland              |
| 2008 - 2012 | Teaching assistant for freshmen chemistry (40 h), EPFL, Switzerland                          |

### Institutional Responsibilities

- 2019 - Member of the Laboratory Council, ENS de Lyon, France  
2017 - Organizer of Laboratory Seminars, ENS de Lyon, France  
2016 - Organizer of Group Talks, ENS de Lyon, France  
2010 - 2012 Member of Hiring Committee for two professors in Chemistry; Student Representative, University of Basel, Switzerland

### Organization of Scientific Meetings

- 2019 Co-Organizer of Solvate2019: Scientific Meeting of the GdR SolvATE, Lyon, France  
2018 Co-Organizer of the 1st CP2K day at the Centre Blaise Pascal, Lyon, France

### Commissions of Trust

- 2013 - Referee for Journals: Joule, Nano Letters, ACS Catalysis, The Journal of Physical Chemistry Letters, The Journal of Physical Chemistry, Electrochimica Acta, RSC Advances, ChemistrySelect, Journal of Molecular Modeling, Computational and Theoretical Chemistry, Catalysts  
2019 Master Jury Member, Florence Szczepaniak, ENS de Lyon, France  
2019 PhD Advancement Committee Member of Pauline Colinet and Muhammad Akif Ramzan, ENS de Lyon, France  
2017 - 2018 PhD Advancement Committee Member of Qingyi Gu, Antton Curutchet and Kamila Kazmierczak, ENS de Lyon, France  
2018 Master Jury Member, Georges Menzildjian, ENS de Lyon, France  
2018 PhD Jury Member, B. Schweitzer, ENS de Lyon, France  
2017 PhD Advancement Committee Member, Magdalena Piskorz, University Grenoble-Alpes, France  
2017 PhD Jury Member, E. Vignola, ENS de Lyon, France

### Academic Honors and Awards

- ISIC Best Thesis Award 2013 of the EPFL Chemistry Departement
- Fellowship for prospective researchers from the Swiss National Science Foundation in the group of Prof. Weitao Yang at the Department of Chemistry, Duke University, USA.
- 2012 Award of the EPFL Chemistry Departement for dedicated teaching
- Finalist of the European Young Chemist Award 2012

- 2010 SCNAT/SCS Chemistry travel award from the Swiss Academy of Sciences and the Swiss Chemical Society
- SCS Metrohm Prize for the best oral presentation in the section Computational Chemistry of the SCS Fall Meeting 2010

## Scientific Vulgarization

**Girls@Science** Introduction to chemistry for 12 years old girls.  
University of Basel, 2004.

**Pôle sciences du collège Gabriel Rosset** Organic synthesis for a class of 12 year olds.  
ENS de Lyon, 2015.

**Fête de la Science** Organization of a “Fold-It” workshop.  
ENS de Lyon, 2015 and 2016.

**L'Actualité chimique** Calculs et chimie verte – Vers de meilleures simulations pour de meilleurs catalyseurs; Steinmann, S.N. and Michel, C., 2016, 413, 35.

**Meetup** Introduction à la physique quantique  
La Cordée Lyon, 2019.

## Invited Talks

6. 70th Annual ISE Meeting, Aug. 2019, Durban (South Africa)  
*Modelling Reactive Electrified Interfaces: From DFT to Force Fields*
5. Rencontres Prospectives 2019 : Modélisations multi-échelle, Jun. 2019, Nantes (France)  
*On the gap between physical soundness and computational feasibility for modeling solid/liquid interfaces*
4. Spring Meeting of the Swiss Association of Computational Chemistry, Feb. 2019, Geneva (Switzerland)  
*Energy Decomposition Analysis and Solvation Effects in Heterogeneous Catalysis*
3. ACS Spring Meeting, Apr. 2017, San Francisco (USA)  
*When modelling bridges electro-catalysis and heterogeneous catalysis: The case of the formic acid decomposition*
2. Materials Challenges for Fuel Cells and Hydrogen Technologies: from Innovation to Industry Workshop, Sept. 2016, Grenoble (France)  
*Towards Modelling Heterogeneous Electrocatalysis under Realistic Conditions*
1. ACS Spring Meeting, Mar. 2016, San Diego (USA)  
*Mechanistic Study of the Electro-Carboxylation of Alkenes*

## Contributed Talks

24. Insitut de Chimie de Lyon, Jan. 2019, Lyon (France)  
*Schéma de décomposition de l'énergie*  
*Une meilleure compréhension des interactions adsorbât—surface métallique*
23. Group Seminar, Nov. 2018, Montpellier (France)  
*Energy Decomposition Analysis and Solvation Effects in Heterogeneous Catalysis*
22. 16ième Rencontre des Chimistes Théoriciens Francophones, Oct. 2018, Toulouse, (France)  
*Energy Decomposition Analysis for Metal Surface - Adsorbate Interactions by Block Localized Wave Functions*
21. 1ère Rencontre du GdR Solvate, May 2018, Nancy, (France)  
*Modelling Solvation Effects at the Metal/Liquid Interface: Force Field Development and Approximate QM/MM Free Energies*
20. Rencontre scientifique of IFP Energies nouvelles – Slimaia, March 2018, Reuil-Malmaison, (France)  
*A Force Field for Water Over Pt(111): Development, Assessment And Comparison*
19. EuropaCat, Aug. 2017, Florence (Italy)  
*Modelling Formic Acid Decomposition: What are the Differences Between Electrocatalysis and Promoted Heterogeneous Catalysis?*
18. ACS Spring Meeting, Apr. 2017, San Francisco (USA)  
*Challenges in calculating the bandgap of triazine-based carbon nitride structures*
17. FCCat, May 2016, Frejus (France)  
*Ethanol Electrooxidation on Palladium Revisited using PM-IRRAS and DFT: Why is it difficult to break the C–C bond?*
16. ACS Spring Meeting, Mar. 2016, San Diego (USA)  
*Ethanol Electrooxidation on Palladium Revisited using PM-IRRAS and DFT: Why is it difficult to break the C–C bond?*
15. Group Seminar, Dec. 2015, Dijon (France)  
*Towards Modelling Heterogeneous Electrocatalysis under Realistic Conditions*
14. Group Seminar, Dec. 2015, Poitiers (France)  
*Towards Modelling Heterogeneous Electrocatalysis under Realistic Conditions*
13. Group Seminar, Nov. 2015, Nancy (France)  
*Modelling Heterogeneous Electrocatalysis under Realistic Conditions*
12. GECat 2015, May 2015, Obernai, (France)  
*Modélisation de la réaction électrocatalytique HCOOH/CO<sub>2</sub>: Quand les détails sont les clés*
11. ACS Spring Meeting, Apr. 2015, Denver (USA)  
*Modelling the HCOOH/CO<sub>2</sub> Electrochemical Couple: When Details Are Key*
10. ACS Spring Meeting, Apr. 2015, Denver (USA)  
*Modelling heterogeneous electrocatalytic CO<sub>2</sub> valorization*

9. Group Seminar, Dec. 2014, Montpellier (France)  
*Modelling Heterogeneous Electrocatalysis for CO<sub>2</sub> Valorization*
8. Swiss Chemical Society Fall Meeting, Sept. 2012, Zürich (Switzerland)  
*Exploring the Limits of Modern Density Functional Approximations for Interaction Energies*
7. 4<sup>th</sup> EuCheMS Chemistry Congress, Aug. 2012, Prague (Czech Republic)  
*Why are the Interaction Energies of Charge-Transfer Complexes Challenging for DFT?*
6. DFTM 2012, Challenges in Density Matrix and Density Functional Theory, Apr. 2012, Ghent (Belgium)  
*Why are the Interaction Energies of Charge-Transfer Complexes Challenging for DFT?*
5. WATOC 2011, Ninth triennial congress of the World Association of Theoretical and Computational Chemists, July 2011, Santiago de Compostela (Spain)  
*A Generalized-Gradient Approximation Exchange Hole Model for Dispersion Coefficients*
4. STC 2010, 46<sup>th</sup> Symposium on Theoretical Chemistry, Sept. 2010, Münster (Germany)  
*A System-Dependent Density-Based Dispersion Correction*
3. Swiss Chemical Society Fall Meeting, Sept. 2010, Zürich (Switzerland)  
*A System-Dependent Density-Based Empirical Dispersion Correction*
2. ESPA 2010, Electronic Structure: Principles and Applications, June 2010, Oviedo (Spain)  
*A System-Dependent Density-Based Empirical Dispersion Correction*
1. Swiss Chemical Society Fall Meeting, Sept. 2009, Lausanne (Switzerland)  
*Universal inter- and intramolecular empirical correction formula for generalized gradient approximation density functional theory*

## Poster Presentations

14. 15ième Rencontre des Chimistes Théoriciens Francophones, July 2016, Lyon, (France)  
*Improving the Electrolyte Description for Modelling Heterogeneous Electrocatalysis: from Homogeneous Background Charges to QM/MM*
13. NAP-XPS Workshop, Dec. 2014, Paris, (France)  
*Modelling the HCOOH/CO<sub>2</sub> Electrochemical Couple: When Details Are Key*
12. 14ième Rencontre des Chimistes Théoriciens Francophones, July 2014, Paris, (France)  
*Modélisation de la valorisation de CO<sub>2</sub> par l'électrocatalyse hétérogène*
11. Cat1P, May 2014, Ulm, (Germany)  
*Modelling Heterogeneous Electrocatalytic CO<sub>2</sub> Valorization*

## Curriculum Vitae

---

10. DFT13 15<sup>th</sup> International Conference on the Applications of Density Functional Theory in Chemistry and Physics, Sept. 2013, Durham, (UK)  
*Wave Function Methods for Fractional Electrons*
9. Swiss Chemical Society Fall Meeting, Sept. 2012, Zürich (Switzerland)  
*Non-bonded Interactions in Solution: Interplay between Theory and Experiment*
8. ICQC, 14<sup>th</sup> International Congress of Quantum Chemistry, June 2009, Boulder (USA)  
*Why are the Interaction Energies of Charge-Transfer Complexes Challenging for DFT?*
7. CUSO 2011 Summer School, August 2011, Villars-sur-Ollon (Switzerland)  
*A Generalized-Gradient Approximation Exchange Hole Model for Dispersion Coefficients*
6. Swiss Chemical Society Fall Meeting, Sept. 2011, Lausanne (Switzerland)  
*A Generalized-Gradient Approximation Exchange Hole Model for Dispersion Coefficients*
5. Swiss Chemical Society Fall Meeting 2010, Sept. 2010, Zürich (Switzerland)  
*A Novel Approach Clarifying the Electronic and Magnetic Anomalies of Norbornene*
4. IX Girona Seminar, July 2010, Girona (Spain)  
*A System-Dependent Density-Based Dispersion Correction*
3. CECAM Workshop, van der Waals forces in DFT, RPA and beyond, June 2010, Lausanne (Switzerland)  
*A System-Dependent Density-Based Dispersion Correction*
2. DFT09, 13<sup>th</sup> International Conference on the Applications of Density Functional Theory in Chemistry and Physics, Sept. 2009, Lyon (France)  
*Unified Inter- and Intramolecular Empirical Correction Formula for Generalized Gradient Approximation Density Functional Theory*
1. ICQC, 13<sup>th</sup> International Congress of Quantum Chemistry, June 2009, Helsinki (Finland)  
*Universal Inter- and Intramolecular Empirical Correction for Density Functional Approximations*





## Publication List

If I am (co-)corresponding author, my name is underlined.

58. *Theoretical insight into the origin of the electrochemical promotion of ethylene oxidation on ruthenium oxide*  
Hajar, Y.M.; Treps, L.; Michel, C.; Baranova, E. A. and Steinmann, S. N. *Catalysis, Science & Technology*, DOI:10.1039/c9cy01421g.
57. *Theory-guided materials design: two-dimensional MXenes in electro- and photocatalysis*  
Handoko, A. D.; Steinmann, S. N. and Seh, Z. W. *Nanoscale Horizons*, **2019**, 4 809.
56. *The Pressure Gap for Thiols: Methanethiol Self-Assembly on Au(111) from Vacuum to 1 bar*  
Mom, R.V.; Melissen, S.T.A.G.; Sautet, P.; Frenken, J.W.N; Steinmann, S. N. and Groot, I. M. N. *J. Phys. Chem. C*, **2019**, 123 12382.
55. *Theory and experiments join forces to characterize the electrocatalytic interface*  
Steinmann, S. N.; Wei, Z.-Y. and Sautet, P. *Proc Natl Acad Sci USA*, **2019**, 116 7611.
54. *Energy Decomposition Analysis for Metal Surface–Adsorbate Interactions by Block Localized Wave Functions*  
Staub, R.; ; Iannuzzi, M.; Khaliullin, R. Z. and Steinmann, S. N. *J. Chem. Theory Comput.*, **2019**, 15 265.
53. *C6 Diacids from homocitric acid lactone using relay heterogeneous catalysis in water*  
Thapa, I.; Ntais, S.; Clement, R.; Baranova, E. A.; Gu Q.; Steinmann, S. N.; Michel C.; Lau, M. K.; Hass C. S.; Millis, J.; Baker, R. T. *Catalysis Today*, **2019**, 319 191.
52. *Can microsolvation effects be estimated from vacuum computations? A case-study of alcohol decomposition at the H<sub>2</sub>O/Pt(111) interface*  
Schweitzer, B.; Steinmann, S. N. and Michel, C. *Phys. Chem. Chem. Phys.*, **2019**, 21 5368.
51. *Tetrazine-Based Ligand Transformation Driving Metal–Metal Bond and Mixed-Valence HgI/HgII*  
Lemes, M. A.; Stein, H. N.; Bulat, G. Steinmann, S. N. and Murugesu, M. *ACS Omega*, **2018**, 3 10273.

## Publication List

---

50. *Acetylene Adsorption on Pd-Ag Alloys: Evidence for Limited Island Formation and Strong Reverse Segregation from Monte Carlo Simulations*  
Vignola, E.; Steinmann, S. N.; Le Mapihan, K; Vandergehuchte, B. D.; Curulla, D. and Sautet, P. *J. Phys. Chem. C*, **2018**, 122, 15456.
49. *Shining Light on Carbon Nitrides: Leveraging Temperature To Understand Optical Gap Variations*  
Li, X.; Melissen, S.; Le Bahers, T.; Sautet, P.; Masters, A. F.; Steinmann, S. N. and Maschmeyer, T. *Chem. Mater.*, **2018**, 30, 4253.
48. *Force Field for Water over Pt(111): Development, Assessment, and Comparison*  
Steinmann, S. N.; De Morais, R. F.; Gotz, A. W.; Fleurat-Lessard, P.; Iannuzzi, M.; Sautet, P. and Michel, C. *J. Chem. Theory Comput.*, **2018**, 17, 3238.
47. *Computational screening for selective catalysts: Cleaving the C-C bond during ethanol electro-oxidation reaction*  
Monyoncho, E. A.; Steinmann, S. N.; Sautet, P.; Baranova, E. A. and Michel, C. *Electrochimica Acta*, **2018**, 274, 275.
46. *Evaluating the Risk of C-C Bond Formation during Selective Hydrogenation of Acetylene on Palladium*  
Vignola, E.; Steinmann, S. N.; Al Farra, A. Vandergehuchte, B. D.; Curulla, D. and Sautet, P. *ACS Catal.*, **2018**, 8, 1662.
45. *Group Additivity for Aqueous Phase Thermochemical Properties of Alcohols on Pt(111)*  
Gu, G. H.; Schweitzer, B.; Michel, C. Steinmann, S. N.; Sautet, P.; Vlachos, D. G. *J. Phys. Chem. C*, **2017**, 121, 21510.
44. *Molecular Mechanics Models for the Image Charge, a Comment on "Including Image Charge Effects in the Molecular Dynamics Simulations of Molecules on Metal Surfaces"*  
Steinmann, S. N.; Fleurat-Lessard, P.; Gotz, A. W.; Michel, C.; De Morais, R. F. and Sautet, P. *J. Comp. Chem.*, **2017**, 38, 2127.
43. *A machine learning approach to graph-theoretical cluster expansions of the energy of adsorbate layers*  
Vignola, E.; Steinmann, S. N.; Vandergehuchte, B. D.; Curulla, D. Stamatakis, M. and Sautet, P. *J. Chem. Phys.*, **2017**, 147, 054106.
42. *Challenges in Calculating the Bandgap of Triazine-Based Carbon Nitride Structures*  
Steinmann, S. N.; Melissen, S.; Le Bahers, T. and Sautet, P. *J. Mater. Chem. A*, **2017**, 5, 5115.
41. *Key Role of Anionic Doping for H<sub>2</sub> Production from Formic Acid on Pd(111)*  
Wang, P.; Steinmann, S. N.; Fu, G.; Michel, C. and Sautet, P. *ACS Catal.*, **2017**, 7, 1955.
40. *Solvation Free Energies for Periodic Surfaces: Coupling of Implicit and Explicit Solvation Models*  
Steinmann, S. N.; Sautet, P. and Michel, C. *Phys. Chem. Chem. Phys.* **2016**, 18, 31850.

39. *C<sub>2</sub>H<sub>2</sub> Induced Surface Restructuring of Pd-Ag Catalysts: Insights from Theoretical Modelling*  
Vignola, E.; Steinmann, S. N. and Sautet, P. *J. Phys. Chem. C*, **2016**, *120*, 26320.
38. *DFT Perspective on the Thermochemistry of Carbon Nitride Synthesis*  
Melissen, S.; Steinmann, S. N.; Le Bahers, T. and Sautet, P. *J. Phys. Chem. C*, **2016**, *120*, 24542.
37. *Ethanol electrooxidation mechanism: Why it is difficult to break the C–C bond?*  
Monyoncho, E. A.; Steinmann, S. N.; Michel, C.; Baranova, E. A.; Woo, T. K., Sautet, P. and Michel, C. *ACS Catal.*, **2016**, *6* 4894.
36. *Electro-carboxylation of butadiene and ethene over Pt and Ni catalysts*  
Steinmann, S. N.; Michel, C.; Schwierdernoch, R.; Wu, M. and Sautet, P. *J. Catal.*, **2016**, *343*, 240.
35. *Study of a novel hepta-coordinated FeIII bimetallic complex with an unusual 1,2,4,5-tetrazine-ring opening*  
Lemes, M. A.; Pialat, A.; Steinmann, S. N.; Korobkov, I.; Michel, C. and Murugesu, M. *Polyhedron*, **2016**, *108* 163.
34. *Assessing a First-Principles Model of an Electrochemical Interface by Comparison with Experiment*  
Steinmann, S. N. and Sautet, P. *J. Phys. Chem. C*, **2016**, *120*, 5619.
33. *The Relationship Between Carbon Nitride Structure and Exciton Binding Energies: A DFT Perspective*  
Melissen, S.; Le Bahers, T. Steinmann, S. N. and Sautet, P. *J. Phys. Chem. C*, **2015**, *119*, 25188.
32. *Molecular adsorption at Pt(111). How accurate are DFT functionals?*  
Gautier, S., Steinmann, S. N.; Michel, C; Fleurat-Lessard, P. and Sautet, P. *Phys. Chem. Chem. Phys.*, **2015**, *17*, 28921.
31. *Modelling the HCOOH/CO<sub>2</sub> Electrocatalytic Reaction: When Details Are Key*  
Steinmann, S. N.; Michel, C; Schwierdernoch, R.; Filhol, J.-S. and Sautet, P. *ChemPhysChem* **2015**, *16*, 2307.
30. *A fast charge-dependent atom-pairwise dispersion correction to DFTB3*  
Petraglia, R.; Steinmann, S. N. and Corminboeuf, C. *Int. J. Quantum Chem.* **2015**, *115*, 1265.
29. *Impact of Electrode Potential and Solvent on the Electroreduction of CO<sub>2</sub>: A Comparison of Theoretical Approaches*  
Steinmann, S. N.; Michel, C; Schwierdernoch, R. and Sautet, P. *Phys. Chem. Chem. Phys.* **2015**, *17*, 13949.
28. *How Important is Self-Consistency for the dDsC Density Dependent Dispersion Correction?*  
Bremond, E.; Golubev, N.; Steinmann, S. N. and Corminboeuf, C. *J. Chem. Phys.* **2014**, *140*, 18A514.

## Publication List

---

27. *Layer-dependent Electrocatalysis of MoS<sub>2</sub> Atomic Films for Hydrogen Evolution*  
Yu, Y.; Huang, S.; Li, Y.; Steinmann, S. N.; Yang, W. and Cao, L. *Nano Lett.* **2014**, *14*, 553.
26. *Benchmark tests and spin adaptation for the particle-particle random phase approximation*  
Yang, Y.; Van Aggelen, H.; Steinmann, S. N.; Peng, D. and Yang, W. *J. Chem. Phys.* **2013**, *139*, 174110.
25. *Dynamical second-order Bethe-Salpeter equation kernel: a method for electronic excitation beyond the adiabatic approximation*  
Zhang, D.; Steinmann, S. N. and Yang, W. *J. Chem. Phys.* **2013**, *139*, 154109.
24. *Equivalence of Particle-Particle Random Phase Approximation Correlation Energy and Ladder-Coupled-Cluster Doubles*  
Peng, D. ; Steinmann, S. N.; Van Aggelen, H. and Yang, W. *J. Chem. Phys.* **2013**, *139*, 104112.
23. *Wave function methods for fractional electrons*  
Steinmann, S. N. and Yang, W. *J. Chem. Phys.* **2013**, *139*, 074107.
22. *Hierarchically Structured Microfibers of Single Stack Perylene Bisimide and Quaterthiophene Nanowires*  
Marty, R.; Szilluweit, R.; Tian, L.; Sanchez-Ferrer, A.; Bolisetty, S.; Adamcik, J.; Mezzenga, R.; Spitzner, E.-C.; Feifer, M.; Magerle, R.; Steinmann, S. N.; Corminboeuf, C. and Frauenrath, H. *ACS Nano* **2013**, *7*, 8498.
21. *Bonding analysis of planar hypercoordinate atoms via the generalized BLW-LOL*  
Bomble, L.; Steinmann, S. N.; Perez-Peralta, N.; Corminboeuf, C. and Merino, G. *J. Comput. Chem.* **2013**, *34*, 2242.
20. *Exploring the Limits of DFT for Interaction Energies of Molecular Precursors to Organic Electronics*  
Steinmann, S. N.; Corminboeuf, C. *J. Chem. Theory Comput.* **2012**, *8*, 4305.
19. *How are small endohedral silicon clusters stabilized?*  
Avaltroni, F.; Steinmann S. N.; Corminboeuf, C. *Phys. Chem. Chem. Phys.* **2012**, *14*, 14842.
18.  *$\pi$ -Depletion as criterion to predict  $\pi$ -stacking ability*  
Gonthier, J.; Steinmann, S. N.; Roch, L.; Ruggi, A.; Luisier, N.; Severin K.; Corminboeuf C. *Chem. Commun.* **2012**, *48*, 9239.
17. *A ratiometric fluorescence sensor for caffeine*  
Luisier, N.; Ruggi, A.; Steinmann, S. N.; Favre, L.; Gaeng, N.; Corminboeuf, C.; Severin, K. *Org. and Biomol. Chem.* **2012**, *10*, 7487.
16. *Quantification of "fuzzy" chemical concepts: a computational perspective*  
Gonthier, J.; Steinmann, S. N.; Wodrich, M. D. and Corminboeuf, C., *Chem. Soc. Rev.* **2012**, *41*, 4671.

15. *Why are the Interaction Energies of Charge-Transfer Complexes Challenging for DFT?*  
Steinmann, S. N.; Piemontesi, C.; Delachat, A. and Corminboeuf, C. *J. Chem. Theory Comput.* **2012**, 8, 1629.
14. *Role of  $\pi$ -acceptor effects in controlling the lability of novel monofunctional Pt(II) and Pd(II) complexes. Crystal structure of [Pt(triipyridinedimethane)Cl]Cl*  
Petrovic, B., Bugarcic, Z. D.; Dees, A.; Ivanovic-Burmazovic, I.; Heinemann, F. W.; Puchta, R.; Steinmann, S. N.; Corminboeuf, C.; van Eldik, R. *Inorg. Chem.* **2012**, 51, 1516.
13. *Comprehensive Benchmarking of a Density-Dependent Dispersion Correction*  
Steinmann, S. N.; Corminboeuf, C. *J. Chem. Theory Comput.* **2011**, 7, 3567.
12. *Fluorescence sensing of caffeine in water with polysulfonated pyrenes*  
Rochat, S.; Steinmann, S. N.; Corminboeuf, C.; Severin, K. *Chem. Commun.* **2011**, 47, 10584.
11. *How do electron localization functions describe  $\pi$ -electron delocalization?*  
Steinmann, S. N.; Mo, Y.; Corminboeuf, C. *Phys. Chem. Chem. Phys.* **2011**, 13, 20584.
10. *Dispersion-Corrected Energy Decomposition Analysis for Intermolecular Interactions Based on the BLW and dDXDM Methods*  
Steinmann, S. N.; Corminboeuf, C., Wu, W.; Mo, Y. *J. Phys. Chem. A* **2011**, 115, 5467.
9. *A Density Dependent Dispersion Correction*  
Steinmann, S. N.; Corminboeuf, C. *Chimia, Special Issue Laureates* **2011**, 65, 240.
8. *A generalized-gradient approximation exchange hole model for dispersion coefficients*  
Steinmann, S. N.; Corminboeuf, C. *J. Chem. Phys.* **2011**, 134, 044117.
7. *The Norbornene Mystery Revealed*  
Steinmann, S. N.; Mo, Y.; Vogel, P.; Corminboeuf, C. *Chem. Commun.* **2011**, 47, 227.
6. *Overcoming systematic DFT errors for hydrocarbon reaction energies*  
Steinmann, S. N.; Wodrich, M.; Corminboeuf, C. *Theor. Chem. Acc.* **2010**, 127, 429.
5. *Branched Alkanes Have Contrasting Stabilities*  
Gonthier, J.; Wodrich, M. D.; Steinmann, S. N.; Corminboeuf, C. *Org. Lett.* **2010**, 12, 3070.
4. *How Strained are Carbomeric-Cycloalkanes?*  
Wodrich, M. D.; Gonthier, J.; Steinmann, S. N.; Corminboeuf, C. *J. Phys. Chem. A* **2010**, 114, 6705.
3. *A System-Dependent Density Based Dispersion Correction*  
Steinmann, S. N.; Corminboeuf, C. *J. Chem. Theory Comput.* **2010**, 6, 1990.

## Publication List

---

2. *Unified Intra- and Intermolecular Dispersion Correction Formula for Generalized Gradient Approximation Density Functional Theory*  
Steinmann, S. N.; Csonka, G.; Corminboeuf, C. *J. Chem. Theory Comput.* **2009**, *5*, 2950.
1. *Direct Assessment of Electron Delocalization on NMR Chemical Shifts*  
Steinmann, S. N.; Jana, D. F.; Wu, J. I.-C.; Schleyer, P. v. R.; Mo, Y.; Corminboeuf, C. *Angew. Chem. Int. Ed.* **2009**, *48*, 9828.